New applications to in situ-produced cosmogenic nuclides in river sediment:

High mountain belt denudation in the Swiss Alps and Bolivian Andes and sediment transfer and storage in the Amazon basin

Von der Naturwissenschaftlichen Fakultät

der Gottfried Wilhelm Leibniz Universität Hannover

zur Erlangung des Grades einer

DOKTORIN DER NATURWISSENSCHAFTEN

Dr. rer. nat.

genehmigte Dissertation

von

Dipl.-Geow. Hella Wittmann

geboren am 30.04.1979, in Witzenhausen

2008

Referent: Prof. Dr. Friedhelm von Blanckenburg
(Leibniz Universität Hannover)

Koreferent: Prof. Dr. Jérôme Gaillardet
(Institut de Physique du Globe de Paris, Université Paris)

Tag der Promotion: 27.08.2008

Erklärung zur Dissertation

Hierdurch erkläre ich, dass die Dissertation selbständig verfasst und alle benutzten Hilfsmittel sowie evtl. zur Hilfeleistung herangezogene Institutionen vollständig angegeben wurden. Die Dissertation wurde nicht schon als Diplom- oder ähnliche Prüfungsarbeit verwendet.

Hannover, den 27.08.2008

Hella Wittmann

You know a dream is like a river
Ever changin' as it flows
And a dreamer's just a vessel
That must follow where it goes
Trying to learn from what's behind you
And never knowing what's in store
Makes each day a constant battle
Just to stay between the shores...and

I will sail my vessel
'Til the river runs dry
Like a bird upon the wind
These waters are my sky
I'll never reach my destination
If I never try
So I will sail my vessel
'Til the river runs dry

There's bound to be rough waters
And I know I'll take some falls
But with the good Lord as my captain
I can make it through them all...yes

I will sail my vessel
'Til the river runs dry
Like a bird upon the wind
These waters are my sky
I'll never reach my destination
If I never try
So I will sail my vessel
'Til the river runs dry

Yes, I will sail my vessel
'Til the river runs dry
'Til the river runs dry

GARTH BROOKS
▪The River▪

DANKSAGUNG

Mein größter Dank gilt meinem Betreuer, Prof. Friedhelm von Blanckenburg, für die immerwährende Unterstützung, Führung und die Möglichkeit, diese Arbeit durchzuführen. Seine fachliche Kompetenz und Rat sind immer eine große Hilfe gewesen. Auch möchte ich ihm für das Vertrauen danken, mich diese Arbeit eigenständig gestalten zu lassen und für die immer nette Gesellschaft, wie z.B. auf Dienstreisen in Frankreich und Brasilien.

I thank Prof. Jérôme Gaillardet for reviewing my thesis so quickly, coming to my defense, help, discussions, and good company on the Amazon River. Ich danke auch dem Prüfungsvorsitzenden Prof. Andreas Mulch

Big thanks go to my French collaborators, who are Laurence Maurice, thanks very much for the numerous discussions, and Jean-Loup Guyot for sampling, advice, and fruitful discussions on the Amazon. Ein ganz großes Dankeschön geht an Peter Kubik, der mit seinem Engagement, Rat und präzisen Messungen einen großen Teil zum Gelingen dieser Arbeit beigetragen hat. Many thanks also go to Niels Hovius, for sharing his great expertise on rivers in always helpful discussions. I also would like to thank Liz Safran for providing detailed Beni data. Ich danke ebenfalls Tina Kruesmann für die Aufbereitung und Messung der „Valle Maggia“ Proben. Ein ganz großes Dankeschön geht auch an Kevin Norton, für die tolle Bürogemeinschaft, Spaß bei der Feldarbeit und Rat. Vielen Dank auch an Thomas Hoffmann, für die bereitwillige Weitergabe seiner Rhein-Daten.

Ein ganz großer Dank geht and die Mitarbeiter des Instituts für Mineralogie, besonders der Arbeitsgruppe Geochemie, die mir mit vielen anregenden Diskussionen immer wieder gute Impulse gegeben haben, und von denen ich viel gelernt habe. Ich danke daher Ronny Schönberg, Ingo Horn, Michael Staubwasser, Jan Schüssler, Kevin Norton, Monika Gülke, Grit Steinhöfel, Sonja Zink, Jane Willenbring, Jérome Chmeleff und Veerle Vanacker. Spezieller Dank geht an Ronny, der mir das Arbeiten im Labor beigebracht hat, to Jane for help on the Beni, discussions on the model chapter, and reading my Amazon chapter, und an Ingo für die Messung meiner Zirkone und Hilfe bei technischen Fragen und Problemen. Ich danke auch Alexandra Tangen für die Unterstützung im Labor. Meiner „Hiwine“ Kirsten Fromme danke ich für die immer zuverlässige Probenaufbereitung, ein Job der später ebenso zuverlässig von Eva Stiller übernommen wurde. Ich danke ebenfalls dem Team der Werkstatt, insbesondere Willi Hurkuck, Bettina Aichinger, und Otto Diedrich, für die immer super schnelle Bearbeitung von technischen Anfragen. Allen anderen Mitarbeiter des Instituts möchte ich ein universelles Dankschön aussprechen, weil ich mich immer wohl gefühlt habe und Dienstreisen, Seminare und Geländearbeit ohne Eure Gesellschaft nur halb soviel Spaß gemacht hätten.

Den Mitarbeitern des Instituts für Geologie, allen voran Andreas Mulch, danke ich für die Bereitstellung des „Ausweich-Labors“. Ich danke Andreas für die große Hilfe bei der Heilung der „Kinderkrankheiten“ des Labors, die er mir hat zukommen lassen.

I thank Patrick and Fréderique Seyler for assistance in Toulouse and sampling the Branco. I also thank Patricia Moreira-Turcq for matchless organization of the field trip to Brazil, which I had the pleasure to attend. At this point I would also like to say thanks to the boat crew of the *Comandante Quadros II* for help during sampling and the scientists attending the trip, who were good fun. These were Laurence & Patricia, João Bosco, Julien Bouchez, Marc Benedetti, and Polyana Dutra, my boat-roommate. I also thank Emmanuèle Gautier for great discussions on the Beni River, Naziano Filizola for advice on the Amazon basin, and Rolf Aalto for sharing knowledge on the Beni.

Last but not least möchte ich meiner Familie danken, die mir durch finanzielle Unterstützung mein Studium ermöglicht und mir immer mit Rat und Tat zu Seite gestanden hat. Meinem Freund Marcus dank ich, weil er mir Kraft gegeben hat, mich immer geduldig unterstützt, und mir über einige mathematische Schwächen hinweg geholfen hat.

CONTENTS

ABSTRACT I

ZUSAMMENFASSUNG VI

INTRODUCTION 1

I.I Aim, structure, and objectives of this thesis 2
I.II Extensions of the method to applications in non-traditional settings 3
I.II.I State of the art 3
I.II.II Sediment transfer and storage in large depositional basins 4
I.II.III Intrinsic problems of the method encountered in non-glaciated and glaciated mountain ranges 7

CHAPTER 1 The Amazon basin: sediment source areas, evolution of the central lowlands, and sediment transport and depostion during floodplain-channel interaction 9

1.1 Overview 10
1.2 The sediment source areas of the Amazon basin 10
1.2.1 The Andes 11
1.2.1 The Shields 12
1.3 Quaternary evolution of the Amazon lowlands 14
1.3.1 Overview 14
1.3.2 Amazon basin channel patters, floodplain geomorphology, and assessment of sediment transport and deposition 16

CHAPTER 2 Modeling the accumulation and decay of cosmogenic nuclides during sediment storage in floodplain systems 23

Abstract 24
2.1 Introduction 25
2.2 Model setup 25
2.3 Choice of parameters for representative river settings 28
2.4 Model results 29
2.4.1 Testing the model sensitivity to changes in fluvial boundary conditions: the Beni River example 32
2.4.2 The cosmogenic nuclide composition of old deposits 33
2.5 Summary 35

CHAPTER 3 The erosion of the Central Andes and the preservation of the denudation signal in large foreland basins as inferred from cosmogenic ^{10}Be nuclides and river loads 37

Abstract 38
3.1 Introduction 39
3.2 Study area 40

3.3 Sample processing and methodology 43
3.4 ^{10}Be nuclide concentrations measured in floodplain settings 46
3.4.1 The Beni River 46
3.4.2 The Napo River 48
3.4.3 The Mamoré River 49
3.5 Discussion 53
3.5.1 Denudation rates in the upper Beni and Napo catchments 53
3.5.1.1 The upper Beni basin 53
3.5.1.2 The upper Napo basin 55
3.5.2 Denudation rate monitors in the Mamoré basin 56
3.5.3 Assessment of source area denudation rates over different time scales 58
3.5.4 Implications for denudation rate calculations in floodplain settings and comparison with erosion rate data from sediment gauging 62
3.6 Conclusion 66

CHAPTER 4 The quantification of sediment production, mixing, and floodplain burial in the Amazon basin from in situ-produced ^{10}Be and ^{26}Al in river sediment 69

Abstract 70
4.1 Introduction 71
4.2 Study area 73
4.3 Sampling 77
4.4 Methodology 77
4.5 Nuclide concentration results, estimates of denudation rates, and floodplain burial 79
4.5.1 Tributaries to the central Amazon River 79
4.5.1.1 Andean tributaries 79
4.5.1.2 The Guyana craton 82
4.5.1.3 The Brazilian craton 89
4.5.1.4 The Madeira River 91
4.5.2 The main Amazon River system 93
4.5.2.1 The Amazon trunk stream 79
4.5.2.2 The central Amazon floodplain 82
4.6 Discussion 96
4.6.1 Sediment provenance and mixing in the Amazon basin 96
4.6.2 Comparison with gauging-derived erosion rates and sediment flux estimates 99
4.6.3 Sediment budget for the Amazon basin 99
4.7 Summary 103

CHAPTER 5 The relation between rock uplift and denudation from cosmogenic nuclides in river sediment in the Central Alps of Switzerland 107

Abstract 108
5.1 Introduction 108
5.2 Study area, sample characteristics, and lab processing 110
5.2.1 Tectonic evolution of the Alps and Alpine glacial history 110
5.2.2 Recent geodetic uplift pattern 116
5.2.3 Sample characteristics 116

5.2.3.1 Prerequisites 116
a) LGM moraine deposits 116
b) Recent glacial erosion products 118
c) Appropriate catchment sizes for cosmogenic sampling 118
5.2.3.2 Characteristics of basins sampled along an Alpine north-south traverse 119
a) High-Alpine basins 119
b) Swiss Mittelland basins 119
5.2.4 Lab processing and uncertainty assessment 122
5.3 Methodological principles 122
5.3.1 Spatially-averaged denudation, calculation of production rates and corrections applied 122
5.3.1.1 Spatially-averaged denudation rates from cosmogenic nuclides in river sediment 122
5.3.1.2 Production rates 123
5.3.1.3 Corrections for skyline shielding and shielding due to snow and ice 124
5.3.2 Assessment of potential perturbations on denudation rate estimates in complex glaciated mountain ranges 126
5.3.2.1 Approach to cosmogenic steady state after surface zeroing by glaciation 126
5.3.2.2 Cosmogenic nuclide inventory of incorporated moraine material and recent glacial erosion products 127
5.3.2.3 A test of appropriate catchment size 130
5.4 Denudation rate results and basin characteristics 134
5.4.1 Denudation rates for the north-south traverse 134
5.4.2 Assessment of grain size effects 136
5.5 Discussion 137
5.5.1 Comparison with denudation rates from lake fills, river gauging, and fission track data 137
5.5.2 Constraints on factors controlling denudation rates 141
5.5.3 Are denudation and rock uplift rates in equilibrium? 143
5.6 Conclusion 145

REFERENCES 147

APPENDIX A.1 Data 163
A.1.1 ^{10}Be data 163
A.1.2 ^{26}Al data 170

APPENDIX A.2 Sample preparation and laboratory methodology for the separation of cosmogenic ^{10}Be and ^{26}Al 171
A.2.1 Quartz preparation 171
A.2.2 Sample decomposition and ^{10}Be and ^{26}Al separation 172
A.2.3 ^{27}Al-specific methodology 177

CURRICULUM VITAE 178

ABSTRACT

In this thesis, new applications to in situ-produced cosmogenic nuclides in river sediment are developed. I propose that long-lived cosmogenic nuclides (^{10}Beryllium and ^{26}Aluminium) can be used for fingerprinting sediment transfer and routing in large continental-scale basins. Using this method, I identified the sediment source areas to the Amazon basin, and calculated a long-term (several kyr) sediment mass budget from measurements of cosmogenic nuclide concentrations in river sediment. In another complex geomorphic setting, strategies for the application of cosmogenic nuclides were developed in the Central Alps of Switzerland, providing the groundwork for the application of this method in previously glaciated mountain ranges.

Cosmogenic ^{10}Be and ^{26}Al are generated by irradiation of material at the Earth's surface by cosmic rays. Because these nuclides are usually not present in the lithosphere, the accumulation of nuclides can be used for dating of surfaces or measuring erosion rates. In the mineral quartz, usually used due to its simple chemical composition and resistance to weathering, the production rate of ^{10}Be is only 2-60 atoms/$g_{(Qz)}$/yr, depending on altitude and latitude, while that of ^{26}Al is ~6.5 times higher. The production ratio of ^{26}Al/^{10}Be, constant under normal cosmic ray exposure, changes when these nuclides decay radioactively. Therefore, the ratio can be used, for example, to date burial of sediment and rock samples. Cosmogenic ^{10}Be, measured in a handful of stream sediment, is now routinely used to constrain basin-wide denudation rates. This method makes use of ^{10}Be nuclide accumulation due to irradiation on hill slopes and its simultaneous loss during weathering and erosion. In this case the nuclide concentration in sediment is inversely proportional to the denudation rate. In this approach, not much attention has been paid to the potential accumulation of cosmogenic nuclides during transport and storage of sediment in streams. While the transport time scale of bedload in streams is usually too short and cosmogenic nuclides are shielded by water, cosmogenic nuclides may primarily be produced during long-term floodplain storage.

In the Amazon basin storage time scales exceed several kyr. For example in the Beni basin of Bolivia, which is a primary sediment-delivering basin to the Amazon River, 40% of the total sediment volume eroded from its Andean source area is deposited in the river floodplain, not reaching the Amazon trunk stream for possibly thousands of years. However, cosmogenic nuclide measurements of sediment from active, floodplain-traversing rivers suggest that a uniform Andean denudation signal is preserved over floodplain distances of ~800 km, even though sediment is continuously in the state of storage and relocation due to

rapid lateral river migration processes. Invariant nuclide signals in rivers traversing foreland basins were also detected in the Mamoré (Bolivia) and in the Napo (Ecuador) basin.

The fact that neither irradiation nor radioactive decay takes place during floodplain storage was independently confirmed with a depth- and time-dependent numerical box model. Model results show no significant increase in nuclide concentration due to irradiation during time scales of <0.5 Myr, because floodplains are usually very deep and stored sediment is shielded from cosmic rays. At very long time scales (>1 Myr), nuclide decay may substantially reduce nuclide concentrations inherited from previous erosion cycles. However, such long storage times are unlikely in most floodplains, and, as a consequence, a sediment sample collected at any point within the basin up to the outlet will record the denudation rate of the sediment-producing area.

Once this behavior was understood, cosmogenic nuclides were used for fingerprinting source area denudation rates in the Amazon basin. Coarse-grained sediment from cratonic areas records much higher ^{10}Be nuclide concentrations, whereas fine-grained (<500 µm) sediment seems to preserve the low nuclide concentration signal of the Andes. Low ^{26}Al/^{10}Be ratios in some samples show that a fraction of deeply excavated sediment from old (several Myr) floodplain is admixed into the active stream sediment. The low ^{26}Al/^{10}Be signal is primarily inherited from sediment-starved rivers draining cratonic shields (Branco, Negro, Tapajós rivers), but local reworking of Miocene floodplain by the Amazon River is possible, too. When coarse-grained and formerly buried sediment samples are excluded, the fine-grained fraction yields uniform ^{10}Be concentrations over a 3000 km long distance across the Amazon basin from Iquitos to Óbidos. This concentration provides exactly the average denudation rate of the Amazon-draining Central Andes. A cosmogenic nuclide-derived sediment mass budget for the Amazon basin may be calculated. Surprisingly perhaps, sediment discharge from cosmogenic nuclides is only half to one third of the mass budget derived from short-term sediment gauging. Observed discrepancies are attributed to differences in integration time scale.

In the Central Swiss Alps, extensive Last Glacial Maximum (LGM) glaciation has fundamentally perturbed the landscape, so that cosmogenic nuclide steady state assumptions are possibly violated. I therefore investigated the potential influence of shielding from cosmic rays due to snow and glaciers, calculated possible memory from LGM glaciation, and identified the size of watershed appropriate for systematic sampling. I found that memory effects from LGM in rapidly denuding mountain belts can be excluded, as cosmogenic nuclide-derived denudation rates approach steady state within the time scale following LGM

glaciation. It is hence not only possible to measure basin-wide denudation rates in such a setting, but also meaningful results are provided that contribute to the understanding of landscape-forming processes, such as interactions between uplift, denudation, and topography at orogenic scale.

Keywords: Cosmogenic Nuclides, Amazon Basin, Sediment Transfer, Sediment Burial, Cosmogenic nuclide-derived Denudation Rates, Bolivian Andes, Central Alps, Rock Uplift, Numerical Modeling

ZUSAMMENFASSUNG

Die vorliegende Doktorarbeit befasst sich mit der Entwicklung neuer Anwendungen von in situ-produzierten kosmogenen Nukliden aus Flusssediment. Langlebige kosmogene Nuklide wie ^{10}Beryllium und ^{26}Aluminum können in kontinentalen Ablagerungsbecken als charakteristische Indikatoren für Transfer- und Einlagerungsprozesse von Sediment dienen, und sie vermögen die Sedimentliefergebiete unverwechselbar durch eigenständige Nuklidsignale zu repräsentieren. Diese Signale erlauben gleichzeitig quantitative Rückschlüsse auf die Sedimentproduktionsrate des Liefergebiets. Die Sedimentliefergebiete des Amazonasbeckens wurden so identifiziert und außerdem eine auf kosmogenen Nukliden basierende Sediment-Massenbilanz erstellt. Des Weiteren wurden Strategien für die Anwendbarkeit der Methode in ehemals vergletscherten Gebieten entwickelt.

Kosmogenes ^{10}Be und ^{26}Al werden durch kontinuierliche Bestrahlung der Erdoberfläche mit kosmogenen Partikeln produziert. Diese Nuklide sind normalerweise nicht in der Lithosphäre vorhanden, bevor eine Erzeugung durch induzierte Kernreaktionen mit kosmogenen Partikeln im oberflächennahen Material erfolgt. Daher ermöglicht die Akkumulation von Nukliden mit der Zunahme der Expositionszeit die Datierung von Oberflächen, wie z.B. Flussterrassen, Moränen und Lavaströmen, aber auch die Quantifizierung von Erdoberflächenprozessen durch die Ermittlung von Denudationsraten. Die Produktionsrate von ^{10}Be im Mineral Quarz, welches bevorzugt wegen des simplen Chemismus und der hohen Verwitterungsresistenz benutzt wird, beträgt nur ca. 2-60 Atome/$g_{(Qz)}$/Jahr, und ist abhängig von der geografischen Breite und Höhe des Probenpunktes. Die Produktionsrate von ^{26}Al ist an der Erdoberfläche 6.5-mal höher als die von ^{10}Be. Unter konstanten Bestrahlungsbedingungen an der Erdoberfläche resultiert daraus ein konstantes Verhältnis von ^{26}Al/^{10}Be, welches sich aber durch radioaktiven Zerfall bei Abschirmung vor kosmogener Bestrahlung ändert. Daraus resultiert die Anwendbarkeit der Methode für die Datierung von Sediment oder Gestein, welches von kosmogener Bestrahlung abgeschirmt war. Die Messung von kosmogen-produziertem ^{10}Be in Flusssediment ist heute Routine für die Ermittlung Einzugsgebiet-weiter Denudationsraten. Basierend auf Nuklidakkumulation durch Bestrahlung auf Talhängen und gleichzeitigem Verlust durch Verwitterung und Erosion ist die Nuklidkonzentration eine inverse Funktion der Denudationsrate des Liefergebiets. Dieser Ansatz berücksichtigt jedoch nicht die Akkumulation von kosmogenen Nukliden während des Sedimenttransports in Flüssen und die Ablagerung von Sediment in Überflutungsebenen. Die Akkumulation von Nukliden während des Sedimenttransports im

Fluss ist vernachlässigbar aufgrund der Abschirmung durch Wasser, so dass eine Produktion von Nukliden primär während der Ablagerung in großen Überflutungsebenen und Flussauen stattfindet.

Im Amazonasbecken erstreckt sich der Zeitraum der Sedimentablagerung über mehrere tausend Jahre. Zum Beispiel wird angenommen, dass ca. 40% des Sediments welches aus dem Liefergebiet der Anden stammt, in den großen Flussauen der Vorlandbecken des Amazonas (z.B. im Becken des Beni in Bolivien) abgelagert wird und somit vorerst nicht den Hauptfluss erreicht. Eine Bestimmung der kosmogenen Nuklidkonzentration von Sediment aus aktiven, lateral beweglichen Flüssen ergab, dass ein gleichförmiges kosmogenes Denudationssignal von den Anden an die Flussauen weitergegeben wird, obwohl das in den Überflutungsebenen befindliche Sediment kontinuierlich abgelagert, eingelagert und umgelagert wird durch fortwährende, schnelle laterale Migration des Flussbetts. Konstante Denudationssignale der Anden wurden ebenfalls über Vorlandbecken-weite Distanzen in den Einzugsgebieten des Napo (Ecuador/ Peru) und des Mamoré (Bolivien) festgestellt.

Eine zeit- und tiefenabhängige numerische Modellierung von kosmogenen Nuklid-konzentrationen liefert eine unabhängige Bestätigung dessen, dass weder Bestrahlung noch radioaktiver Zerfall während der Sedimentablagerung und -einlagerung in großen Flussauen über Zeitskalen von mehreren hunderttausend Jahren (<0.5 Ma) von Bedeutung sind. Dies ist der Fall, da eine tiefe Einlagerung weitere Bestrahlung stark vermindert. Über sehr lange Einlagerungszeiträume findet jedoch eine Verminderung durch radioaktiven Zerfall der aus vorangegangenen Erosionszyklen ererbten Nuklidkonzentration statt. Eine solche erheblich längere Einlagerungszeit ist allerdings nicht für in dynamischen Überflutungsebenen abgelagertes Sediment charakteristisch, sondern in alten, möglicherweise tertiären Sedimentablagerungen anzutreffen, die heute von Flüssen mit großen Abfluss aber geringen Sedimentfrachten angeschnitten werden.

Das Verständnis dieser Zusammenhänge und Prozesse führte zu der Anwendung kosmogener Nuklide als charakteristische Sedimentliefergebiets-Indikatoren im Amazonas-becken. Grobkörniges (>500 µm) Sediment liefert wesentlich höhere ^{10}Be Nuklid-konzentrationen als feinkörniges Sediment, welches das charakteristisch niedrige Nuklidsignal der Anden zu konservieren scheint. Niedrige ^{26}Al/^{10}Be Verhältnisse für einige Proben zeigen auf, dass Sedimentmischung zwischen ehemals abgeschirmtem, alten Sedimentmaterial und rezentem fluvialem Erosionsmaterial vorliegt. Am häufigsten auffindbar ist dieser Prozess in Flüssen der alten präkambrischen Schilde (Branco, Negro, und Tapajós), allerdings ist die Erosion von miozänen Sedimentschichten im Amazonas

Hauptfluss ebenfalls stellenweise angezeigt. Ein Ausschluss der grobkörnigen und ehemals abgeschirmten Sedimentfraktion resultiert in der Überlieferung eines über tausende von Kilometern von den Zentralanden bis Manaus in Brasilien hinweg konstanten kosmogenen Nuklidsignals, welches exakt dem Denudationssignal des andinen Liefergebiets entspricht. Demzufolge kann eine Sediment-Massenbilanz für das Amazonasbecken auf der Basis kosmogener Nuklide erstellt werden. Beachtenswert ist, dass der anhand kosmogener Nuklide gemessene Sedimentaustrag nur ca. die Hälfte bis ein Drittel dessen beträgt, was mittels kurzzeitiger Flussfrachtmessungen als Sedimentaustrag für das Amazonasbecken ermittelt wurde. Diese Diskrepanz wird den unterschiedlich langen Integrationszeiträumen beider Methoden zugesprochen.

Ebenfalls im Rahmen dieser Promotionsarbeit entwickelte Strategien für die Anwendung der Methode in den Schweizer Zentralalpen beinhalten die Berücksichtigung von einstmals signifikanter Vereisung während des letzen glazialen Zyklus (LGM), was zu einer bis heute andauernden Störung des geomorphologischen Gleichgewichts führte und somit auch eine potenzielle Beeinträchtigung der kosmogenen Nuklidmethode nach sich zieht. Eine Untersuchung einer möglichen Einflussnahme von Abschirmung kosmischer Bestrahlung durch Vereisung und Schnee, der Quantifizierung des kosmogenen „Gedächtnisses“ durch LGM Vereisung und der Bewertung geeigneter Beprobungsskalen wurde durchgeführt. Diese Studie zeigt, dass kosmogene Nuklide sehr wohl anwendbar sind in ehemals vereisten Gebieten, da sich das Gleichgewicht zwischen Nuklidproduktion und -export in Gebieten mit hohen Erosionsraten innerhalb des Zeitraumes nach der letzten Vereisung wiederhergestellt hat. Demzufolge ist die Ermittlung von Denudationsraten basierend auf der Messung kleinster Mengen von kosmogenen Nukliden nicht nur in ehemals und auch teilweise heute noch vereisten Gebieten möglich, sondern sie liefert auch bedeutende Ergebnisse, die zu unserem Verständnis der Landschaftsentwicklung beitragen, da sie die dynamische Interaktion von z.B. Hebung, Denudation und Topographie in Orogenen zu entschlüsseln vermögen.

Schlagwörter: Kosmogene Nuklide, Amazonasbecken, Sedimenttransfer, Sediment-ablagerung, Kosmogene Nuklid-Basierende Denudationsraten, Bolivianische Anden, Zentralalpen, Hebung, Numerische Modellierung

INTRODUCTION

I.I AIM, STRUCTURE, & OBJECTIVES OF THIS THESIS

Since the mid-1990´s, the quantification of spatially-averaged denudation rates from in situ-produced cosmogenic nuclides has advanced to a robust method for which the field work requires no more than a handful of sediment from a stream, followed by chemical sample preparation and measurement of these rare isotopes by Accelerator Mass Spectrometry. In a brief period, the application of this method to a variety of geomorphic settings has profoundly changed our understanding of rates of landscape change, and still does. It is the main objective of this study to broaden the range of potential applications to non-steady state settings like formerly glaciated orogens and depositional basins that may become routinely investigated with this method in the years to come. In a step towards this aim, I have firstly tested the feasibility of determining denudation rates in a large Amazon tributary, where sediment is subjected to significant storage. I then proceeded to investigate an even larger system, the central Amazon basin, to evaluate nuclide behavior during large-scale channel-floodplain interaction. Finally, a further complicated non-traditional setting was investigated in the form of a once glaciated mountain range, because here, extensive LGM glaciation has fundamentally perturbed the landscape, so that cosmogenic nuclide steady state assumptions are possibly violated.

This thesis is subdivided into five main chapters preceded by an introductory section. The introduction will address prerequisites that are necessary to follow when cosmogenic-nuclide based denudation rates are applied to non-traditional settings.

Chapter 1 presents an extensive introduction on the geologic and tectonic framework of the Amazon basin, on sediment routing from the source areas, and sediment residence time in Amazonian lowlands, and will serve to give a broad, comprehensive overview.

Chapter 2 presents the validation for using cosmogenic nuclide-derived denudation rates in floodplain settings by numerically modeling cosmogenic nuclide response to channel-floodplain interaction in depositional basins. Model runs show no significant increase or decrease in nuclide concentrations for most fluvial settings except sediment-starved systems in old cratonic areas. Thus, I will show that the cosmogenic nuclide signal of the sediment-generating source area is preserved over foreland basin distances and spatially-averaged cosmogenic nuclide-based denudation rates may be calculated for these settings.

Chapter 3 shows that basin-wide denudation rates from cosmogenic nuclides can be measured in floodplain settings of the Beni and Mamoré rivers in Bolivia, and the Napo River in Ecuador. Comparison with Andean source-area denudation rates shows that cosmogenic nuclides measured in the floodplain yield the robust denudation signal of the sediment-contributing areas over foreland basin distances despite millennial-scale sediment storage.

In chapter 4, cosmogenic nuclides are used as fingerprints within the central Amazon River system. Coarse-grained sediment from cratonic areas is much more abundant in ^{10}Be nuclides, and also seems to be affected by long-term floodplain storage, indicated by low ^{26}Al/^{10}Be ratios. The Andean nuclide signal is best preserved in fine-grained (<500 μm) sediment, as this signal is shown to be invariant over a 3000 km distance across the Amazon basin. Thus, this method can be used for the long-term estimation of sediment volumes transferred across large-scale depositional basins.

Chapter 5 presents a study conducted in the Central Alps of Switzerland that gives an overview of necessary prerequisites of using the cosmogenic nuclide-method in a formerly heavily glaciated mountain belt. It is not only possible to measure basin-wide denudation rates in such a setting, but also meaningful results are provided that contribute to the understanding of landscape-forming processes, such as interactions between uplift, denudation, and topography at orogenic scale. This work is published in the *Journal of Geophysical Research-Earth Surface*, Volume 112, doi: 10.1029/2006JF000729 in 2007.

I.II EXTENSIONS OF THE METHOD TO APPLICATIONS IN NON-TRADITIONAL SETTINGS

I.II.I State of the art

The determination of spatially-averaged denudation from cosmogenic nuclides in river sediment has profoundly changed our understanding landscape evolution, as cosmogenic nuclides provide a denudation rate tool that can quantify rates of landscape change at weathering-relevant time scales, thus filling the gap between long-term denudation rates from thermochronology and sediment budgets from lake fills (10^4 to 10^6 yr), and short-term river loads (10^1 yr). The measured cosmogenic denudation rates integrate over a time scale (10^2 to 10^4 yr) that is sufficiently robust to be insensitive to very short-term denudational

perturbations (human influence, short-term climate oscillations), and that is meaningful for time scales of both rock weathering and rock uplift [von Blanckenburg, 2005]. It can be used to decipher feedbacks between denudation, topography, and rock uplift [Riebe *et al.*, 2000; Matmon *et al.*, 2003a; Safran *et al.*, 2005; Binnie *et al.,* 2007; Hancock & Kirwan, 2007; Reinhardt *et al.*, 2007], to unravel the relationships between physical erosion and chemical weathering when coupled with zirconium-normalized mass balances or river water chemistry [Riebe *et al.*, 2001a; Riebe *et al.*, 2003; von Blanckenburg *et al.*, 2004; Kirchner *et al.*, 2006; Burke *et al.,* 2007], and to determine Quaternary rates of landscape change [Granger *et al.*, 2001; Schaller *et al.*, 2002; Schaller *et al.*, 2004; Ferrier *et al.,* 2005; Norton *et al.*, 2008]. Escarpment retreat rates can be quantified [Heimsath *et al.*, 2000; Bierman & Caffee, 2001; Vanacker *et al.*, 2007a], and locii of neotectonic forcing can be identified [Riebe *et al.*, 2000; Benedetti *et al.,* 2002; Wobus *et al.*, 2005; Quigley *et al.*, 2007]. In combination with other radioactive or stable cosmogenic nuclides, we can quantify glacial erosion [Balco & Stone, 2005; Miller *et al.*, 2006; Staiger *et al.*, 2006; Heimsath & McGlynn, 2008], investigate the discrete burial or exposure of landscape features, or assess complex burial histories [Granger *et al.*, 2001; Matmon *et al.*, 2003b; Balco & Schaefer, 2006; Anthony & Granger, 2007; Haeuselmann *et al.*, 2007]. Important for this study however are the attempts made to quantify sediment transport and mixing rates, and to identify sediment source areas [Clapp *et al.,* 2000; Clapp *et al.*, 2002; Perg *et al.*, 2003; Nichols *et al.*, 2005], for which Bierman & Steig [1996] have provided a first theoretical framework.

I.II.II Sediment transfer and storage in large depositional basins

Cosmogenic nuclides accumulate in minerals on hill slopes during weathering and denudation, where the nuclide accumulation is a function of the prevailing denudation rate. If the removal of nuclides from the hill slope by erosion or decay equals their production by cosmic rays, conditions for spatially-averaged erosion are fulfilled [Lal, 1991; Bierman, 1994; Granger *et al.*, 1996], and if the time required to erode a layer of thickness z^* (≈60 cm in rock), defined by the erosion time scale z^*/ε, is much longer than the time scale of sediment transport in rivers. On the other hand, cosmogenic nuclides also can accumulate during transport and storage of sediment in streams. The time scale of bedload transport in streams is usually much shorter than that of hill slope processes [Whipple & Tucker, 1999]. During storage of sediment in floodplains however, which may encompass several thousand to even

million years in continental-scale basins, nuclide accumulation at the floodplain surface is proportional to the sediment storage time, while at depth it is also a function of the exponentially decreasing production rate. If shielding from cosmic rays is high at great depths, then nuclide concentrations decrease due to radioactive decay. As a consequence, the prerequisites for calculating spatially-averaged denudation rates are not met in depositional basins, where the rate of nuclide production does not necessarily equal the nuclide export rate.

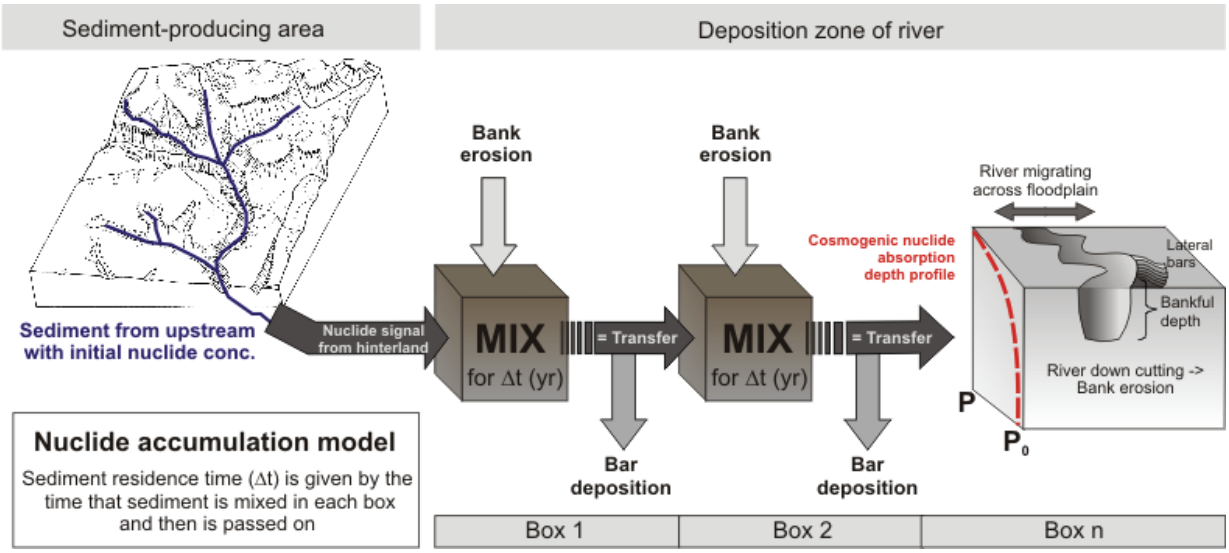

Figure I.1 Illustration of compartment-based nuclide accumulation model

During the course of this PhD, this problem was tackled by a) numerical modeling cosmogenic nuclide behavior (that is decrease or increase in nuclide concentration with respect to that of the sediment-producing area) during floodplain-channel interaction; and b) by measuring the ^{10}Be and ^{26}Al nuclide concentrations of sediment from the active floodplain river bed in large Amazon tributaries. Our model setup is outlined in Figure I.1.

Modeling results suggest that for most settings at sediment residence time scale less than ~0.5 Myr, the accumulation due to irradiation or decrease of nuclides due to decay in the floodplain is negligible with respect to analytical precision and variability of source area denudation rates. This is because floodplain storage is usually deep, so that nothing but the uppermost meters of sediment are being irradiated, and routing of sediment discharged from the source areas is rapid, which precludes production of nuclides in the floodplain due to long-term cosmic ray exposure. Thus, cosmogenic nuclides with long half-lives such as ^{10}Be and ^{26}Al do not record the transport and storage component of cosmogenic nuclide production associated with floodplain residence, but preserve the erosion signal of the sediment-producing area. Measurements of cosmogenic nuclides in large Amazon depositional systems

support our model results; one prerequisite for calculating spatially-averaged hinterland denudation rates from floodplain samples is however that cosmogenic nuclide production rates are scaled to altitudes and latitudes of the areas that produce sediment, because otherwise, denudation rates will decrease artificially as more and more lowland area is included in the production rate estimation (see Figure I.2).

The potential of this method when applied to large depositional basins could involve "in-situ" stratigraphic sediment-budgeting with a long-term temporal resolution in order to deconvolve sediment deposition and associated petroleum reservoir potentials on continental scales.

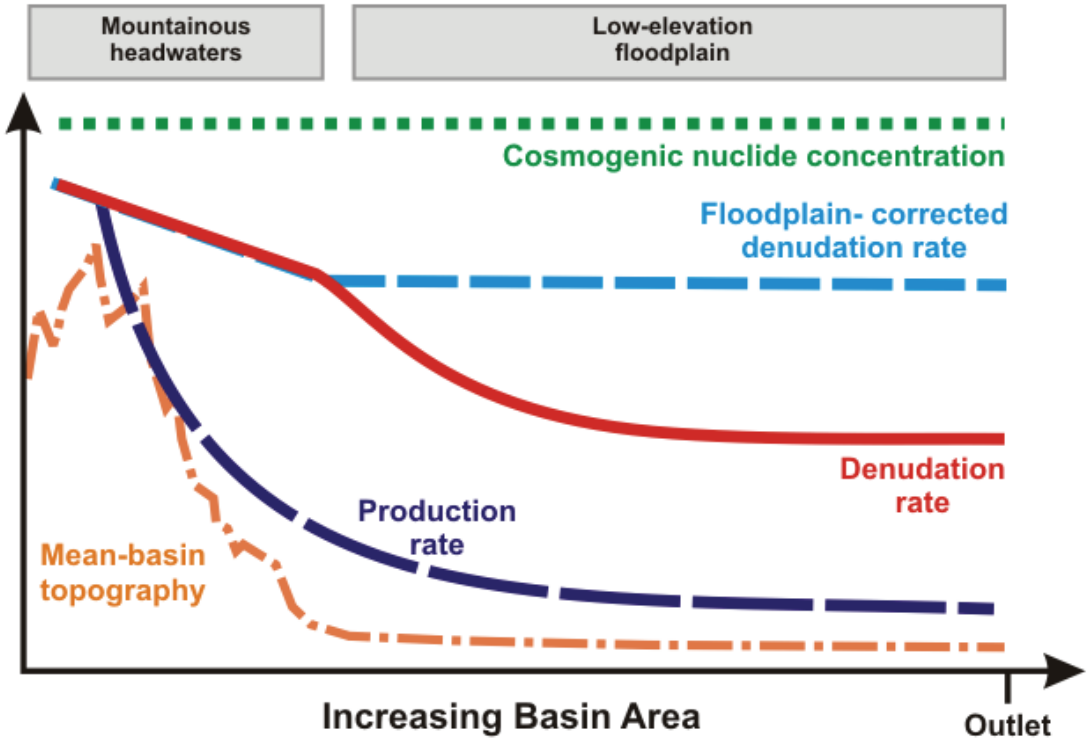

Figure I.2 Schematic illustration of the relations between basin topography, production rate of cosmogenic nuclides, and basin-wide cosmogenic nuclide-derived denudation rate. A floodplain-corrected denudation rate may be calculated for any point within the basin up to the outlet if a production rate scaled to the high-topography sediment-providing area is used. Otherwise, denudation rates will decrease artificially as the production rate integrates over lowland area that does not produce sediment.

I.II.III Intrinsic problems of the method encountered in non-glaciated and glaciated mountain ranges

In order to decipher the sediment routing and storage in large depositional basins using cosmogenic nuclides, the denudation magnitude of the sediment-supplying area as well as its temporal and spatial variability have to be known. For this reason, I evaluated the denudation history of the presently non-glaciated Bolivian Andes from existing databases including long-term fission-track [Safran *et al.*, 2006], medium-term cosmogenic-based [Safran *et al.*, 2005], and short-term gauging-derived [Guyot, 1993; Guyot *et al.,* 1996] monitors. It may not be surprising that the different methods record different rates of erosion due to their different integration time scales, but aside from methodological bias, temporal non-uniform denudation is nevertheless indicated by Holocene rates being higher than preexisting during the Neogene in the Bolivian Andes. Spatially-non uniform denudation is introduced by large mass wasting events, preferably discharging deeply buried, low-concentrated sediment into streams, thus overestimating resulting denudation rates. The trigger to massive land sliding is usually found in abnormally high rainfalls due to the El Niño/ Southern Oscillation (ENSO) phenomenon, which could cause temporally non-uniform denudation rates. Also, non-uniform quartz distribution biases the denudation rate towards basins with high quartz content, which in some parts of the Bolivian Andes coincides with locally high anthropogenic disturbance due to gold mining and recent road construction.

In the formerly glaciated Central Alps of Switzerland, the sensitivity of the method as applied to high mountain belts to certain perturbations first has to be established; these specifically are (a) the approach of cosmogenic nuclides to steady state after LGM (Last Glacial Maximum) glaciation, (b) the nuclide inventory of potentially incorporated moraine and glacial material, and (c) watershed sizes that are too small or too large for representative sampling.

CHAPTER 1

THE AMAZON BASIN: SEDIMENT SOURCE AREAS, EVOLUTION OF THE CENTRAL LOWLANDS, AND SEDIMENT TRANSPORT AND DEPOSITION DURING FLOODPLAIN-CHANNEL INTERACTION

1.1 OVERVIEW

The Amazon River is the world's largest fluvial system in terms of discharge and drainage area; it comprises 15% of the world's total runoff (~210,000 m^3/s; [Molinier *et al.*, 1996]) and about 40% of the total area of South America (~6.1×10^6 km^2). The Amazon basin extents roughly from 5°N to 20°S latitude and discharges its water to the Atlantic through its ~330 km wide estuary located at ~1°S (see Figure 1.1). The tectonic setting comprises the rapidly eroding Andean range, which accounts for ~11% of the total basin area, the ancient crystalline shields, e.g. the Guyana shield to the north and the Brazilian shield to the south, together accounting for 44% of the total basin area, and the low-lying areas of the Amazon basin, which comprises the deforming foreland basins to the west, and the subsiding central Amazonian lowlands to the east.

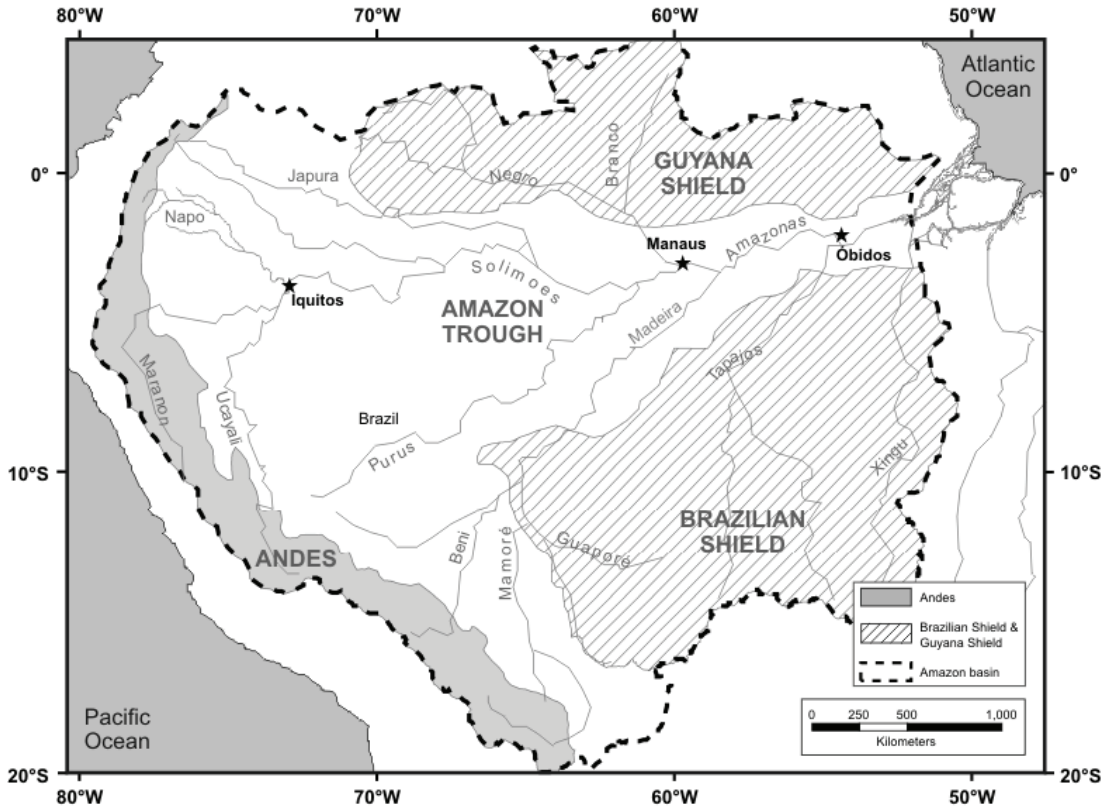

Figure 1.1 Extent and structural units of the Amazon basin

In the following, we will first give an overview of the sediment-producing areas, the Andes and the shields, respectively, and will then proceed to assess the Quaternary evolution of rivers and floodplains of the Amazonian lowlands in terms of geology, tectonics, channel-floodplain interaction, and sediment storage and transfer.

1.2 THE SEDIMENT SOURCE AREAS OF THE AMAZON BASIN

1.2.1 The Andes

The Andes (e.g. the Eastern Cordillera) and the adjacent fold-and-thrust belt of the Sub-Andes (also called "Piedmont") cover only about 800,000 km^2 of the basin, but they contribute more than 90% of the total suspended load carried by the Amazon River [Meade *et al.*, 1985]. The Andes consist primarily of high relief zones of sedimentary and igneous rocks, metamorphosed to a varying degree [Putzer, 1984]. Their tectonic setting is complex, with ongoing subduction of the Nazca plate causing spatially-variable uplift of the orogen. The uplift history of the Andes was recently reviewed by Gregory-Wodzicki [2000], finding that uplift has been absent for the northern Andes from late-Tertiary to modern times, and in the central Andean case, uplift rates were constant at a rate of 0.2-0.3 mm/yr for the last 10 Myr.

For the central Bolivian Andes, estimates on the medium- and long-term denudation rate histories are available. Denudation rates derived from fission track average over ~0.3 mm/yr at time scales of 10^6 yrs [Safran *et al.*, 2006], and denudation rates from cosmogenic nuclide analyses average over ~0.5 mm/yr for ~10^3 yr time scales [Safran *et al.*, 2005]. New cosmogenic nuclide data from this study for the southern central Andes (>15°S) average to ~0.4 mm/yr on the same time scale (see Chapter 3). Short-term erosion rate estimations are available for the central and southern Bolivian Andes, using several different methods [e.g. gauging and land-slide mapping; Guyot, 1993; Guyot *et al.*, 1996; Blodgett & Isacks, 2007]. Methods integrating over short time scales (e.g. a few years) generally record notably higher erosion rates than medium- to long-term denudation meters (see Figure 1.2). Taking the long-term estimation, the central Andean range has been supplying 500-600 Mt/yr of sediment into the Amazon basin throughout the late Cenozoic [Mertes & Dunne, 2007].

Climatic diversity within the Andes is reflected by basins featuring semi-arid zones of the Altiplano to hyper-humid basins with tropical forest [Guyot *et al.*, 1996]. Generally, the equatorial Andes are not subjected to a strong seasonality in climate, but annual precipitation exceeds 2000 mm/yr [Roche & Jauregui, 1988]. However, the climate in the Andes has not been stable during the late Cenozoic, but has alternated between cooler-drier and warmer-wetter stages [Iriondo, 1999; van der Hammen & Hooghiemstra, 2000; Mertes & Dunne, 2007], which may have affected denudation magnitude in the Andes. For example, the Central Andes are thought to have experienced a phase of aridity with very low rates of precipitation during the mid-Holocene [Rowe *et al.*, 2002; Abbott *et al.,* 2003; Servant & Servant-Vildary, 2003].

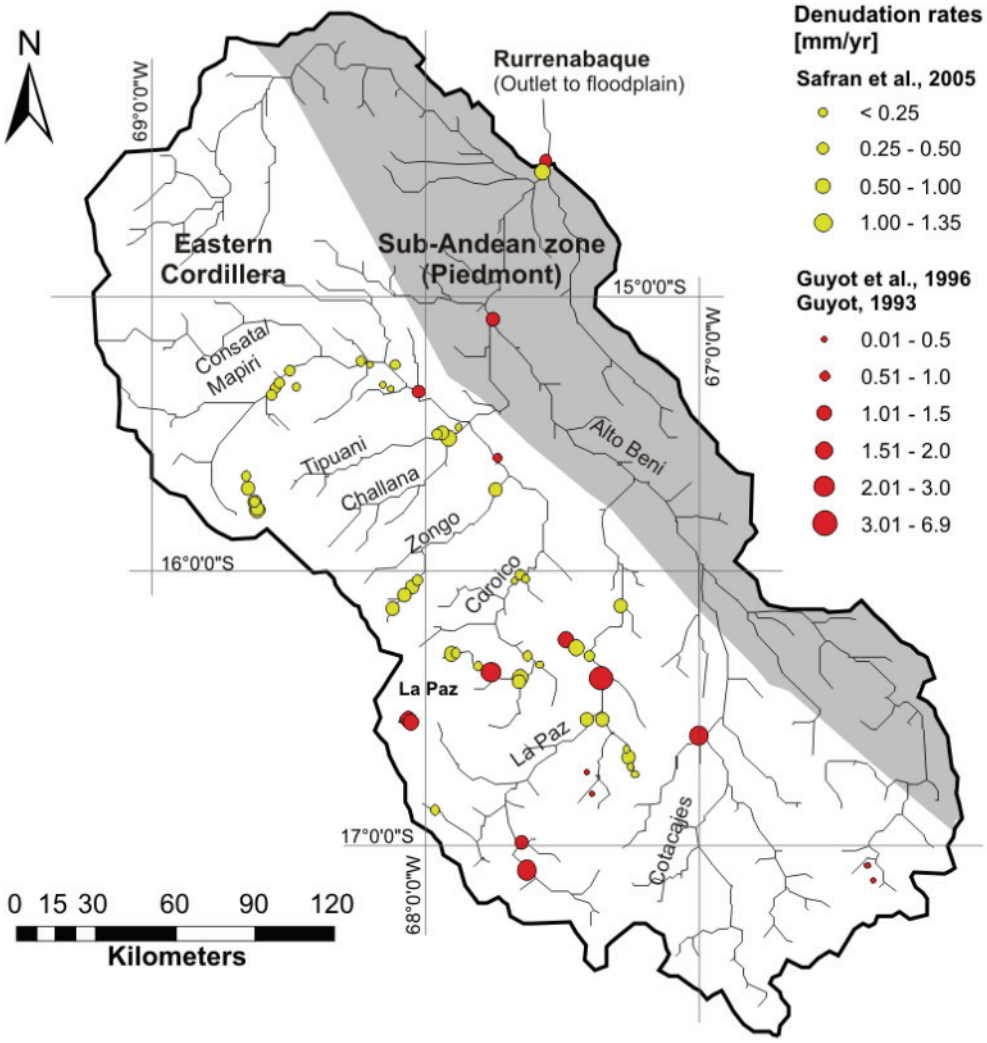

Figure 1.2 Upper Beni basin, Bolivian Andes. Yellow circles denote cosmogenic-nuclide derived denudation rates measured by Safran *et al.* [2005], and red circles denote sediment-gauging derived erosion rates from Guyot et al. [1996] and Guyot [1993], illustrating the different integration time scales of cosmogenic nuclide-based denudation rates (several kyr) and erosion rates from river loads (several decades).

1.2.2 The Shields

The Brazilian and the Guyana shields flank the Amazon trough to the south and to the north; they are developed on Precambrian crystalline rocks with deeply weathered low-gradient terrains, interrupted by steeper slopes with thin soils on upstanding granitic tafelbergs, and also display younger sedimentary rocks at the edges of the cratonic platforms [Hasui & Almeida, 1985; Mertes & Dunne, 2007]. According to Stallard [1985], long-term uplift of the shields persisted since the Tertiary at an order of 0.01-0.02 mm/yr, which should encompass very low long-term denudation rates. According to a more modern view by Edmond *et al.*

[1995], low denudation rates in the shields persist because relief-rejuvenation processes are absent due to long-term tectonic stability incorporating only a passive uplift component causing slow incision in basement rocks, apparently not enhancing erosion over long time periods as hill slopes are covered by thick, heavily weathered regoliths [Gibbs & Barron, 1983; Voicu *et al.*, 2001]. This results in very low suspended sediment loads, but high discharge of water [Sioli, 1957]. For example, the Negro river draining the Guyana shield is ranked as the fifth largest river of the world in terms of discharge, but its suspended load is negligible ([Franzinelli & Igreja, 2002; Laltrubesse & Franzinelli, 2005]; see Figure 1.3).

Climate is tropical for both shields with mean annual precipitation rates of ~1000 mm, and vegetation is dense with tropical rain forest in the Guyana headwaters, and in lower basin parts displaying flat savannas with sparse vegetation [Franzinelli & Igreja, 2002; Latrubesse *et al.*, 2005]. In the Brazilian shield, the headwaters display more savanna-type dry forest, with an increasing fraction of tropical rain forest present to the northern, lowland shield areas [Irion *et al.*, 2006].

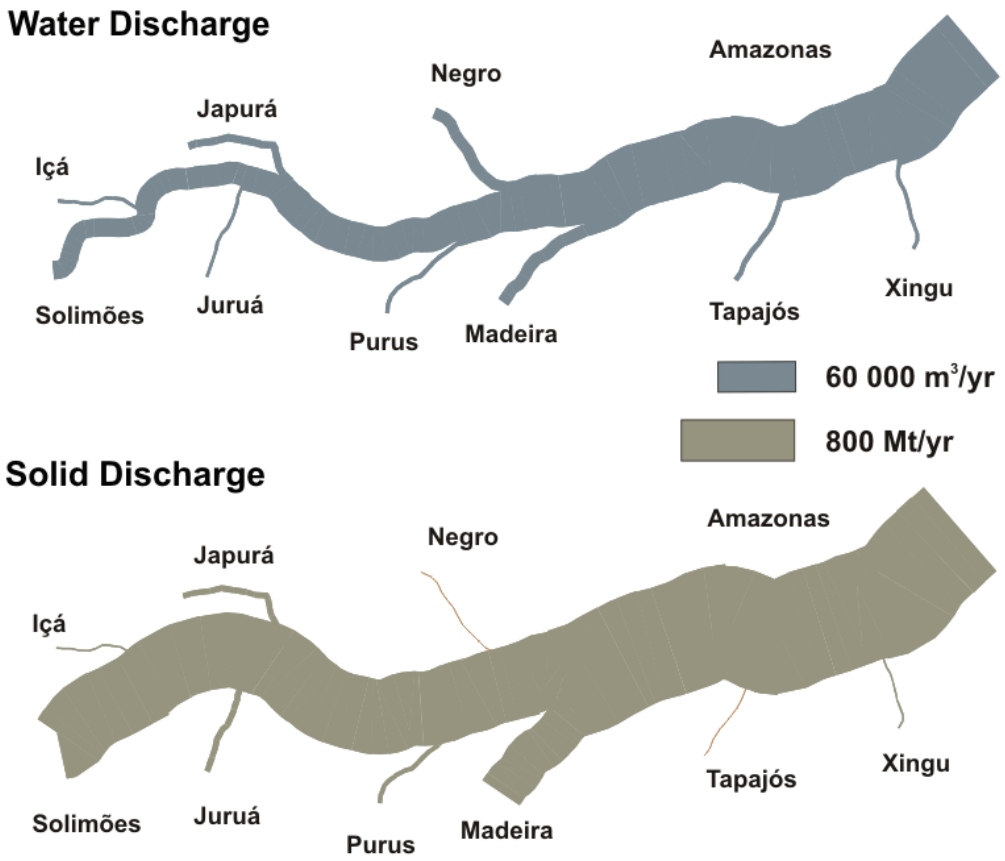

Figure 1.3 Water and solid discharge of the Amazon at its confluence (modified after HIBAM, 2003; graphic courtesy of P. Seyler). Solid discharge is total suspended solid, based on sediment gauging data of the last ~10 years.

Mining has recently become an important economically factor in the Guyana and Brazilian shields. Ore deposits of tin, gold, and associated sulphides are enriched due to the high degree of tropical weathering [Gibbs, 1967], and are mined on the large scale since the 1980´s [Roulet *et al.*, 2000].

1.3 QUATERNARY EVOLUTION OF THE AMAZON LOWLANDS

1.3.1 Overview

The formation of the modern Amazon drainage network with east-ward flow to the Atlantic is a relatively modern feature and tightly linked to the rise of the Andean range during Miocene times [Hoorn *et al.*, 1995]. In detail, during middle Miocene times, the Amazon River was first established due to uplift of the Eastern Cordillera, but drainage was still connected to the Orinoco system. Substantial Andean uplift in the late Miocene caused the Orinoco to change its course, and the Amazon River established a connection to the Atlantic, which is indicated by the mineralogical composition of Early Miocene deposits in northwestern Amazonia [Hoorn *et al.*, 1995]. Climate in the Amazon basin is tropical with dense, rain forest vegetation and average annual precipitation rates of ~2000 mm/yr with a pronounced rainy season [Clapperton, 1993].

The overall trough architecture comprises two distinct settings, with the deforming Molasse foreland basins to the northwest and southwest, and the subsiding central Amazonian valley, that is underlain by a 6000 m deep east-west trending sag in the crust between the Guyana and the Brazilian shields [Caputo, 1984; Mertes & Dunne, 2007]. In the Andean foreland basins, substrate lithology is young due to Andean sediment discharge, but with increasing distance from the Andean front, surface rocks become successively older up to Cretaceous age east of the Amazon-Negro confluence, and also display a trend from more fluvial to more lacustrine units [Rossetti *et al.*, 2005]. The Andean foreland basin to the north is mainly fed by the Solimões, formed by the Marañón and Ucayali rivers, which drain the Ecuadorian and Peruvian Andes, and the southern Amazonian foreland basin is mainly fed by the Beni and Mamoré rivers, which drain the Bolivian Andes [Dumont & Fournier, 1994; Dumont, 1994]. It has been estimated by Guyot [1993] that roughly 40% of Andean sediment flux is intercepted and deposited in the basins close to the Andean foothills. Modern tectonic control on fluvial aggradation is for example very clearly indicated for the Marañón basin, where annual inundation of an area of ~70,000 km^2 is attributed to Quaternary uplift at the

basin's eastern margin, known locally as the Iquitos arch [Putzer, 1984; Rasanen *et al.*, 1990; Dumont & Garcia, 1991; Roddaz *et al.*, 2005]. The resulting fluvial pattern is characterized by highly mobile rivers that rework large parts of their floodplain beds by rapid migration and frequent avulsion [Kalliola *et al.*, 1992; Gautier *et al.,* 2007;], with their channel belts only being confined by ~30 m high, never flooded terraces ("terra firme") on either side of the river channels that are attributed to Quaternary arch-related uplift [Dumont *et al.,* 1991; Mertes & Dunne, 2007].

The central Amazon lowland is dominated by a vast alluvial plain of an approximate extent of 90,000 km^2 [Sippel *et al.*, 1992], bordered by discontinuous Quaternary and Tertiary terraces that are generally ~5-15 m above the regularly inundated surface, except in reaches where recent uplift has generated terraces of up to 300 m in elevation (e.g. in the lower Tapajós reach, see Costa *et al.* [2001] and Mertes & Dunne [2007]).

The evolution and geographic trend of the modern Amazon drainage pattern is attributed to intra-plate tectonics, which involves large-scale faults of the basement that propagate through overlying sedimentary rocks [Caputo, 1984; Putzer, 1984; Costa *et al.*, 2001]. A major feature is the occurrence of four structural highs, or arches (the Iquitos, Jutaí, Purús, and Gurupá arch; see Figure 1.4), from near the Peruvian border to the Amazon mouth, which cause the Amazon river to steepen in gradient, narrow its floodplain, and generally restrict channel movement [Mertes *et al.*, 1996; Dunne *et al.,* 1998].

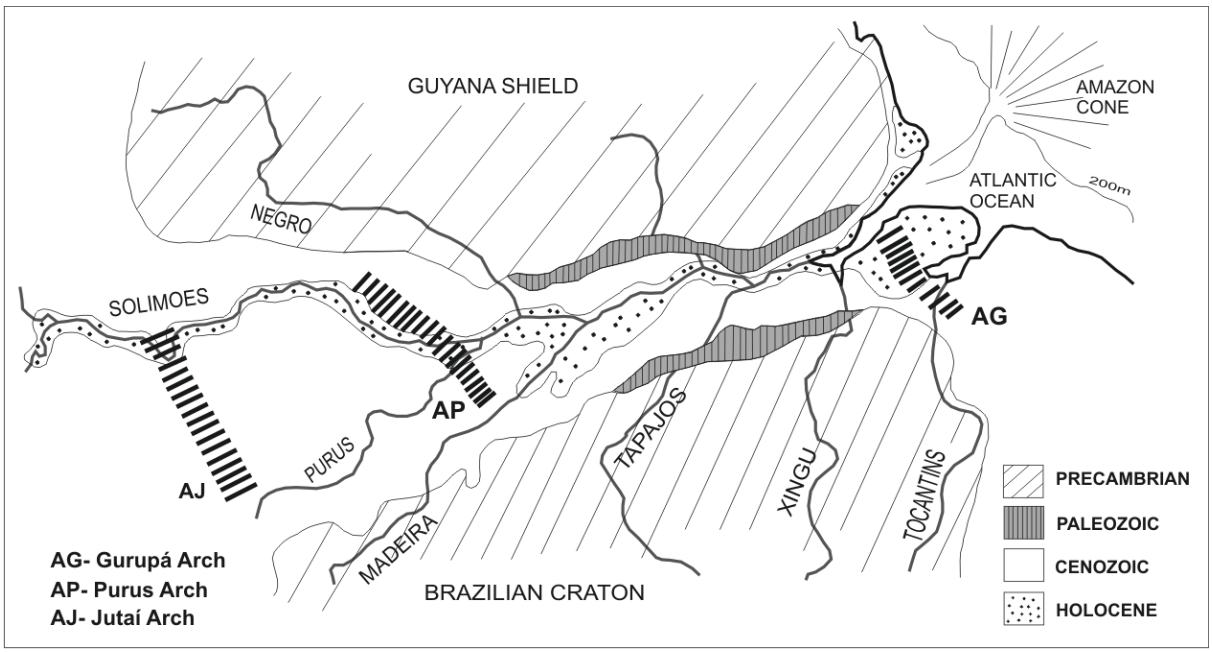

Figure 1.4 Simplified geologic map of the central Amazon lowlands, modified after Putzer [1984]. Not to scale.

Other effects of intra-plate tectonics on the central Amazonian River system, such as the development of the Tapajós River mouth into a river-lake, are attributed to the presence of reverse faults and fold and strike-slip systems mainly trending NE-SW, which have been reactivated since the Miocene, and ultimately cause alternating uplift and subsidence of crustal segments along the Amazon plain [Costa *et al.*, 2001]. Besides tectonic influence on the modern drainage, the impoundment of river-lakes for example could also be attributed to Holocene sea level rise, because low sea levels had produced incised valleys that began to fill as the sea level rose again except for rivers with very low sediment load [Irion *et al.,* 1995; Irion *et al.*, 2006]. For example, the modern Negro still features an over-deepened channel due to its low sediment load. According to Irion *et al.* [1995] and Irion *et al.* [2006], changing sea level may have affected the Amazon basin since Pleistocene times as far as Iquitos by causing several incision and depositional phases that led to terrace formation and lake development. However, it is most commonly accepted that although fluvial transport re-established a channel-floodplain system in response to post-glacial sea level rise, the principle control on sediment delivery and floodplain construction is exerted by ancient and partly re-activated modern tectonic structures [Mertes & Dunne, 2007].

1.3.2 Amazon basin channel patterns, floodplain geomorphology, and assessment of sediment transport and deposition

The channel pattern of a river is closely related to the amount and character of the available sediment and to the quantity and variability of discharge [Leopold & Wolman, 1957; Leopold *et al.*, 1964]. White water rivers draining Andean territory such as the Amazon and the Madeira display very active channel patterns, as they have high sediment loads and, combined with very low channel gradients, need to compensate their energy by high meander or avulsion frequencies [Junk, 1997]. On the other hand, black and clear water rivers such as the Negro and the Tapajós rivers, respectively, have high bed stabilities due to their low sedimentation rates [Junk, 1997; Kuechler *et al.*, 2000].

The modern channel of the lower Amazon is mainly anastomosing [Mertes *et al.*, 1996], which means that multiple channels coexist, being separated by vegetated, semi-permanent islands [Knighton & Nanson, 1993; Nanson & Knighton, 1996]. The channel itself however is relatively straight in most of its Brazilian course, displaying sinuosities of only 1.0 to 1.2 [Mertes *et al.*, 1996]. Low-water channel depth increases from 10 to 20 m during its Brazilian course, and single-channel width increases from 2.2 km to an average of 4.5 km

[Mertes *et al.*, 1996]. However, several workers so far have noted that the channel is confined to a much more narrow course with additionally increasing channel gradient and channel depth when crossing a tectonic lineament or arch [Mertes *et al.*, 1996; Dunne *et al.*, 1998; Costa *et al.,* 2001]. In spite of its occasional tectonic confinement and being restricted in movement by stable "terra firme", the Amazon clearly is a very active channel, relocating and mixing bank and floodplain material as it flows. Mertes *et al.* [1996] have computed the percental channel change for the Brazilian part of the Amazon, and generally found that the total rate of channel change decreases along the river, until it increases again below the Madeira river confluence. Average rates reported are between 0.1% to 2% of the total channel width per year [Mertes *et al.*, 1996], resulting in an average relocation rate of ~35 m/yr for the reach immediately downstream of the Madeira River confluence, for example (see Figure 1.5).

According to Irion *et al.* [1995], the Negro River channel has not changed its position and depth since at least the last glacial period, and its present size and depth greatly exceeds the dimensions required by its present water and sediment discharge. As a consequence, the Negro floodplain probably has not been reworked by changes in river course during the Holocene and therefore should be much older than the Amazon floodplain.

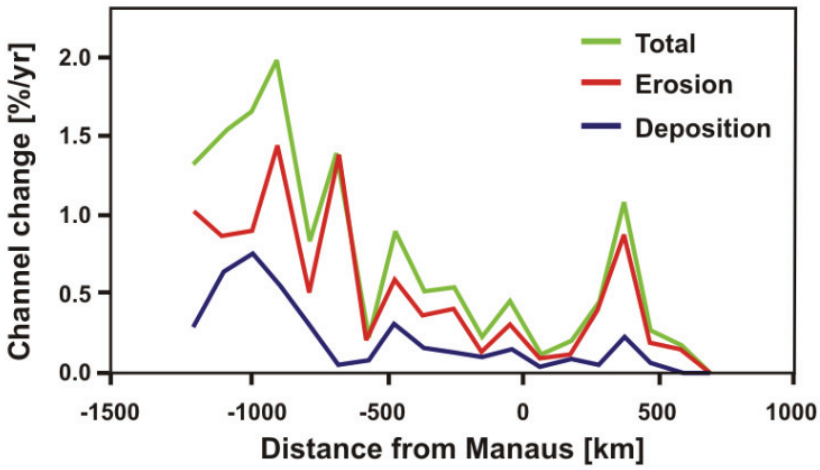

Figure 1.5 Channel change in (%/yr) in the lower Amazon River plotted against distance from Manaus (modified after Mertes *et al.* [1996]). Data was acquired during the years 1971-1972 and 1979-1980. Channel change is reported as reworked land area, that is eroded, deposited, or total change, expressed in percent from the total active channel area.

This finding would be concordant with erosion time scales derived from U-series disequilibria in the Amazon River and its main tributaries including the Negro River by Dosseto *et al.* [2006a]. These authors have found much longer residence times for suspended sediment in

rivers draining cratonic areas (e.g. Negro; residence time scale [Δt] ≥500 kyr) than in rivers draining the Andes (e.g. Amazon at Óbidos; Δt ~6.3 kyr; also see Dossetto *et al.* [2006b].

The sediment load of a river is usually composed of fine grained matter (mostly silt and clay) carried in suspension, and the coarser bed material (>fine sand) is transported by sliding and rolling along the channel bottom [Leopold *et al.*, 1964]. The suspended sediment concentration of the Amazon near Manaus averages to ~100 mg/l (see Figure 1.6; Gibbs [1967]; Meade *et al.* [1985]), and the total sediment load of the Amazon at Óbidos ranges between ~0.8 and 1.4×10^3 Mt/yr, depending on the sampling method and period [Meade *et al.*, 1979; Meade *et al.*, 1985; Dunne *et al.,* 1998; Filizola, 2003; Guyot *et al.*, 2005; Laraque *et al.*, 2005]. It has been estimated that between 80-90% of the total suspended load of the Amazon at Óbidos originates in the Andes, although they only account for 12% of the total basin area [Gibbs, 1967; Meade *et al.*, 1985]. As Figure 1.6 illustrates, the obtained sediment flux is highly dependent on the sampling period. The extrapolation of short-term gauging-derived erosion rates (time scale 10^1 to 10^2 years) to long-term denudation rate estimations (time scales >1 kyr) is perhaps the most limiting factor in the use of sediment load data, as accurate sediment load measurements rely on climate-driven river discharge.

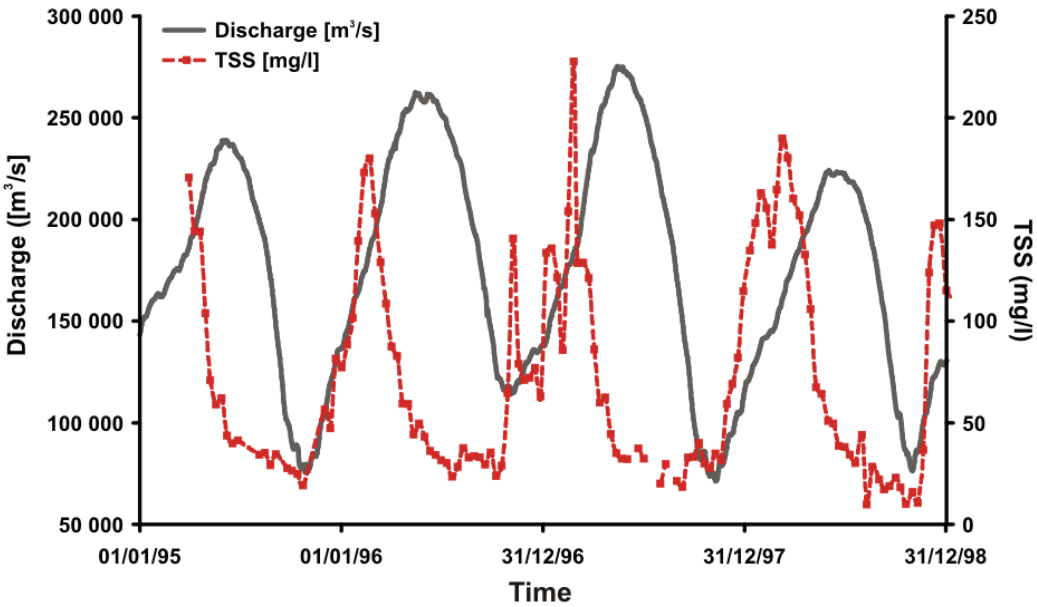

Figure 1.6 Water and sediment discharge for the Amazon River at Óbidos for the years 1995 to 1998 (modified after HIBAM, 2003; graphic courtesy of P. Seyler).

The bedload of the Amazon comprises about only 1% of its total load (~5 Mt/yr, estimated by Guyot *et al.* [2005]), and is transported in huge sand waves several m in height along the bottom of major Amazon rivers. Grain sizes range between 100 and 1000 µm with a median

size of 250 µm [Mertes & Meade, 1985], and particle size is, according to Nordin *et al.* [1980] and Mertes & Meade [1985] uniform from Iquitos to well below Óbidos, e.g. apparently no reduction in particle size (referred to as downstream fining) takes place. For the Madeira River and its Bolivian tributaries, the Beni and the Guaporé, grain size fines abruptly to ~100 µm as the rivers enter their respective floodplains, but grain sizes remain stable during subsequent course across the floodplain, e.g. no further downstream fining is observed [Guyot *et al.*, 1999]. The Guaporé tributary draining the Brazilian shield on the other hand contributes much coarser bedload sediment to the Madeira with a mean diameter of ~340 µm [Guyot *et al.*, 1999].

In terms of sand composition and provenance, large variations in the main Amazon channel along the Iquitos - Óbidos reach have been reported by Landim *et al.* [1978]; Franzinelli & Potter [1983], and Potter [1994]. Upstream of Manaus, high proportions of unstable minerals (lithic arenites rich in metamorphic and volcanic grains) of Andean source are dominant, where downstream of Manaus, coarse quartz-rich sands from the cratonic areas progressively become the prevailing fraction. This increase is attributed to sediment input from the Negro (only 10-20 Mt/yr; [Laraque *et al.*, 2005]) and Madeira (600-700 Mt/yr; [Guyot *et al.*, 1996; Dunne *et al.,* 1998]; see Figure 1.3 and Figure 1.8) rivers, which drain the northern and the southern cratonic areas, respectively. According to Mertes & Dunne [2007], only sediment being finer than 500 µm is able to leave the Andean foreland basins, and coarser sediment found in the Amazon may therefore entirely stem from cratonic shields. However, since sediment load is negligible in cratonic rivers, Guyot *et al.* [1999] argue that this sediment has been transported during pre-modern hydraulic conditions, which cannot be observed at present.

Periodic flooding of large areas in South America is caused by high rainfall with a seasonal distribution. Due to its flat topography with stream gradients between 1-3 cm/km for the lower Amazon, Junk & Furch [1993] and also Hess *et al.* [2003] estimated that each year during the rising water level, an area of ~300,000 km^2 along the Amazon and its main tributaries is inundated. The floodplain adjacent to the Amazon River is a highly complex and heterogeneous system, composed of thousands of temporary or perennial lakes, levee systems with scroll-bars, and in more mobile parts of the floodplain also ridge and swale patterns. Floodplains play a major role in the storage of sediments; it is assumed that more than 80% of the suspended sediment flux entering the floodplain is also deposited [Mertes *et al.*, 1996],

although this storage is temporary and its duration has been estimated for the central Amazon basin to be in the order of several kyr [Dosseto *et al.,* 2006b; Junk, 1997].

Detailed studies of discharge (see Figure 1.7) and suspended solid fluxes in an Amazonian floodplain system are available from Maurice-Bourgoin *et al.* [2007] and Bonnet *et al.* [2008]. These authors focus on the "Lago Grande de Curuaí" floodplain, located south of Óbidos, which at high water stage covers an area of 2500 km^2 (or 13% of the Amazon floodplain area between Manaus and Óbidos, excluding tributary varzeas; [Maurice-Bourgoin *et al.*, 2005]). The floodplain of Curuaí is comprised of numerous white water (e.g. Lago Grande) and also black water lakes (e.g. Lago Curumucuri), and is connected to the main Amazon by a series of channels, of most of them are activated as the water level starts to rise in December (cf. Figure 4.3).

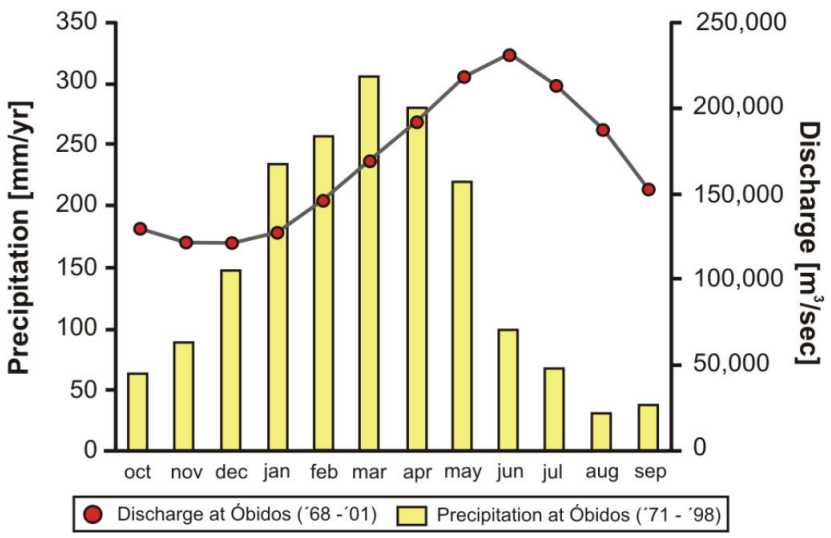

Figure 1.7 Average monthly precipitation (mm/yr; for years 1971-1998) and mean monthly discharge (m^3/yr; for years 1968-2001) at Óbidos on the main Amazon stream (modified after Maurice-Bourgoin *et al.* [2007]). X-axis is denoted as hydrological year.

Suspended sediment exchange modeling (for model details see Bonnet *et al.* [2008]) based on total suspended solid (TSS) measurements every 10 days and daily water discharge records at gauging stations between the floodplain and the Amazon permits the calculation of a sediment balance and the evaluation of sediment being stored in the Varzea do Curuaí. Maurice-Bourgoin *et al.* [2007] have estimated that for the years 2000 to 2003, 0.7 Mt/yr of sediment is deposited in the floodplain, which represent ~50% of the total sediment flux entering the floodplain, resulting in a mean sediment deposition rate of ~520 t/km^2/yr. Expressed in linear distances, this corresponds to ~0.005 Mt/km/yr. This rate does not seem representative for the whole Amazon River system, because sedimentation rates reported for the Amazon expressed

in linear distances are between 0.25 to 0.9 Mt/km/yr, which corresponds to an annual flux of ~1200-1400 Mt/yr passing Óbidos, based on thorough sediment budget by Dunne *et al.* [1998]. Main stream deposition rates are thus larger by factors between 50 and 180 than Curuaí deposition rates. According to Lima *et al.* [2005], the difference between the derived fluxes probably reflects the differences in sampling techniques used in the different studies. Additionally, sampling on different temporal scales may also be highly relevant [Meade *et al.*, 1985], because suspended sediment discharge strongly varies with climate-coupled discharge.

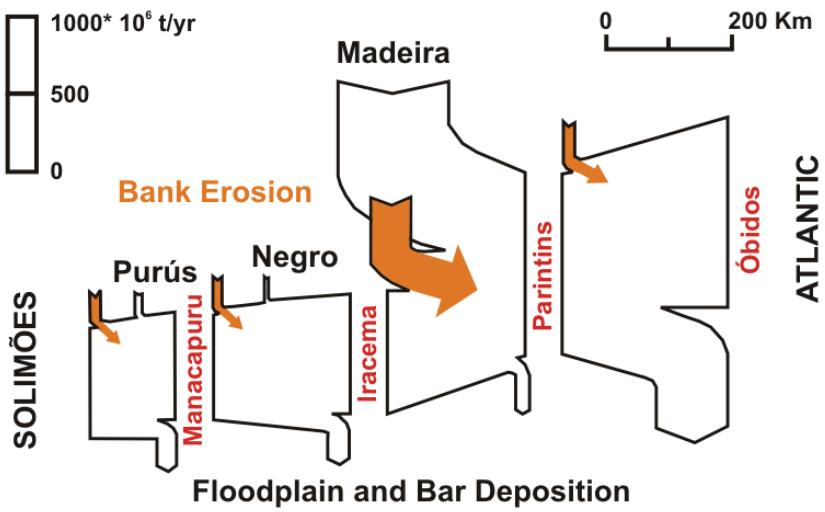

Figure 1.8 Sediment budget for the lower Amazon reach from the Purús confluence to Óbidos, modified after Dunne *et al.* [1998]. Bank erosion of each reach is denoted in the upper left corner (orange arrows); tributaries are in the upper middle. Represented in the lower right of each reach is the sediment deposition on bars and on the floodplain. Local names have been changed to correspond to our sampling scheme; Iracema is denoted as Amatari, and Parintins as Paurá in Dunne *et al.* [1998].

Dunne *et al.* [1998] have also estimated that the fluxes interchanged within the Amazon floodplain are in the order of 3600 Mt/yr, with a net accumulation of ~200 Mt/yr (Figure 1.8), which means that in the Amazon basin as a whole, the quantities of sediment exchanges between channels and floodplain far exceed the quantities of downriver flux [Dunne *et al.,* 1998; Meade, 2007]. Consequently, it is reasonable to expect that most sediment passing Óbidos has resided in the floodplain for some time since its initial denudation in the Andes, although this storage is temporary and has been estimated for the Amazon to be in the order of several kyr, ranging from <5 kyr on the basis of sediment budgets [Mertes & Dunne, 2007; Mertes *et al.*, 1996], to ~15 kyr from Uranium-series constraints [Dosseto *et al.,* 2006a; Dosseto *et al.*, 2006b].

CHAPTER 2

MODELING THE ACCUMULATION AND DECAY OF COSMOGENIC NUCLIDES DURING SEDIMENT STORAGE IN FLOODPLAIN SYSTEMS

ABSTRACT

We have modeled depth- and time-dependent nuclide transport and storage in floodplain settings to identify processes acting to control nuclide accumulation or decay in long-term stored alluvium. Six settings were chosen, spanning the dynamic range of floodplain settings from confined, shallow rivers with minor floodplains to foreland basin-scale, actively migrating river floodplains, where storage time scales estimated from channel migration rates range from 0.4-9 kyr for the Beni basin in Bolivia and the Amazon basin, respectively.

Model results show no significant increase in nuclide concentration due to irradiation during deposition or decrease due to deep burial for settings where the sediment flux eroded from the hinterland is in the same order of magnitude as fluxes exchanged in the floodplain, which is the case for all investigated settings. For these settings, even long-term deposition (<0.5 Myr) or the removal of deeply stored sediment via river migration and avulsion do not dramatically change the nuclide signal inherited from the source area. If sediment fluxes interchanged within the floodplain are much greater than source area fluxes, minor net nuclide accumulation will occur for settings with storage time scales of <0.5 Myr, and net nuclide decrease at time scales >1 Myr. For storage and transfer time scales <20 kyr, in situ-produced ^{14}C will sensitively provide these residence times.

Thus we have confirmed that cosmogenic ^{10}Be and ^{26}Al irradiation and radioactive decay are not relevant on time spans usually encompassed by large-scale fluvial processes (e.g. $<10^5$ yrs) in floodplain basins. These prerequisites are met in most depositional settings except in sediment-depleted rivers traversing very old (>1 Myr) floodplains. Consequently, we suggest that a sediment sample collected at the outlet of the floodplain will record the denudation magnitude of the sediment-producing area within its potential spatial and temporal variability, indicating that it is temporal variations of denudation rates in sediment-delivering areas that introduce variability into large river denudation rates, rather than storage within the floodplain.

2.1 INTRODUCTION

Cosmogenic nuclides accumulate in minerals on hill slopes during weathering and denudation, where a denudation rate can be calculated from cosmogenic nuclide concentrations. The time scale over which this denudation rate integrates is z^*/ε, where z^* is the e-folding depth of cosmic ray absorption, typically 600 mm. Rates therefore integrate over 1-100 kyr, depending on the denudation rate ε [Lal, 1991; Bierman & Steig, 1996; von Blanckenburg, 2005]. Cosmogenic nuclides also may accumulate during transport and storage of sediment in streams. However, the time scale of active bedload transport in streams is usually much shorter than that of hill slope processes [Whipple & Tucker, 1999], and moreover shielding by water takes place, yielding the active transport step negligible in terms of nuclide accumulation. During storage and shielding of sediment in floodplains however, which may encompass several thousand to even million years in continental-scale basins, nuclide accumulation at the floodplain surface is proportional to the sediment storage time, while at depth it is also a function of the exponentially decreasing production rate. At great depths where shielding from cosmic rays is high, nuclide concentrations decrease due to radioactive decay. As a consequence, the prerequisites for calculating spatially-averaged denudation rates are not met in depositional basins, where the rate of nuclide production does not necessarily equal the rate at which nuclides are being exported from a basin.

In order to resolve for processes governing cosmogenic nuclide behavior during channel-floodplain interaction, we have modeled depth- and time-dependant nuclide production and radioactive decay for different areas, depths, and reworking time scales. These examples, which are the Amazon, the Mississippi, the Beni, the Rhine, the Pearl, and the Vermillion rivers cover the full spatial range of dynamic fluvial settings, and are representative for the evolution of channel-floodplain systems at multi-millennial time scales.

2.2 MODEL SETUP

In our compartment model, sediment is eroded in the source area, obtaining a nuclide concentration C_{up} in the process, and is introduced into the upstream area of our model at a discharge rate Q_{up}. This sediment is then being mixed with sediment eroded from the river

bank as the river migrates laterally by meandering ($Q_{be/bd}$; see Figure 2.1 and Figure 2.2), and the resulting mix obtains a nuclide concentration that is:

$$C_{mix} = \frac{Q_{up} \times C_{\mathrm{up}} + Q_{\mathrm{be/bd}} \times C_{\mathrm{bank}}}{Q_{total}} \tag{2.1}$$

The total sediment flux (Q_{total}) is defined as the sum of sediment discharged upstream into the floodplain as measured, for example, from sediment gauging (Q_{up}), and the flux eroded from bank retreat ($Q_{be/bd}$) with a nuclide concentration of C_{bank}.

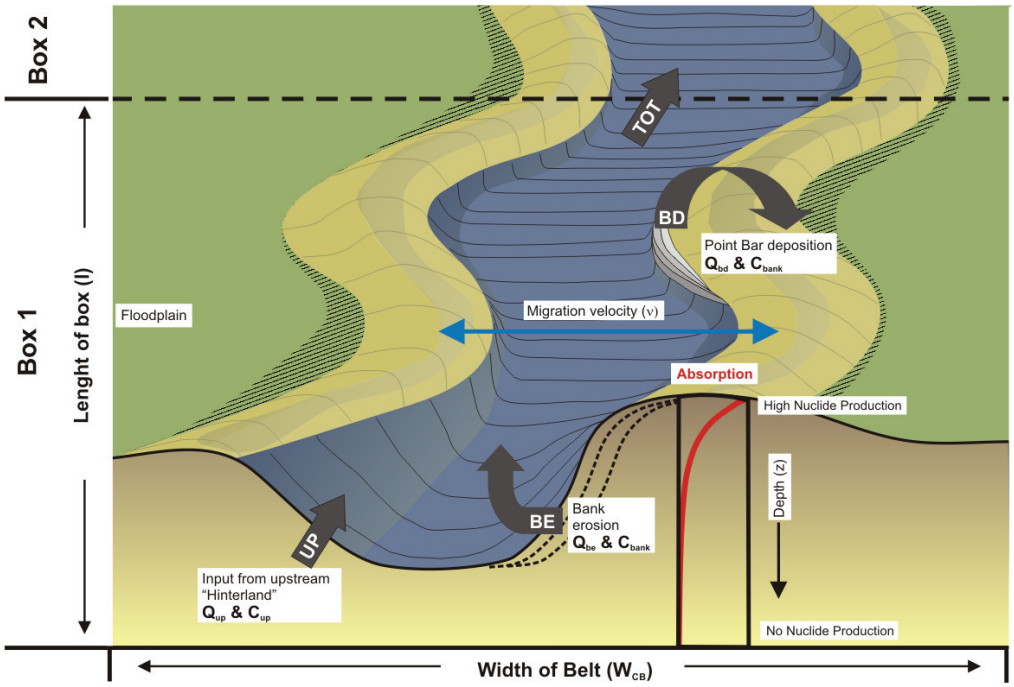

Figure 2.1 Cartoon of the model setup. The two main compartments are shown, which are the sediment input from the hinterland (Q_{up}) with its characteristic nuclide concentration (C_{up}), and the sediment flux eroded from the bank (Q_{be}) with its nuclide concentration C_{bank}. Sediment deposition on the point bar (Q_{bd}) is equal to Q_{be} in flux magnitude and nuclide concentration C_{bank}. C_{bank} is calculated by averaging over the bank depth, equal to the river channel depth, by applying the depth-dependency of nuclide production from Schaller *et al.* [2002], e.g. due to material absorption, cosmic ray flux decreases with depth. Sediment is stored in the floodplain for a duration defined by Δt, the sediment residence time, before it is eroded. The residence time is defined by the time its takes the river to migrate laterally at a certain rate (the migration rate v) across the width of its channel belt (W_{cb}).

The model assumes steady state between sediment flux from bank erosion and bar deposition, a simplification termed quasi-steady state, which is valid for most fluvial conditions [Mackin, 1948; Trimble, 1995; Lauer & Parker, 2008]. This assumption may not be valid on short time scales, but on time scales encompassed by channel belt formation due to sediment

accumulation and aggradation (~10^5 yrs), the vertical accretion of floodplains is counterbalanced by the lateral erosion of the exposed bank [Wolman & Leopold, 1957; Trimble, 1995; Bridge, 2003; Meade, 2007].

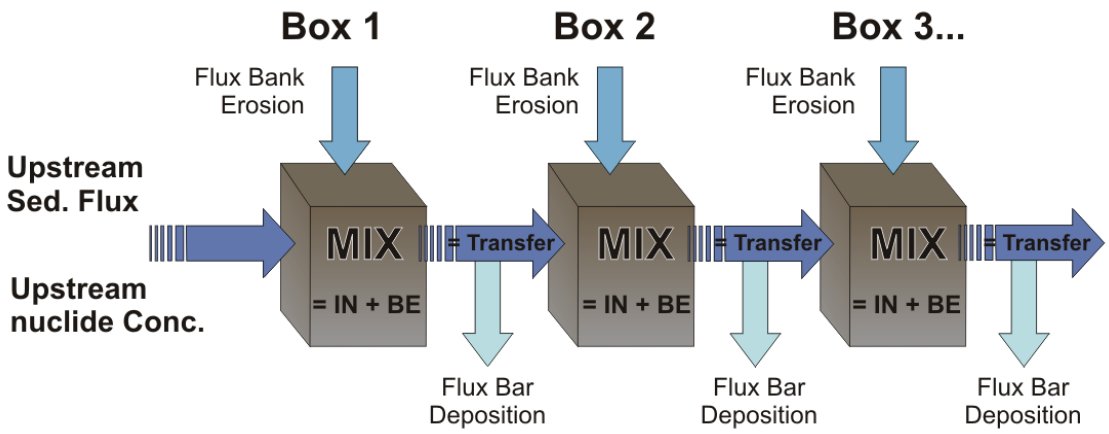

Figure 2.2 Illustration of stream sediment being passed from one box to the next while being mixed with bank erosion flux.

The model floodplain is traversed by lateral river migration. The width of the floodplain-channel belt can be conveniently measured from topographic maps. The residence time of sediment in the floodplain is defined for each river as the time necessary to meander across its channel belt:

$$\Delta t = \frac{W_{CB}}{v} \tag{2.2}$$

where Δt is the sediment residence time (yr), W_{CB} is the channel belt width (m), and ν is the channel migration rate (m/yr). The residence time of sediment in the floodplain gives the time the sediment is exposed to cosmic rays, resulting in nuclide accumulation at its surface. The residence time per box is defined as a sediment liberation cycle; given that the total number of cycles remains unknown, we plot our data as a function of the cumulative time spent in the floodplain, which is $\Delta t \times n$ (n = 25 boxes; see Figure 2.3). The inventory of cosmogenic nuclides in a vertical section of sediment resulting from exposure and storage in the river bank (C_{bank}) is calculated by applying the depth-dependency of nuclide production by nucleons, fast muons, and stopped muons following Schaller *et al.* [2002]. Nuclide concentrations were scaled to sea level high latitude (SLHL), using total production rates of 5.53 at/$g_{(Qz)}$/yr [Kubik *et al.*, 1998] for ^{10}Be, and a respective ^{26}Al production rate of 35.95 at/$g_{(Qz)}$/yr, because the

surface production ratio of $^{26}Al/^{10}Be$ is 6.5 according to Kubik *et al.* [1998]. For a total ^{14}C production rate we used 15.1 at/$g_{(Qz)}$/yr [Lifton *et al.*, 2001]. Radioactive decay ($t_{1/2}$ for ^{10}Be is 1.5 Myr, for ^{26}Al it is 0.72 Myr [Hofmann *et al.,* 1987; Samworth *et al.*, 1972], and for ^{14}C it is 5730 yrs [Libby, 1955]) is also calculated by $C_{(\Delta t)} = C_0/\lambda\times(1-e^{-\lambda\Delta t})$, where $C_{(\Delta t)}$ is the concentration of nuclides after storage and C_0 approximates the nuclide signal incorporated along with the stored sediment additionally to that produced during storage.

In order to calculate bank erosion fluxes, the floodplain is divided into n boxes of equal length l, where l = floodplain channel length divided by n. Now the bank erosion flux Q_{be}, which is equal to the bar deposition flux Q_{bd}, can be calculated:

$$Q_{be/bd} = l * v * z * \rho \tag{2.3}$$

where z is the bankfull depth (m), and ρ is the sediment density in g/cm^3. This mix of sediment, comprising the upstream flux from the previous box and bank erosion flux (eq. 2.1), is now passed from one box to the next, where it is incorporated again in the floodplain for the same duration Δt. All parameters are held constant for all boxes, and the sediment concentration is always calculated from equation 2.1. Thus, the accumulation or decay of sediment can be monitored as sediment moves downstream from one floodplain compartment to the next.

2.3 CHOICE OF MODEL PARAMETERS FOR REPRESENTATIVE RIVER SETTINGS

The upstream nuclide concentration was calculated from a known spatially-averaged erosion rate using Lal´s [1991] formalism:

$$C_{up} = \frac{P_0}{\lambda + \frac{\varepsilon}{z*}} \tag{2.4}$$

where the mean basin elevation was taken to calculate a mean production rate based on production rate scaling following Dunai [2000] (see Table 2.1). The hinterland denudation

rate was estimated by dividing a given rivers´ total sediment flux at the respective gauging station by the upstream (hinterland) sediment-producing area, and converting the resulting sediment yield (t/km^2/yr) into a denudation rate by dividing it by the eroding bedrock density (in this case 2.7 g/cm^3). The density of floodplain sediment was assumed to be 2.0 g/cm^3. We have chosen to model six characteristic river settings, which encompass the entire range of shallow, deep, high sediment discharge, low sediment discharge, high and low channel belt widths, and high and low channel migration rates. The latter was usually estimated from meander bend migration, which might lead to an over-estimation of the migration rate, also, the process might be unsteady due to involvement of avulsions.

2.4. MODEL RESULTS

The maximum increase in nuclide concentration in (%) for each river is given in Table 2.1 and shown in Figure 2.3. The increase in ^{10}Be nuclide concentration for all rivers is between 0.5 and 13% relative to the starting ^{10}Be nuclide concentration C_{up}. The relative increase in ^{26}Al concentration is virtually identical, because the production mechanisms are similar to ^{10}Be and storage time scales are too short to allow for detectable radioactive decay. Some inter-river differences in accumulation are predicted, however.

In the Pearl River case, increase for the model is ~13%, which is due to a relatively low ratio of ingoing sediment flux (Q_{up}) to total flux eroded from the banks (eq. 2.3). This ratio governs the mixing ratio between the two end members and controls the magnitude in increase of the mixed nuclide concentration. If the bank erosion flux is higher than the sediment input from upstream, nuclides produced due to exposure in the floodplain surface and upper subsurface will dominate the sediments´ nuclide budget, resulting in net nuclide accumulation. In contrast, in a sediment-laden river with high hinterland denudation rates like the Beni, the ratio of Q_{up}/Q_{be} is high. Thus, the nuclide increase from bank erosion is not pronounced, amounting to only 0.7%.

Table 2.1 Model input parameters

River	Gauging station	Total drainage area [$\times 10^4$ km^2]	Channel length[a] [km]	Channel migration rate [m/yr]	Bankfull channel depth [m]	Channel belt width[b] [km]	"Q_{up}" sediment flux [Mt/yr]	"C_{up}" ^{10}Be initial conc.[c] [$\times 10^4$ at/g$_{(Qz)}$]	Sediment residence time[d] [kyr]	^{10}Be nuclide change[e] [%]	^{26}Al nuclide change[e] [%]	^{14}C nuclide change[e] [%]
Amazon[1,2]	Manacapuru, Brazil	220	3500	4	23	35	700	7.2[#]	9.0	2.6	2.3	-42.9
Mississippi[3,4,5,6]	Tarbert Landing, USA	390	1500	25*	6[$]	100	140	11[##]	4.0	9.0	8.4	-62.3
Beni[7,8,9]	C. Esperanza, Bolivia	28	800	15	20	6	210	3.8[§]	0.4	0.7	0.6	-8.8
Rhine[10,11]	Rees, Netherlands	15	700	5	4[$$]	3	3.5	7.2[&]	0.6	6.4	6.3	-29.6
Pearl[12]	Jackson, USA	1.7	150	1	6	4	2.0	2.5[##]	4.0	12.6	12.4	-19.8
Vermillion[12]	Empire, USA	0.03	25	0.4	1	0.2	0.1**	1.2[##]	0.5	2.8	2.8	1.6

[1]Mertes *et al.* [1996]
[2]Dunne *et al.* [1998]
[3]Kesel [1988]
[4]Kesel *et al.* [1992]
[5]Hudson & Kesel [2000]
[6]Soar *et al.* [2005]
[7]Aalto [2002]
[8]Guyot *et al.* [1996]
[9]Gautier *et al.* [2007]
[10]Asselman [1999]
[11]personal communication Th. Hoffmann, 2007
[12]Lauer & Parker [2008]

[a]Gives the total lenght of the river as it crosses the floodplain, e.g. from mountain foothills to gauging station
[b]Measured at distinct intervals on Google Earth satellite imagery
[c]Calculated from the given production rate estimate and erosion rate derived from "Q_{up}" sediment flux, which is calculated with a rock density of 2.7 g/cm^3 and the upper basin area, e.g. in the Pearl and Vermillion river cases, these denote 1/3 of the total basin area, and for the Mississippi, the upper basin area was estimated to be 1/6 of the total basin area
[d]Gives the residence time per box, calculated for each box from channel belt width divided by channel migration rate
[e]Observed increase or decrease in nuclide concentration from model run based on parameters shown here

[#]From sample Pe 101 (Solimoes at Tamshiyacu; see Chapter 3)
[##]Calculated from mean upper basin elevation of 1500, 120, and 300 m, and a total ^{10}Be production rate of the upper basin of 15.0, 4.5, and 7.0 at/g$_{(Qz)}$/yr for the Mississippi, Pearl, and Vermillion Rivers, respectively (atmospheric production rate scaling after Dunai [2000])
[§]Mean from samples Be 1a & 1b (see Chapter 3)
[&]Estimation from Schaller *et al.* [2001] from middle European river sediment
[$]Minimum depth estimation based on drainage area-depth relation developed by Magilligan [1985]
[$$]Mean channel depth
*Conservative average for lower alluvial reach (from[3,4])
**Estimate based on drainage area-sediment load relation developed by Milliman & Syvitski [1992]

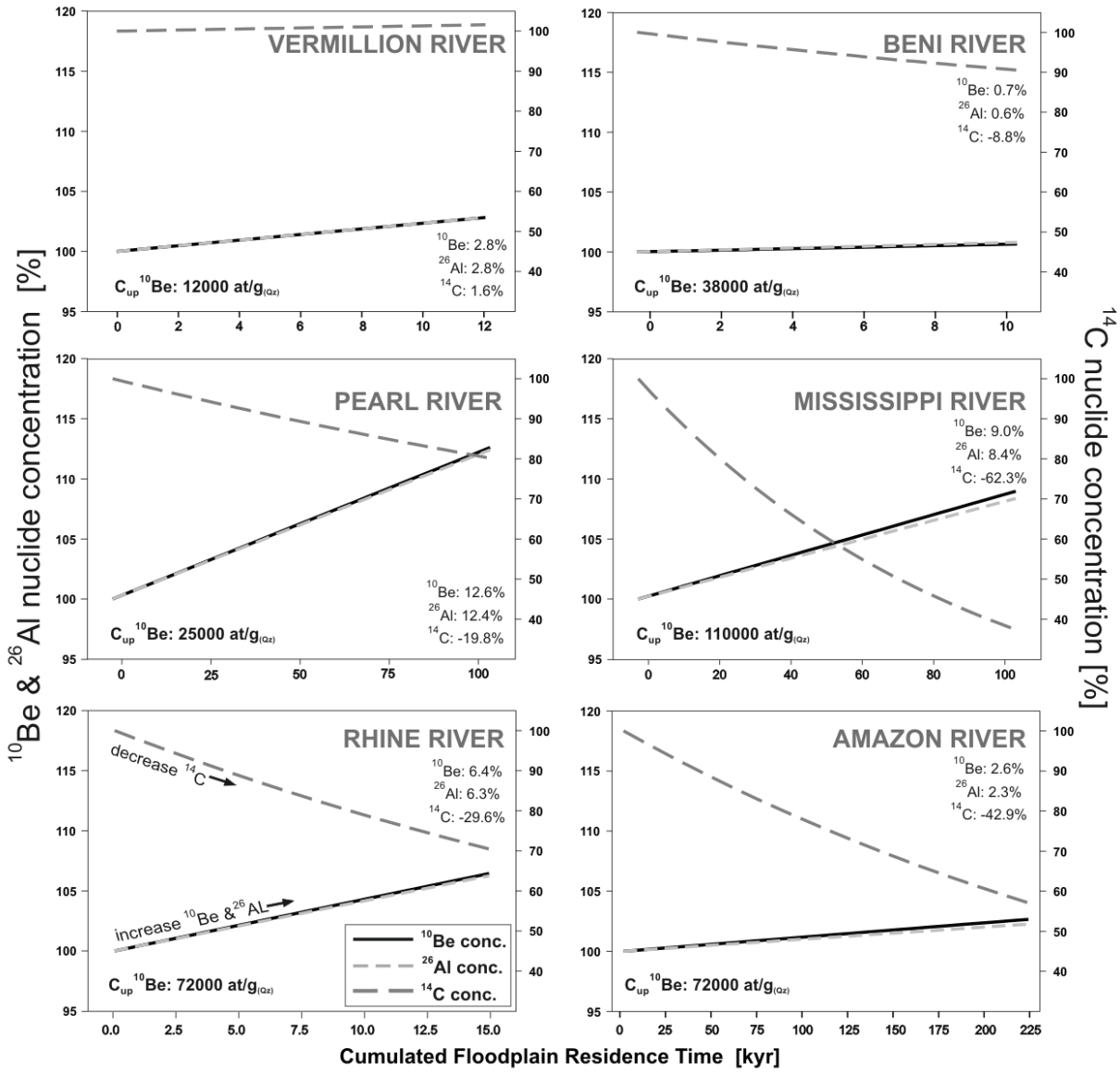

Figure 2.3 Model results for each river setting. Plots denote the accumulated plus upstream ^{10}Be and ^{26}Al nuclide concentration normalized to 100% on the left Y-axis, and the ^{14}C concentration on the right Y-axis. The X-axis gives the cumulated floodplain residence time. ^{14}C nuclide concentrations decay more rapidly, depending on the prevailing residence time for each setting, than ^{26}Al and ^{10}Be, which slightly accumulate for each setting, except in the Vermillion River, where sediment routing is very fast.

The observed increase in ^{10}Be nuclide concentrations for all investigated settings is with 1-10% in the typical range of analytical precision for nuclide concentrations measurements in river sediment, and therefore just barely detectable for the case of lowest analytical error and highest possible increase. However, even if the detection of a change in nuclide concentration in real floodplains can be achieved analytically, the variation of denudation rates in space and time is mostly larger than the predicted model increase. The maximum observed increase in nuclide concentration of ~13% is not large enough to be detected when measured in remobilized floodplain sediment.

We conclude that floodplain storage in all modeled dynamic river settings does not result in a change in ^{10}Be or ^{26}Al concentration. Hence, it is apparent that the overall change in ^{10}Be and ^{26}Al nuclide concentration is small. For deep rivers like the Beni or the Amazon River, this can be attributed to the high portion of well-shielded sediment, leading to a lack of irradiation within the floodplain.

In shallow rivers, like the Vermillion River, floodplain sediment is well-irradiated, but the mass eroded from the floodplain is small and is diluted by upstream sediment. In all cases, total storage times are too short to allow for radioactive decay of ^{10}Be or ^{26}Al (see Figure 2.3). The result for in situ-produced ^{14}C is different. Because in the model we used the same production and absorption laws as for ^{10}Be and ^{26}Al, the effect of irradiation is similar. Decay, however, is much more pronounced due to the short half life. Therefore, significant decrease in ^{14}C is observed for all rivers except for the rapidly meandering Vermillion River. The half life of ^{14}C appears to be in the perfect range to detect storage effects.

2.4.1 Testing the model sensitivity to changes in fluvial boundary conditions: the Beni River example

^{10}Be concentrations have been investigated in detail in the Beni floodplain within this thesis (Chapter 3). Therefore, the sensitivity of the model to changes in boundary conditions is explored more thoroughly in this section.

For the Beni, the steady state assumption has been validated by Aalto *et al.* [2002], who have measured Beni cutbank erosion flux (~210 Mt/yr) as well as fluxes from point bar re-deposition (200 Mt/yr), which are identical to the total annual flux passed on from the sediment-producing area to the floodplain (210 Mt/yr; Table 2.1). Standard model runs were performed using parameters representative of the natural Beni system (see Table 2.1), for which the increase in ^{10}Be concentration at the floodplain outlet is only 250 at/g$_{(Qz)}$, corresponding to an increase of 0.7% (Figure 2.4). Changes to these boundary conditions result in the following conclusions: The system is most sensitive to the magnitude of sediment discharged from the sediment-producing hinterland. If this flux, for example, is decreased by four orders of magnitude from 200 to 0.02 Mt/yr, the nuclide signal produced within and eroded from the river banks will increase by ca. 3000 at/g$_{(Qz)}$, corresponding to 7.8% of the initial nuclide budget. A 15-fold increase in sediment storage time, as expected from changes in climatic or tectonic conditions, does not cause ^{10}Be nuclides to accumulate over Beni River floodplain distances. A four-fold decrease in channel depth, from 20 m to 5 m, would also

result in no significant nuclide concentration change, because most nuclides are produced within the uppermost meters of sediment. This is also the reason why the occurrence of large but locally-limited avulsions would not matter much: floodplain storage is usually so deep, that only the uppermost meters are being irradiated. We conclude that the ^{10}Be nuclide concentration of the Beni River is likely to be preserved throughout transfer of sediment through the floodplain.

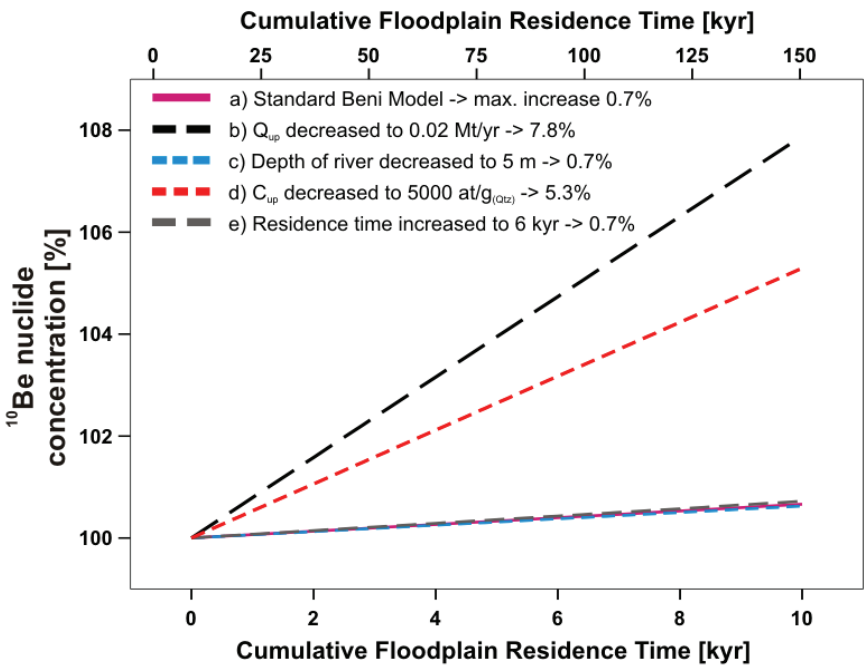

Figure 2.4 Model runs for the Beni River system. ^{10}Be concentration (Y-axis) is normalized to 100%. X-axis give cumulated time sediment is stored in floodplain. For the standard Beni model (a, pink line), parameters are taken from Table 2.1. Four other models runs give test runs for fluvial boundary conditions in the Beni system as indicated. Upper X-axis gives residence time for model case e). For all models, maximum increase (%) in accumulated nuclide concentration of last box with respect to input is given.

2.4.2 The cosmogenic nuclide composition of old deposits

Here we assess the effect of non-steady state settings. These are, for example, the episodic tapping of previously unmodified floodplain deposits that can reach substantial age in the range of 10^5-10^6 yrs. Schaller *et al.* [2004] have shown that old (Myr age) terraces contain ^{10}Be and ^{26}Al concentrations that are distinguishable from those in modern stream sediment. Incorporation of such old deposits into the active stream might take place if sediment is eroded from terraces, or the river is re-routed during channel avulsion, which is driven by tectonic faulting, high discharge events, and channel sedimentation [Slingerland & Smith, 2004; Jerolmack & Mohrig, 2007]. The impact of an avulsion on the prevailing nuclide signal

thereby depends on the age, burial depth, the inherited nuclide concentration of the deposits, and on the fraction of reworked sediment that is admixed into the modern stream. For example, in old (>1 Myr) cratonic settings where rivers are sediment-starved, a net decrease in ^{10}Be nuclide concentration would occur if an avulsion would admix a large fraction of deeply buried material into the stream.

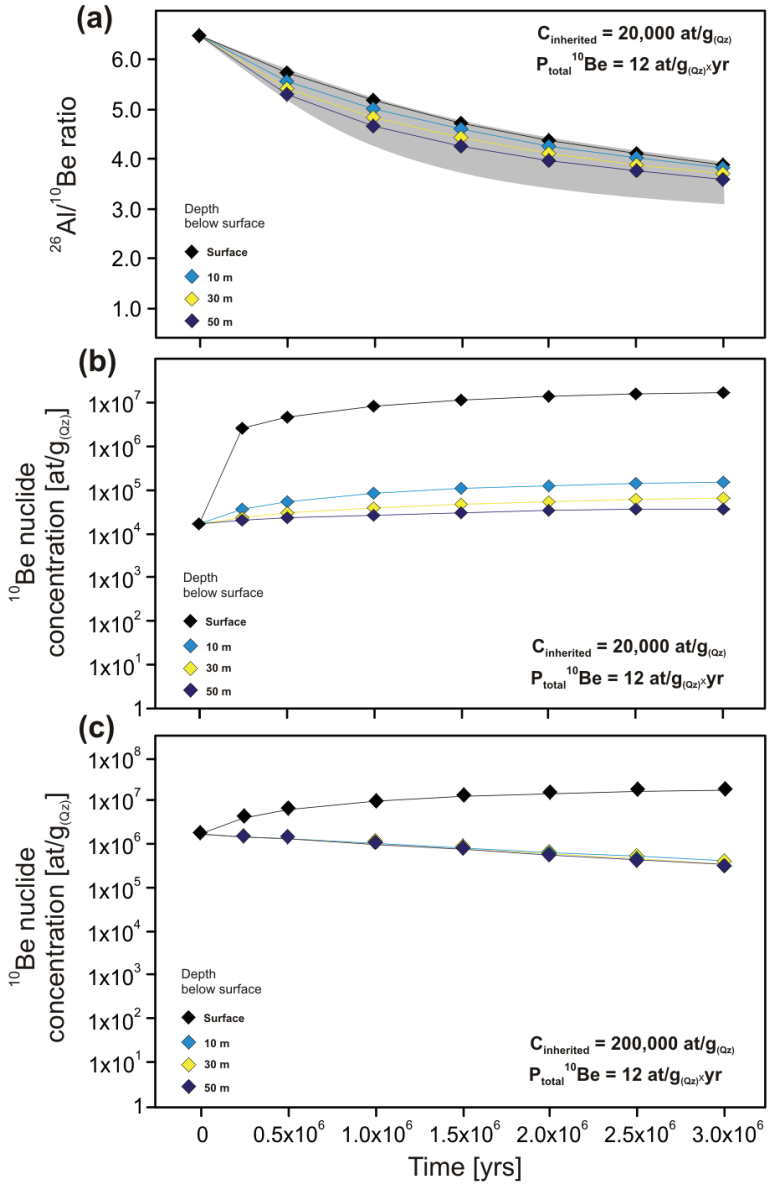

Figure 2.5 a) Evolution of the ^{26}Al/^{10}Be ratio with time, calculated with a depth-dependency for nuclide production (including muons) following Schaller *et al.* [2002] and a sediment density of 2.0 g/cm^3. Nuclide inheritance was set to 20,000 at/g$_{(Qz)}$ for ^{10}Be, which corresponds to a high mountain erosion rate (~1.0 mm/yr). For ^{26}Al, this value was multiplied by the surface production ratio. The shaded area indicates the area where the depth- and age dependant lines would plot if a nuclide inheritance of 70,000 at/g$_{(Qz)}$ (corresponds to a slow upland erosion rate of ~0.1 mm/yr) is used. b) Corresponding evolution of the ^{10}Be nuclide concentration with ongoing irradiation during burial due to low inheritance; and c) corresponding evolution of the ^{10}Be concentration, but $C_{inherited}$ set to 200,000 at/g$_{(Qz)}$, indicating that radioactive decay becomes more rapidly more important relative to nuclide production on shorter time scales as for lower $C_{inherited}$.

We have modeled the evolution of the $^{26}Al/^{10}Be$ ratio to decipher the effects of burial and remobilization depth, nuclide inheritance (C_{up}), and reworking time scale on nuclide concentrations (Figure 2.5). The results show that burial age has the largest effect on nuclide concentrations, because the $^{26}Al/^{10}Be$ ratio strongly decreases with increasing deposit age, whereas the effect of depth on nuclide concentration is not so pronounced. This is because muons penetrate deep into the subsurface, causing post-depositional irradiation, an effect counterbalancing decay to some extent. However, the depth-dependency becomes more pronounced with increasing nuclide inheritance, because as more nuclides decay relative to new production, the depth at which decay becomes more important than production is moved upwards towards the surface. Nevertheless, the overall effect on our model settings is small, because channel depths are usually less than 10 m (see Table 2.1), and ^{10}Be nuclide concentrations are robust even at large inherited nuclide concentrations (Figure 2.5a and b). Taking, for example, a residence time of 2.0 Myr for a shallow river like the Vermillion (depth = 1 m), a ten-fold increase of the estimated nuclide inheritance from 1.2×10^4 at/$g_{(Qz)}$ to 12×10^4 at/$g_{(Qz)}$ would result in a ~0.5% decrease of the $^{26}Al/^{10}Be$ ratio with respect to the surface production rate of 6.5. For a deep river like the Beni (20 m), a ten-fold increase of the nuclide inheritance (taking the same $C_{upstream}$ as the Vermillion in this case for means of comparison) would result in a decrease of 10.0% of the $^{26}Al/^{10}Be$ ratio.

2.5 SUMMARY

For all tested settings encompassing a wide range of dynamic fluvial settings from confined, shallow rivers with minor floodplains to foreland-basin scale, actively migrating rivers, our model results suggest that as long as the sediment flux that is eroded from the hinterland and transported to the floodplain is in the same order of magnitude as fluxes exchanged in the floodplain, even long-term deposition (<0.5 Myr) or the removal of deeply stored sediment via river migration and avulsion do not dramatically change the signal of the long-lived nuclides inherited from the source area. In sediment-rich rivers, the upstream flux is overwhelming the signal contributed by bank erosion. In sediment-starved rivers, usually deep floodplain erosion results in the incorporation of sediment that has been shielded from irradiation. In shallow rivers, the bank erosion flux is too small to change the concentration of the mixed signal in the stream. In all cases, the source signal will be preserved.

The consequence for ^{10}Be and ^{26}Al transfer through dynamic floodplains is that a denudation rate of the hinterland can in all cases be determined. Because the floodplain storage does not modify the nuclide concentration, the production rate used for calculation of denudation rates has to be limited to the sediment-producing area, however. In the context of this PhD, this correction is called "floodplain-corrected".

If times of residence, storage, and transfer shall be determined, then in situ-produced ^{14}C is the method of choice. Given that irradiation is almost absent, the radioactive decay of this shorter-lived nuclide potentially provides the sought residence times. Analytical methods are not yet routine, but are expected to be so within a few years [Lifton *et al.,* 2001; Pigati *et al.*, 2007].

Similarly, for tapping of long (10^5-10^6 yr) stored sediment, the differential decay of ^{10}Be versus ^{26}Al has the potential to provide storage durations and storage depths. Most promising are these long-lived nuclides in sedimentary records, where paleo-denudation rates can be determined from the inheritance and deposition age from $^{26}Al/^{10}Be$ ratios [Schaller *et al.*, 2004], or for shorter intervals^{14}C. In this approach lies real promise.

CHAPTER 3

THE EROSION OF THE CENTRAL ANDES AND THE PRESERVATION OF THE DENUDATION SIGNAL IN LARGE FORELAND BASINS AS INFERRED FROM COSMOGENIC ^{10}BE NUCLIDES AND RIVER LOADS

ABSTRACT

Enormous volumes of sediment are produced in the Central Andes and are then delivered into the foreland basins of large tributaries to the Amazon basin (Mamoré, Madre de Dios, Beni, Ucayali, Marañón, and Napo rivers). While cosmogenic nuclides in sediment are a suitable tool to measure the denudation rates of sediment-producing areas, the requirement of steady state between nuclide production and nuclide removal by denudation appears to make this method less obvious in depositional foreland basins. The tributaries of the Amazon River are ideal to test the sedimentary dynamics of this system. New concentrations of cosmogenic ^{10}Be and published data in basins within the Andean and the Piedmont range yield mean denudation rates of 0.39 ± 0.09 mm/yr for the upper Mamoré basin, 0.4 to 0.7 mm/yr for the upper Beni basin, and 0.48 ± 0.12 mm/yr for the upper Napo basin. Further downstream within the Mamoré and Napo basins, these rates increase to 0.9 ± 0.4 and 0.85 ± 0.31 mm/yr, respectively, by addition of lowland sediment or by temporal variability in the sediment source. Our cosmogenic nuclide measurements of sediment from the active floodplain river bed suggest that a steady, uniform denudation signal is preserved over ~800 km of the Beni River floodplain and ~600 km of the Napo River floodplain distances, respectively, although sediment is continuously in the state of storage and relocation due to rapid lateral river migration processes. The magnitude of the denudation signal transferred to the floodplain primarily depends on the denudation rate in the sediment-generating source area and its temporal and spatial variability (see Chapter 2). Therefore, while a denudation rate can be calculated from floodplain river sediment, a necessary prerequisite is the calculation of the cosmogenic nuclide production rate for the sediment-producing area only.

In order to constrain the dependence of the source area denudation rate on spatial and temporal scales, we carried out a comparison of different published erosion rate meters in the Beni hinterland (Bolivia). The variability of denudation rates decreases smoothly in both space and time. The evaluation also shows that modern rates of erosion from sediment loads in the Beni are significantly higher than long-term averages from both cosmogenic nuclides and fission track analyses, which are in the same range as long-term Andean uplift rates. In contrast for the Mamoré hinterland, new cosmogenic nuclide data on several sub-catchments yield significantly higher rates than modern erosion rates derived from sediment loads.

Sediment gauging records from stations in the Mamoré, Beni, and Napo floodplains at which we also sampled for cosmogenic nuclides show that large-scale deposition of sediment occurs in the Beni floodplain. On the other hand, in the actively uplifting Napo setting, sediment gauging rates record addition of sediment from the floodplain to the active stream.

Neither effect alters cosmogenic nuclide concentrations which robustly record the denudation signal from the sediment-generating Andean area, as predicted from modeling cosmogenic nuclide concentrations (see Chapter 2). In each setting, a sample collected from the active river channel inside the floodplain will reveal the denudation rate of the source area at any point along the river course.

3.1 INTRODUCTION

To date, cosmogenic nuclides in detrital material have been used to determine catchment-wide mountain erosion and weathering rates, but the question is whether denudation rates can be measured in depositional settings, because the effect of sediment storage and transport in large river basins has never been addressed in a rigorous manner. Bierman & Steig [1996] provided a theoretical framework for storage, and Nichols *et al.* [2002] and Nichols *et al.* [2005] have used cosmogenic nuclides in arid, piedmont-type settings for a sediment and nuclide budgeting approach, from which the sediment transport time was inferred.

The tributaries to the Amazon basin are an ideal setting to test this approach. The sediment-generating areas within the Andes have high denudation rates, hence they deliver sediment with low cosmogenic nuclide concentrations, which is then stored in the floodplain basins over geological significant time scales [Irion, 1989]. The focus here is on the Beni and the adjoining Mamoré River, which are meandering rivers that have developed large, accumulating floodplains. Sediment deposition in this floodplain is enormous; Guyot *et al.* [1996] found that the ingoing sediment flux decreases to about 40% of its volume across the floodplain of the Beni River.

The Napo River on the other hand is an anastomosing river with relatively stable banks. Results from preliminary, short-term sediment gauging data in the upper Napo floodplain indicate sediment removal rather than deposition [Laraque *et al.*, 2004; Guyot *et al.,* 2007a].

In the Bolivian Andes, we have the unique situation that we can compare different erosion rate monitors operating at entirely different time scales. Cosmogenic nuclide-derived denudation rates (10^2 to 10^3 yr time scale; [Safran *et al.*, 2005]) are available as well as modern sediment gauging data (10^1 yr time scale; [Guyot, 1993; Guyot *et al.,* 1996]). Very long-term exhumation rate monitors are available from fission-track analysis (10^6 yr time

scale; [Safran *et al.*, 2006]), and the regional uplift history is well constrained over the last ~10 Myr, although spatial resolution is lacking [Gregory-Wodzicki, 2000]. From this set of data, we can infer possible control mechanisms for the temporal variability of denudation in the Bolivian Andes, in order to constrain the denudation signal carried to the floodplain. After constraining the nuclide and sediment fluxes transported from the sediment-producing hinterland to the sediment-depositing floodplains, we will compare our cosmogenic-nuclide data with modern sediment yield data from gauging stations directly in the floodplain.

We will show here that it is indeed possible to calculate meaningful catchment-wide denudation rates in such environments, and we do so by providing new cosmogenic nuclide concentrations of the Beni and Napo trunk streams. But to test whether this sediment carries a meaningful denudation rate signal, knowledge of this signal introduced into the floodplain by sediment delivered from upstream is crucial. Therefore, we will address the denudation rate of the upper Beni basin at Rurrenabaque, which is the main sediment-provider to the Beni River floodplain. For the upper Mamoré basin, we have sampled the principle sediment-providing rivers in order to constrain the mean Andean denudation rate in this region and will also address short-term sediment yield data from sediment gauging.

3.2 STUDY AREA

During late Oligocene to early Miocene times, subsidence-related flexural basins were formed in the Andean foreland [Dumont & Fournier, 1994]. The two major foreland basins are the Marañón basin, located mainly at the Ecuadorian-Peruvian border, including the major tributaries of the Napo, Marañón, and Ucayali rivers, and the Beni and Mamoré basins, which are located at the southern edge of the Peruvian-Bolivian border (see Figure 3.1).

The Beni River at Cachuela Esperanza (CE, Be 17) has an extent of ~300.000 km^2 upstream of its confluence with the Rio Mamoré (see Figure 3.2 and Table 3.1). River channel migration rates average at ~15 m/yr [Aalto, 2002], with migration rates up to ~30 m/yr [Gautier *et al.*, 2007], accounting for rapid sediment exchange between the floodplain and the mainstream. Downstream of the Beni- Mamoré confluence at Villabella, the river is called the Madeira. The Mamoré River basin has an extent of almost 600.000 km^2 at its confluence with the Beni River.

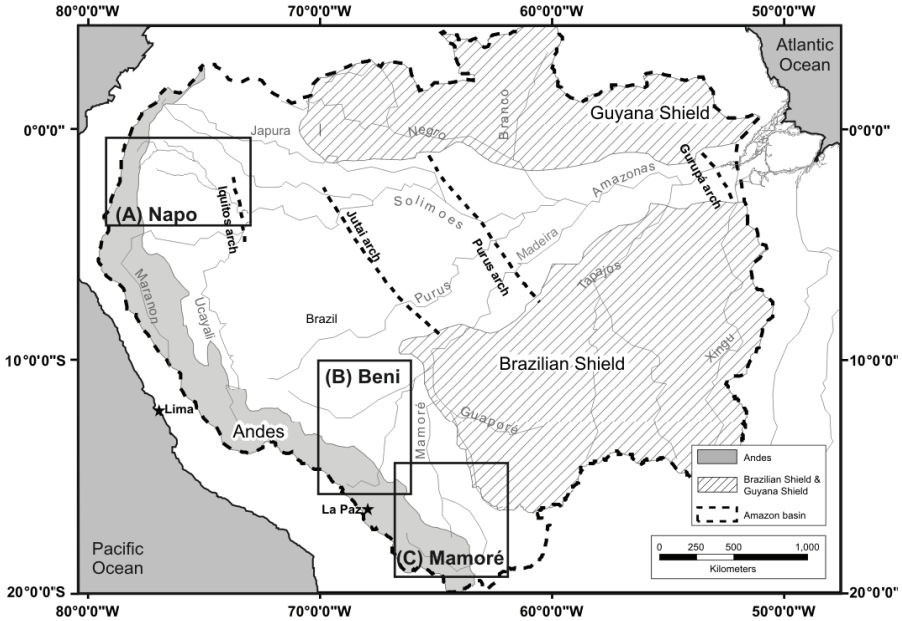

Figure 3.1 Overview over the sampled regions within the Amazon basin

In the Beni and Mamoré basins, three major morpho-structural units are present: The Bolivian segment of the Andes, the Amazon plain featuring vast flooded areas at altitudes <200 m; and the Brazilian shield, constituting old Precambrian rocks (outcropping only in lower Mamoré areas). The Andean part of the basin features semi-arid zones developed on Quaternary sediments to hyper-humid basins with tropical forest developed on Paleozoic rocks of the Andean Cordillera [Guyot *et al.*, 1996]. Andean precipitation patterns vary from 500 to 5000 mm/yr; rainfall in the lowlands is more regularly distributed at 1800 mm/yr [Guyot *et al.,* 1996; Ronchail *et al.*, 2002]. From the transition of erosional Andean to depositional floodplain setting at Rurrenabaque to its confluence with the Mamoré River, the Beni River has two large tributaries, the Madre de Dios River at Miraflores which drains the Peruvian and Bolivian Andes, and the Orthón River, draining lowland sediments only. In the vicinity of the Mamoré confluence, the river has to cross several hydraulic thresholds, so-called "Cachuelas", where the thalweg drops ~50 m. This is due to outcrops of Brazilian shield rocks, separating upstream from downstream floodplain areas. The Andean part of the Mamoré basin is mainly drained by the Grande and Pirai rivers in the southernmost part where the Andean chain is widest, and by the Chaparé and Ichilo rivers in the southern part of the Bolivian Andes. These rivers are tributaries of the Mamoré River (Figure 3.2), which drains the vast lowland areas of the "Llanos de los Mojos" and is fed by many small floodplain rivers. About 100 km upstream of Guayaramerin, the Guaporé-Itenez River joins the Mamoré, a river having low sediment loads due to the highly weathered and slowly denuding Precambrian rocks of the Brazilian Shield.

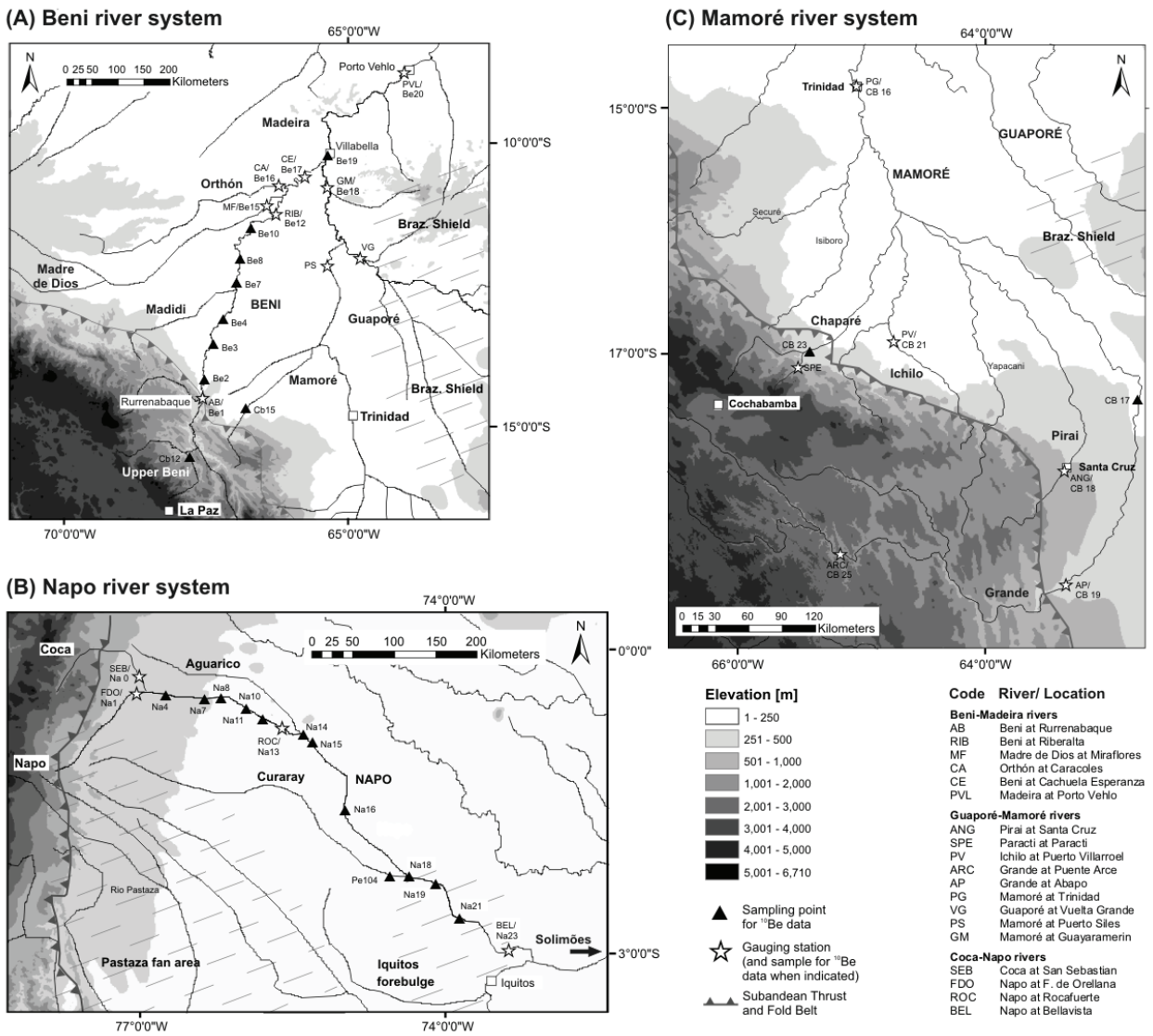

Figure 3.2 (A) Detailed map of Beni River with sediment gauging stations operated by HYBAM and sampling points for cosmogenic ^{10}Be; (B) detailed map of Napo River with sampling points, HYBAM sediment gauging stations, and tectonic features, such as the Iquitos forebulge (location drawn after Bes de Berc et al. [2005], and (C) detailed map of Mamoré River for the basin near Trinidad with sampling points and HYBAM sediment gauging stations. In case a cosmogenic sample was taken at the same location as a gauging station, the sample name is indicated below the HYBAM gauging station code.

The basin of the mainly anastomosing Napo River has an extent of ~140.000 km^2 at its confluence with the Solimões. The Napo originates in the precipitation-rich Ecuadorian Andes (mean rainfall of 2900 mm/yr; [Laraque *et al.*, 2004]). The Andean area comprises ~13% of the total catchment area, where lithology in the headwaters is mostly pyroclastic due to heavy Tertiary volcanism.

The Napo headwaters constitute the Coca River draining the northern and the Napo draining the southern Andean flank, where the Pastaza megafan already influences the morphology of the basin (see Figure 3.2). The transition between the erosional setting of the Andean Piedmont to the depositional setting of the floodplain is in case of the Coca at 77.3° W and in the case of the upper Napo at 77.8° W (see Fig. 1 in Laraque *et al.* [2004]). Below the Coca-Napo confluence in the floodplain, the Napo has only two tributaries, the Aguarico River, which also drains the Colombian and Ecuadorian Andes, and the Curaray River, a lowland river mainly draining the Pastaza megafan. On the flat alluvial plain of the lower Napo, up to 5000 m thick late Mesozoic to early Tertiary sediments crop out [Dumont & Fournier, 1994].

3.3 SAMPLE PROCESSING AND METHODOLOGY

Fluvial sediment for ^{10}Be analysis was collected from the active river channel in the floodplain and Andes during cruises in July 2001 (Cb samples), October 2002 (Beni), and October 2004 (Napo). All samples were collected by J.L. Guyot in the frame of the HYBAM project, a collaboration of the French IRD Institute with South American Institutes and Universities. Samples were sieved into narrow grain size ranges and quartz was extracted using HF leaching methods and magnetic separation. ^{10}Be was extracted using standard methods [von Blanckenburg *et al.,* 1996; von Blanckenburg *et al.*, 2004], ^{10}Be/^{9}Be ratios were measured in BeO targets with accelerator mass spectrometry at PSI /ETH Zurich and corrected as described by Synal *et al.* [1997]. Between 150 and 300 µg of ^{9}Be carrier were added to each sample, which was determined to contain a ^{10}Be/^{9}Be ratio of $0.55 \pm 0.28*10^{-14}$, except samples denoted by an asterisk in Table 3.2 that had a higher blank ratio. Analytical as well as blank error corrections are described in Table 3.2. Calculations of production rates and adsorption laws were done following Schaller *et al.* [2002]. Corrections of the production rate due to past variations in the intensity of the Earth's magnetic dipole field were only necessary for sample Be 16b, which has an apparent age of 32 kyr at a basin-averaged latitude of 15°S. Correction amounts to additional 20% in total production due to enhanced dipole intensity according to Gosse & Phillips [2001] and Masarik *et al.* [2001]. All other samples are ±10 kyr or younger in age at basin-averaged latitudes of 15°S for the Beni and Mamoré, and 0° to 1°S for the Napo River basin, which means that a correction for dipole variability is not necessary.

Table 3.1: Sampling locations and sample characteristics

Sample	River/ Location	Distance from first sample downstream [km]	Latitude[a] [°S]	Longitude[a] [°W]	Drainage Area[b] [x10^4 km^2]	Basin-avg. minimum altitude[b] [m]	Basin-avg. mean altitude[b] [m]	Basin-avg. relief[b,c] [m]	Basin-avg. slope[b] [%]
Beni River									
Cb 12a	Coroico (within upper Beni)	-135[$]	-15.686	-67.673	0.47	500	2361	1861	15.1
Cb 15b	Maniqui (within upper Mamoré)[§]	35[$]	-14.864	-66.738	0.53	199	865	666	3.4
Be 1	Beni at Rurrenabaque	0	-14.527	-67.497	6.8	490	2119	1629	9.8
Be 2	Beni	30	-14.284	-67.474	7.3	197	2094	1897	9.7
Be 3a	Beni	110	-13.571	-67.353	8.0	182	1921	1739	8.9
Be 4	Beni	170	-13.119	-67.185	9.3	175	1685	1510	7.8
Be 7	Beni at Puerto Cavinas	230	-12.512	-66.950	10.5	168	1511	1343	6.9
Be 8a	Beni	290	-12.078	-66.882	11.0	161	1443	1282	6.6
Be 10a	Beni	350	-11.559	-66.677	11.3	150	1405	1255	6.3
Be 12a	Beni at Riberalta	400	-11.212	-66.249	12.4	141	1293	1152	5.9
Be 15a	Madre de Dios at Miraflores	415	-11.112	-66.416	14.0	141	906	765	3.2
Be 16b	Orthón at Caracoles	450	-10.820	-66.110	3.2	132	236	104	0.5
Be 17a	Beni at Cachuela Esperanza	510	-10.550	-65.600	30.4	121	960	839	3.9
Be 18	Marmoré at Guayaramerin	475[$]	-10.808	-65.346	59.9	120	448	328	1.9
Be 19a	Madeira at Villabella	570	-10.229	-65.281	88.2	115	594	479	2.5
Be 20a	Madeira at Porto Velho	800	-8.770	-63.909	95.4	79	560	481	2.4
Napo River									
Na 0	Coca at San Sebastian	0	-0.340	-77.005	0.59	295	1817	1522	8.8
Na 1b	Upper Napo at F. de Orellana	5	-0.462	-76.925	0.61	266	1657	1391	7.1
Na 4b	Napo*	25	-0.460	-76.699	1.9	277	1468	1191	6.3
Na 7b	Napo	72	-0.478	-76.305	2.4	251	1249	998	5.2
Na 8b	Napo	91	-0.447	-76.124	2.5	240	1220	980	5.0
Na 10b	Napo	127	-0.634	-75.774	2.6	217	1164	947	4.8
Na 11a	Napo	150	-0.735	-75.582	2.7	205	1153	948	4.6
Na 13a	Napo at Rocafuerte	174	-0.882	-75.456	3.0	197	1033	836	4.1

Table 3.1 ▪CONTINUED▪

Sample	River/ Location	Distance from first sample downstream [km]	Latitude[a] [°S]	Longitude[a] [°W]	Drainage Area[b] [x10^4 km^2]	Basin-avg. minimum altitude[b] [m]	Basin-avg. mean altitude[b] [m]	Basin-avg. relief[b,c] [m]	Basin-avg. slope[b] [%]
Na 14b	Napo	205	-0.972	-75.180	3.9	182	1062	880	3.3
Na 15b	Napo	215	-1.025	-75.122	3.9	181	1060	879	3.2
Na 16b	Napo	320	-1.779	-74.704	4.9	146	711	565	2.6
Pe 104b	Curaray	426	-2.346	-74.077	4.3	145	817	672	2.9
Na 18	Napo below Curaray confl.	441	-2.353	-74.079	8.7	142	495	353	1.5
Na 19a	Napo	471	-2.482	-73.682	8.7	136	492	356	1.5
Na 21b	Napo	526	-2.899	-73.487	9.3	127	471	344	1.4
Na 23	Napo at Bellavista	602	-3.505	-73.109	10.1	110	456	346	1.4
Rivers within the	**Mamoré river basin at Puerto Ganadero near Trinidad**								
Cb 16	Marmoré at Puerto Ganadero	0	-14.864	-64.990	15.9	130	956	826	3.7
Cb 17b	Grande at Puerto Pailas	-390	-17.655	-62.777	8.1	222	2104	1882	8.5
Cb 18	Pirai at Angostura	-420	-18.082	-63.457	0.16	650	1207	1007	6.2
Cb 19b	Grande at Abapo	-570	-18.909	-63.410	6.0	450	2501	2196	10.3
Cb 21a	Ichilo at Puerto Villarroel	-260	-16.841	-64.787	0.76	170	678	511	5.3
Cb 23a	Chaparé at Villa Tunari	-300	-16.974	-65.414	0.49	294	2413	2119	15.0
Cb 25a	Grande near Puente Arce	-820	-18.609	-65.162	2.4	1550	3321	1771	11.7

[a]Reference frame is UTM coordinate system

[b]Derived from GIS analysis using spatial grid resolution of 1 km

[c]Basin-averaged relief is calculated from the mean altitude minus the minimum altitude

[$]Distance measured parallel to Beni River even for samples Cb 15b and Be 18

[§]Sample Cb 15b is located outside of the Mamoré basin at Trinidad

*Below the Napo-Coca confluence, the river is called the Napo.

3.4 ^{10}BE NUCLIDE CONCENTRATIONS MEASURED IN FLOODPLAIN SETTINGS

3.4.1 The Beni River

Nuclide concentrations of ^{10}Be have been measured over distances of 800 km along the river course at various points from Rurrenabaque to Porto Velho (see Figure 3.3a). An additional sample from the Andean Beni basin (Cb 12) has been measured for comparison. With its nuclide concentration of $10.0 \pm 1.1\times10^4$ at/g$_{(Qz)}$ it is at the upper end of nuclide concentrations measured in the Andean range by Safran *et al.* [2005]. ^{10}Be nuclide concentrations for the Beni trunk stream at Rurrenabaque at the upper Beni basin outlet are $3.8 \pm 0.6\times10^4$ at/g$_{(Qz)}$ (average of Be 1a and b, where in this study "a" denotes the 125-250 µm and "b" the 250-500 µm grain size fraction; see Table 3.2). 30 km downstream in the Beni floodplain, nuclide concentrations decrease to $2.3 \pm 0.4\times10^4$ at/g$_{(Qz)}$ (avg. of Be 2a and b). 110 km from Rurrenabaque, the ^{10}Be concentration of river sediment is $3.1 \pm 0.4\times10^4$ at/g$_{(Qz)}$ for Be 3a. Shortly upstream of the Beni-Madidi confluence at 170 km from Rurrenabaque, the ^{10}Be concentration amounts to $6.7 \pm 0.8\times10^4$ at/g$_{(Qz)}$ (derived from two lab replicate samples Be 4a-1 and -2). At Puerto Cavinas downstream of the Madidi confluence the measured nuclide concentration is $2.5 \pm 0.4\times10^4$ at/g$_{(Qz)}$ for Be 7 (n = 2), and 290 km downstream of Rurrenabaque at Be 8a, concentration is $3.5 \pm 0.5\times10^4$ at/g$_{(Qz)}$. For the samples Be 10a and 12a at 350 and 400 km downstream from Rurrenabaque, respectively, nuclide concentrations are $4.1 \pm 0.4\times10^4$ and 4.0 ± 1.0 at/g$_{(Qz)}$. At Cachuela Esperanza downstream of the confluences of the Madre de Dios and Orthón, the trunk stream yields a nuclide concentration of $3.7 \pm 0.7\times10^4$ at/g$_{(Qz)}$ (Be 17a).

Tributary input to the Beni is characterized by samples from the rivers Madre de Dios at Miraflores (Be 15a, nuclide concentration is $2.1 \pm 1.0\times10^4$ at/g$_{(Qz)}$) and the Orthón at Caracoles (Be 16b, $11.1 \pm 1.1\times10^4$ at/g$_{(Qz)}$). The Madre de Dios is a river comparable in size, Andean headwater rock type, and cosmogenic nuclide concentration with the Beni at their confluence, but the Orthón River is a tributary exclusively draining Miocene lowland sediments of the Fitzcarrald Arch formation [Espurt *et al.*, 2007], at which the nuclide flux is visibly different than Andean flux carried by the Beni River.

Admixing sediment of higher nuclide concentrations into the Beni does not seem to play a major role to mainstream mixed concentrations, since downstream of the confluence no increase in nuclide concentration (sample Be 17a) is observed.

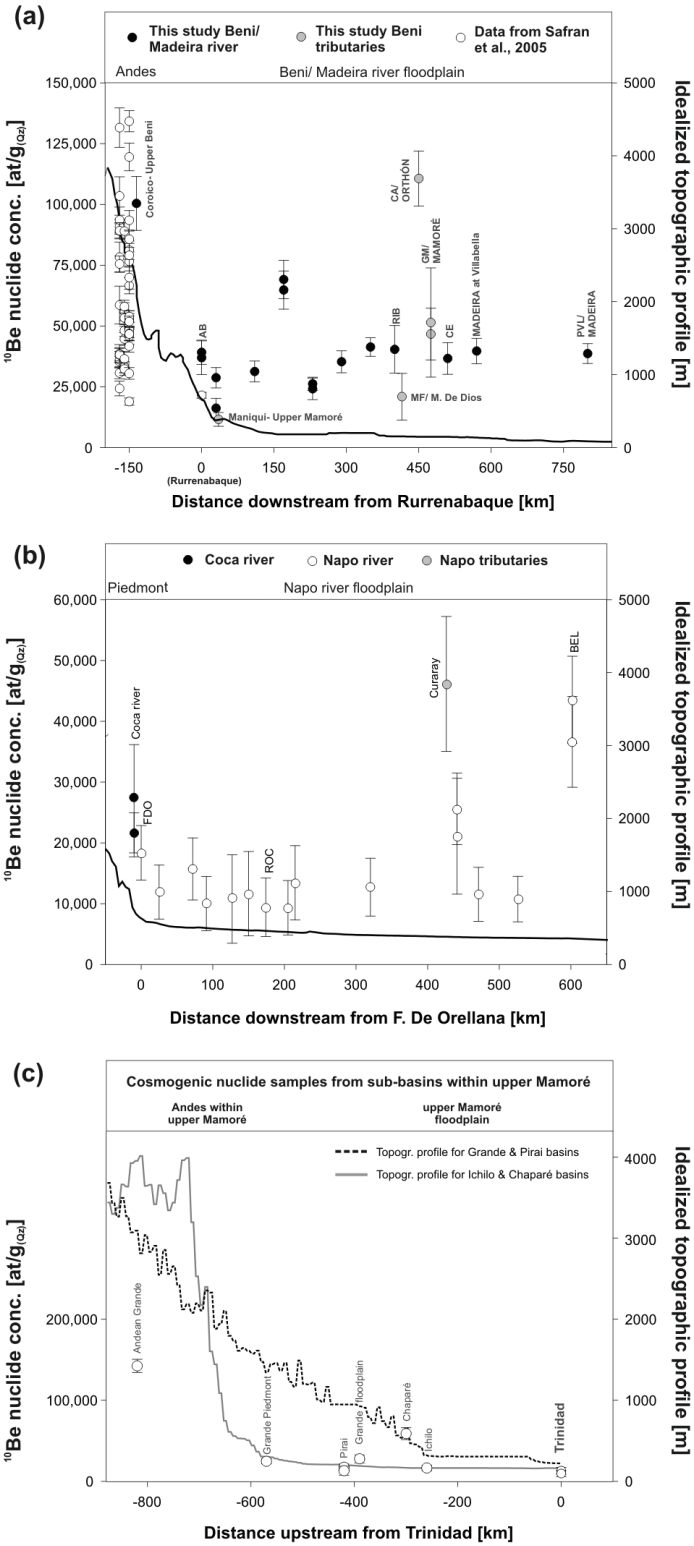

Figure 3.3 Cosmogenic nuclide concentration profiles for Beni (a), and Napo (b), and nuclide concentrations for upper Mamoré sub-basins (c) plotted against distance from a reference point (km). Right axis gives elevation of idealized topographic profile of the basin (m), which has been projected from several valley-perpendicular profiles into a single plane. For abbreviations, see Figure 3.2 or Table 3.3. For a), Andean nuclide concentrations and nuclide concentration at Rurrenabaque measured by Safran *et al.* [2005] are shown (white circles). In case of c), samples are from individual basins within the upper Mamoré at Trinidad. Two averaged topographic basin profiles are shown, because they are distinctly different for northern Bolivian Andes near Cochabamba and southern Andes where Andean chain is widest.

The samples Cb 15 and Be 18 characterize the Mamoré River outside of the actual Beni basin, but this data is presented here rather than in section 4.3 that characterizes the Mamoré basin because these samples contribute to the Beni trunk stream. Sample Cb 15b was taken from the Mamoré at San Borja (Maniqui River), which has a very low nuclide concentration of 1.2 ± 0.3×10^4 at/g$_{(Qz)}$ when compared to samples measured in the Bolivian Andes. Samples Be 18a-1 and -2 characterize the lower Mamoré at Guayaramerin, thereby characterizing the nuclide flux transported into the Madeira River. The samples yield an average of 4.9 ± 1.7×10^4 at/g$_{(Qz)}$. This river drains to ~60% old cratonic shield areas (Rio Guaporé) and to ~40% Andean territory (upper Mamoré River), and the measured concentration agrees with one that can be calculated for this mixture using the sediment flux data from [Guyot *et al.*, 1996], and end member concentrations of ~4.0×10^4 at/g$_{(Qz)}$ measured for the Andean part of the Mamoré River (mean from all upper Mamoré samples), and a nuclide concentration of 25×10^4 at/g$_{(Qz)}$ measured for the Brazilian shield (see Chapter 4).

The samples Be 19a (Madeira at Villabella; nuclide concentration is 4.0 ± 0.5×10^4 at/g$_{(Qz)}$) and 20a (Madeira at Porto Velho; 4.0 ± 0.4×10^4 at/g$_{(Qz)}$) integrate over the entire Mamoré River basin including the Beni and Mamoré, which at Porto Velho has an extent of more than 1 million km^2. Both samples essentially have the same nuclide concentration as measured at Rurrenabaque, portraying the low sediment flux coming into the Madeira River from the cratonic shield areas as well as the high sediment flux with dominate nuclide concentration from the Beni River.

3.4.2 The Napo River

^{10}Be nuclide concentrations have been measured over floodplain distances of 600 km along the Napo River course at various points from the Coca-Napo confluence to Bellavista (see Table 3.2 and Figure 3.3b). The Coca River has been characterized by sample Na 0 at San Sebastian; average nuclide concentrations are 2.4 ± 0.6×10^4 at/g$_{(Qz)}$ (average of Na 0a-1 and 2). The sample Na 1 from Francesco de Orellana on the Napo River covers in part conglomerates of the Pastaza megafan; the measured nuclide concentration of Na 1b amounts to 1.8 ± 0.5×10^4 at/g$_{(Qz)}$. The reduced precision of all Napo samples stems from very low ^{10}Be nuclide concentrations measured in the samples, or from the very low ^{10}Be/^{9}Be ratios, which are close to detection limit.

Below the Napo-Coca confluence at sample Na 4b, ca. 25 km downstream of Francisco de Orellana, the measured nuclide concentration decreases slightly to 1.2 ± 0.4×10^4

at/g$_{(Qz)}$; at Na 7b ~70 km downstream, ^{10}Be concentration increases again at 1.6 ± 0.5×10^4 at/g$_{(Qz)}$. Along the floodplain to Rocafuerte nuclide concentrations are constant at 1.0 ± 0.4, 1.1 ± 0.7, and 1.2 ± 0.7×10^4 at/g$_{(Qz)}$, for samples Na 8b, 10b, and 11a, respectively. At Rocafuerte (Na 13a) and 25 km further downstream (Na 14b), concentrations are slightly lower at 0.9 ± 0.5 and 0.9 ± 0.4×10^4 at/g$_{(Qz)}$, respectively. At Na 15b, 10 km downstream from this sample, nuclide concentration amount to 1.3 ± 0.6×10^4 at/g$_{(Qz)}$. Although there is a distance of ~100 km between Na 15b and the following downstream sample, Na 16b, nuclide concentrations do not change much (1.3 ± 0.5×10^4 at/g$_{(Qz)}$ at Na 16b). Nuclide flux input from Curaray River (sample Pe 104b, 4.6 ± 1.1×10^4 at/g$_{(Qz)}$) is significantly higher than the average Napo nuclide concentration. The Curaray drains the alluvial Pastaza megafan, providing a nuclide signal evidently distinct from that of the Ecuadorian Andes. Measured nuclide concentrations at Na 18 (average of 2.3 ± 0.8×10^4 at/g$_{(Qz)}$) immediately below the Napo-Curaray confluence are elevated, but concentrations are back at average floodplain levels again further downstream at Na 19a (30 km downstream from confluence, nuclide concentration of 1.2 ± 0.4×10^4 at/g$_{(Qz)}$) and 21b (60 km downstream; 1.1 ± 0.4×10^4 at/g$_{(Qz)}$). Nuclide concentrations at Bellavista gauging station (samples Na 23a-1 and 23-2; lab replicates) close to the Napo-Solimões confluence, are, similar to Curaray concentrations, slightly elevated. We have measured this sample twice to exclude analytical problems; its elevated nuclide concentration seems to be due to mixing of Solimões with Napo sediment at high river water stage, when the sampling campaign was carried out. In the case of the Solimões at Iquitos, water level changes of more than 10 m can occur between the seasons and vast areas are periodically inundated. Alternatively, an influence from the Mazan River (see Guyot *et al.* [2007b]), a tributary draining Miocene sediments could also result in increased nuclide concentrations, an observation that is similar to the Madidi River in the Beni River basin.

3.4.3 The Mamoré River

Within the Mamoré River basin at Puerto Ganadero near Trinidad, we have measured primary sediment-delivering Andean sub-catchments in order to characterize the sediment-generating areas and to decipher the transfer of cosmogenic nuclides from the Andes to the floodplain. We sampled several basins within the floodplain to account for sediment deposition and

Table 3.2: Analytical Results

Sample[a]	Grainsize [µm]	^{10}Be concentration[b] [x10^4 at/g$_{(Qz)}$]			Total production rate[c] [at/g$_{(Qz)}$/yr]	Total production rate corrected for floodplain area[d] [at/g$_{(Qz)}$/yr]	Denudation rate[e] [mm/yr]			Apparent age[f] [yr]	Floodplain-corrected denudation rate[g] [mm/yr]			Total sediment load[h] [Mt/yr]
Beni River														
Cb 12a*	125-250	10.04	±	1.11	20.4	-	0.15	±	0.02	4970	-	-	-	2
Cb 15b*	250-500	1.16	±	0.28	6.5	-	0.49	±	0.11	1730	-	-	-	10
Be 1a	125-250	3.92	±	0.50	15.3	-	0.36	±	0.05	2570	-	-	-	70
Be 1b	250-500	3.69	±	0.69	15.3	-	0.39	±	0.08	2420	-	-	-	70
Be 2a	125-250	2.87	±	0.42	15.0	15.3	0.49	±	0.08	1920	0.50	±	0.07	100
Be 2b	250-500	1.62	±	0.41	15.0	15.3	0.87	±	0.23	1080	0.89	±	0.22	180
Be 3a	125-250	3.13	±	0.43	13.3	15.3	0.40	±	0.06	2350	0.46	±	0.06	100
Be 4a-1	125-250	6.48	±	0.79	11.3	15.3	0.16	±	0.02	5750	0.22	±	0.03	60
Be 4a-2*	125-250	6.91	±	0.79	11.3	15.3	0.15	±	0.02	6130	0.21	±	0.02	50
Be 7a	125-250	2.42	±	0.44	10.0	15.3	0.39	±	0.07	2430	0.59	±	0.11	170
Be 7b	125-250	2.62	±	0.27	10.0	15.3	0.36	±	0.04	2630	0.55	±	0.06	150
Be 8a	125-250	3.53	±	0.45	9.5	15.3	0.25	±	0.04	3720	0.40	±	0.05	120
Be 10a	125-250	4.14	±	0.38	9.2	15.3	0.21	±	0.02	4500	0.34	±	0.03	110
Be 12a	125-250	4.04	±	0.98	8.5	15.3	0.19	±	0.05	4760	0.35	±	0.09	120
Be 15a*	125-250	2.09	±	0.96	6.4	-	0.28	±	0.13	3280	-	±	-	110
Be 16b	250-500	11.06	±	1.13	4.2***	-	0.03	±	0.00	32000	-	±	-	2
Be 17a	125-250	3.66	±	0.65	6.6	15.3	0.17	±	0.03	5520	0.39	±	0.07	320
Be 18a-1	125-250	4.67	±	1.06	4.5	-	0.09	±	0.02	10380	-	±	-	140
Be 18a-2*	125-250	5.14	±	2.25	4.5	-	0.08	±	0.04	11450	-	±	-	130
Be 19a	125-250	3.97	±	0.52	5.0	-	0.12	±	0.02	7900	-	±	-	280
Be 20a	125-250	3.87	±	0.41	4.9	-	0.12	±	0.01	7940	-	±	-	300
Napo River														
Na 0a-1	125-250	2.13	±	0.36	13.7	-	0.47	±	0.08	1780	-	-	-	10
Na 0a-2	125-250	2.73	±	0.89	13.7	-	0.37	±	0.12	2270	-	-	-	10
Na 1b	250-500	1.84	±	0.45	10.7	12.0	0.55	±	0.13	1720	0.60	±	0.15	10
Na 4b	250-500	1.19	±	0.44	9.4	12.0	0.74	±	0.28	1270	0.93	±	0.35	50
Na 7b*	250-500	1.57	±	0.51	8.0	12.0	0.48	±	0.16	1960	0.70	±	0.23	50
Na 8b	250-500	1.00	±	0.45	7.9	12.0	0.74	±	0.34	1270	1.10	±	0.49	80
Na 10b*	250-500	1.08	±	0.73	7.6	12.0	0.66	±	0.45	1430	1.02	±	0.65	70
Na 11a	125- 250	1.16	±	0.69	7.5	12.0	0.60	±	0.36	1560	0.95	±	0.56	70
Na 13a*	125- 250	0.94	±	0.48	6.9	12.0	0.68	±	0.35	1370	1.17	±	0.60	100

Table 3.2 ▪CONTINUED▪

Sample[a]	Grainsize [µm]	^{10}Be concentration[b] [x10^4 at/g$_{(Qz)}$]			Total production rate[c] [at/g$_{(Qz)}$/yr]	Total production rate corrected for floodplain area[d] [at/g$_{(Qz)}$/yr]	Denudation rate[e] [mm/yr]			Apparent age[f] [yr]	Recalculated denudation rate[g] [mm/yr]			Total sediment load[h] [Mt/yr]
Na 14b	250-500	0.93	±	0.45	7.0	12.0	0.70	±	0.34	1330	1.18	±	0.57	120
Na 15b*	250-500	1.34	±	0.61	7.0	12.0	0.49	±	0.22	1920	0.82	±	0.37	90
Na 16b	250-500	1.27	±	0.48	5.4	12.0	0.40	±	0.15	2360	0.87	±	0.33	120
Pe 104b	250-500	4.62	±	1.11	5.9	-	0.12	±	0.03	7900	-	±	-	10
Na 18a	125- 250	2.56	±	0.59	4.6	12.0	0.17	±	0.04	5600	0.43	±	0.10	100
Na 18b*	250-500	2.11	±	0.95	4.6	12.0	0.20	±	0.09	4610	0.52	±	0.23	120
Na 19a*	125- 250	1.15	±	0.44	4.6	12.0	0.37	±	0.15	2530	0.95	±	0.36	230
Na 21b	250-500	1.08	±	0.37	4.5	12.0	0.39	±	0.14	2390	1.02	±	0.36	260
Na 23b-1	250- 500	3.66	±	0.75	4.4	12.0	0.11	±	0.02	8250	0.30	±	0.06	80
Na 23b-2*	250- 500	4.35	±	0.71	4.2	12.0	0.09	±	0.02	10300	0.25	±	0.04	70
Rivers within the	**Mamoré river basin near Trinidad**													
Cb 16a**	160-250	1.32	±	0.42	6.5	11.4	0.47	±	0.15	1160	0.72	±	0.23	310
Cb 16b**	250-400	0.96	±	0.37	6.5	11.4	0.64	±	0.25	840	0.99	±	0.38	430
Cb 17b*	250-500	2.77	±	0.49	14.5	18.3	0.42	±	0.07	1530	0.51	±	0.09	110
Cb 18b**	250-500	1.75	±	0.40	7.8	-	0.40	±	0.10	2230	-	±	-	2
Cb 18c**	500-800	1.32	±	0.55	7.8	-	0.54	±	0.23	1680	-	±	-	2
Cb 19b*	250-500	2.47	±	0.32	20.1	-	0.62	±	0.08	1240	-	±	-	100
Cb 21a*	125-250	1.65	±	0.34	5.6	6.9	0.32	±	0.06	2450	0.38	±	0.07	10
Cb 23a*	125-250	5.88	±	0.73	20.2	-	0.26	±	0.03	2940	-	±	-	3
Cb 25a**	160-250	14.24	±	0.82	24.5	-	0.13	±	0.01	4670	-	±	-	10

[a]"a" and "b" denote different grain size fractions, and "1" and "2" denote lab replicates

[b]Corrected for blank, with combined analytical and blank error

[c]Total production rate, calculated for fast and slow muonic and nucleogenic components after Dunai [2000]. No shielding correction applied

[d]Gives only the hinterland production rate excluding floodplain area

[e]Combined errors on ^{10}Be measurement, blank, and 5% production rate error due to shielding and spatial resolution effects

[f]Gives the time spent in upper ~60 cm of an eroding layer

[g]Recalculated denudation rate with hinterland production rate corrected for floodplain area

[h]Calculated from floodplain-corrected denudation rate, or, for floodplain-area free basins, with normal denudation rate using a mean density of 2.7 g/cm^3

*^{9}Be carrier added to these samples contains a ratio of ^{10}Be/^{9}Be of 2.35 ± 1.08x10^{-14}

**^{9}Be carrier added to these samples contains a ratio of ^{10}Be/^{9}Be of 1.10 ± 0.66x10^{-14}

***Production rate corrected for paleomagnetic intensity changes, correction calculated with uncorrected apparent age given in column "Apparent Age"

rapid exchange due to river migration. We decided against an intensive floodplain profile along the river in the case of the Mamoré, as this river has many small tributaries of which some of them drain either floodplain areas only, or highly-concentrated Brazilian shield areas, possibly resulting in a composite nuclide signal that is difficult to interpret. For the southern part of the Bolivian Andes where the Andean chain is widest, the basin of the Grande was sampled three times at Puente Arce (high Andes), downstream at Abapo (Piedmont) and again at Puerto Pailas, near Santa Cruz de la Sierra in the floodplain. The upper Grande basin at Puente Arce yields a very high nuclide concentration of $14.2 \pm 0.8\times10^4$ at/g$_{(Qz)}$) (sample Cb 25a). At Abapo, nuclide concentration of sample Cb 19b have decreased to $2.5 \pm 0.3\times10^4$ at/g$_{(Qz)}$, which agrees well with sample Cb 17b measured near Santa Cruz ($2.8 \pm 0.5\times10^4$ at/g$_{(Qz)}$, see Figure 3.3c).

The Pirai River was sampled at Angostura at the Piedmont-floodplain transition. Measured nuclide concentrations of $1.8 \pm 0.4\times10^4$ and $1.3 \pm 0.6\times10^4$ at/g$_{(Qz)}$ for samples Cb 18b and c (two different grain sizes; see Table 3.2) are somewhat lower than those of the downstream Grande. For the northern Bolivian Andes ~60 km NE of Cochabamba, nuclide concentrations of the Chaparé (Cb 23a) and the Ichilo (Cb 21a) basins were measured, although only the Chaparé accounts for pure Andean denudation, because in the Ichilo case, the sample was taken at Puerto Villarroel which is situated in the floodplain ~30 km from the Piedmont front. For these two samples, two significantly different signals were detected. For the Ichilo, a nuclide concentration of $1.7 \pm 0.3\times10^4$ at/g$_{(Qz)}$ was measured, and for the Chaparé, a nuclide concentration of $5.9 \pm 0.7\times10^4$ at/g$_{(Qz)}$ has been detected. For the Ichilo, addition of floodplain sediment cannot be discounted, but the Chaparé sample on the other hand was taken at the immediate Piedmont outlet at Villa Tunari therefore recording a pure Andean signal.

Near Trinidad at Puerto Ganadero (Cb 16), the nuclide signal of the entire Mamoré basin should average over the tested sub-catchments provided that the nuclide signal from the Andes does not vary with time and that storage of sediment is negligible within the resolution of cosmogenic ^{10}Be measurements, over periods of several thousands years. Measurements of two different grain sizes for this sample reproduce well (see Table 3.2) at concentrations of $1.3 \pm 0.4\times10^4$ and $1.0 \pm 0.4\times10^4$ at/g$_{(Qz)}$. This sample should integrate over the entire Mamoré, being more or less representative of the measured sub-catchments. Mixing calculations of nuclide concentrations with gauging-derived sediment fluxes [Guyot *et al.*, 1996] for the Grande at Abapo, the Pirai at Angostura, and an average calculated for the Ichilo and Chaparé rivers do not result in a concentration equivalent to the one measured at Trinidad, but one that is slightly higher at ~2.5×10^4 at/g$_{(Qz)}$. However, in this calculation, several sections of the

Mamoré basin are not included, because neither cosmogenic nuclide nor river load data was available. Regarding the high variability of the nuclide flux passed on from the Andes to the floodplain as shown by the Grande River profile, this discrepancy could also be caused in the Andes itself by spatially different sources of sediment.

3.5 DISCUSSION

A denudation rate can be calculated for the entire Beni basin upstream of sample Beni 1 at Rurrenabaque. This denudation rate is 0.36 ± 0.05 and 0.39 ± 0.08 mm/yr from the two measured grain sizes (see Table 3.2). For the Napo basin above the Napo-Coca confluence, denudation rates are 0.42 ± 0.1 mm/yr for Na 0 on the Coca River (average of two replicates) and 0.55 ± 0.13 mm/yr for Na 1 on the Napo River. For the Mamoré basin, an average Andean denudation rate from the samples Cb 18, 19, 23, and 25 which do not cover any floodplain area, is 0.39 ± 0.09 mm/yr.

In this discussion, we will first assess the significance of these hinterland denudation rates in the light of published cosmogenic nuclide data from small catchments of the Bolivian Andes [Safran *et al.*, 2005]. We will then proceed to compare these rates to those that have been obtained over shorter (river loads) and longer (fission track) denudation rate meters. Finally, we will assess how much of both cosmogenic nuclide-derived denudation rate signal and short-term sediment yield from river loads is preserved during storage and remobilization as sediment moves down the course of the Beni, Napo, and Mamoré trunk streams.

3.5.1 Denudation rates in the upper Beni and Napo catchments

3.5.1.1 The upper Beni basin

The upper Beni basin can be divided into the high-relief, steeply sloped Andean part and the low-relief Piedmont section, which is also called the Subandean Belt [e.g. Dumont & Fournier, 1994; Horton, 1999; Horton & Decelles, 2001]. The Piedmont section comprises ~30% or 2.1×10^4 km^2 of the total upper Beni basin; no cosmogenic nuclide-derived data is available from this part. Denudation rates from cosmogenic nuclides in the Andean part of the upper Beni basin by Safran *et al.* [2005] were recalculated following production rate

(including muons) and scaling calculations suggested by Schaller *et al.* [2002]. The analyzed main areas (La Paz and Mid region) are located at 15-16°S and 67-69°W and give averages of 0.59 ± 0.03 mm/yr (n = 20) and 0.50 ± 0.03 mm/yr (n = 27), respectively. Data analysis by Safran *et al.* [2005] reveal channel steepness as first-order controlling parameter on denudation in the Bolivian Andes. According to these authors, lithology does not play a dominant role.

The denudation rate measured at Rurrenabaque should average over the entire upper Beni basin, including the Andean and Piedmont section, and this rate has been measured by Safran *et al.* [2005] (sample BOL-50) and this study (samples Be 1a and 1b). However, results from both studies differ considerably. Safran *et al.* [2005] have measured a nuclide concentration of 2.2 ± 0.1×10^4 at/g$_{(Qz)}$ at Rurrenabaque (BOL-50), while this study has measured a mean nuclide concentration of 3.8 ± 0.6×10^4 at/g$_{(Qz)}$ (n = 2, Be 1a + b; Figure 3.3a). Recalculating Safran's production rates using Dunai scaling laws [Dunai, 2000] and a SLHL production rate of 5.53 at/g$_{(Qz)}$/yr [Kubik *et al.*, 1998], results in denudation rates of 0.66 ± 0.04 and 0.37 ± 0.06 mm/yr for the two studies, respectively. The observed difference in measured nuclide concentrations at the same location can possibly be attributed to a temporal variability of source areas providing sediment. Safran *et al.* [2005] have sampled in June 1998, at the end of the flood period, while samples for this study have been taken in October 2002, during the low water stage. One possible cause of this could, for example, be massive mass input from deeply buried landslide material discharged irregularly with time, as it was observed during flood stage at Rurrenabaque by Guyot *et al.* [1993]. According to Blodgett & Isacks [2007], land sliding is the dominant process of hillslope erosion in high-relief zones of the Eastern Cordillera. Mapping of small, undisturbed watersheds from multi-temporal aerial photographs suggest locally highly increased erosion rate estimates of 9 ± 5 mm/yr, and this enhanced short-term erosion rate, integrating over a few decades, may even be typical across a 40-km-wide swath within the Bolivian cordillera [Blodgett & Isacks, 2007]. The trigger to massive landslides is mostly found in abnormally high rainfalls which in the Beni basin are often associated with the El Niño/ Southern Oscillation (ENSO) phenomenon. More precisely, cold phase ENSO (or La Niña) events cause the Beni River to flood due to heavy rainfalls in the Bolivian Andes, and it is depositing most of its sediment on the downstream floodplain during such an event [Aalto *et al.*, 2003]. Our sediment material has been sampled during October 2002, which was, in terms of the southern oscillation, a normal year. Safran *et al.* [2005] have sampled during June 1998, of which the beginning of the year was influenced by a strong El Niño phenomenon, and the end of the year was influenced by a moderately strong La Niña.

At Rurrenabaque, the sediment mix comprises that of the Andean part of the Beni basin which has an area-weighted average concentration of 6-7×10^4 at/$g_{(Qz)}$ [Safran *et al.*, 2005], which corresponds to a denudation rate of 0.53 ± 0.03 mm/yr. This concentration is much higher than that determined by the two studies at Rurrenabaque, hinting at the erosion of low-concentration material in the Piedmont, from which no samples have been measured. The Piedmont zone in the Beni basin corresponds to the Sub-Andean zone defined by Horton [1999]. Some of this can be explained by much lower production rates in the Piedmont section (7.0 at/$g_{(Qz)}$/yr) than in the Andean part (21.4 at/$g_{(Qz)}$/yr). A simple binary mixing calculation implies that nuclide concentrations for the Piedmont section range between 0.4 and 1.4×10^4 at/$g_{(Qz)}$, respectively. Corresponding denudation rates in the Piedmont are between ~1 mm/yr when using the Safran estimate for the nuclide concentration at Rurrenabaque and identical quartz abundances throughout the upper Beni, and ~0.3 mm/yr, using the nuclide concentration estimates of this study. Overall, the denudation rate in the Piedmont section is at least as high, but probably higher than that of the Bolivian Andes.

In the discussion to follow, we will use a cosmogenic nuclide concentration range of 4 to 6×10^4 at/$g_{(Qz)}$ and a corresponding denudation rate range of ~0.4 to 0.7 mm/yr as denudation signal of the Bolivian Andes including the Piedmont area at Rurrenabaque, which is delivered into the floodplain of the Beni River.

3.5.1.2 The upper Napo basin

The samples Na 0a-1 and -2 give an average denudation rate of 0.42 ± 0.10 mm/yr, which is similar to the rate measured at Francisco de Orellana (0.55 ± 0.13 mm/yr). The denudation rates measured at San Sebastian on the Coca River and at Francisco de Orellana on the Napo River may already be influenced by input from the Pastaza megafan in the Napo River case or by addition of floodplain sediment in the Coca River case, because upstream distance to the Piedmont front is ~20 km. All main stream samples taken downstream of the Napo-Coca confluence (Na 4 to Na 21, except Na 23, average to 1.3 ± 0.6×10^4 at/$g_{(Qz)}$) have somewhat lower nuclide concentrations than the upper Napo/ Coca samples (n = 3, average 2.2 ± 0.6×10^4 at/$g_{(Qz)}$), and denudation rates are correspondingly higher (0.48 ± 0.12 mm/yr in the upper basin part versus 0.9 ± 0.4 mm/yr below the Coca-Napo confluence, see Table 3.2). It could be possible that the conglomerates of the megafan contribute to higher denudation rates, e.g. low-concentration material is added from the Pastaza megafan. The Napo headwaters along

the Pastaza depression are constituted of the upper Miocene age "Chambira Formation", which consist mainly of quartz pebbles-bearing conglomerates [Christophoul *et al.*, 2002]. The Andean part of the Coca headwaters on the other hand feature mostly andesitic rocks with rather low Quartz contents and might therefore be underrepresented in the Napo trunk stream signal.

3.5.2 Denudation rate monitors in the Mamoré basin

Results from cosmogenic nuclide analysis show that the Andean range within the Mamoré basin is denuding at highly variable rates (see Table 3.2). Samples from the upper Grande River range from 0.13 to 0.62 mm/yr (samples Cb 25 and 19), the Pirai River is denuding at an averaged rate of 0.47 mm/yr, and denudation of the Chaparé is 0.26 mm/yr. The mean denudation rate for these basins is 0.39 ± 0.09 mm/yr, resulting in an averaged integration time scale of ~2.5 kyr. These results from the Andean part of the Mamoré basin are similar in magnitude and variability to what has been obtained by Safran *et al.* [2005] for the upper Beni. Given that our dataset does not provide full spatial cover, the agreement is remarkable. A latitudinal variation of denudation as suggested by Barnes & Pelletier [2006] cannot be inferred from this data.

From cosmogenic nuclides we can calculate a mean Andean denudation rate of 0.4 mm/yr, albeit with a large error, and one has to keep in mind that this figure is subjected to strong spatial and possibly temporal variations. For samples that are taken within the floodplain (Cb 16, 18, and 21), we corrected the denudation rates by using the mean production rate (including nucleonic and muonic components) for the sediment-producing area only (see Table 3.2; procedure explained in Section 3.5.4). For sample Cb 17b near Santa Cruz de la Sierra in the Grande floodplain, the denudation rate corrected for floodplain area (see Table 3.2) is 0.51 ± 0.09 mm/yr, which corresponds well to the overall mean and also agrees well with the denudation rate derived from the Grande at the Piedmont outlet (Cb 19b). The floodplain-corrected denudation rate for sample Cb 21a (Ichilo River) amounts to 0.38 ± 0.07 mm/yr, also agreeing well to the overall mean Andean denudation rate. Sample Cb 16 in the Mamoré floodplain samples the entire Mamoré catchment near Trinidad; the floodplain-corrected denudation rate amounts 0.85 ± 0.31 mm/yr (n = 2).

Although this rate is within error of the upstream samples, the slight increase with respect to the Andean mean could be potentially be due to an addition of sediment due to bank erosion with different nuclide concentrations in the floodplain However, as it has been shown

in Chapter 2, this is unlikely to be due to irradiation or decay during storage. Rather, the recorded denudation variation near Trinidad is more likely to be large because of the temporal variability introduced by spatially variable discharge events, similar to the source-area denudation rates in the upper Beni and supported by the variation already encompassed by the two grain sizes.

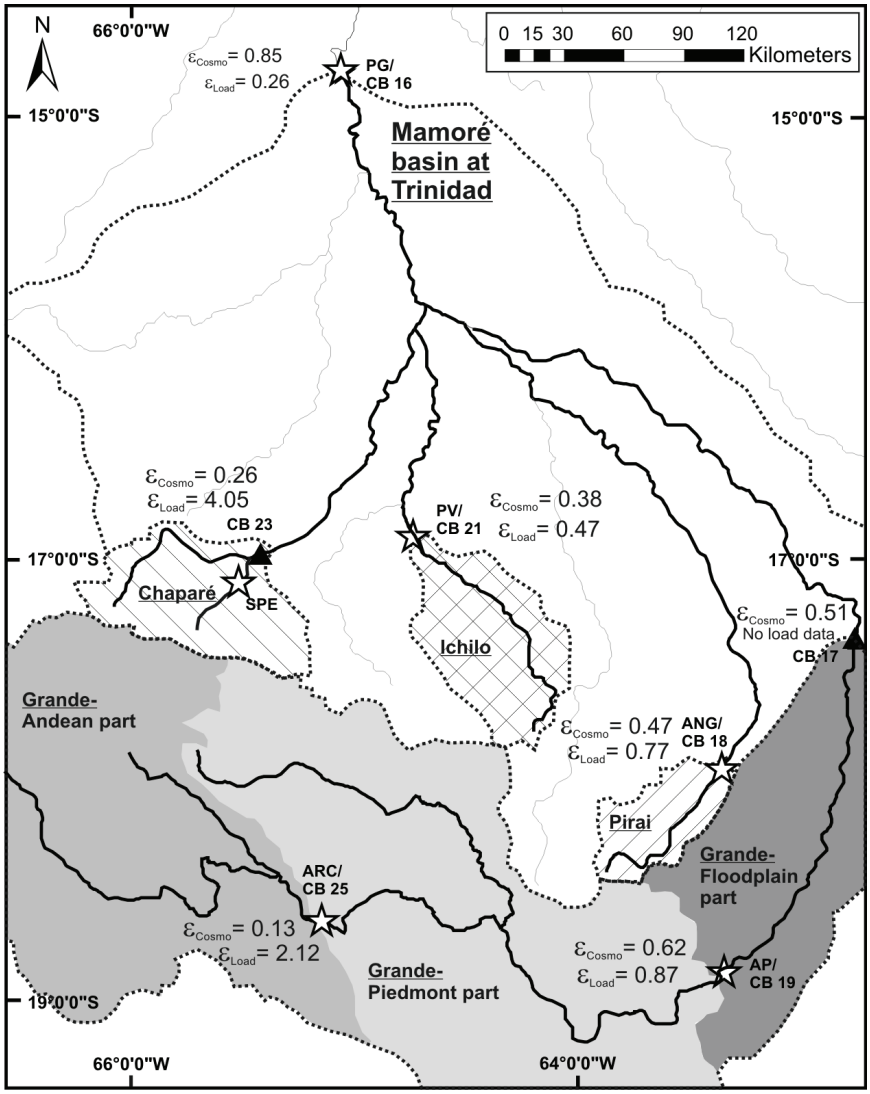

Figure 3.4 Detailed map of the Mamoré basin at Puerto Ganadero near Trinidad showing cosmogenic nuclide-derived denudation rates (ε_{cosmo}) and erosion rates calculated from sediment load data at HYBAM gauging stations (ε_{load}). For abbreviations, see Figure 3.2 or Table 3.3. Cosmogenic denudation rate calculation is based on the sediment-generating area only. Basins, cosmogenic samples, and gauging stations are indicated as in Figure 3.2. Different fill patterns denote different basins; in case of the Grande River, the three sub-areas (Andes, Piedmont and floodplain) are indicated with different shades of grey. Additional gauging data (not shown here) from other Mamoré sub-catchments is available (see Guyot *el al.* [1996] for details, not documented in Table 3.3) for the Grande basin at Abapo, where mean the gauging-derived erosion rate is 1.73 mm/yr (n = 7). For the Pirai basin at Angostura, the average erosion rate from sub-basins is 0.43 mm/yr (n= 6). For the northern Andean part, data from three gauging stations (LOC, ICO, and SPE; where single SPE is shown here to compare with sample Cb 23) are available, which average in erosion rate to 2.42 mm/yr. Gauging periods are 6 years for the Pirai and Grande dataset and only 2 years for the data from the northern Andean part [Guyot, 1993].

3.5.3 Assessment of source area denudation rates over different time scales

Denudation rate data over three different time scales in the Andean part of the Beni River headwaters show that rates are anti-correlated with time scale (see Figure 3.5a). Data derived from short-term (10^1 yr time scale) sediment loads record highest erosion rates (average of 1.64 mm/yr; [Guyot, 1993; Guyot *et al.,* 1996]); medium-term (10^3 yr) denudation rates from cosmogenic nuclides record an average of 0.53 mm/yr [Safran *et al.*, 2005]; and long-term (10^6 yr) denudation rates derived from fission-track analysis average to 0.3 mm/yr [Safran *et al.*, 2006]. The same data plotted against catchment area shows an anti-correlation with increasing catchment area (Figure 3.5b).

River loads from the Bolivian segment of the Eastern Andean Cordillera were studied by Guyot *et al.* [1996], who have focused their study on mesoscale sediment-sink free, purely denudational basins. For the upper Beni region, the data was collected from 16 stations integrating over 1-21 yrs, exhibiting a large range in erosion rates (0.01 to 6.9 mm/yr), corresponding to sediment yield of 30 to 19000 t/km^2/yr), respectively. Aalto *et al.* [2006] (using the same dataset as Guyot [1993] and Guyot *et al.* [1996]) have thoroughly analyzed geomorphic variables possibly exerting control on erosion rates in the Bolivian Andes, and have found that topographic steepness and lithology execute strongest dominance. Lithology in the La Paz region of the upper Beni basin, where most of the data was collected, features thick (1000 m), plio-quaternary fluvioglacial deposits with high clay contents, that have been eroding heavily since the LGM [Dosseto *et al.*, 2006b]. This weak substratum causes modern, gauging-derived erosion rates to be high in the La Paz area.

The in general much lower rates measured by cosmogenic nuclides, and their much lower variance can be explained by several effects: (i) Different integration time scales of the methods. Cosmogenic denudation rates integrate over time scales set by the prevailing denudation rate itself, because the apparent age gives the time spent within the uppermost ~60 cm of an eroding layer. In the case of the Bolivian Andes, this is 0.6-15 kyr [Safran *et al.*, 2005]. Human-induced acceleration in erosion rates on very short time scales would therefore not be recorded by cosmogenic nuclides [von Blanckenburg, 2005]. Such observations have been made in the Ecuadorian Andes [Vanacker *et al.*, 2007b], where land use change has induced very high recent erosion rates, but long-term cosmogenic denudation rates are still low. Maurice-Bourgoin *et al.* [2002] found an increase in the Hg-influx in upper Beni tributaries over the last 30 years revealed from isotope analysis in sediment cores. These authors attribute this effect to accelerated erosion of Hg-enriched soils, due to increased gold-mining activities, together with recent colonization, road construction, and other human activities following the 1970-1980´s gold boom [Cleary, 2000]. It was also around this time

that sediment gauging has recorded the highest erosion rates (>3 mm/yr) in the upper Beni basin [Guyot, 1993].

Barnes & Pelletier [2006] have already recognized that short-term denudation rates reach higher values and have greater variability than long-term denudation rates from cosmogenic nuclides in the upper Beni basin of the Bolivian Andes. According to these authors, the combined effects of the positive feedback mechanisms between uplift, climate, and denudation may have caused this disparity, which in their view has prolonged over the Holocene or even the late Miocene, and has recently been increasingly influenced by anthropogenic disturbances [Barnes & Pelletier, 2006].

Interestingly, we found that the Central Alps of Switzerland are subjected to the reversed situation (see Chapter 5). Here, cosmogenic nuclide-derived denudation rates are consistently higher by a factor of 5 to 10 than short-term erosion rates calculated from sedimentary river loads and are also slightly higher than the long-term denudation trend recorded by fission track analysis. Apart from method-related discrepancies, we found that the long history of human settlement in the Central Alps (>10 kyr) could have perturbed the system a long time ago due to prehistoric intensified land use and accelerated erosion (Chapter 5). Today, the sediment produced by this early event could have been flushed out of the system.

Another possibility is that the anti-correlation of denudation rates with time scale is caused by an artificial effect. Gardner *et al.* [1987] have found that a process rate, e.g. denudation, is not necessarily independent of the integration time of the method. According to these authors, a decrease in denudation rate with time scale does not have a priori natural geomorphic, tectonic, or climatic reason; the decrease is caused by the ability of the system to damp effects by reversing them over the long time scale.

The linearly decreasing trend in denudation versus catchment area (Figure 3.5b) illustrates how variation in denudation rate data decreases as integrated surface area increases. This is due to large-scale processes becoming more and more important, and small-scale processes are averaged out. Modern erosion rates from sediment gauging, however, are sensitive to catchment area once hillslope erosion is negligible, because with increasing catchment area, there is an increase in the relative importance of depositional processes [Hovius, 1998]. This inverse relation between sediment yield (t/km^2/yr) and drainage area has been noted by a number of workers [Milliman & Meade, 1983; Milliman & Syvitski, 1992]. Denudation rates from cosmogenic nuclides, however, are not subjected to this effect. Even though their variability decreases with catchment area (Figure 3.5b), their area-weighted average is similar at 0.53 ± 0.03 mm/yr for basins smaller than 1000 km^2, 0.52 ± 0.03 mm/yr

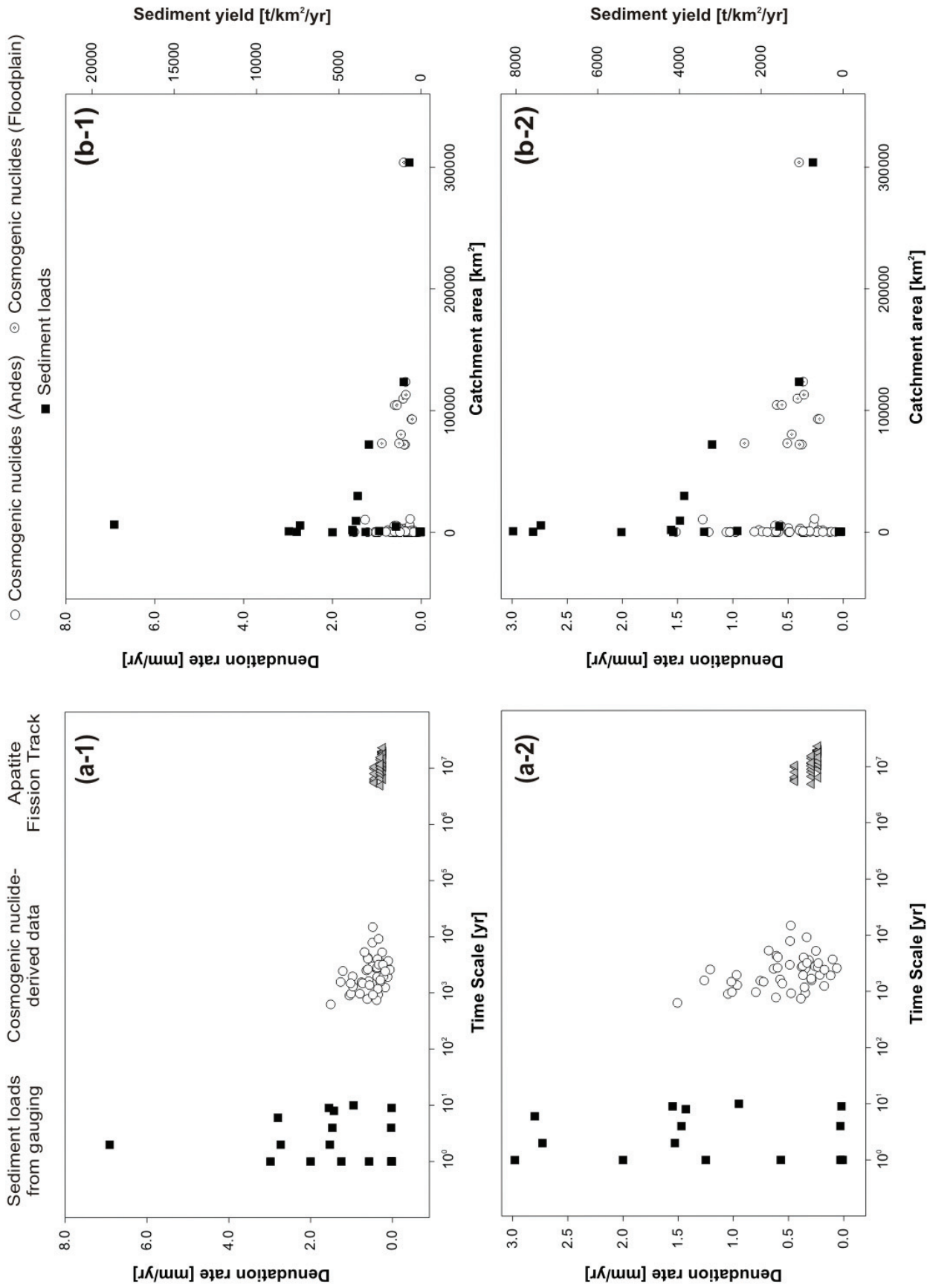
Sediment loads from gauging
Cosmogenic nuclide-derived data
Apatite Fission Track
(a-1)
(a-2)
Denudation rate [mm/yr]
Time Scale [yr]
Cosmogenic nuclides (Andes)
Cosmogenic nuclides (Floodplain)
Sediment loads
(b-1)
(b-2)
Sediment yield [t/km²/yr]
Catchment area [km²]

Figure 3.5 (see Left) Denudation rate estimations for the Andean Beni basin over different time scales (left panels a-1 and a-2). Data from sediment gauging give highest denudation rates (up to 6.9 mm/yr, average 1.64 mm/yr) and average over decadal time scales (data from Guyot *et al.* [1996]). Cosmogenic nuclide-derived denudation rates average to 0.53 mm/yr and integrate over millennial time scales (data recalculated from Safran *et al.* [2005]; see text). Denudation rates derived from AFT ages are between 0.2 to 0.6 mm/yr and integrate in mean over ~10 Myr (data from Safran *et al.* [2006]). Denudation rate estimations for the total Beni basin at Cachuela Esperanza plotted against drainage area (right panels b-1 and b-2). Andean cosmogenic nuclide data is from Safran *et al.* [2005], floodplain samples are Be 1 to 17 excluding tributaries; sediment load data from Guyot *et al.* [1996]. The data shows that with increasing basin area, variation in denudation decreases and that the cosmogenic sample taken at 300.000 km^2 (Cachuela Esperanza) is identical (within 2 sigma error) with the Andean average cosmogenic denudation rate from Safran *et al.* [2005]. The lower panels a-2 and b-2 are close-ups of the upper panels a-1 and b-1.

for basins between 1000-10,000 km^2, and basins between 50,000-300,000 km^2 average to 0.43 ± 0.07 mm/yr. This means that deposition does not alter the rate and the source signal that is conveyed throughout the fluvial transport system (see Chapter 2).

Rapid soil removal could also be the cause for the deviation in denudation rates derived from ^{230}Th-^{238}U disequilibria, which has been observed by Dosseto *et al.* [2006b]. For the upper Beni catchment, denudation rates from this method are up to a factor of 30 lower than present day (sediment gauging) erosion rates and up to a factor of 10 lower than denudation rates from cosmogenic nuclides. (ii) A climatic change with higher precipitation rates in recent decades could cause enhanced modern erosion rates. During the mid-Holocene, the Central Andes experienced a phase of aridity with very low rates of precipitation [e.g. Rowe *et al.*, 2002; Servant & Servant-Vildary, 2003; Abbott *et al.,* 2003]. All studies suggest that the mid-Holocene level of Lake Titicaca was ~100 m lower than today, with a termination of the arid phase at the latest around 1.5 kyr [Tapia *et al.*, 2003]. Additionally, Peruvian ice-core records suggest that tropical mid-tropospheric temperatures have been higher in recent decades than at any time during the past 2-3 kyr [Thompson *et al.*, 1995; Diaz & Graham, 1996], which would consequently enhance the tropical hydrological cycle including the El Niño phenomenon [Diaz & Graham, 1996; Barry & Seimon, 2000]. (iii) Short-term sediment gauging in the upper Beni records both the clay and the fine sand fraction that is still supported by transport energy. However, large outcrops of clay-rich quaternary fluvio-glacial deposits in the La Paz area may overestimate erosion from this area with respect to other tributaries that are eroding slower and merely contributing the sand fraction that cosmogenic nuclide-derived rates are based on.

Long-term rates of exhumation from apatite-fission-track analyses average over 5 to 20 Myr and the observed rates are with 0.2-0.6 mm/yr in the range of cosmogenic nuclide-derived denudation rates [Safran *et al.*, 2006]. Even a debated exponential increase in

exhumation rate at 10-15 Myr from 0.2 to ~0.7 mm/yr as suggested by Benjamin *et al.* [1978] and Anders *et al.* [2002] would agree with long-term cosmogenic nuclide-derived denudation rate estimations.

3.5.4 Implications for denudation rate calculations in floodplain settings and comparison with erosion rate data from sediment gauging

We have shown that the cosmogenic nuclide flux in the Beni depositional setting does not show and is not expected to show variations that are larger than the temporal variability introduced by spatially variable discharge events. Therefore, unperturbed catchment-wide denudation rates from such nuclide concentrations can be calculated. However, given that the catchment area increases along the river course, and the catchment-wide production rate decreases due to the increase in lowland area included in the calculation, the use of this lowland production rate results in an artificial drop in calculated denudation rate along the river course across the floodplain. To avoid this, we recalculated the denudation rates for the Beni, Napo, and Mamoré rivers to include the sediment-producing areas only. For the Beni, we defined the upstream area of Rurrenabaque as our sediment-delivering hinterland, because Andean as well as Piedmont area contribute. For the Napo, both Coca and Napo areas upstream of their confluence are defined as sediment-delivering hinterland, because we cannot exclude sediment contribution from the Pastaza fan area. For the individual sub-basins of the Mamoré, no common hinterland for all basins can be defined. Thus, we reclassified our digital elevation model to exclude areas <300 m, as this is the approximate transition elevation from Piedmont to floodplain area in the Mamoré, and then proceeded to calculate production rates with this modified elevation dataset.

For the Beni River floodplain, results from recalculation show that within two sigma error, all samples except Be 2b and replicates of Be 4 are in the same range as denudation rate estimates at Rurrenabaque. In Figure 3.6, we have additionally plotted erosion rates calculated from sediment loads recorded in the respective setting. The Beni yields high erosion rates from sediment loads in the transition zone from the Andes to the depositional floodplain setting at Rurrenabaque (km 0 to 400; see Figure 3.6a); as discussed in Section 3.5.3, this is unlikely to represent the long-term sediment flux into the Beni River floodplain.

At Riberalta gauging station (km 400), deposition of sediment has resulted in a decrease in the sediment load from initially 220 to 120 Mt/yr (Table 3.3). At the Bolivian floodplain outlet at Cachuela Esperanza (km 510), sediment loads are increasing again, recording sediment

remobilization and/ or high sediment input from the Madre de Dios River. Sediment yield data also show this decreasing trend from Rurrenabaque to Riberalta (Figure 3.6a), but these data are known to be subjected to area-induced bias.

To exclude this effect, we have recalculated sediment yield data using the sediment-producing areas only as we have done for cosmogenic nuclide production rate calculation, so in principle, we divide the sediment load measured at the respective station by the sediment-providing area, and thus we obtain area-corrected sediment yields (see Table 3.3).

If this approach is used, an increase in erosion rates from Riberalta to Cachuela Esperanza can be observed (Table 3.3). This increase is attributed to high sediment input from the Madre de Dios River. As for inter-method comparison, floodplain-corrected Beni floodplain gauging-derived erosion rates are significantly higher than cosmogenic denudation rates. If our cosmogenic nuclide measurements record the robust, time-integrated signal of denudation for the last ~2.5 kyr, the short-term erosion rates from sediment gauging would then on the other hand record an increase in erosion within the last few decades due to changes in land use or climate in the sediment-providing area.

The Napo dataset suffers from reduced precision resulting from very low nuclide concentrations and low quartz contents, making an interpretation difficult. Upstream of the Napo-Coca confluence, somewhat lower denudation rates are observed than downstream of the confluence (see Section 3.5.1.2). However, the increase in denudation (corresponding to a decrease in nuclide concentration) below the confluence is in our view due to the mixing of sediment from different sources rather than dilution effects from additional amounts of floodplain sediment, because if the latter were the case, high nuclide concentrations in the floodplain of the upper Coca from sample Na 0 would not be observed. Since the Coca River is the principle sediment provider to the Napo main stream, but its specific stream power being by a factor of 5 lower than the one of the upper Napo [Laraque *et al.*, 2004], it is unlikely that floodplain sediment are heavily eroded in the Coca basin.

The invariance of cosmogenic nuclide-derived denudation rates at ca. 0.8 to 1.0 mm/yr of the Napo trunk stream when using the production rate of the sediment-producing areas only (Figure 3.6b) would also favor the mixing of different sources of sediment by the two rivers, because even as vast amounts of sediment are removed from the floodplain between Rocafuerte and Bellavista (Figure 3.6b) as reported by gauging-derived erosion rates [Guyot *et al.*, 2007a], cosmogenic nuclide concentrations are not altered, as predicted by nuclide-accumulation modeling (see Chapter 2).

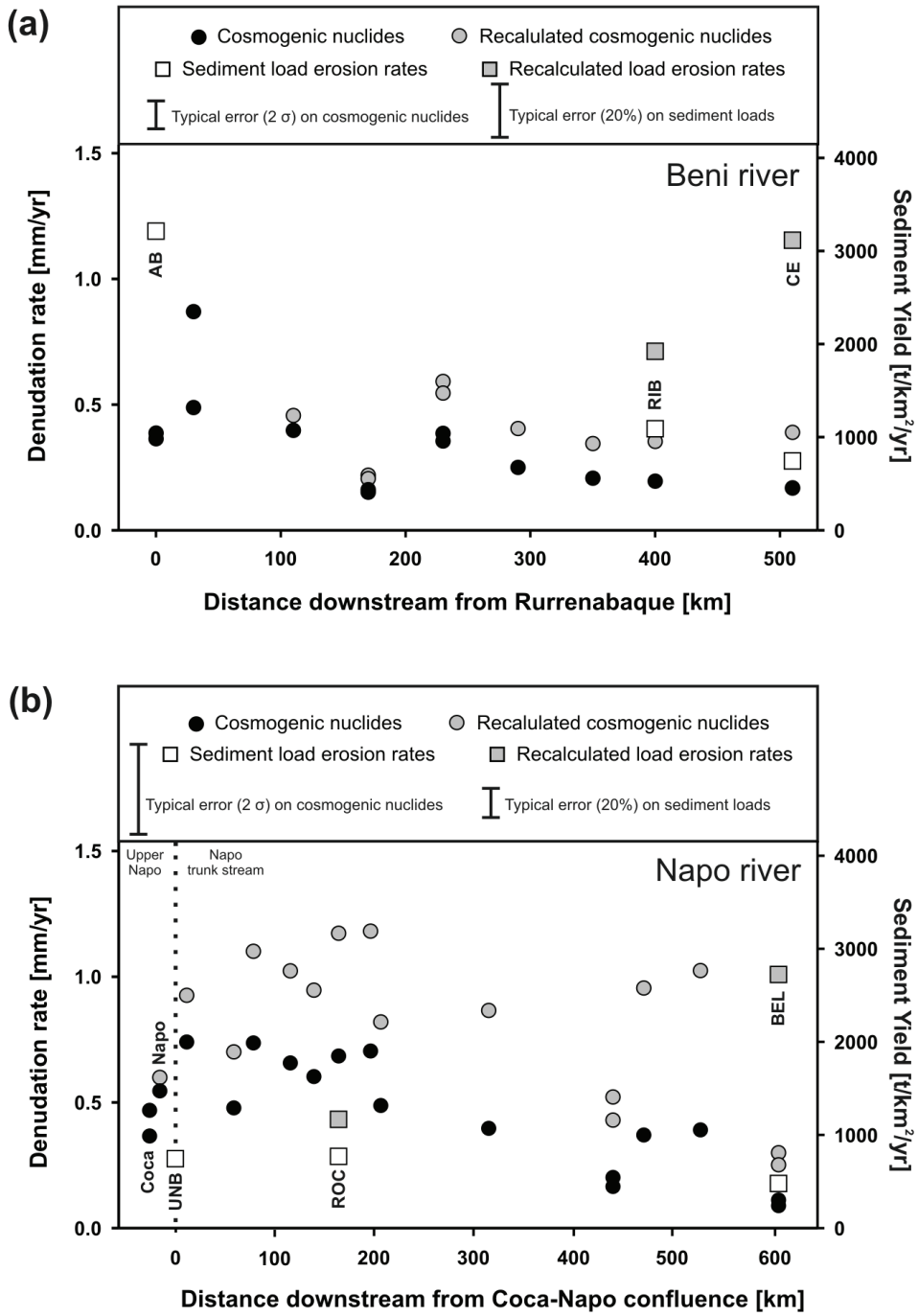

Figure 3.6 (A) Basin-averaged denudation rates for the Beni River (black circles; left axis) from Rurrenabaque to Cachuela Esperanza. Using a production rate value of 15.3 at/$g_{(Qz)}$/yr, the cosmogenic denudation rates of the Beni River floodplain were recalculated (grey circles) to exclude the effect caused by decreasing basin-averaged production rates away from sediment-producing areas. White squares show sediment yield data from gauging stations (right axis), which also have been recalculated with the surface area of the sediment-providing area (grey squares; 6.8×10^4 km^2). The rivers Madre de Dios, Orthón, Mamoré, and Madeira are not included, because their basins integrate over different Andean source areas and thus have different starting production rates. (B) For the Napo River, black circles give basin-averaged denudation rates. Recalculated denudation rates (grey circles) are plotted using a hinterland production rate of 12.0 at/$g_{(Qz)}$/yr. White squares show sediment yield data from gauging stations (right axis), which also have been recalculated (grey squares) with the surface area of the hinterland (1.77×10^4 km^2), which is the total area of the Andean headwaters below the Napo-Coca confluence. For both rivers, yield was calculated from erosion rates using a density of 2.7 g/cm^3 and thus, right and left axis scale linearly. Typical two sigma error bars for both methods are also given. For abbreviations, see Figure 3.2 or Table 3.3.

Table 3.3: Sediment gauging data

Gauging station[a]	River/ Location	Drainage Area [x10^4 km^2]	Period [yr]	Suspended sediment load [Mt/yr]	Dissolved load [Mt/yr]	Suspended sediment yield [t/km^2/yr]	Specific dissolved yield [t/km^2/yr]	Erosion rate[b] [mm/yr]	Floodplain-corrected erosion rate[c] [mm/yr]
Beni-Madeira rivers									
AB†	Beni at Rurrenabaque	6.8	1969-1990	212	5.2	3140	41	1.18	-
RIB†	Beni at Riberalta	11.9	1983-1990	122	8.2	1020	34	0.39	0.71
MF†	Madre de Dios at Miraflores	12.4	1983-1990	71	11	570	40	0.23	-
CA†	Orthón at Caracoles	3.2	1983-1990	2	0.9	55	15	0.03	-
CE†	Beni at Cachuela Esperanza	28.3	1983-1990	191	20	680	34	0.26	1.15
PVL†	Madeira at Porto Velho	95.4	1978-1993	306$	-	320	-	0.12	-
Coca-Napo rivers									
SEB*	Coca at San Sebastian	0.53	2001-2002	7	-	1260	-	0.47	-
FDO*	Napo at F. de Orellana	1.2	2001-2002	7	-	557	-	0.21	-
UNB	Upper Napo basin (SEB+FDO)	1.8	-	14	-	-	-	0.28	-
ROC§	Napo at Rocafuerte	2.7	2001-2006	21	-	770	-	0.29	0.43
BEL§	Napo at Bellavista	10.1	1989-2006	49	-	480	-	0.18	1.01
Guaporé-Mamoré rivers									
ANG	Pirai at Angostura	0.14	1976-1985	3	-	2080	-	0.77	-
SPE	Paracti at Paracti	0.03	1972-1973	4	-	10940	-	4.05	-
PV†	Ichilo at Puerto Villarroel	0.76	1983-1990	9	1	1150	110	0.47	0.79
ARC	Grande at Puente Arce	2.4	1969-1974	136	-	5730	-	2.12	-
AP	Grande at Abapo	6.0	1976-1990	138	5	2310	48	0.87	-
PG†	Mamoré at Puerto Ganadero	15.9	1983-1990	64	9	400	28	0.16	0.26
VG†	Guapore-Itenez at Vuelta Grande	35.4	1983-1990	2	3	5.0	4.0	0.003	-
PS†	Mamore at Puerto Siles	21.6	1983-1990	47	14	220	31	0.09	-
GM†	Mamore at Guayaramerin	59.9	1983-1990	66	17	110	13	0.05	-

[a]As indicated in Figure 3.2.2

[b]Calculated with a mean density of 2.7 g/cm^3

[c]Recalculated with area of sediment-providing hinterland: in Beni case, this is 6.75x10^4 km^2 (area at AB); in the Napo case, it is 1.77x10^4 km^2 (area at UNB); for Mamoré sub-basins, this is 0.45x10^4 km^2 for PV, and 8.91x10^4 km^2 for PG

*From Laraque *et al.* [2004]

†From Guyot *et al.* [1996]

§From Guyot *et al.* [2007a]

$This value has been updated to 230 Mt/yr by Guyot *et al.* [1999]

However, contrary to the Beni basin, erosion rates from sediment gauging in the Napo basin are mostly lower than our cosmogenic denudation rates. In the light of modern deforestation in the Napo basin and intense colonization on the river banks [Sierra, 2000; Mainville *et al.,* 2006], similar magnitudes in sediment loads as in the Beni would be expected. Erosion rates corrected for the area effect from sediment loads along the Napo River course are low in the upper reach (~0.3 mm/yr), increase slightly to 0.4 mm/yr at Rocafuerte and amount to ~1.0 mm/yr at Bellavista (see Figure 3.6b). Laraque *et al.* [2004] and Guyot *et al.* [2007a] suggest that this steady increase in sediment flux from the convergence of the Napo and the Coca rivers to Bellavista is attributed to basal uplift of the Iquitos forebulge altering local base level and eroding the floodplain [Bes de Berc *et al.*, 2005]. Given the very short integration time scales especially for the headwater gauging stations (Table 3.3), this effect could also be partially due to not recording high-magnitude low-frequency events over which cosmogenic nuclide-derived denudation rates integrate.

Similar to our observations in the upper Beni basin, the erosion rates calculated from sediment loads are higher than mean rates derived from cosmogenic nuclides. The rates range between 0.47 and 4.05 mm/yr. As in the Beni basin, we assume that either human disturbances or an abrupt recent change in climate could as well be responsible for the discrepancy from cosmogenic nuclide-derived rates (see Section 3.5.3).

3.6 CONCLUSION

A nuclide signal representative of the entire upper Beni basin was measured at the Beni outlet into the floodplain at Rurrenabaque and corresponds to a denudation rate in the order of ~0.4 to 0.7 mm/yr. These rates agree well with 0.53 ± 0.03 mm/yr representing the weighted average of ca. 50 catchments in the Andean part of the Beni basin [Safran *et al.*, 2005]. It appears that cosmogenic nuclide-derived rates are subject to temporal scatter. At Rurrenabaque, ^{10}Be nuclide concentrations have been measured in June 1998 [Safran *et al.*, 2005] and in October 2002 (this study), where results differ by a factor of ~2, despite using the same analytical procedures for cosmogenic nuclides. This scatter is attributed to a temporal variability of source areas providing the discharged sediment. Due to high altitudes and correspondingly high production rates, Andean sediment contains higher nuclide concentrations, which is diluted with low-concentration Piedmont-derived sediment. For the

Napo River, the Andean source signal passed on to floodplain has been characterized by sampling the two main upstream tributaries. These headwater tributaries yield somewhat lower denudation rates (0.48 ± 0.12 mm/yr) than the floodplain-derived average (0.9 ± 0.4 mm/yr), which might be due to temporal variability in the nuclide signal, dilution effects from very old (several Myr) floodplain sediment now being remobilized, or low analytical precision. In the Napo area, analytical precision is limited by very low nuclide concentrations and low quartz contents. In the Mamoré basin, we have tested several sub-basins for their cosmogenic nuclide concentrations in order to estimate the nuclide flux transferred from the Andes to the floodplain. An Andean mean denudation rate passed on to the floodplain is 0.39 ± 0.09 mm/yr, but denudation for the entire Mamoré basin near Trinidad which encompasses floodplain area of 44% is slightly higher (0.85 ± 0.31 mm/yr). We assume that a temporal variability is introduced by spatially variable discharge events, and that this is unlikely to be due to irradiation or decay during floodplain storage (see Chapter 2). From this set of data encompassing the northern and the southern Bolivian Andes, we cannot infer a latitudinal trend in denudation as suggested by Barnes & Pelletier [2006].

In the upper Beni basin at Rurrenabaque, several studies have documented denudation rates over various time scales. Short-term gauging-derived erosion rates record highest rates (up to 6.9 mm/yr, on average 1.64 mm/yr) over shortest time scales (up to 20 yrs; [Guyot *et al.*, 1996]). Denudation rates from in situ-produced cosmogenic ^{10}Be measurements in the Beni headwaters integrate over 10^3 yr time scales and average to 0.53 ± 0.03 mm/yr [Safran *et al.*, 2005]. Long-term denudation rates derived from fission-track analysis average to 0.3 mm/yr at time scales of several million years [Safran *et al.*, 2006]. These rates are in the same range as uplift rates from the Bolivian Andes since the late Miocene [Gregory-Wodzicki, 2000]. The disagreement between short- and long-term denudation monitors could be due to human- or climatic-induced accelerated erosion in the upper Beni, which would not perturb the cosmogenic nuclide signal, but would affect modern rates of erosion.

The same dataset, showing a linear decrease in denudation with increasing integration time scale, also shows a decrease in denudation with increasing catchment area. Sediment yield data is subjected to this well-known effect, because depositional processes become more important with increasing basin area. However, when recalculating sediment yields relative to the sediment-producing area thereby excluding depositional areas, meaningful erosion rates can be derived. In the Beni basin, these rates are higher than those from cosmogenic nuclides. For cosmogenic nuclides, a similar artifact would be introduced by production rate calculations because of an increase in lowland area not contributing any sediment. In this study, cosmogenic nuclide-derived denudation rates are corrected for this effect by

recalculating basin-wide production rate for sediment-producing areas only. Thus, basin-wide denudation rates from cosmogenic nuclides are invariant over floodplain distances. This means that the source signal detected in the upper Beni is conveyed to the floodplain and preserved throughout the fluvial transport system, not altering cosmogenic nuclide-derived denudation rates. Sediment loads show that ~40% of the sediment discharged from the Andes is stored in the Beni floodplain [Guyot *et al.*, 1996; Aalto *et al.,* 2003] an effect unnoticed by cosmogenic nuclides. Similarly over the entire Napo floodplain distance, neither decrease nor increase in nuclide concentrations is observed. While sediment load data record removal of sediment over Napo floodplain distances, cosmogenic nuclide signals are not altered.

The absence of nuclide concentration changes during floodplain storage was modeled by simulating depth- and time- dependent ^{10}Be nuclide production and decay in the Beni River setting during floodplain storage, remobilization, and mixing with upstream sediment (see Chapter 2). Neither for the well-known present-day fluvial dynamics, nor for all possible deviations from the natural Beni boundary conditions is a significant gain or decrease in nuclide concentrations predicted. This model result supports our observation that, regardless of the actual fluvial setting, the cosmogenic nuclide signal of the sediment-generating source area is preserved over foreland basin distances. Evidently, cosmogenic nuclides are the method of choice for tracing denudation rate signal over large floodplain distances. The denudation rates of the sediment-producing areas are conserved. We suggest that it is temporal variations in sediment-delivering areas that introduce variability into large river denudation rates, rather than storage within the floodplain.

CHAPTER 4

THE QUANTIFICATION OF SEDIMENT PRODUCTION, MIXING, AND FLOODPLAIN BURIAL IN THE AMAZON BASIN FROM IN SITU-PRODUCED ^{10}BE AND ^{26}AL IN RIVER SEDIMENT

ABSTRACT

In this chapter, sediment production, mixing, and floodplain burial in the Amazon trunk stream, its tributaries, and the adjacent floodplain are quantified using denudation rates from in situ-produced ^{10}Be in river sediment and burial histories from ^{26}Al/^{10}Be ratios. In all Amazon trunk stream samples and in the Solimões and Madeira tributaries, the fine grain size fractions (125-250 µm) contains a ^{10}Be nuclide signal of 6.5×10^4 at/$g_{(Qz)}$, which is similar to that of the principle Andean source areas, as characterized by the Beni, Mamoré, Napo, Ucayali, and Marañón rivers. Also the weighed-area denudation rate from these fractions is 0.23 ± 0.04 mm/yr which compares well with the integrated signal of all main Andean tributaries (0.39 ± 0.09 mm/yr). The main source of Amazon sediment is therefore Andean, and its cosmogenic nuclide signal is preserved virtually unaltered over 1000s of km of sediment transport. The headwaters of the Guyana and Brazilian shields denude at very low rates (0.01 and 0.02 mm/yr, respectively), as is expected for a tectonically stable tropical highland, and correspondingly, they contribute only small amounts of sediment into the Amazon trunk stream. ^{26}Al/^{10}Be ratios show that all rivers draining cratonic areas contain variable fractions of formerly buried floodplain sediment that was buried between 0.5 to 2 Myr at depths of 2.5-5 m in the smaller tributaries (e.g. Branco River, and smaller streams draining the Brazilian shield) and 4-12 m in larger streams (e.g. Negro, Tapajós). The magnitude of the paleo-denudation in the shields is estimated to be in the range of modern erosion rates. This low denudation cratonic signal is mixed into the Amazon trunk stream mostly in the form of coarse quartz grains, which survived the 100 kyr weathering history in the shield areas. Therefore, we found that coarse-grained material records the nuclide signal of the cratonic shield, whereas the Andean signal is best represented by the fine sand fraction.
Sediment from white water lakes within the Holocene "Varzea do Curuaí" floodplain yields ^{10}Be concentrations as those measured in the Amazon trunk stream, and ^{26}Al/^{10}Be ratios that indicate the absence of burial, but sediment from black waters of a Miocene floodplain lake displays low ^{26}Al/^{10}Be ratios, suggesting that this part of the local floodplain has not been reworked by the Amazon for more than 1 Myr.

We can use this data to calculate sediment mass budgets. The mass of sediment expected from the cosmogenic nuclide-derived denudation rates amounts to >540 Mt/yr at Óbidos, where only ~40 Mt/yr are from non-Andean source areas. This value can be compared to the total load estimated from sediment gauging which amounts to 800-1400 Mt/yr at Óbidos. This finding is unexpected, as at least 40% of the sediment discharged in the

Andes is stored in floodplains; a process not detectable with cosmogenic ^{10}Be. The longer denudation integration time scale of ~8 kyr for cosmogenic nuclides possibly includes a period of drier climate than the wet conditions during the late Holocene, where a wetter modern climate possibly favors more rapid erosion in the Andes and more efficient sediment transport in the large rivers.

4.1 INTRODUCTION

The sediment fluxes transported by rivers play an important role in geochemical cycles, because they are important agents of CO_2 sequestration and consumption by acid degradation of continental rocks [Gaillardet *et al.,* 1997; Mortatti & Probst, 2003], and the transport and respiration of organic carbon [Mayorga *et al.*, 2005; Battin *et al.,* 2008]. The Amazon River is the world's largest fluvial system in terms of water discharge, drainage area, and sediment yield, thus potentially a key river to study for its role in large geochemical cycling. It comprises 15% of the world's total runoff at an average discharge of 210,000 m^3/s [Molinier *et al.*, 1996]; its basin covers an area that denotes ~40% of the total area of South America with over 6 million km^2, and it carries a sediment load of ~800 to 1400 Mt/yr [Dunne *et al.,* 1998; Guyot *et al.*, 2005].

The sediment source areas to the Amazon basin are primarily the rapidly denuding Andes, which comprise only 11% of the total basin area but are thought to contribute about 90% of the total suspended load carried by the Amazon River at Óbidos [Meade *et al.*, 1985]. The Amazon trough is flanked by the Guyana shield to the north and by the Brazilian shield to the south, which together account for ~44% of the total basin area, but sediment contribution from these cratons is negligible (~2%) in terms of total sediment discharge [Martinelli *et al.*, 1989]. In order to decipher the sources and sinks of sediment within the large Amazon basin, and to be able to monitor their relative changes, the construction of sediment budgets is crucial [Trimble, 1999], because the annual sediment mass that is discharged from the Andes and shields is not in steady state with the mass discharged past Óbidos to the Atlantic Ocean. It has been estimated by Guyot [1993] that roughly 40% of Andean sediment flux is intercepted and deposited in the basins close to the Andean foothills. According to Dunne *et al.* [1998], a net amount of ~200 Mt/yr of sediment are accumulated mostly via overbank deposition in the central Amazon lowlands before Óbidos, and another 300-400 Mt/yr are

deposited in the delta plain downstream of Óbidos. Consequently, it is reasonable to expect that most sediment passing Óbidos has resided in the floodplain for some time since its initial denudation in the Andes. This storage is temporary, and floodplain residence times have been estimated for the central Amazon to be in the order of several kyr, ranging from <5 kyr on the basis of sediment budgets [Mertes *et al.*, 1996; Mertes & Dunne, 2007], to ~15 kyr from Uranium-series constraints [Dosseto *et al.,* 2006a; Dosseto *et al.*, 2006b]. Storage of sediment for unknown durations disconnects the linkage between hinterland erosion rate and the amount of sediment that is being discharged at the river mouth and potentially compromises sediment load estimates from gauging (time scale 10^1 to 10^2 yrs) [Walling, 1983; Trimble, 1999], so that an increasing need arises for methods that a) estimate sediment production by erosion that are insensitive to the large storage effects in floodplains; and b) integrate over a time scale that is relevant for sediment storage and thus are capable to detect storage.

In situ-produced cosmogenic isotopes (^{10}Be, ^{26}Al) are routinely measured in quartz from modern river sediment for estimating denudation rates in steady state settings over time scales relevant to soil formation processes. These rates are usually insensitive to short-term perturbations in the erosion rate [von Blanckenburg, 2005]. In a recent extension to the method, we have modeled the effect of sediment storage on cosmogenic nuclide-derived denudation rates (Chapter 2). It was shown that the nuclide concentrations accumulated in the source area are under most conditions conserved during storage. This conservation is the case if a) the average storage depth is deep (>2 m), so that no further irradiation occurs and b) storage duration is short (<0.5 Myr), such that neither radioactive decay nor production of ^{10}Be and ^{26}Al nuclides in deep sediment by deeply penetrating muons occurs. However, if storage times in deep floodplains exceed ~1 Myr, then the duration of storage can be detected using the differential radioactive decay of ^{26}Al versus ^{10}Be.

We will provide a robust estimate of the denudation rates of the Amazon River and its source areas, will show that the Andean signal is preserved over thousands km of transport in tributaries, and will show that sediment-starved rivers draining the cratonic areas excavate sediment that has been stored between 0.5 and 2 Myr. Finally, we will construct a cosmogenic nuclide-based sediment budget to the Amazon trunk stream, the major tributaries, the floodplain, the Andean source areas, and the cratonic shields that are altogether the main regions contributing sediment to the Amazon River. We will compare our budget with that calculated from short-term sediment gauging data.

4.2 STUDY AREA

The trunk stream of the Amazon River is formed by three main tributaries that are the Solimões at Manaus (~2.3×10^6 km^2; mainly formed by the Marañón and Ucayali rivers), the Negro (~0.9×10^6 km^2), and the Madeira (~1.5×10^6 km^2), which together account for ~90% of the Amazon discharge. Minor tributaries are the Tapajós, Xingu, and Tocatins rivers (~1.8×10^6 km^2). The tectonic setting is composed of the rapidly eroding Andean range, which accounts for ~11% of the total basin area (see Figure 4.1). The Ecuadorian Andes are drained by the Napo and Marañón rivers, the Peruvian Andes by the Ucayali, and the Bolivian Andes are drained by the Madeira River, with its primary sediment deliverer being the Beni and Grande rivers ([Roche & Jauregui, 1988]; see Chapter 3). In the Beni catchment, denudation rates from cosmogenic nuclides average over ~0.5 mm/yr for ~10^3 yr time scales [Safran *et al.*, 2005]. New cosmogenic nuclide data for the southern central Andes (>15°S) average to ~0.4 mm/yr on the same time scale (see Chapter 3).

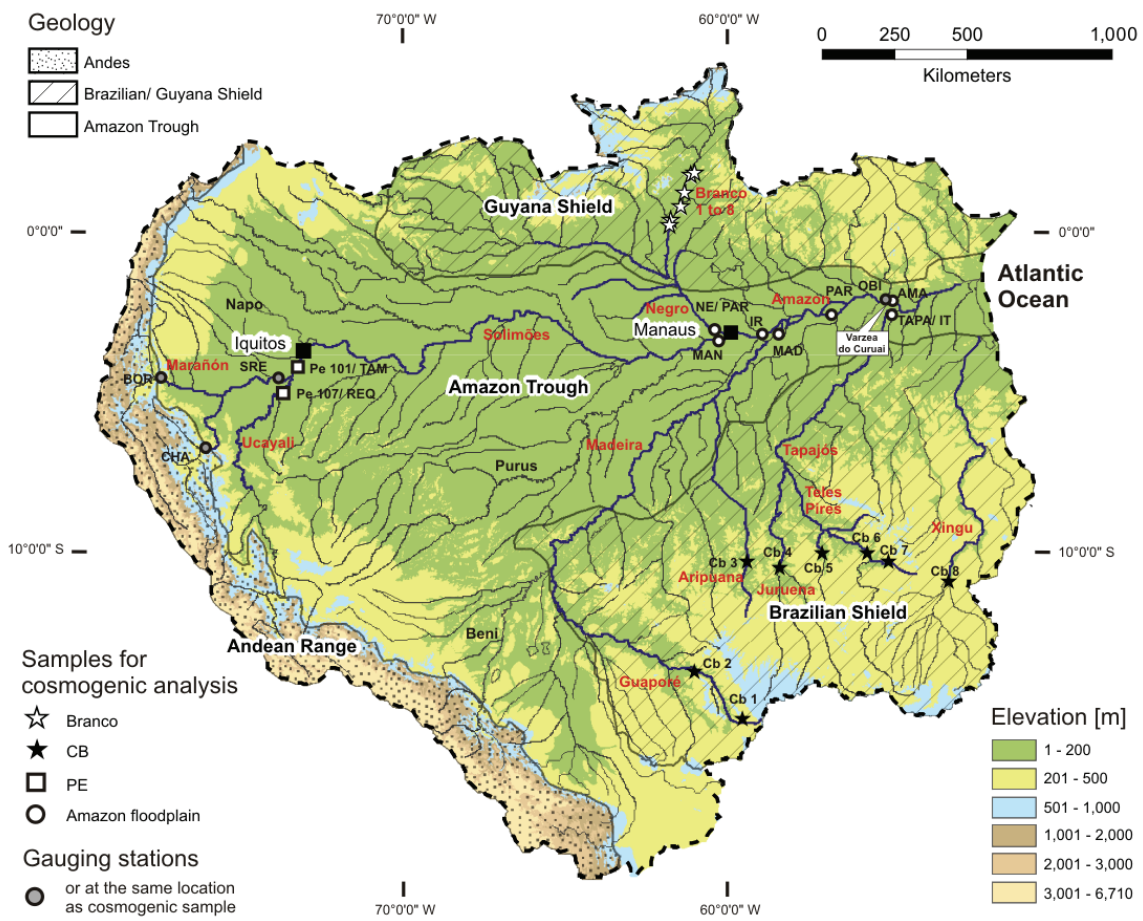

Figure 4.1 Overview of the Amazon basin with sampled regions and rivers. At several sampling points for cosmogenic nuclides, a sediment gauging station is also located.

The Brazilian and the Guyana shields flank the Amazon trough to the south and to the north and account for 44% of the total Amazon basin area. They consist of granitic Precambrian basement of mostly Proterozoic age, but at platform edges, younger sedimentary rocks crop out [Hartmann & Delgado, 2001; Mertes & Dunne, 2007]. In their headwaters, the shields feature dense vegetation, with the lowland part displaying flat savannas with sparse vegetation and tafelbergs [Gibbs & Barron, 1983; Mathieu *et al.*, 1995; Franzinelli & Igreja, 2002]. According to Stallard [1985], long-term uplift of the shields persisted since the Tertiary at a pace of 0.01-0.02 mm/yr, which is consistent with very low long-term denudation rates. According to a more modern view by Edmond *et al.* [1995], low denudation rates in the shields persist because relief-rejuvenation processes are absent due to long-term tectonic stability incorporating only a passive margin uplift component resulting in slow incision into basement rocks covered by thick, heavily weathered regoliths [Gibbs & Barron, 1983; Voicu *et al.*, 2001]. Climate is tropical for both shields with mean annual precipitation rates of ~1500 mm [Gibbs & Barron, 1983; Hasui & Almeida, 1985]. The Brazilian shield is mainly drained by the Madeira and Tapajós rivers, where the Madeira is a mixed load river mainly carrying Andean sediment. The Guyana shield is drained by the Negro River, with its main tributary, the Branco River.

The architecture of the Amazon trough comprises two distinct settings, with the deforming foreland basins the northwest and southwest (drained mainly by the Solimões and Beni rivers, respectively), and subsiding central Amazonia with elevations below 200 m that converges on ancient rift structures [Mertes & Dunne, 2007]. The evolution of the Amazon drainage pattern is attributed to intra-plate tectonics, which involves large-scale fractures of the basement that propagate through overlying sedimentary rocks [Caputo, 1984; Putzer, 1984; Caputo, 1991]. A major feature is the occurrence of four structural highs, or arches, from near the Peruvian border to the Amazon mouth, that cause the Amazon River to steepen in gradient, narrow its floodplain, and generally restricts channel movement [Mertes *et al.*, 1996; Dunne *et al.,* 1998]. The modern channel of the lower Amazon is mainly anastomosing, that is, a relatively straight channel being separated by vegetated, semi-permanent islands. In spite of its occasional tectonic confinement by an arch or being restricted in movement by stable “terra firme”, the Amazon clearly is a very active channel, relocating and mixing bank and floodplain material as it flows. For example, Mertes *et al.* [1996] have estimated an average relocation rate of ~35 m/yr for the reach immediately downstream of the Madeira.

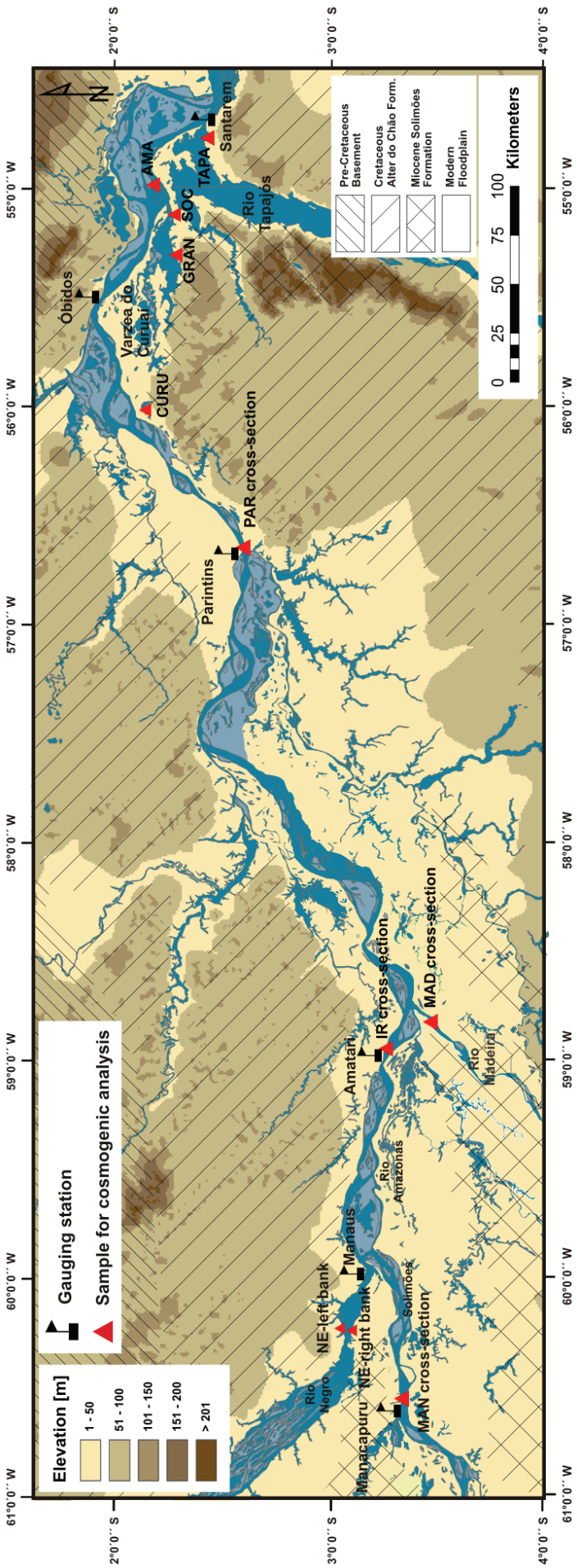

Figure 4.2 Overview over the central Amazon lowlands from Manaus to Óbidos, showing locations of the Amazon trunk stream samples, the tributaries, and the varzea. Samples labeled as "cross-section" denote several samples taken perpendicular to the left bank at different distances across the channel. Other samples were taken from the active river bank. Also displayed is the regional geology simplified after Rossetti *et al.* [2005]. The map was constructed from 1 km- resolution SRTM data.

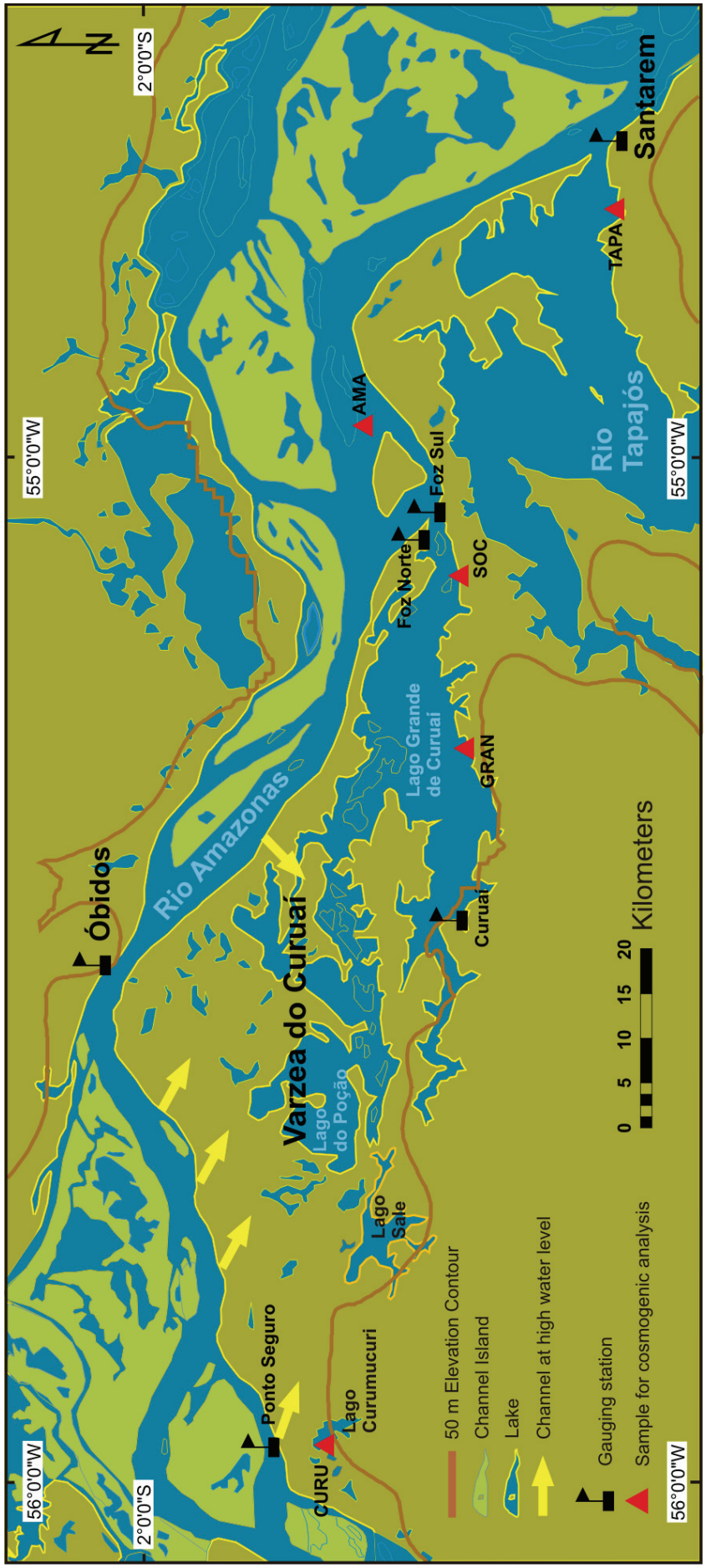

Figure 4.3 Overview over the "Varzea do Curuaí", a representative floodplain system of the central Amazon basin, located south of Óbidos. Map was constructed from 1 km- resolution SRTM data, which was acquired during low water level.

4.3 SAMPLING

In order to quantify the cosmogenic nuclide input and the corresponding denudation rate signals from the sediment-providing areas to the Amazon lowlands, sampling of the main Amazon tributaries was carried out (see Figure 4.1). The Brazilian and Guyana shields were characterized by "Cb" and "Branco" river samples (see Table 4.1), respectively, where Cb samples are from individual river basins taken by J.L. Guyot during a HYBAM campaign in 2001, and Branco samples taken in 2005 by F. Seyler denote a longitudinal profile along the river. For the cosmogenic nuclide signature of Bolivian Andean rivers, we refer to Chapter 3. In the Llanos itself, we sampled main upstream tributaries to the Solimões River in 2001 (Marañón and Ucayali rivers) to account for source area nuclide signals from the Ecuadorian/ Peruvian Andes. During a field campaign in 2006, the Amazon trunk stream, the Negro, the Madeira, and the Tapajós rivers (see Figure 4.2), as well as floodplain sediments from the Varzea do Curuaí (see Figure 4.3) were sampled by dredging sediment from the river bottom and also sampling bank deposits.

4.4 METHODOLOGY

Sample preparation and AMS measurements where identical to those of previous studies ([von Blanckenburg *et al.*, 1996; Synal *et al.,* 1997; Wittmann *et al.*, 2007], and simplified by von Blanckenburg *et al.* [2004]). Between 50 g and 100 g quartz was usually processed and between 150-300 µg ^{9}Be carrier was added. Given that some samples had low ^{10}Be concentrations this resulted in ^{10}Be/^{9}Be AMS ratios as low as 1×10^{-13}. Prior to chromatographic isotope (^{10}Be, ^{26}Al) separation, a small aliquot was taken from the dissolved solution, and the stable Al concentration of the sample was measured by standard addition and an ICP-OES, using an Al-sensitive wavelength of 167 nm (see Appendix A.2).

Calculations of production rates (using pixel-based altitudes derived from 1 km resolution SRTM-DEM) and absorption laws for ^{10}Be were done following Schaller *et al.* [2002]; we used a sea-level high-latitude (SLHL) production rate of 5.53 at/$g_{(Qz)}$ [Kubik *et al.*, 1998], and followed the atmospheric scaling procedure of Dunai [2000]. We used a spallogenic fraction of 0.964; the rest was assigned to fast (0.017) and slow (0.019) muonic

production [Schaller *et al.*, 2002]. We used a surface production ratio for $^{26}Al/^{10}Be$ of 6.5 following Kubik *et al.* [1998]. Decay constants of $4.62*10^{-7}$ 1/yr for ^{10}Be and $9.72*10^{-7}$ 1/yr for ^{26}Al were used [Samworth *et al.,* 1972; Hofmann *et al.*, 1987]. Possible burial of samples was investigated using $^{26}Al/^{10}Be$ ratios, which were plotted using "CosmoCalc" Version 1.3 [Vermeesch, 2007] with the above mentioned references for scaling, production rates, half lives, and a density of 2.0 g/cm^3 for alluvial sediment. $^{26}Al/^{10}Be$ ratios from the main Amazon stream have generally large uncertainties resulting from low ^{26}Al count rates due to high amounts of native ^{27}Al (see Table 4.2).

Corrections for variations in the intensity of Earth's magnetic dipole field were carried out following Masarik *et al.* [2001] for all Branco and Cb samples, as these samples integrate over long time scales and are located between 0° and 20°S latitude. Resulting production rate corrections are between 13 and 30%. For floodplain samples, no correction has been carried out, because they are located at latitudes between 5°N and 15°S, for which a correction is not necessary [Masarik *et al.*, 2001].

We have shown elsewhere (Chapter 2 and 3), that under most conditions of floodplains storage samples conserve the nuclide concentration of their source area. Therefore, denudation rates have to be calculated using the cosmogenic nuclide production rate of the source area, not of the entire catchment. In Table 4.2, we have provided this correction, which we call "floodplain-corrected". We have used a cut-off altitude of 200 m that conveniently defines the boundary between areas producing sediment and those storing sediment. Although this cut-off elevation serves as an approximation only, it is justified, because at Iquitos, 3600 km upstream from the Atlantic, the level of the Solimões River is ~110 m above sea level [Irion, 1989; Irion *et al.,* 1995]. An elevation of ~100 m however would not encompass the vast lowlands directly adjacent to the Andean foothills, where a cut-off elevation of ~200 m with steeper slopes above can be observed on hypsometric curves. We assumed that sediments of the Barreiras formation in the Tapajós area that reach ~300 m in altitude are negligible due to their localized occurrence. Similarly, if sediment loads are converted into erosion rates, the sediment-producing area has to be used for calculating yields, rather than the entire drainage area. Again, we will call these corrected yields "floodplain-corrected".

4.5 NUCLIDE CONCENTRATION RESULTS, ESTIMATES OF DENUDATION RATES, AND FLOODPLAIN BURIAL

4.5.1 Tributaries to the central Amazon River

4.5.1.1 Andean tributaries

Representative for the northern Andean foreland basin are the rivers Ucayali (sample Pe 107) and Marañón, which form the Solimões River upstream of Iquitos, Peru (sample Pe 101). The measured ^{10}Be nuclide concentrations are 5.6×10^4 at/g$_{(Qz)}$ for the Ucayali, and 7.3×10^4 at/g$_{(Qz)}$ for the Solimões River. At Iquitos, the Napo River draining the Ecuadorian Andes joins the Solimões River (see Figure 4.1). The average nuclide concentration of the lower Napo is $1.7 \pm 0.6\times10^4$ at/g$_{(Qz)}$ (n = 4; see Chapter 3). To the south, the headwaters of the Ucayali directly border the Madre de Dios basin, which is part of the Beni drainage basin. The Beni and the Mamoré form the Madeira River near Porto Velho, draining the southern Andean foreland basin. The Andean headwaters of the Beni basin have been characterized by Safran *et al.* [2005] in terms of cosmogenic ^{10}Be nuclides; average nuclide concentration is $6.3 \pm 0.4\times10^4$ at/g$_{(Qz)}$ (n = 47). The Madeira basin at Porto Velho at the outlet at the Bolivian floodplain yields a nuclide concentration of 4.2×10^4 at/g$_{(Qz)}$ (Chapter 3). Resulting cosmogenic nuclide-derived denudation rates of which the production rates were corrected for floodplain area are 0.19 mm/yr for the Solimões, 0.25 mm/yr for the Ucayali, 0.25 mm/yr for the Madeira basin at Porto Velho, 0.53 mm/yr for the upper Beni basin, and 0.73 mm/yr for the Napo River.

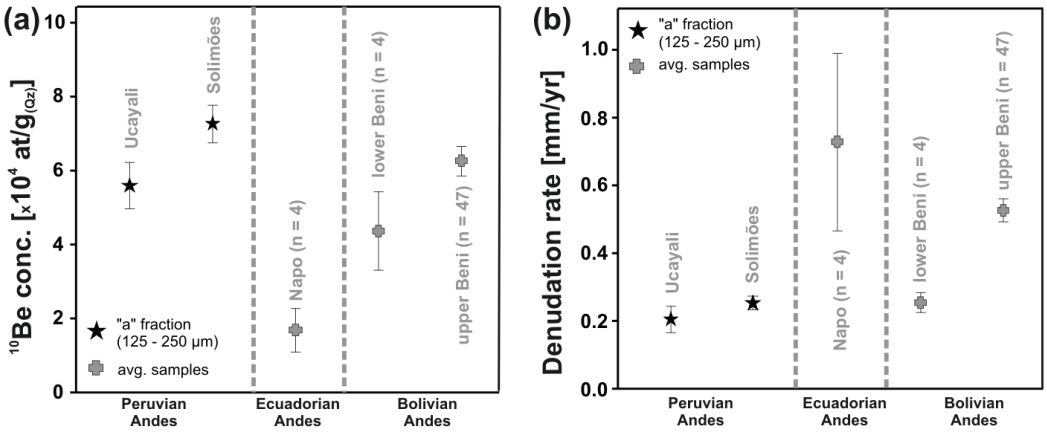

Figure 4.4 Cosmogenic ^{10}Be nuclide concentrations (a) and cosmogenic nuclide-derived denudation rates (b); all errors are 1σ. Data from the Ecuadorian and Bolivian Andes are presented in Chapter 3; upper Beni data is from Safran *et al.* [2005]. For Ucayali and Solimões rivers, the "a" fraction has been analyzed; all other samples are averages calculated from several individual cosmogenic analyses, the number of which is given in brackets after the sample name. Denudation rates are corrected for production-rate induced area effect, except upper Beni data.

Table 4.1: Sample and basin characteristics

Sample[1]	Setting / River	Note[2]	Latitude [°S]	Longitude [°W]	Distance from Manaus[3] [km]	Drainage area [x10^4 km^2]	Basin-avg. min. altitude [m]	Basin-avg. max. altitude [m]	Basin-avg. mean altitude [m]	Basin-avg. relief[4] [m]
Guyana shield samples										
Br 1	Branco		1.9162	-61.0185	0	14.6	66	2392	397	-
Br 2	Branco		1.8167	-61.0422	18	14.7	65	2392	397	-
Br 4	Branco		1.3015	-61.2993	79	15.1	58	2392	386	-
Br 5	Branco		0.9779	-61.2890	132	17.5	48	2392	358	-
Br 6	Branco		0.2259	-61.7592	214	21.3	48	2392	329	-
Br 8	Branco		0.7500	-61.8500	194	21.0	48	2392	332	-
Brazilian shield samples										
Cb 1*	Tributary of the Guaporé at Pontes e Lacerda		-15.2159	-59.3536		0.7	261	813	449	188
Cb 2*	Guaporé at Pimenteiras		-13.4829	-61.0446		11.0	195	950	350	155
Cb 3*	Aripuana at Aripuana		-10.1696	-59.4661		2.0	193	524	260	67
Cb 4[$]	Juruena at Juruena		-9.8811	-58.2343		17.7	205	813	403	198
Cb 5[$]	Apiacás		-9.9357	-56.9372		1.2	187	525	298	111
Cb 6[$]	Teles Pires near Rochedo		-9.6391	-56.0191		9.4	161	869	371	210
Cb 7[$]	Tributary of Teles Pires at P. Azevedo		-10.2203	-54.9669		1.6	254	545	363	109
Cb 8	Xingu near Sao José do Xingu		-10.7774	-53.1016		16.9	194	800	346	152
Brazilian Highland samples										
Cb 10[§]	Brazilian Highlands, Araguaia		-14.5600	-51.0500		10.2	240	1046	524	284

Table 4.1 ▪CONTINUED▪

Sample[1]	Setting / River	Note[2]	Latitude [°S]	Longitude [°W]	Distance from Manaus[3] [km]	Drainage area [x10^4 km^2]	Basin-avg. min. altitude [m]	Basin-avg. max. altitude [m]	Basin-avg. mean altitude [m]	Basin-avg. relief[4] [m]
Amazon lowland ("Llanos") samples										
Pe 101	Solimoes at Tamshiyacu		-3.5988	-73.1383	-1908	71.8	101	6603	1432	-
Pe 107	Ucayali at Requena		-4.4794	-73.4263	-2048	32.5	101	6187	1713	-
Ne RB	Negro south of Paricatuba	right bank	-3.0821	-60.2255	81	83.2	24	2392	225	-
Ne LB	Negro south of Paricatuba	left bank	-3.0700	-60.2200	81	83.2	24	2392	225	-
Man 0.2	Solimoes at Manacapuru	0.2 km flb	-3.3130	-60.5539	0	227.0	21	6880	592	-
Man 1.1	Solimoes at Manacapuru	1.1 flb	-3.3202	-60.5541	0	227.0	21	6880	592	-
Man 2.85	Solimoes at Manacapuru	2.85 flb	-3.3387	-60.5525	0	227.0	21	6880	592	-
Ir 0.4	Amazon at Iracema	0.4 flb	-3.3189	-58.8236	212	315.4	20	6880	491	-
Ir 1.5	Amazon at Iracema	1.5 flb	-3.3375	-58.8040	212	315.4	20	6880	491	-
Ir 1.75	Amazon at Iracema	1.75 flb	-3.3288	-58.8287	212	315.4	20	6880	491	-
Mad 0.5	Madeira at Amazon confl.	0.5 flb	-3.4044	-58.7883	225	143.8	18	6880	552	-
Mad 1.1	Madeira at Amazon confl.	1.1 flb	-3.4076	-58.7847	225	143.8	18	6880	552	-
Mad 1.8	Madeira at Amazon confl.	1.8 flb	-3.4107	-58.7793	225	143.8	18	6880	552	-
Par 1.2	Amazon at Parintins	1.2 flb	-2.5831	-56.6550	521	473.6	12	6880	498	-
Par 2.2	Amazon at Parintins	2.2 flb	-2.5992	-56.6667	521	473.6	12	6880	498	-
Ama	Amazon at Lago Grande outlet	midchannel	-2.1756	-54.9915	743	508.8	8	6880	478	-
Tapa	Tapajos near Santarem		-2.4298	-54.7745	809	59.8	6	6880	288	-
Samples from "Varzea do Curuai" floodplain										
Curu	Lago Curumucuri	lake	-2.1335	-56.0152	-	0.4	6	-	-	-
Soc	Lago Grande de Curuai at V. Soccurru	lake	-2.2656	-55.1363	-	0.4	6	-	-	-
Gran	Lago Grande de Curuai at Curuai	lake	-2.2724	-55.3150	-	0.4	6	-	-	-

[1]In case of samples Man, Ir, Mad, and Par, the position (km) from the left bank (flb) is also given
[2]Samples were dredged from positions perpendicular to the left bank (in km from left bank "flb"); other samples were taken from the active river bank/beach
[3]In case of Branco, this denotes the distance from the first sample
[4]Calculated from the mean altitude minus the minimum altitude for Cb samples
*Draining to Madeira River
$Draining to Tapajos River
§Draining to Tocatins River

4.5.1.2 The Guyana craton

The headwaters of the Guyana craton were characterized by sampling the Branco River (samples "Br") at different intervals along the main stream, and in lower reaches near the Amazon confluence, the Negro was sampled (samples "Ne"), which is the main river draining the Guyana craton and also one of the main tributaries in terms of discharge (29000 m^3/s) to the Amazon river, but carrying only a minor sediment load in downstream reaches (~9 Mt/yr, [Filizola, 2003; Laraque *et al.*, 2005]). Cosmogenic ^{10}Be-nuclide measurement for the Branco yield high nuclide concentrations at an average of 39.2×10^4 at/$g_{(Qz)}$ (n = 12; see Figure 4.5).

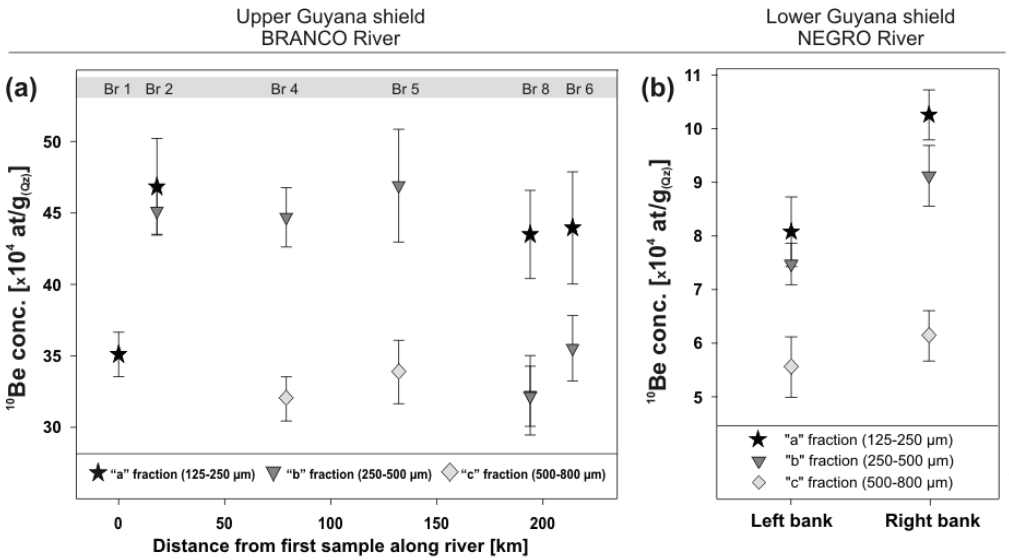

Figure 4.5 Cosmogenic ^{10}Be concentrations for the upper Guyana shield (left; Branco River), and the lower Guyana shield (right; Negro River). Uncertainties are 1σ. Note different X-axis scale. Also shown are different grain size fractions, ranging from 125-800 µm. The Branco River was sampled from the active river bank along the river; Negro River samples were taken from the right and left river bank near Paricatuba close to the Amazon River confluence.

For five Branco samples, we measured ^{26}Al/^{10}Be ratios in order to identify the possible admixture of buried floodplain sediment. ^{26}Al/^{10}Be ratios are for most samples significantly lower than the production ratio of 6.5 (Table 4.2), indicating burial. The ^{26}Al/^{10}Be ratio of buried sediment eroded into the active channel from an old floodplain depends on the burial duration, the storage depth, and the inherited nuclide concentration which is a function of the denudation rate of the buried sample. To model the ^{26}Al and ^{10}Be in terms of these variables, we have developed a modified version of the erosion island plot (Figure 4.6a). In the traditional "erosion island" plot [Lal, 1991], samples that plot on the island have not been affected by burial and record continuous irradiation at the surface and simultaneous erosion, whereas samples beneath the island have experienced complete shielding for the duration indicated by the iso-burial age curves (Figure 4.6a).

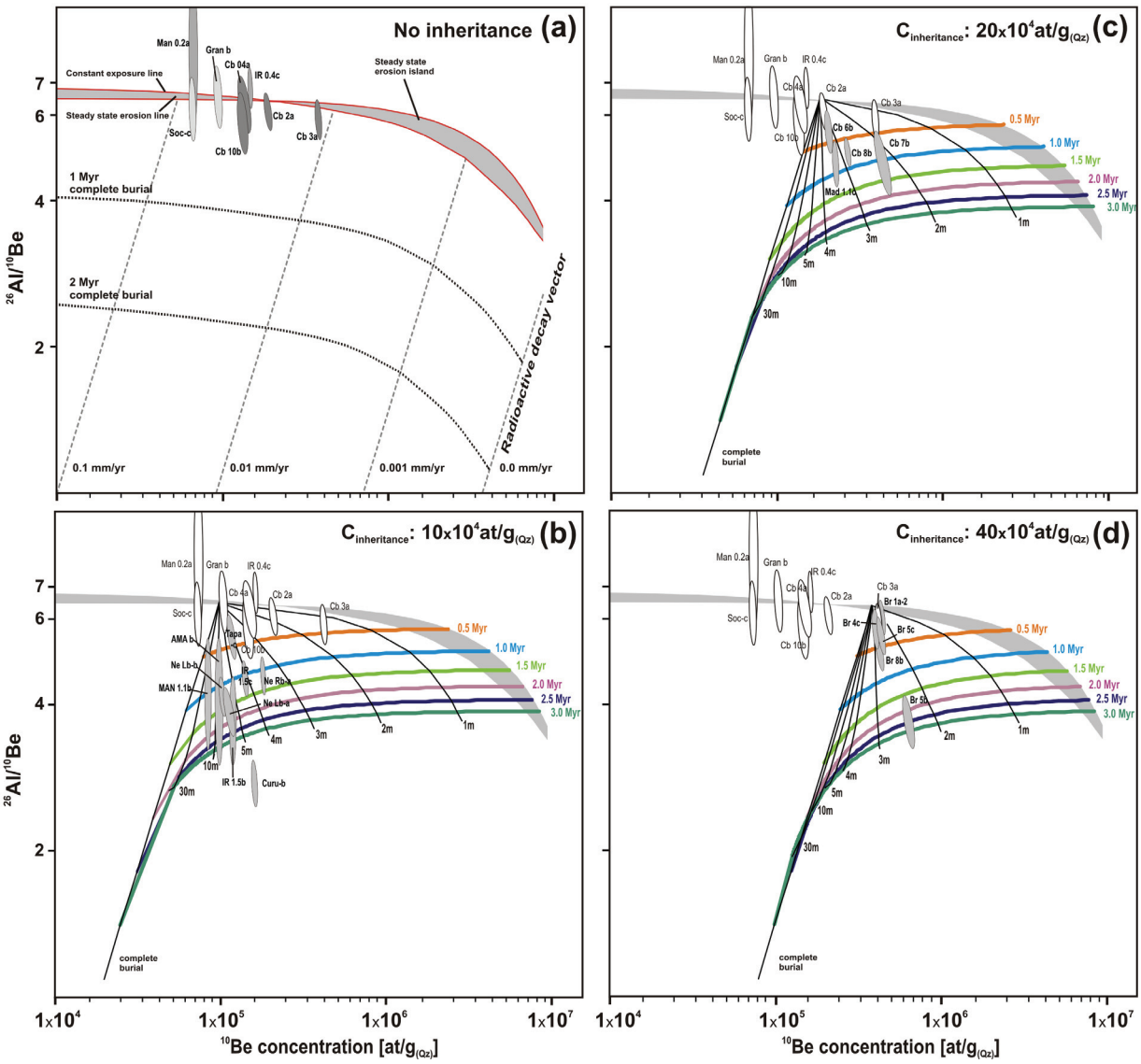

Figure 4.6 $^{26}Al/^{10}Be$ ratios and ^{10}Be concentrations, for samples codes see Table 4.2. Error ellipses denote 1σ uncertainty. (a) Samples that show normal exposure histories, without indications of burial. Samples that have experienced long-term steady state denudation will plot on the lower red line of the "steady state erosion island" [Lal, 1991], where the steady state erosion rates are indicated by the dashed grey lines. The dotted black lines give the burial age of the sample assuming burial with complete shielding. (b), (c), and (d) Modified erosion island diagrams to estimate burial depth and burial duration for the case that samples are subjected to continuing irradiation during shallow burial. Colored curves give burial duration in Myr. Black lines are iso-depth curves, with the corresponding depth indicated below in m. Panels b, c, and d show these models for three different nuclide inheritance levels (10, 20, and 40×10^4 at/$g_{(Qz)}$), corresponding to the paleo-denudation rate prevailing before burial. All modes were scaled for SLHL-production rates and calculated with a sediment density of 2.0 g/cm^3, and the constants of Schaller *et al.* [2002] as explained in the methods section.

Complete shielding is not necessarily achieved in a floodplain, because irradiation by muons is still effective at several meters depth [Schaller *et al.*, 2004]. To take this post-depositional irradiation into account, we have contoured the area beneath the erosion island for depth of burial (Figure 4.6 b-d). The remaining unknown, the nuclide inheritance, was estimated from

samples of the same stream that experienced minimum burial, to be 10, 20, and 40×10^4 at/$g_{(Qz)}$ for panels 6b, c, and d, respectively. For example, nuclide inheritance for Branco samples has been estimated to be 40×10^4 at/$g_{(Qz)}$ based on the nuclide concentrations of sample Br 1a that shows only very shallow, short-term burial. Resulting typical burial durations are <0.5 Myr for Branco samples except Br 5b, which denotes a burial duration of ~2.5 Myr. Burial depths are between 2-3 m (see Figure 4.6d). Apparently, Branco samples plot on a distinct mixing line between recent erosion products displaying no burial and shielded material from various depths within the floodplain that is admixed into the stream. This mixed signal indicates that formerly buried material is now actively eroded by the stream, implying that channel position has shifted during the cosmogenic nuclide time scale, now eroding very old (>1 Myr) floodplain. Additionally, grain size effects add to the complication of floodplain admixing at different $^{26}Al/^{10}Be$ ratios because finer sediment is more readily subjected to overbank sedimentation due to decreasing stream power at vicinities distal to the channel [Nanson & Croke, 1992; Asselman & Middelkoop, 1995; Walling & He, 1998; Alexander & Fielding, 2006]. This prediction might partially explain the observation of the finer-grained sample Br 5b displaying a stronger degree of burial than the coarser fraction Br 5c. Also, the higher concentration of the fine-grained sample would be expected because shallow burial, as assumed for the Branco samples, results in higher ^{10}Be concentrations for samples of longer burial duration (Figure 4.5a). In any case, it may well be that the pronounced difference in nuclide concentrations between grain sizes for the Branco samples and several other samples discussed below is due to different degrees of burial.

Strictly speaking, a spatially-averaged cosmogenic denudation rate can not be calculated in a setting where the nuclide signal of the sediment-producing headwaters is altered by incorporation of old floodplain sediment. For Br 1a, where burial is minimal, a denudation rate of 0.012 mm/yr can be calculated, resulting in a denudation time scale of ~60,000 yrs (see Table 4.2). This rate agrees well with an denudation rate calculated for the Guyana shield (0.01 mm/yr) from suspended and dissolved loads measured by Edmond *et al.* [1995], and are also in close agreement with long-term uplift rates (0.01-0.02 mm/yr) suggested by Stallard [1985].

Table 4.2: Analytical Data

Sample	Grain size [µm]	Sample weight [g]	^{10}Be conc.[1] [x10^4 at/g$_{(Qz)}$]	^{26}Al conc.[2] [x10^4 at/g$_{(Qz)}$]	^{27}Al conc.[3] [µg/g]	^{10}Be production rate[4] [at/g$_{(Qz)}$/yr]	Denudation rate[5] [mm/yr]	Floodplain area [%]	^{10}Be prod. rate corr. for area[6] [at/g$_{(Qz)}$/yr]	Denudation rate[7] [mm/yr]	Apparent age[8] [kyr]
Guyana shield samples											
Br 1a	125-250	34.70	35.10 ± 1.56	216.0 ± 13.2	219.3 ± 7.6	5.2	0.012 ± .0008	34	5.9	- -	60.1
Br 2a	125-250	44.62	46.82 ± 3.38			5.2	0.009 ± .0008	34	5.9	- -	80.4
Br 2b	125-250	31.09	45.13 ± 1.62			5.2	0.009 ± .0006	34	5.9	- -	77.5
Br 4b	250-500	25.15	44.69 ± 2.07			5.2	0.009 ± .0006	36	6.0	- -	76.3
Br 4c	125-250	35.08	31.99 ± 1.55	185.6 ± 13.2	165.1 ± 9.2	5.2	0.013 ± .0009	36	6.0	- -	54.3
Br 5b	250-500	8.97	46.91 ± 3.95	183.3 ± 15.9	93.9 ± 3.2	5.1	0.008 ± .0008	39	5.8	- -	81.8
Br 5c	500-800	54.58	33.87 ± 2.22	189.8 ± 9.3	75.6 ± 3.0	5.1	0.012 ± .0010	39	5.8	- -	58.8
Br 6a	250-500	50.28	43.95 ± 3.92			5.0	0.009 ± .0009	44	5.8	- -	76.4
Br 6b	250-500	48.85	35.53 ± 2.29			5.0	0.011 ± .0010	44	5.8	- -	61.6
Br 8a	250-500	23.42	43.49 ± 3.09			5.0	0.009 ± .0008	43	5.8	- -	75.7
Br 8b-1	250-500	61.88	32.24 ± 2.78			5.0	0.012 ± .0013	43	5.8	- -	55.8
Br 8b-2	250-500	16.59	32.17 ± 2.11	169.6 ± 10.3	103.4 ± 3.9	5.0	0.011 ± .0013	43	5.8	- -	64.0
Brazilian shield samples											
Cb 1a	160-250	50.20	23.18 ± 1.12			5.8	0.021 ± .0015		-	- -	40.4
Cb 2a	125-250	28.20	16.14 ± 0.88	101.9 ± 6.5	94.2 ± 2.2	5.1	0.028 ± .0033		-	- -	30.9
Cb 3a-1	125-250	41.20	37.79 ± 3.97			4.7	0.010 ± .0012		-	- -	81.4
Cb 3a-2	125-250	32.08	31.23 ± 1.58	184.7 ± 12.7	128.8 ± 4.7	4.7	0.012 ± .0014		-	- -	67.9
Cb 4a-1	125-250	20.34	11.73 ± 1.08	78.4 ± 6.6	64.0 ± 3.1	4.9	0.041 ± .0092		-	- -	21.8
Cb 4a-2	125-250	51.20	13.64 ± 1.59			4.9	0.031 ± .0040		-	- -	28.3
Cb 4a-3	125-250	45.80	15.54 ± 1.43			4.9	0.027 ± .0028		-	- -	32.3
Cb 5b	250-500	61.06	26.76 ± 0.95			4.9	0.015 ± .0009		-	- -	55.2
Cb 6b-1	250-500	64.51	19.00 ± 1.20			5.3	0.024 ± .0020		-	- -	36.0
Cb 6b-2	250-500	55.11	18.05 ± 1.23			5.3	0.025 ± .0022		-	- -	34.2
Cb 6b-3	250-500	37.18	17.48 ± 0.95	99.3 ± 7.7	66.1 ± 2.6	5.3	0.027 ± .0032		-	- -	32.0
Cb 7a	125-250	55.10	41.93 ± 3.88			5.1	0.010 ± .0010		-	- -	83.9
Cb 7b-1	125-250	40.22	39.95 ± 2.33			5.1	0.010 ± .0008		-	- -	79.9
Cb 7b-2	250-500	11.90	32.90 ± 4.04	164.7 ± 9.1	96.8 ± 6.8	5.1	0.013 ± .0017		-	- -	65.6
Cb 8a	125-250	68.35	25.45 ± 1.89			5.1	0.016 ± .0015		-	- -	51.0
Cb 8b-1	250-500	72.42	23.24 ± 1.91			5.1	0.018 ± .0018		-	- -	46.5
Cb 8b-2	250-500	36.51	22.44 ± 0.96	114.8 ± 5.7	60.1 ± 1.3	5.1	0.019 ± .0022		-	- -	45.5

Table 4.2 ▪CONTINUED▪

Sample	Grain size [µm]	Sample weight [g]	^{10}Be conc.[1] [x10^4 at/g$_{(Qz)}$]	^{26}Al conc.[2] [x10^4 at/g$_{(Qz)}$]	^{27}Al conc.[3] [µg/g]	^{10}Be production rate[4] [at/g$_{(Qz)}$/yr]	Denudation rate[5] [mm/yr]	Floodplain area [%]	^{10}Be prod. rate corr. for area[6] [at/g$_{(Qz)}$/yr]	Denudation rate[7] [mm/yr]	Apparent age[8] [kyr]
Brazilian Highland samples											
Cb 10a	250-500	49.43	17.37 ± 0.96			5.3	0.026 ± .0020		-	- -	32.9
Cb 10b-1	250-500	62.90	11.86 ± 1.08			5.3	0.040 ± .0042		-	- -	22.4
Cb 10b-2	250-500	16.58	12.20 ± 0.91	73.1 ± 7.8	67.6 ± 4.3	5.3	0.041 ± .0071		-	- -	21.8
Amazon lowland ("Llanos") samples											
Pe 101a	125-250	50.40	7.30 ± 0.51			14.3	0.154 ± .013	47	19.5	0.189 ± .017	3.8
Pe 107a	125-250	58.84	5.64 ± 0.63			18.0	0.245 ± .030	45	24.0	0.245 ± .031	2.3
Ne Rba	125-250	98.32	10.28 ± 0.47	47.7 ± 2.9	31.3 ± 1.1	3.9	0.038 ± .003	81	5.4	0.050 ± .003	18.9
Ne RBb	250-500	59.49	9.14 ± 0.57			3.9	0.043 ± .004	81	5.4	0.056 ± .004	16.8
Ne RBc	500-800	77.62	6.15 ± 0.47			3.9	0.066 ± .006	81	5.4	0.085 ± .008	11.3
Ne Lba	125-250	78.45	8.05 ± 0.65	32.6 ± 2.2	27.8 ± 1.2	3.9	0.050 ± .005	81	5.4	0.064 ± .006	14.8
Ne LBb	250-500	101.16	7.45 ± 0.39	32.1 ± 2.3	30.6 ± 1.1	3.9	0.054 ± .004	81	5.4	0.070 ± .005	13.7
Ne LBc	500-800	44.55	5.53 ± 0.56			3.9	0.074 ± .008	81	5.4	0.095 ± .011	10.2
Man 0.2a	125-250	77.81	6.36 ± 0.40	53.9 ± 20.3	1473.7 ± 85.7	7.1	0.099 ± .008	75	17.1	0.208 ± .017	3.7
Man 0.2b	250-500	57.48	4.64 ± 0.42			7.1	0.137 ± .014	75	17.1	0.286 ± .030	2.7
Man 0.2c	500-800	65.44	7.73 ± 0.87			7.1	0.081 ± .010	75	17.1	0.171 ± .020	4.5
Man 1.1a	125-250	81.59	6.05 ± 0.75			7.1	0.104 ± .014	75	17.1	0.219 ± .030	3.5
Man 1.1b	250-500	80.94	7.59 ± 0.33	32.8 ± 8.7	203.3 ± 5.7	7.1	0.082 ± .006	75	17.1	0.174 ± .012	4.4
Man 1.1c	500-800	74.61	7.31 ± 0.52			7.1	0.086 ± .008	75	17.1	0.181 ± .016	4.3
Man 2.85a	125-250	68.07	6.81 ± 0.54			7.1	0.092 ± .009	75	17.1	0.194 ± .018	4.0
Man 2.85b	250-500	73.33	7.30 ± 0.45			7.1	0.086 ± .007	75	17.1	0.181 ± .015	4.3
Ir 0.4b	250-500	92.06	8.77 ± 0.56	92.9 ± 6.3	101.0 ± 5.8	5.9	0.062 ± .005	77	15.0	0.134 ± .011	5.8
Ir 0.4c	500-800	98.47	13.31 ± 0.47	38.3 ± 8.0	201.1 ± 7.0	5.9	0.040 ± .003	77	15.0	0.088 ± .005	8.9
Ir 1.5b	250-500	99.36	10.10 ± 0.44	72.4 ± 5.6	82.1 ± 2.3	5.9	0.053 ± .003	77	15.0	0.116 ± .008	6.7
Ir 1.5c	500-800	99.00	15.50 ± 0.57			5.9	0.034 ± .002	77	15.0	0.075 ± .005	10.3
IR 1.75a	125-250	48.13	6.72 ± 0.55			5.9	0.082 ± .008	77	15.0	0.176 ± .017	4.5
IR 1.75b	250-500	52.75	6.02 ± 0.62			5.9	0.091 ± .011	77	15.0	0.196 ± .022	4.0
IR 1.75c	500-800	81.34	12.52 ± 0.73			5.9	0.043 ± .003	77	15.0	0.094 ± .007	8.4
Mad 0.5a	125-250	36.17	6.40 ± 0.57			5.3	0.079 ± .008	71	12.2	0.154 ± .015	5.3
Mad 0.5b	250-500	36.93	8.84 ± 0.84			5.3	0.057 ± .006	71	12.2	0.111 ± .012	7.3
Mad 1.1b	250-500	55.65	11.49 ± 0.95			5.3	0.043 ± .004	71	12.2	0.085 ± .008	9.5
Mad 1.1c	500-800	69.18	21.80 ± 0.97	104.4 ± 9.8	184.5 ± 5.9	5.3	0.022 ± .001	71	12.2	0.044 ± .003	18.0

Table 4.2 ▪CONTINUED▪

Sample	Grain size [µm]	Sample weight [g]	^{10}Be conc.[1] [x10^4 at/g$_{(Qz)}$]	^{26}Al conc.[2] [x10^4 at/g$_{(Qz)}$]	^{27}Al conc.[3] [µg/g]	^{10}Be production rate[4] [at/g$_{(Qz)}$/yr]	Denudation rate[5] [mm/yr]	Floodplain area [%]	^{10}Be prod. rate corr. for area[6] [at/g$_{(Qz)}$/yr]	Denudation rate[7] [mm/yr]	Apparent age[8] [kyr]
Mad 1.8a	125-250	42.45	4.70 ± 0.63			5.3	0.109 ± .015	71	12.2	0.211 ± .030	3.9
Mad 1.8b	250-500	87.66	6.56 ± 0.38			5.3	0.077 ± .006	71	12.2	0.150 ± .012	5.4
Par 1.2b	250-500	48.85	9.42 ± 0.71			5.6	0.055 ± .005	76	12.2	0.104 ± .009	7.7
Par 1.2c	500-800	49.04	16.73 ± 1.78			5.6	0.030 ± .004	76	12.2	0.058 ± .007	13.8
Par 2.2a	125-250	32.26	6.88 ± 0.80			5.6	0.076 ± .010	76	12.2	0.143 ± .018	5.6
Par 2.2b	250-500	52.64	7.29 ± 0.76			5.6	0.072 ± .008	76	12.2	0.135 ± .016	6.0
Ama-a	125-250	51.74	7.22 ± 0.65			5.7	0.073 ± .008	77	12.0	0.135 ± .014	6.0
Ama-b	250-500	76.57	8.31 ± 0.40	34.6 ± 10.2	547.7 ± 18.6	5.7	0.063 ± .004	77	12.0	0.117 ± .008	6.9
Tapa-b	250-500	126.52	9.65 ± 0.52			4.0	0.041 ± .003	60	4.4	- -	22.2
Tapa-c	500-800	95.73	8.85 ± 0.56	50.6 ± 3.8	57.1 ± 1.9	4.0	0.045 ± .004	60	4.4	- -	20.4
Samples from "Varzea do Curuai" floodplain											
Curu-a	125-250	46.18	14.73 ± 0.79			4.7	0.026 ± .002		-	- -	37.6
Curu-b	250-500	89.59	10.17 ± 0.44	28.5 ± 2.8	62.0 ± 1.9	4.7	0.039 ± .003		-	- -	25.9
Soc-b	250-500	51.96	4.72 ± 0.42			4.7	0.088 ± .009		-	- -	12.0
Soc-c1	500-800	89.72	4.72 ± 0.22	30.4 ± 4.3	124.6 ± 5.8	4.7	0.088 ± .006		-	- -	12.0
Soc-c2	500-800	47.97	4.24 ± 0.41			4.7	0.098 ± .011		-	- -	10.8
Gran-b	250-500	98.88	6.83 ± 0.41	45.8 ± 5.7	76.0 ± 3.7	4.7	0.060 ± .005		-	- -	17.4
Gran-c	500-800	100.45	5.45 ± 0.35			4.7	0.076 ± .006		-	- -	13.8

[1]Uncertainty contains analytical as well as blank error propagation; ^{10}Be/^{9}Be ratio of process blank was 1.1 ± 0.66*10^{-14}

[2]Uncertainty contains analytical error of AMS measurement

[3]Uncertainty contains analytical error of ICP-OES measurement and weighing errors of aliquots and standards

[4]Total ^{10}Be production rate from spallogenic and muonic production; in case of Br and Cb samples: corrected for variations in Earth´s magnetic field after Masarik *et al.* [2001]

[5]Denudation rates for Branco, Negro and Tapa are partly affected by buried sediment and thus are non-steady state denudation rates

[6]Calculated using a sediment-contributing area >200 m in elevation, includes Andean as well as cratonic shield area

[7]Calculated with floodplain-corrected production rate

[8]Calculated with floodplain-corrected denudation rate where possible

The Branco River is a main tributary to the Negro River, which is a main tributary in terms of discharge to the Amazon River. Negro River samples were taken near Paricatuba gauging station, ~50 km upstream of the Negro-Solimões confluence. Because dredging was impossible in the very deep (~50 m) and sediment-starved Negro, samples were taken from both river banks. ^{10}Be nuclide concentrations are 7.8×10^4 at/g$_{(Qz)}$ (n = 6; see Figure 4.5b)- about 5 times lower than Branco River concentrations. For three Negro samples, we have measured ^{26}Al/^{10}Be ratios that display a burial duration of 1.5-2.0 Myr at a depth between 5-10 m for samples from the left bank of the river, and a burial duration of ~1.0 Myr at a depth between 4-5 m below the surface (Figure 4.6b). Here, a nuclide inheritance of 10×10^4 at/g$_{(Qz)}$ is assumed. This inheritance is concordant with a denudation rate of ~0.04 mm/yr, which can be seen as a minimum estimation of denudation in the lower Negro basin. A higher nuclide inheritance (e.g. lower denudation rates) for Negro samples is unlikely, because then samples would plot to the left of the burial-age field denoted in Figure 4.6b, while a lower nuclide inheritance (e.g. higher denudation rate) is unlikely given that these were not observed in any modern or buried sample in a shield-draining river. As it is the case in the Branco River, different grain sizes yield different ^{10}Be concentrations in the Negro (see Table 4.2 and Figure 4.5b), that are consistently increasing with decreasing grain size. Moreover, the sampled river banks display large differences in nuclide concentrations. All these observations can be interpreted in several ways. (i) The Negro is a low energy river despite its high discharge; its low sediment load and great depth result in high bed stability in its lower reach [Irion *et al.*, 1995; Franzinelli & Igreja, 2002], where our samples were taken. However, despite the high bed stability, seasonal erosion events, e.g. due to backwater effects from the Amazon, might lead to the observed incorporation of old floodplain deposits into modern Negro stream sediment. (ii) The Negro shows progradational behavior, where local, faulting-induced basins are successively filled with coarser sediment in upper reaches, which, as a consequence, does not reach the Negro downstream section [Latrubesse & Franzinelli, 2005]. This observation has been validated by grain size and sediment provenance analysis [Franzinelli & Igreja, 2002; Latrubesse & Franzinelli, 2005] showing that, in the lower reach, coarser sand transported in the river does not originated from Guyana shield areas, but from the very friable Cretaceous "Alter do Chão" formation (see Figure 4.2) that crops out in the lower Negro reach (mainly on the left bank) only. Apparently, finer sediments originate in upstream cratonic areas, and coarser sediment may originate from the local Cretaceous formation, which may have been deposited from more rapidly eroding terrains, thus having lower nuclide concentrations. (iii) Differences in nuclide concentration with respect to the two sampled bank

sides may be explained by the local river bed configuration, because the right, concave bank may receive more fine-grained sediment from upper cratonic reaches due to higher specific stream energy. Local lithology differences could also affect cosmogenic nuclide concentrations, because on the right river bank, mostly recent (e.g. few kyr) Holocene floodplain deposits crop out [Rossetti *et al.*, 2005]. These sediments might partly originate from low-nuclide concentration Andean source rocks, which are mixed during flooding and backwater effects at high Solimões water levels [Meade *et al.,* 1991; Latrubesse & Franzinelli, 2005] with old cratonic and/or Cretaceous Alter do Chão sediments, resulting in a very complex burial and erosion history of the lower Negro.

4.5.1.3 The Brazilian craton

The headwaters of the Brazilian craton were characterized by sampling various rivers at various spatial scales- the smallest basin being ~6,700 km^2 (upper Guaporé River) and the largest being 176,000 km^2 (Juruena River; Table 4.1). The lower Brazilian shield was characterized by sampling the Tapajós River near Santarem.

The small headwater basins (Cb 1, 3, 5, and 7) drain mostly the Proterozoic (>1.1 Gyr) granitic to gneissic provinces of the Brazilian craton. The larger basins (Cb 2, 4, 6, and 8) drain mostly Phanerozoic (≤ 350 Myr) rocks, minor cratonic lithology, and younger, more friable sedimentary rocks that are cropping out at the edges of the cratonic platforms [Hasui & Almeida, 1985; Hartmann & Delgado, 2001; Mertes & Dunne, 2007]. On average, ^{10}Be nuclide concentrations in the Brazilian craton are significantly lower than in the Guyana shield with 22.9×10^4 at/$g_{(Qz)}$ (n = 20; see Figure 4.7a). $^{26}Al/^{10}Be$ ratios were measured for samples Cb 2, 3, 4, 6, 7, and 8 (see Table 4.2). Of these samples, Cb 2, 3, and 4 plot on the erosion island (Figure 4.6a), indicating the absence of burial. Corresponding denudation rates average at 0.025 mm/yr (n = 7). Burial was detected for Cb 6, 7, 8, and 10. Assuming a nuclide inheritance of 20×10^4 at/$g_{(Qz)}$ (as in unburied samples), Cb 6b plots at burial depths between 3-4 m at a burial duration of <0.5 Myr. Samples Cb 7b and 8b plot at depths between 2-3 m, with burial ages of ~1.2 and ~0.75 Myr, respectively (Figure 4.6c). This estimated inheritance would mean that paleo-denudation rates were also ~0.02 mm/yr for these samples.

We assume that only small amounts of recently remobilized shielded sediment is admixed into the stream, because large floodplains are absent in these basins. When plotted versus basin-averaged relief, a negative correlation between ^{10}Be concentration and relief is visible, resulting in a positive trend of denudation rates with relief (see Figure 4.7c).

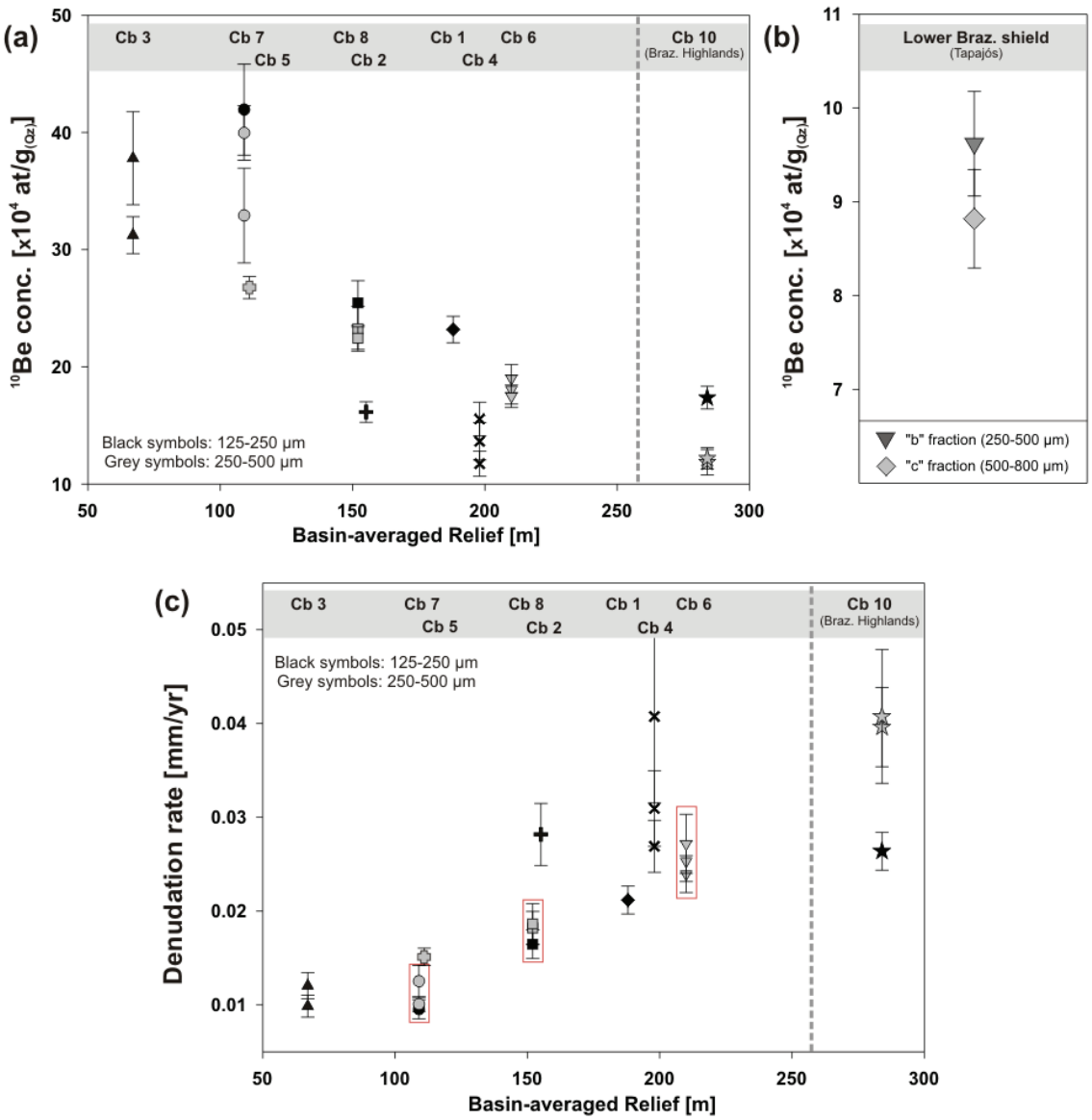

Figure 4.7 (a) Cosmogenic nuclide concentrations for the upper ("Cb") and (b) lower (Tapajós) Brazilian shield, and (c) cosmogenic nuclide-derived denudation rates for the upper Brazilian shield, all error bars shown are 1σ uncertainties. Note different X-axis scales for cosmogenic nuclide concentration plots a) and b). Denudation rates are not corrected for floodplain-area effects. In c), samples that are marked by a red square experienced burial, thus, strictly speaking no denudation rate can be calculated, but estimated nuclide inheritance is very close to modern concentrations. This is also the reason why no denudation rate was calculated for the Tapajós (see Figure 4.6 for burial durations and depths). Cosmogenic nuclide concentrations and denudation rates for Cb samples are plotted against basin-averaged relief (calculated from the average elevation minus the minimum elevation of the basin). A correlation coefficient of $r^2 = 0.86$ (including buried samples) denotes a significant relation between denudation rate and basin relief. Geographically, Cb 1, 2, and 3 drain the Madeira basin, Cb 4, 5, 6, and 7 the Tapajós basin, Cb 8 the Xingu, and Cb 10 the Tocatins basin.

Since paleo-denudation rates seem to be similar to modern denudation, this effect may actually be driving long-term denudation in the Brazilian shield. It has been suggested that hill slopes adjust to changes in base level due to slow but sustained uplift since the Tertiary [Stallard, 1985]. This base level adjustment may be the reason for denudation rates in the

Brazilian craton being so much higher than those of the Guyana shield. Lithology as a factor cannot be entirely excluded, because the larger basins studied in the Brazilian craton integrate over possibly more friable, younger sedimentary rocks with respect to the massive crystalline basement, which may have resulted in different development of weathered regolith or might reflect different soil formation rates.

The lower reaches of the Brazilian shield are drained by the Tapajós River. The Tapajós basin was sampled for bulk sediment from the river bank near Santarem, where it integrates over the Brazilian shield in its headwaters, and in its lower course over the central plateau of the Barreiras formation which is stratigraphically above the Cretaceous Alter do Chão formation [Roulet *et al.*, 2001; Rossetti *et al.,* 2005]. ^{10}Be nuclide concentrations are 9.3×10^4 at/$g_{(Qz)}$ (n = 2; see Figure 4.7b), which is significantly lower than average headwater nuclide concentrations of samples Cb 4 to 7, thus mixing of two different end members is assumed. This mixing is supported by the measured ^{26}Al/^{10}Be ratio, because Tapa-c plots on a mixing line between modern Amazon stream sediment (e.g. in Figure 4.6 represented by samples Man 0.2a and Soc-c), and Brazilian shield samples Cb 6 to 8 (Figure 4.6c), representing the other end member. The inherited nuclide concentration is estimated to be not higher than 10×10^4 at/$g_{(Qz)}$, resulting in a minimum denudation rate of ~0.04 mm/yr for the Tapajós. Present mixing with Amazon sediment is plausible because of the very strong Amazon hydrograph blocking water and sediment delivery from the Tapajós River, which in its lower course has evolved to a "ría" lake.

4.5.1.4 The Madeira River

The Madeira River at its confluence with the Amazon drains both Andean and shield terrain. ^{10}Be nuclide concentrations of the Madeira have been measured from dredged samples taken at 0.5 km, 1.1 km, and 1.8 km distance perpendicular to the left bank from the bedload of the river, where the sample code gives the distance to the left bank ("flb") in km. For example "Mad 0.5" corresponds to a sample dredged from the channel bottom at 500 m distance away from the left bank. Nuclide concentrations show large variations with the corresponding grain size, where the coarser grain sizes display higher ^{10}Be concentrations (see Figure 4.8a). Average nuclide concentrations for the "a" fraction amount to 5.6×10^4 at/$g_{(Qz)}$ (n = 2), and the "b" fraction averages 9.0×10^4 at/$g_{(Qz)}$ (n = 3). The "c" fraction was analyzed for cross-section

Mad 1.1 only, displaying a much higher concentration at 21.8×10^4 at/$g_{(Qz)}$. This sample was also analyzed for its ^{26}Al concentration, and the calculated ^{26}Al/^{10}Be ratio plots in the same range as Cb samples 6, 7, and 8, displaying a burial duration of ~0.75 Myr at depths of 3-4 m, if the inherited concentration was 20×10^4 at/$g_{(Qz)}$ (see Figure 4.6c). These Madeira nuclide concentrations are 1.4 to 5.5 (mean of ~2) times those of the Andean nuclide signal recorded in the Beni River system, which is the principle sediment deliverer to the Madeira (see Chapter 3), and average to $4.2\text{-}6.4\times10^4$ at/$g_{(Qz)}$.

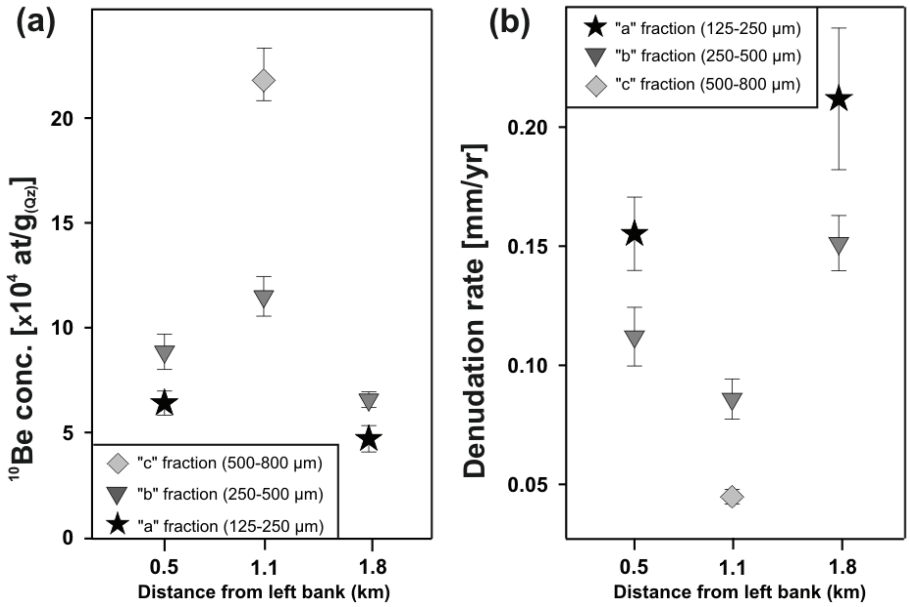

Figure 4.8 (a) Cosmogenic nuclide concentrations and (b) cosmogenic nuclide-derived denudation rates for the Madeira River, error bars denote 1σ uncertainties. Horizontal axis gives the distance in km from the left bank. Only sample Mad 1.1c was measured for its ^{26}Al/^{10}Be ratio and shows burial at an approximate duration of ~0.75 Myr. Thus, a calculation of spatially-averaged cosmogenic denudation rate for samples taken at 1.1 km flb is strictly speaking not valid.

This means that the sediment either records significant irradiation of sediment on the way across the llanos from the Andes to the mouth, or it records an admixing of high-concentration sediment from the cratonic areas, which averages to 27.1×10^4 at/$g_{(Qz)}$ (samples Cb 1, 2, and 3 that drain into the Madeira River). The latter explanation is more likely, if one recognizes that especially coarse material originates in the cratonic shields [Franzinelli & Potter, 1983; Potter, 1994; Guyot *et al.*, 1999]. This scenario is supported by the burial observed in the coarse-grained sample Mad 1.1c, indicating that this sediment originates within the Brazilian shield. Unfortunately, we lack additional ^{26}Al data from finer grain sizes to confirm this suggestion. This view is also supported by Guyot *et al.* [1999], who observes coarse-grained bed material in Brazilian shield rivers. These would have dominated the coarse fraction of the rivers during

ancient hydraulic conditions, because present-day hydraulic conditions do not support transport of the sand fraction from the Andean foreland. The fine, non-buried sand fraction of the Madeira on the other hand averages to 5.6×10^4 at/$g_{(Qz)}$ (n = 2), a value that represents the nuclide concentration of the Bolivian Andes measured by Safran *et al.* [2005]. Given that this Andean nuclide signal appears to be preserved over Amazon basin distances, one may calculate floodplain-area corrected denudation rates, using the only Andean area for production rate derivation. For the Madeira, this results in a denudation rate of 0.25 ± 0.03 mm/yr that is equal to a denudation rate calculated for the Madeira basin at Porto Velho (0.25 ± 0.03 mm/yr).

4.5.2 The main Amazon River system

4.5.2.1 The Amazon trunk stream

The main Amazon stream has been measured at intervals of ~200-250 km from Manacapuru near Manaus (samples "Man") to close to Óbidos (sample "Ama"; see Figure 4.2). We also sampled the Amazon upstream of the Madeira confluence near Iracema, samples "Ir"), at Parintins ("Par") below the Madeira confluence, and ~40 km downstream from Óbidos (sample "Ama"). Samples were dredged from bedload along bank-perpendicular cross-sections (sample codes give distance to left bank "flb" in km). The sampled cross-section at Manacapuru shows very small variability in measured ^{10}Be nuclide concentrations with respect to grain sizes, and also within sampling at three different distances from the left bank (see Figure 4.9); average ^{10}Be concentration of 8 samples is 6.7×10^4 at/$g_{(Qz)}$. ^{26}Al results display normal exposure for sample Man 0.2a, but sample Man 1.1b displays burial at a duration of ~1.0 Myr at depths of ~10-20 m when assuming an nuclide inheritance of 10×10^4 at/$g_{(Qz)}$ (see Figure 4.6b). At Iracema below the Negro confluence, variability significantly increases with the coarsest fraction being almost twice as concentrated in ^{10}Be as finer fractions, this variability being consistent for the three distances flb; measured nuclide concentrations amount to 10.4×10^4 at/$g_{(Qz)}$ (n = 7). Measured ^{26}Al/^{10}Be ratios show differences with sampling location: for samples at Ir 1.5 (b and c fractions), burial was detected at differing depths and ages (see Figure 4.6b). For sample Ir 0.4c, normal surface exposure was detected. At Parintins below the Madeira confluence, sample Par 1.2 (fractions a and b) shows large grain size variability, where sample Par 2.2 (fractions b and c) does not. Average nuclide concentrations for both samples (n = 4) are 10.1×10^4 at/$g_{(Qz)}$. Downstream of

Óbidos (sample Ama), measured nuclide concentrations are 7.8×10^4 at/$g_{(Qz)}$ (n = 2). For Ama-b, the measured $^{26}Al/^{10}Be$ ratio suggests a burial at a depth of ~10 m for ~1.2 Myr when assuming an nuclide inheritance of 10×10^4 at/$g_{(Qz)}$ (see Figure 4.6b).

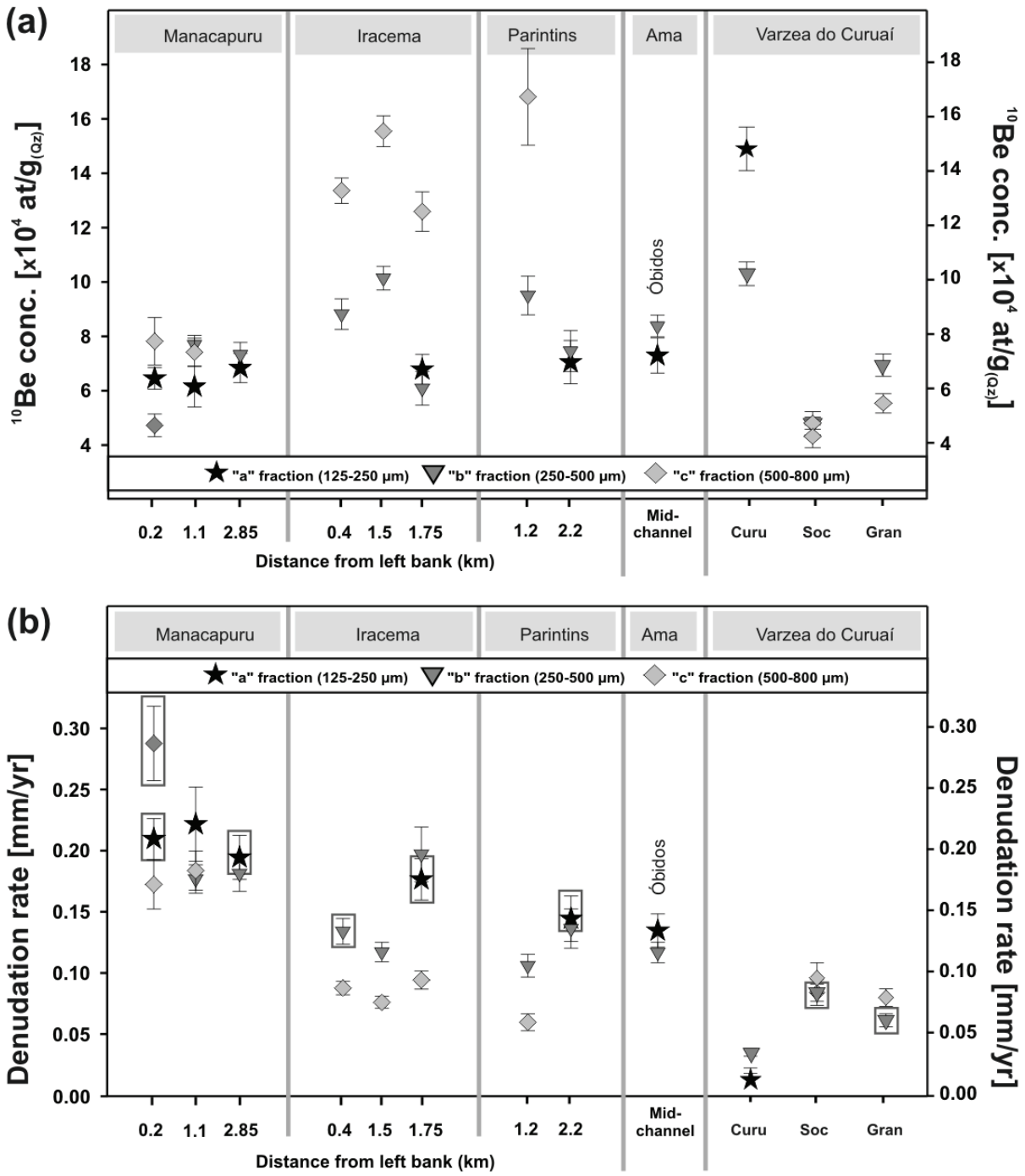

Figure 4.9 (a) Cosmogenic nuclide and (b) denudation rate data for the main Amazon River system using the production rate of the sediment-producing area only (Table 4.2); errors denote 1σ uncertainties. Data from the Curuaí floodplain is included. Red squares indicate samples that were taken for averaging in Figure 4.10 and Figure 4.11. Others were excluded, because they either show burial, or grain size is too coarse to be representative. For samples or sample cross-sections where no $^{26}Al/^{10}Be$ ratios were measured, only the very fine fraction was used for averaging.

4.5.2.2 The central Amazon floodplain

The "Varzea do Curuaí" is taken as a representative floodplain system of the central Amazon River, where the local processes involving water and sediment transport have now been studied for several years [e.g. Moreira-Turcq *et al.*, 2004; Bonnet *et al.,* 2005; Bonnet *et al.*, 2008; Maurice-Bourgoin *et al.*, 2005; Maurice-Bourgoin *et al.*, 2007]. The system is characterized by numerous black water (sample "Curu") and white water lakes (samples "Gran" and "Soc"), where, in general, the white water lakes directly receive sediment from the Amazon during rising water stage, and the black water rivers do not receive sediment from the Amazon but are connected to the system through the ground water table. Geologically, the northern and eastern part of the floodplain is composed of modern floodplain sediments (e.g. Quaternary age, mostly composed of stratified or laminated fine grained sand to mud; [Rossetti *et al.*, 2005]), and the southern part is comprised of Cretaceous to Miocene deposits (Barreiras formation), mostly consisting of fine- to coarse grained massive quartzitic sands [Rossetti *et al.*, 2005; Rossetti & Valeriano, 2007]. Lago Curumucuri (sample Curu) is located at the transition between modern and Miocene floodplain, where the Miocene floodplain has been preserved from inundation due to its slightly increased elevation prohibiting inundation. Both samples Soc and Gran are from the modern floodplain setting that surrounds Lago Grande de Curuaí but from different locations (see Figure 4.3).

Cosmogenic nuclide measurements of varzea samples include one $^{26}Al/^{10}Be$ ratio for Curu, Soc, and Gran each, and in total 7 ^{10}Be nuclide results (see Table 4.2). Nuclide concentrations of Soc average at 4.6×10^4 at/$g_{(Qz)}$ (n = 3; see Figure 4.9), and sample Gran displays similar nuclide concentrations at 6.1×10^4 at/$g_{(Qz)}$ (n = 2). ^{10}Be nuclide concentrations of sample Curu are significantly higher at 12.5×10^4 at/$g_{(Qz)}$ (n = 2). $^{26}Al/^{10}Be$ ratios for Soc-c-1 and Gran-b plot on the constant exposure line in Figure 4.6a, but significant burial has been detected for sample Curu-b that can only be explained by complete, ~1.5 Myr burial without additional irradiation. This observation might reflect the local sediment source within the Plio-Miocene floodplain sediments surrounding Lago Curumucuri. Samples Gran and Soc reflect the active part of the floodplain that receives fine-grained, mostly unshielded sediment from the Amazon, and is therefore similar in ^{26}Al and ^{10}Be nuclide concentration. Regarding the grain size fractions, it seems that coarse grain sizes are not readily transported into the varzea due to changes in the hydraulic regime [Moreira-Turcq *et al.*, 2004], thus the lower nuclide concentrations in coarser particles reflect a local varzea signal that does not originate in cratonic areas.

4.6 DISCUSSION

4.6.1 Sediment provenance and mixing in the Amazon basin

The preceding presentation of our new data has shown that a) in some samples strong grain size dependencies of ^{10}Be concentration exist; b) some samples display a significant ^{26}Al/^{10}Be signature of burial; c) some samples yield significant and regionally variable denudation rates. These patterns are mostly reproducible phenomena that we synthesize here.

a) Grain size. Upstream of the Negro confluence (samples Man), no variation in the ^{10}Be concentration with grain size can be detected, regardless of channel position. Below the confluence at Iracema, grain-size dependent ^{10}Be concentration variability is detected, and variability is preserved from thereon downstream. Interestingly, in those systems into which Andean sediment is contributed (Amazon at Iracema, Madeira, Parintins, Óbidos) the coarse grain sizes contain higher nuclide concentrations than the fine grains. In all settings that drain shield areas or Neogene sediment but that lack the Andean hinterland (Tapajós, Xingu, Tocatins, Branco, Negro, black water floodplain), the fine grains contain higher nuclide concentrations than the coarse sediment. We can only interpret this observation in terms of provenance-specific ^{10}Be concentrations. In the non-Andean catchments, coarse quartz grains are the main survivors of slow (100 kyr) weathering of the cratonic shields, whereas smaller grain sizes are added by more rapidly eroding Cretaceous and younger formations. Where Andean sediment is present, we are dealing with a binary mixture where coarse grains are being supplied by the cratonic and non-Andean landscapes, while fine grains with low nuclide concentrations survive sediment transport and comminution along the long route from the Andes to the central Amazon basin [Franzinelli & Potter, 1983; Potter, 1994]. It is perhaps not so surprising that these grain size effects differ between locations, and even across river-perpendicular cross-sections. First, bedload is transported along the channel bottom in sand waves, where it may be subjected to significant partitioning with respect to particle size depending on bank curvature [Nordin *et al.*, 1980; Mertes & Meade, 1985]. Second, the fine fraction is more readily exchanged with prevailing floodplain sediment. Thus, sampling (dredging) the channel at different water velocity zones might result in sampling of spatially different source areas if the sediment is subjected to the above described sorting effects, and the locally differing nuclide concentrations may largely depend on the prevailing flow regime and the local bed geometry.

b) Burial. A similar picture emerges for our detection of burial, even though the picture is not as clear-cut. Mostly, where grain size-dependent concentration variations are high, samples include a fraction of buried sediment. All cratonic rivers and non-Andean rivers contain buried sediment, where we detect the strongest burial signals in sediment that is coarse-grained, but also fine grains (250-500 µm) stem from buried sediment in cratonic areas. In contrast, in those samples that contain sediment of Andean provenance, burial signals are usually not observed in the fine fraction. The observation that almost all trunk stream Amazon and floodplain samples contain buried sediment at variable fractions seems to suggest that Myr time scale sediment storage and its erosion into the active stream may not only be occuring in very old, sediment-depleted systems like the cratons, but in the floodplain of the Amazon trunk stream too. According to our numerical model, however, a major decrease in nuclide concentrations due to decay is unlikely for the Amazon floodplain, where storage durations of only ~10 kyr have been estimated [Mertes *et al.*, 1996; Dosseto *et al.,* 2006b; Mertes & Dunne, 2007]. Thus, the fact that we observe buried sediment in the active stream can in our view only be explained by the admixture of very old, buried sediment from the non-Andean mainly cratonic tributaries.

c) Denudation rates. An average Amazon trunk stream concentration for the fine fraction (<500 µm), least affected by burial, is $6.5 \pm 1.2\times10^4$ at/$g_{(Qz)}$ (1σ, n = 10). For comparison, the average nuclide concentration in coarse material is $8.5 \pm 3.1\times10^4$ at/$g_{(Qz)}$ (1σ, n = 20). The concentration of the fine fraction is steady along the entire course of the trunk stream (Figure 4.10a). We can now compare this concentration to that of the major Andean tributaries. These values are 7.3×10^4 at/$g_{(Qz)}$ for the Solimões, 5.6×10^4 at/$g_{(Qz)}$ for the Ucayali (both Table 4.2), 4.2-6.4×10^4 at/$g_{(Qz)}$ for the Beni, 1.7×10^4 at/$g_{(Qz)}$ for the Napo, and 4.2×10^4 at/$g_{(Qz)}$ for the upper Mamoré basin (Chaparé and Grande rivers; all Chapter 3). These upstream catchments are representative for 95% of the Andean area draining into the Amazon, and their flux- and area-weighted concentration is $5.0 \pm 0.5\times10^4$ at/$g_{(Qz)}$ (1σ). Similarly, denudation rates of those rivers are 0.25, 0.2, 0.25, 0.73, and 0.44 mm/yr, respectively, and their flux- and area-weighted denudation rate is 0.35 ± 0.05 mm/yr. This average value compares to 0.23 ± 0.04 mm/yr (n = 9) for the Amazon trunk stream samples from Iquitos to Óbidos, excluding formerly buried and coarse sediment, and also disregarding floodplain and shield terrain for production rate calculation (Figure 4.10b). We conclude that fine-grained sediment in the Amazon trunk stream approaches Andean denudation rates.

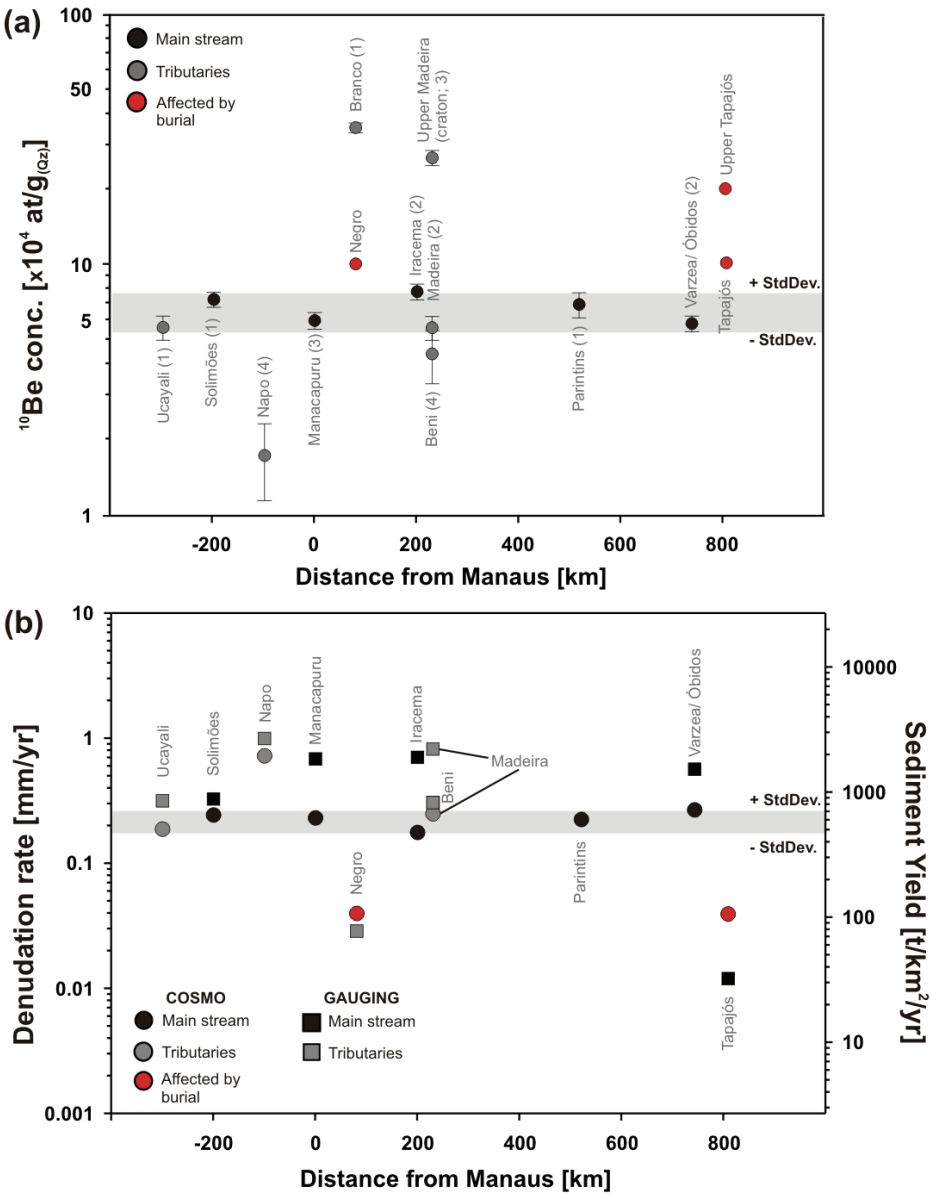

Figure 4.10 (a) Cosmogenic ^{10}Be nuclide concentrations (with 1σ uncertainties) versus distance along Amazon trunk stream from Manaus. Main Amazon stream samples are plotted in black, tributary rivers in grey. For upper Amazon (Pe) and Napo samples (see Chapter 3), an arbitrary distance to Manaus was taken. For each setting/ river, average concentrations taken from Figure 4.9 are calculated from several individual cosmogenic analyses, the number of which is given in brackets after the sample name. Samples affected by burial were excluded, as well as coarse grain fractions. For samples where no ^{26}Al/^{10}Be data was obtained, only the fine sand fraction (125-250 µm) was taken. For Brazilian craton samples draining into the Madeira basin, an average from Cb 1, 2, and 3 was calculated. For upper Tapajós and Negro, nuclide inheritance was plotted (red circles), thus, the calculated denudation rates are minimum estimates. Grey vertical bar denotes the average of 6.5 ± 1.2×10^4 at/g$_{(Qz)}$ calculated for the fine, non-burial fraction of the main trunk stream samples (Pe, Man, Ir, Par, and Varzea).

(b) Denudation rates from cosmogenic nuclide (circles) and sediment gauging (squares). Data is taken from Tables 4.3 and 4.4. Cosmogenic denudation rates are recalculated with the floodplain-corrected production rate, except for Negro and Tapajós samples that denote minimum denudation rate estimations, because they were calculated from nuclide inheritance. For samples that have a shield and an Andean hinterland component (e.g. the Madeira), only the Andean area was included. Sediment gauging erosion rates are floodplain-corrected. Best error estimation for gauging data is ~20%. Tributaries not draining directly into the Amazon (e.g. Branco) are not shown for clarity (except Beni).

4.6.2 Comparison with gauging-derived erosion rates and sediment flux estimates

Gauging in the Amazon basin has been carried out since the 1970´s, mainly operated by French-Brazilian cooperative hydrological program called "HYBAM". To allow for comparison with floodplain-corrected cosmogenic nuclide-derived denudation rates, erosion rates from sediment gauging also have to be corrected by removing the floodplain areas from calculation of sediment yields, which results in a substantial correction ~75-80% for central Amazon data (see Table 4.3). Cosmogenic nuclide-derived denudation rates agree with erosion rates derived from sediment gauging within a factor of ~2-3 (Table 4.4, Figure 4.10b). A detailed comparison between cosmogenic denudation rates and gauging-derived erosion rates shows that gauging erosion rates are consistently higher than cosmogenic nuclide-derived denudation rates. Higher erosion rates obtained from short-term methods is an effect that has already been observed in the Beni basin, where increased short-term sediment gauging with respect to the lower long-term sediment flux recorded by cosmogenic nuclides is attributed to a climate- or land use-induced increase in erosion over the last ~2.5 kyr. In terms of the central Amazon floodplain, cosmogenic denudation time scales are in the order of ~8 kyr, while sediment gauging rates integrate only over the gauging period and cannot be extrapolated to longer time scales [e.g. Walling & Webb, 1981; Walling, 1983]. A drier climate in the Andean source areas persisting over most of the Holocene including the last glacial and a wetter modern climate for the very last few kyr [van der Hammen & Absy, 1994; Abbott *et al.,* 1997; Cross *et al.*, 2000; van der Hammen & Hooghiemstra, 2000; Abbott *et al.*, 2003] would explain our lower long-term denudation rates. However, the overall effect of precipitation on erosion is also a function of vegetation, which stabilizes erosion at a certain threshold; thus, erosion does not increase steadily with increasing precipitation [Langbein & Schumm, 1958].

4.6.3 Sediment budget for the Amazon basin

In Figure 4.11, we compare river loads from gauging data with apparent river loads calculated from cosmogenic nuclides. These rates of sediment flux were calculated by converting the denudation rate into a sediment yield (Table 4.4) and multiplying it with the sediment-source area, which is the floodplain-corrected area. For tributaries from cratonic areas (Negro and Tapajós), where all sediment contains buried components, we estimated their concentration by extrapolating to zero burial age (Figure 4.6). For the calculated sediment flux passing Óbidos,

Table 4.3: Sediment gauging data for the central Amazon

Code	Station	River	Total drainage area [x10^4 km^2]	Floodplain area[a] [x10^4 km^2]	Gauging period for suspended loads	Suspended sediment load [Mt/yr]	Dissolved load[b] [Mt/yr]	Total yield[c] [t/km^2/yr]	Floodplain-corrected total yield[d] [t/km^2/yr]	Erosion rate[e] [mm/yr]	Floodplain-corrected erosion rate[f] [mm/yr]
CHA[1]	Chazuta	upper Maranon	5.9	0.6	2003-2006	42	-	710	790	0.26	0.29
BOR[1]	Borja	upper Maranon	11.5	1.1	1986-2006	103	-	890	980	0.33	0.36
SRE[1]	San Regis	Maranon	36.1	16.7	1986-2006	168	-	470	750	0.17	0.28
REQ[1]	Requena	Ucayali	36.0	16.2	1984-2006	205	-	570	860	0.21	0.32
TAM[1]	Tamshiyacu	upper Solimoes	73.3	34.1	1986-2006	413	-	560	890	0.21	0.33
MAN[2,3]	Manacapuru	lower Solimoes	218.0	160.6	1974-1989	697	102	370	1730	0.14	0.64
MAN[3,4]	- -	- -	- -	- -	98-99 & 02-03	827	102	430	2010	0.16	0.74
PAR[3,4]	Paricatuba	Negro	83.2	67.0	98-99 & 02-03	9	4	15	80	0.006	0.029
IR[2,3]	Amatari[$]	Amazon	315.4	241.8	1974-1989	783	108	280	1930	0.10	0.71
MAD[2,3]	Fazenda Vista Allegre	Madeira	133.6	93.6	1974-1989	715	20	550	2600	0.20	0.96
MAD[3,4]	- -	- -	- -	- -	98-99 & 02-03	511	20	400	1880	0.15	0.70
OBI[2,3]	Obidos	Amazon	506.5	388.7	1974-1989	1239	129	270	1840	0.10	0.68
OBI[3,5]	- -	- -	- -	- -	1995-2003	810	129	190	1260	0.07	0.47
IT[3,6]	Itaituba	Tapajos	59.8	36.0	1997	1	6	13	30	0.005	0.012

[1] Guyot *et al.* [2007a]
[2] Dunne *et al.* [1998]
[3] Gaillardet *et al.* [1997]
[4] Laraque *et al.* [2005]
[5] Guyot *et al.* [2005]
[6] Seyler *et al.* [2003]

[a]Denotes the area below 200 m elevation
[b]From Gaillardet *et al.* [1997]
[c]Includes suspended sediment and specific dissolved yield
[d]Calculated using sediment source area only (e.g. excluding floodplain area) and total yield
[e]Calculated from total yield and a density of 2.7 g/cm^3
[f]Calculated using floodplain-corrected total yield and a density of 2.7 g/cm^3
[$]Corresponds to sample "IR" (Iracema)

Table 4.4: Averaged cosmogenic nuclide and sediment gauging data used for sediment budget calculation

		COSMOGENIC NUCLIDE DATA (see Table 4.2)						SEDIMENT GAUGING DATA (see Table 4.3)			
Code	River/ Setting	N of cosmog. analyses[1] [#]	Sediment source area[2] [x10^4 km^2]	Cosmogenic denudation rate [mm/yr]	Floodplain-corr. cosmog. denudation rate[3] [mm/yr]	Yield from cosmog. denudation rate[4] [t/km^2/yr]	Floodplain-corr. yield from cosmog. denudation rate [t/km^2/yr]	Total sediment yield[5] [t/km^2/yr]	Floodplain-corr. sediment yield [t/km^2/yr]	Erosion rate[6] [mm/yr]	Floodplain-corr. erosion rate [mm/yr]
Pe 107	Ucayali at Requena	1	23.8	0.154 ± .013	0.19	420	510	570	870	0.21	0.32
Pe 101	Solimoes at Tamshiyacu	1	46.2	0.245 ± .030	0.25	660	660	560	890	0.21	0.33
Napo[§]	Napo River avg., near Iquitos	4	1.8	0.282 ± .104	0.73	760	1980	480	2720	0.18	1.01
Manacapuru[+]	Solimoes	3	46.2	0.109 ± .011	0.23	300	630	400	1870	0.15	0.69
Negro*	Negro at Paricatuba	-	16.2	> 0.04	-	> 110	-	14	80	0.01	0.03
Branco[&]	Branco, upper Negro	1	14.6	0.012 ± .001	-	30	-	-	-	-	-
Iracema[&&]	Amazon before Madeira confl.	2	46.2	0.072 ± .006	0.18	190	480	280	1930	0.10	0.71
Madeira[$]	Madeira river at mouth	2	28.2	0.073 ± .008	0.25	250	670	470	2240	0.18	0.83
Cb_Mad**	Brazl. Shield, upper Madeira	3	-	0.018 ± .002	-	50	-	110	-	0.05	-
Beni[#]	Beni River avg., upper Madeira	3	28.2	0.107 ± .017	0.25	290	660	320	850	0.12	0.31
Parintins[%]	Amazon after Madeira confl.	1	74.5	0.076 ± .010	0.23	210	610	-	-	-	-
Varzea[++]	Amazon near Obidos	2	74.5	0.074 ± .007	0.27	200	730	230	1540	0.08	0.57
Tapajos[##]	Tapajós near Santarem	-	23.8	> 0.04	-	> 108	-	10	30	0.005	0.01
Cb_Tapa[$$]	Braz. Shield, upper Tapajos	-	-	~0.025	-	~70	-	-	-	-	-

[1]Number of anayses deviates from total number measured (see Table 4.2), because some samples were excluded for mean calculation (see below)
[2]Denotes the area >200 m elevation; for Andean settings with shield portion, only the Andean area >200 m was taken
[3]Avg. denudation rate, excluding coarse grain sizes and samples that display burial (see below), calculated with sediment source area
[4]Calculated using a density of 2.7 g/cm^3
[5]Includes specific dissolved and suspended yield
[6]Calculated from total yield using a density of 2.7 g/cm^3; uncertainties are not available, but best-case estimates are ~20%

[§]Average of Napo samples Na 18, 19, and 21; gauging data from Bellavista station (see Chapter 3)
[+]Cosmogenic average from samples Man 0.2a & b, and Man 2.85a; gauging data gives average from two estimates (see Table 4.3)
*Minimum estimation from nuclide inheritance; gauging data from Paricatuba station (see Table 4.3)
[&]Denotes Br 1a
[&&]Average from samples Ir 0.4b and 1.75a
[$]Average from Mad 0.5a and 1.8a; gauging data from station at F. Vista Allegre (Table 4.3; average from two estimates was taken)
**Average calculated from samples Cb 1, 2, and 3; gauging data from Guayaramerin station (see Chapter 3)
[#]Average from Beni samples Be 18, 19, and 20; gauging data from Porto Velho station (see Chapter 3)
[%]Denotes sample Par 2.2a
[++]Representative for Amazon at Obidos, from varzea samples Soc-b and Gran-b; gauging data from Obidos station (see Table 4.3; average from two estimates was taken)
[##]Minimum estimation from nuclide inheritance
[$$]Estimate from nuclide inheritance that corresponds well to samples not displaying burial

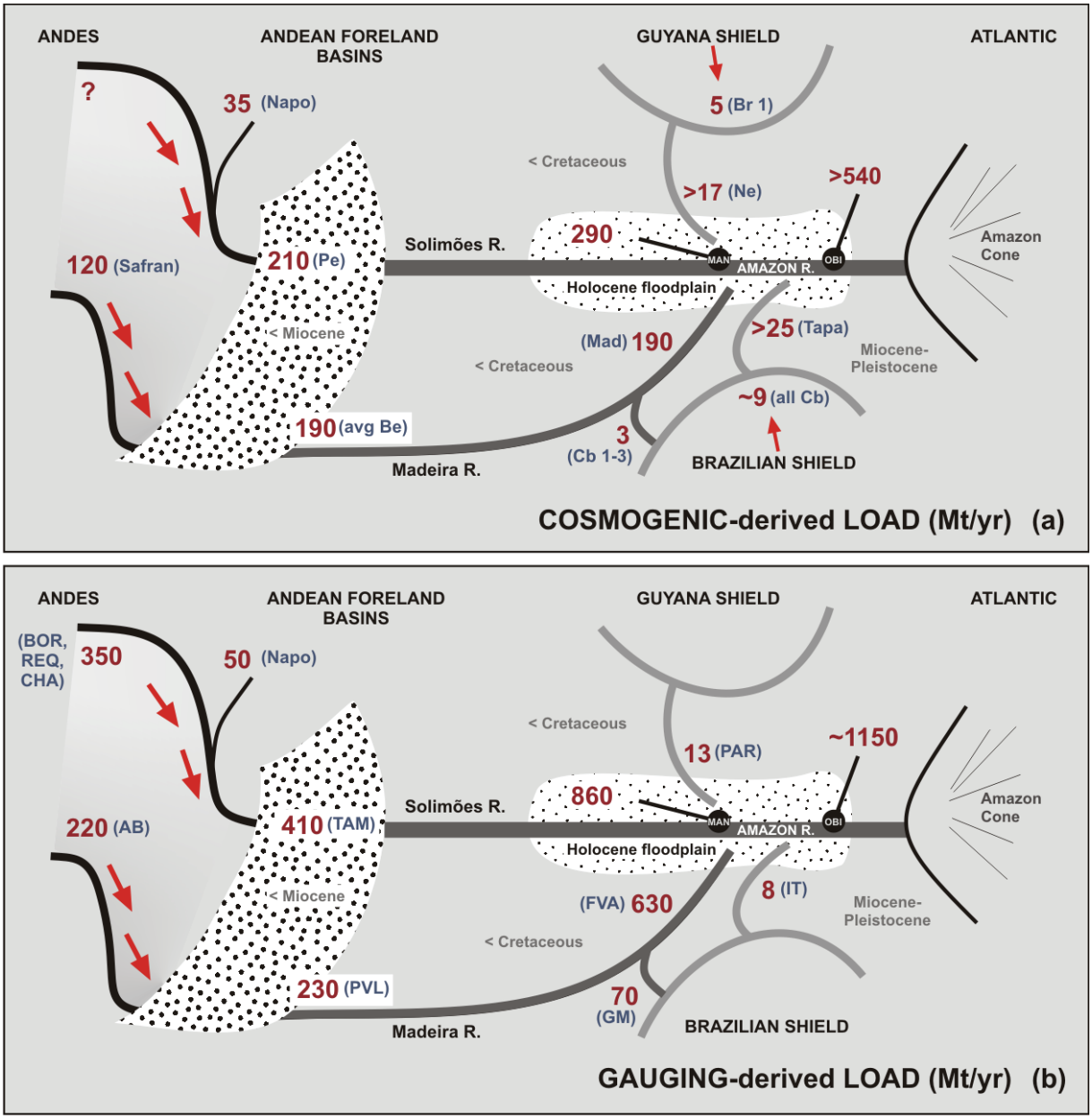

Figure 4.11 Sediment budget (Mt/yr) for the Amazon basin inferred from (a) cosmogenic nuclides and (b) from river load gauging including dissolved loads. Both budgets are calculated from floodplain-corrected or minimum estimation data given in Table 4.4 and Figure 4.10. Abbreviations see Table 4.2 and 4.3. Andean data is from Safran *et al.* [2005], and "avg Be" denotes Beni River average (see Table 4.4). Where more than one gauging estimation was available, we calculated averages (see Table 4.4). Gauging data from "AB" and "GM" are from Rurrenabaque and Guayaramerin gauging stations, respectively (see Chapter 3).

a minimum estimation is given by the nuclide concentration measured in the Varzea do Curuaí, which is the only measured Amazon sediment sample free of burial. The cosmogenic nuclide-based mass budget results in a total sediment mass carried by the Amazon River at Óbidos of >540 Mt/yr. The budget shows that the sums of the individual reaches are relatively consistent with respect to the total flux at Óbidos, although this is a minimum estimation from varzea nuclide concentrations. The nuclide-based fluxes transferred from the Andes across the

Beni and Marañón foreland basins to the Amazon River record the sediment production in the source areas, which is why the average load transported by e.g. the Beni equals that of the Madeira at its mouth (see Figure 4.11).

Despite that not all rivers potentially contributing sediment to the Amazon River are displayed in Figure 4.11, gauging-derived mass fluxes are consistent. For the total flux at Óbidos, the estimation by Dunne *et al.* [1998] (1400 Mt/yr) would fit better than the calculated average of ~1150 Mt/yr (both including the dissolved load from Gaillardet *et al.* [1997]; see Table 4.3 and 4.4). However, the flux at Óbidos is not equal to the flux transported to the Atlantic, because ~400 Mt/yr of sediment are deposited in the delta plain between Óbidos and the Atlantic [Dunne *et al.*, 1998]. Estimations from both methods are roughly concordant with sediment discharge estimates from ^{210}Pb activity profiles in the Amazon delta on the continental shelf, where for the last ~1 kyr, a flux of 630 ± 200 Mt/yr has been estimated [Kuehl *et al.*, 1986].

4.7 SUMMARY

Andean cosmogenic nuclide input to the Amazon basin is characterized by samples from the Ucayali and Solimões rivers (Peruvian Andes), as well as from data measured in the Napo and Beni, and Mamoré basins that drain the Ecuadorian and Bolivian Andes, respectively (see Chapter 3). The Ecuadorian Andes seem to erode somewhat faster (~0.7 mm/yr), and the Peruvian Andes somewhat slower (~0.25 mm/yr) than the Bolivian average (~0.5 mm/yr). This variability mirrors at large scale the local variability detected by Safran *et al.* [2005] and this study, hinting at spatially and temporally non-uniform denudation processes in the Andes.

The cratonic areas of the Guyana shield (Branco River) display very high ^{10}Be nuclide concentrations (~40×10^4 ats/$g_{(Qz)}$) and thus erode at very slow rates of only ~0.01 mm/yr. These rates are similar to chemical weathering rates [Edmond *et al.*, 1995]. ^{10}Be nuclide concentrations from the Brazilian craton (~27×10^4 at/$g_{(Qz)}$) are significantly lower than Guyana shield concentrations, and modern denudation rates amount to 0.023 mm/yr- more than twice of those of the Guyana shield. The geomorphic setting in the Guyana shield turns out to be very similar to that of the similarly steep, wet, and cratonic tropical highlands of Sri Lanka [von Blanckenburg *et al.*, 2004]. There, the absence of recent tectonic activity has led

to all but a cessation of weathering and transport processes. Interestingly, the doubled denudation rates in the Brazilian shield might confirm this hypothesis. Stallard [1985] has suggested that this area is uplifting at ~0.1-0.2 mm/yr, even though the evidence for such uplift in the form of incised and terraced rivers is controversial.

Admixture of old, partly shielded material in the active Branco stream indicates recent erosion of buried material in floodplain-influenced lower reaches, displayed by $^{26}Al/^{10}Be$ ratios lower than those expected for constant exposure. For the lower Guyana shield drained by the Negro River, we found that the local tectonic setting strongly influences sediment transport, so that a complex situation arises, where mainly coarse sediment from local Cretaceous outcrops is mixed with fine-grained higher concentration material originating in the Guyana shield headwaters. This sediment is evidently stored in floodplains at shallow depths for ~1.5 Myr before it reaches the river mouth. ^{10}Be nuclide concentrations of all Negro samples average to ~8×10^4 at/$g_{(Qz)}$, a value that is close to Amazon trunk stream concentrations, thus backwater effects cannot entirely excluded.

$^{26}Al/^{10}Be$ ratios measured for individual basins of the upper Brazilian craton also indicate admixing of buried sediment into active streams for some basins. An estimate of paleo-denudation rates (~0.02 mm/yr) from burial are in the range of modern denudation (0.023 mm/yr) and are consistent with long-term (1 Myr) stability of this erosion rate. A similar situation is present in the Tapajós at its confluence with the Amazon River, where measured $^{26}Al/^{10}Be$ ratios and very low ^{10}Be nuclide concentrations (~9×10^4 at/$g_{(Qz)}$) indicate an evolution along a mixing line between Amazon and Brazilian shield headwater sediment being the two mixing end members.

In the Madeira River, ^{10}Be nuclide concentrations show large variability, ranging from 5-22×10^4 at/$g_{(Qz)}$, where coarse-grained high-nuclide concentration sediment is assumed to originate in the cratonic areas, and fine-grained low-nuclide concentration material evidently originates in the Beni catchment of the Andes. The presence of formerly buried sediment in all craton-draining tributaries can be explained by their high water discharge and at the same time sediment-starved nature. Due to this, these streams have the capability to erode early Quaternary or late Tertiary floodplain sediment.

Burial trends in the Amazon main stream at some sampling locations are interpreted as mixing between modern (Holocene) non-buried floodplain sediment, and old (Miocene), buried floodplain sediment that is being incorporated into the Amazon River from its shield tributaries. The Holocene end member is characterized by fine-grained, unshielded sediment of which the nuclide concentrations are $6.5 \pm 1.2\times10^4$ at/$g_{(Qz)}$ along a 3000 km long reach

from Iquitos to Óbidos. This signal does not deviate much from Andean source area signal (flux- and area-weighted mean of $5.0 \pm 0.5\times10^4$ at/$g_{(Qz)}$). Variations in the nuclide signal along the main stream are related to sorting effects, because cratonic areas may preferably have contributed coarse sediment (> fine sand) with high nuclide concentrations.

The ^{10}Be nuclide characterization of a floodplain system was carried out in the Varzea do Curuaí, located south of Óbidos. Here, we found that the parts of the floodplain that interchange with the Amazon are also composed of sediment carrying its nuclide concentration without burial signal as indicated by modern ^{26}Al/^{10}Be ratios. Older parts of the floodplain on the other hand, which apparently have not been reworked by the Amazon during the Holocene, are indicative of sediment burial since Pliocene times in black-water lake bottom sediments.

This assessment using cosmogenic nuclides demonstrates that the sediment debouched from the Andes is indeed the dominant sediment source for the central Amazon as suggested by Gibbs [1967], Meade *et al.*, [1985], and Meade [1985], with additions from cratonic areas being minor. Consequently, the nuclide concentration detected in fine-grained, non-buried sediment in the central Amazon River is representative of the Andean denudation, thus giving an independent meter of sediment discharge, which we can compare to erosion rates derived from short-term sediment gauging. Cosmogenic nuclide-derived denudation rates are consistently lower by a factor of 2-3 than those from sediment gauging. The discharged mass at Óbidos amounts to a minimum estimation of ~540 Mt/yr from cosmogenic nuclides, and to and average of ~1100 Mt/yr from sediment gauging. This disparity is counterintuitive, as cosmogenic isotopes should yield a maximum possible sediment discharge, while sediment gauging often yields a minimum estimate. This expectation arises from the potentially low sediment delivering ratio affecting suspended loads, while cosmogenic nuclides will always provide the rate of sediment production, regardless of the amount of sediment lost into floodplains. The latter budget integrates over very short time scales, only encompassing the modern climate with increased precipitation in the Andes, whereas during the Holocene, erosion processes might have been less effective due to a dry climate with less precipitation, which might be recorded by cosmogenic denudation rates from in-situ produced ^{10}Be, which average over the past 8 kyr.

CHAPTER 5

THE RELATION BETWEEN ROCK UPLIFT AND DENUDATION FROM COSMOGENIC NUCLIDES IN RIVER SEDIMENT IN THE CENTRAL ALPS OF SWITZERLAND

This chapter is published as: Wittmann, H., v. Blanckenburg, F., Kruesmann, T., Norton, K.P., and Kubik, P.W. "The Relation between rock uplift and denudation from cosmogenic nuclides in river sediment in the Central Alps of Switzerland", Journal of Geophysical Research- Earth Surface, Volume 112, doi: 10.1029/2006JF000729, 2007; Copyright [2007] American Geophysical Union. Reproduced by permission of American Geophysical Union.

ABSTRACT

A north-south traverse through the Swiss Central Alps reveals that denudation rates correlate with recent rock uplift rates in both magnitude and spatial distribution. This result emerges from a study of in situ-produced cosmogenic ^{10}Be in riverborne quartz in Central Alpine catchments. As a prerequisite, we took care to investigate the potential influence of shielding from cosmic rays due to snow, glaciers, and topographic obstructions, to calculate a possible memory from Last Glacial Maximum (LGM) glaciation, and to identify a watershed size that is appropriate for systematic sampling. Mean denudation rates are 0.27 ± 0.14 mm/yr for the Alpine foreland, and 0.9 ± 0.3 mm/yr for the crystalline Central Alps. The measured cosmogenic nuclide-derived denudation rates are in good agreement with post-LGM lake infill rates and about twice as high as denudation rates from apatite fission track ages that record denudation from 9-5 Myr. In general, denudation rates are high in areas of high topography and high crustal thickness. The similarity in the spatial distribution and magnitude of denudation rates and those of rock uplift rates can be interpreted in several ways: (1) postglacial rebound or climate change has introduced a transient change in which both uplift and denudation follow each other with a short lag time; (2) the amplitude of glacial to interglacial changes in both is small and is contained in the scatter of the data; (3) both are driven by ongoing convergence where their similarity might hint at some form of long-term quasi steady state; (4) enhanced continuous Quaternary erosion and isostatic compensation of the mass removed accounts for the distribution of present-day rock uplift.

5.1. INTRODUCTION

In convergent mountains belts with thickened crust, relief forms when the uplift rate exceeds the denudation rate. Once a certain topography that is characteristic of convergence rate, orogen width, crustal thickness, rock strength, and denudational power (set by climate) is achieved, any further rock uplift will be balanced by denudation. Steady state between rock uplift and denudation is established and the characteristic relief will be maintained. These concepts have been detailed in theory [England & Molnar, 1990; Stuewe & Barr, 1998; Whipple *et al.*, 1999; Whipple, 2001; Willett & Brandon, 2002; Whipple, 2004] and documented with field data from various mountain belts [Brandon & Vance, 1992; Small *et*

al., 1997; Hovius *et al.*, 2000; Montgomery & Greenberg, 2000; Kuhlemann *et al.*, 2002; Montgomery & Brandon, 2002].

The significance of these concepts remains disputed because field tests are not sufficiently comprehensive to allow for a self-consistent characterization of the responses to forcing. Further they suffer from the need to bridge the substantial methodological time scales [Hovius & von Blanckenburg, 2007]; rock uplift can be measured with geodetic methods relative to a fixed datum on preserved surfaces (10^1 yr time scale), while the integrated result of rock uplift can be determined by stable isotope-based paleo-altimetry (10^6 yr) [Mulch *et al.*, 2007]. Denudation can be measured by river loads (10^1 yr) [Pinet & Souriau, 1988; Summerfield & Hulton, 1994], sediment budgets (e.g. lake fills; 10^4 to 10^6 yr), and thermochronology (10^6 yr).

Cosmogenic nuclides in river sediment potentially provide a denudation rate tool that is suitable to bridge these time scales. The measured rates integrate over a time scale (10^2 to 10^4 yr) that is sufficiently robust to be insensitive to very short-term denudational perturbations (human influence, short-term climate oscillations), and that is meaningful for time scales of both rock weathering and rock uplift [von Blanckenburg, 2005].

Here, we apply this technique to the European Alps. The Alps, and in particular the Central Alps, are an area of exceptionally high density and quality of geologic data. The collision history is well known [Schmid & Kissling, 2000; Schmid *et al.*, 2004; von Blanckenburg, 2005], long-term denudation rates are known from thermochronological studies [Wagner *et al.*, 1977; Rahn, 2001; Rahn, 2005], and present-day geodetic rock uplift rates have been determined ([Kahle *et al.*, 1997], revised by Schlatter *et al.* [2005]). In addition the spatial and temporal distribution of ice cover during the LGM (last glacial maximum), and post-glacial periods is well constrained [Florineth & Schluechter, 1998; Ivy-Ochs *et al.*, 2004; Kelly *et al.*, 2004].

However, since a systematic investigation of the applicability of cosmogenic nuclides to active, rapidly denuding mountain belts with all their complexities has not yet been done, we first establish the sensitivity of the method to certain potential perturbations. These are (1) the approach of nuclide concentrations to steady state after LGM glaciation; (2) the nuclide inventory of potentially incorporated moraine and glacial material; and (3) watershed sizes that are too small or too large for representative sampling.

Following the establishment of these prerequisites, we proceed to map a first-order north-south traverse of denudation rates across the orogen. We will show that these relate to

topography and rock uplift rates. Finally, we will discuss possible controlling factors and feedback mechanisms.

5.2 STUDY AREA, SAMPLE CHARACTERISTICS, AND LAB PROCESSING

5.2.1 Tectonic evolution of the Alps and Alpine glacial history

Our study area comprises the Swiss Mittelland, the Swiss Central Alps, and the Italian section of the Central Alps (see Figure 5.1 and Table 5.1 and 5.2). In this study, the latter two are called the "high Alps". Continental convergence and collision of the Adriatic microplate and the European continent at 55 Myr initiated the formation of the Alpine orogen [Schmid & Kissling, 2000].

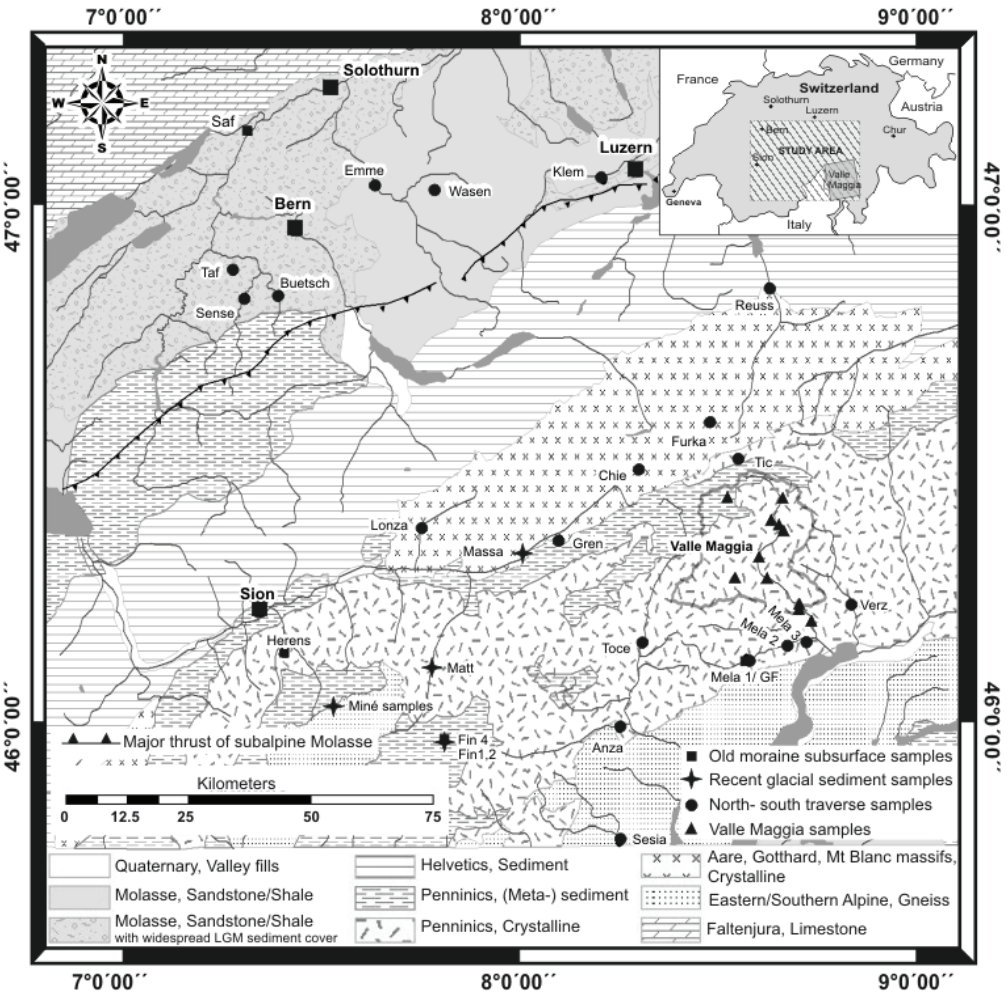

Figure 5.1 Geological overview over the sampling area and sampling locations. Shown are old moraine subsurface samples (squares), recent glacial sediment samples (stars), north-south traverse samples (circles), and samples within the Maggia catchment (Valle Maggia, triangles).

The European Alps feature a crystalline core comprising polymetamorphic rocks and pre-Alpine magmatic rocks overlain by Mesozoic and Cenozoic metasedimentary sequences, which both form the Penninic and Helvetic thrust nappes. Between the Alps to the south and the Jura fold-and-thrust belt to the north, the Swiss Mittelland forms a foreland basin, containing Tertiary molasse sediments with a minimum age of ~5 Myr. In the south of the Central Alps, the Tonale Line, a E-W striking segment of the Insubric Line separates the Southern from the Central Alps. The Southern Alps contain crystalline (magmatic and metamorphic) rocks dated at 300 to 200 Myr and Mesozoic sedimentary sequences. The Insubric Line, a presently inactive fault zone [Prosser, 1998; Schmid *et al.*, 2004] was active from Oligocene to early Miocene times, marking the position of the Adriatic indenter tip during the formation of the Alpine orogen [Schmid *et al.*, 1989]. During the LGM, glaciers extended from the large ice domes in the Alpine core to the foreland basins [Florineth & Schluechter, 1998; Florineth & Schluechter, 2000; Kelly *et al.*, 2004]. During this time, as much as 60% of the Mittelland basin was covered by ice. Beginning at 21 kyr, the piedmont glaciers that occupied the Mittelland rapidly retreated into the Central Alpine valleys [Ivy-Ochs *et al.*, 2004], leaving the foreland basins ice-free. Alpine glaciers never grew large enough during any of the subsequent advances to cover the foreland again. Glaciers continued however to impact the Central Alps. Numerous Late Glacial stadials have been identified in the Alps. Immediately after LGM deglaciation, small fluctuations (Bühl and Steinach advances) were followed by the larger Gschnitz, Clavadel-Senders, and Daun Stadials [van Husen, 1977; Maisch, 1981; Ivy-Ochs *et al.,* 2004]. These colder periods were brought to an end by the Bølling-Allerød Interstadial during which ice retreated into the high Alps [Ohlendorf, 1998]. Glaciers readvanced at the end of the Bølling-Allerød. The Egesen Stadial, time correlative with the Younger Dryas (YD), is characterized by valley and cirque glaciers [Ivy-Ochs *et al.,* 1996; Kerschner *et al.*, 2000]. Climate then warmed again following the YD. While glaciers did advance numerous times in the Holocene during Kartell, Kromer, and Little Ice Age Stadials [Sailer, 2001; Kerschner *et al.,* 2006], they never again reached their YD extents. Several Holocene glacier advances have been dated, however, that indicate that glaciers were larger than today in these phases [Hormes *et al.,* 2001.

Table 5.1: Sample specific and basin characteristics

Sample type	Sample name	Catchment	Grain size fraction [µm]	Sample altitude[a] [m]	Position on Swiss map [m][b] [E]	[N]	Drainage area [km^2]	Mean altitude [m]	Mean slope of catchment [%]
LGM or younger moraine samples									
	Saf 1-1	Aare, Gravel Pit "Biedermann"	400 - 1000	430	592000	224000	7868	1158	14
	Saf 1-2	(Replicate of Saf 1-1)	400 - 1000	430	592000	224000	7868	1158	14
	Herens	Borgne	400 - 1000	1100	599000	112000	236	2536	26
	Fin 4	Findeland Glacier	400 - 1000	2500	629500	95000	12	3272	14
	Mela 1 GF	Melezza, Centovalli at Dissimo	125 - 250	625	688430	112050	106	2959	24
Recent glacial sediment samples									
	Fin 1	Findeland Glacier: Shear plane	400 - 1000	2960	629300	95500	4	3174	21
	Fin 2	Findeland Glacier: Glacier mouth	400 - 1000	2550	629200	95300	30	3168	18
	Miné 4-1	Mount Miné Glacier: southern mouth	400 - 1000	1980	609000	100000	49	2959	24
	Miné 4-2	(Replicate of Miné 4-1)	400 - 1000	1980	609000	100000	49	2959	24
	Miné 5	Mount Miné Glacier: northern mouth	400 - 1000	1980	609000	100000	49	2959	24
	Miné 6	Mount Miné Glacier: Lateral moraine	400 - 1000	1980	609000	100000	49	2959	24
	Massa	Massa, Northern Valais	400 - 1000	800	644000	132000	201	2889	22
	Matt	Mattervispa, Southern Valais	400 - 1000	1525	626000	105000	326	2902	24
Maggia sediment samples									
	Mag 1	Maggia, Val di Gei	500 - 800	310	700410	119560	11	1434	30
	Mag 2	Maggia, Val del Salto	500 - 800	332	698040	122860	20	1439	31
	Mag 4	Rovana, Valle di Campo	500 - 800	780	686000	129410	67	1826	30
	Mag 8	Bavona, Val Bavona	500 - 800	443	690430	133390	119	1930	30
	Mag 10	Maggia, Val di Prato	500 - 800	715	695120	138650	31	2011	31
	Mag 11-2	Maggia, Val di Maggia at Riveo	500 - 800	391	691930	128780	452	1818	29
	Mag 11-4	Maggia, Val di Maggia at Moghegno	500 - 800	314	698980	122930	544	1726	29
	Mag 13	Maggia, Lago Bianco & Lago Nero	800 - 1000	1984	684020	145220	10	2522	27
	Mag 16	Maggia, Val Lavizzara & Val di Peccia	500 - 800	740	693880	139810	88	1966	28
	Mag 17	Maggia, Val di Peccia	500 - 800	880	692120	141600	46	1971	28
	Mag 18	Maggia, side valley of Val Lavizzara	500 - 800	1260	694350	145370	7	2138	27

Table 5.1 ▪CONTINUED▪

Sample type	Sample name	Catchment	Grain size fraction [µm]	Sample altitude[a] [m]	Position on Swiss map [m][b] [E]	[N]	Drainage area [km^2]	Mean altitude [m]	Mean slope of catchment [%]
North-South traverse samples									
	Anza	Anza, Valle Anzasca	125 - 250	248	663540	97230	259	1782	31
	Sesia	Sesia, Valle delle Sesia	125 - 250	428	664720	73370	626	1589	29
	Toce a	Toce, Valle Antigorio	250 - 500	346	668720	115200	361	1940	27
	Toce b	Toce, Valle Antigorio	800 - 1000	346	668720	115200	361	1940	27
	Verz a	Verzasca, Valle Verzasca	500 - 800	519	708830	123470	186	1671	30
	Verz b	Verzasca, Valle Verzasca	800 - 1000	519	708830	123470	186	1671	30
	Mela 1	Melezza, Centovalli at Dissimo	125 - 250	625	688430	112050	106	1349	24
	Mela 2	Melezza, Centovalli at Intragna	125 - 250	260	698070	115910	166	1229	24
	Mela 3a	Melezza, Centovalli at Verscio	125 - 250	245	698580	116040	333	1340	27
	Mela 3b	Melezza, Centovalli at Verscio	250 - 500	245	698580	116040	333	1340	27
	Lonza	Lonza, Northern Valais	400 - 1000	1376	627000	138000	99	2551	28
	Gren	Milibach, Southern Valais	400 - 1000	1037	651000	136000	6	1988	29
	Chie	Chietalbach, Chietal	500 - 800	1344	667500	151040	156	2368	24
	Furka	Furkareuss, Furkatal	250 - 1000	1637	681420	160470	29	2486	23
	Tic a	Ticino, Val Bedretto	125 - 250	1254	686130	152720	78	2169	25
	Tic b	Ticino, Val Bedretto	250 - 500	1254	686130	152720	78	2169	25
	Reuss a	Reuss, Reuss- Valley	125 - 250	453	707940	165830	683	2095	28
	Reuss b	Reuss, Reuss- Valley	250 - 500	453	707940	165830	683	2095	28
	Klem a	Kleine Emme, Emmental	125 - 250	470	659500	211480	434	1088	16
	Klem b	Kleine Emme, Emmental	250 - 500	470	659500	211480	434	1088	16
	Buetsch 1	Bütschelbach, Mittelland (ng)	400 - 1000	742	599200	188200	12	885	9
	Buetsch 2	Bütschelbach, Mittelland (ng)	400 - 1000	742	600600	187200	8	885	9
	Emme	Emme, Mittelland	400 - 1000	600	615000	209000	675	981	13
	Wasen 1-1	Liechtguetbach, Mittelland	400 - 1000	775	628000	208000	12	1047	16
	Wasen 1-2	(Replicate of Wasen 1-1)	400 - 1000	775	628000	208000	12	1047	16
	Taf	Tafersbach, Mittelland	400 - 1000	560	589000	191700	25	692	5
	Sense	Sense, Mittelland	400 - 1000	547	591000	186000	162	1292	16

[a]Taken from Carte Nationale de la Suisse

[b]based on Swiss grid coordinate system, reference frame is CH 1903

(ng): Mittelland catchment that was not covered by LGM glaciers

Table 5.2: Additional data on sample and basin characteristics

Sample type	Sample name	Mean temperature[a] [°C]	Mean precipitation[a] [mm/yr]	Glaciation[b] [%]	Landuse[a] Forest [%]	Tundra [%]	Grass [%]	Crops [%]	Lithology
LGM or younger moraine samples									
	Saf 1-1	8	1200	0	-	-	-	-	moraine
	Saf 1-2	8	1200	0	-	-	-	-	moraine
	Herens	1	600	0	-	-	-	-	moraine
	Fin 4	0	2700	0	-	-	-	-	moraine
	Mela 1 GF	12	2000	0	78	1	7	13	cryst.
Recent glacial sediment samples									
	Fin 1	0	2700	75	-	-	-	-	Glacier
	Fin 2	0	2700	75	-	-	-	-	Glacier
	Miné 4-1	2	2000	75	-	-	-	-	Glacier
	Miné 4-2	2	2000	75	-	-	-	-	Glacier
	Miné 5	2	2000	75	-	-	-	-	Glacier
	Miné 6	2	2000	75	-	-	-	-	Glacier
	Massa	1	1800	66	0	27	5	0	cryst., ophiolite
	Matt	2	1800	54	7	20	16	2	cryst.
Maggia sediment samples									
	Mag 1	9	1400	0	60	0	0	40	cryst.
	Mag 2	9	1400	0	81	0	0	19	cryst.
	Mag 4	7	1800	0	58	34	6	2	cryst.
	Mag 8	7	2200	7	29	54	3	6	cryst.
	Mag 10	5	2200	0	37	60	0	2	cryst.
	Mag 11-2	12	2000	1	48	30	7	14	cryst.
	Mag 11-4	12	2000	1	48	30	7	14	cryst.
	Mag 13	0	3000	4	0	95	0	0	cryst.
	Mag 16	5	2200	0	30	51	8	10	cryst.
	Mag 17	5	2600	0	21	63	14	2	cryst.
	Mag 18	2	2600	0	5	94	0	0	cryst.

Table 5.2 ▪CONTINUED▪

Sample type	Sample name	Mean temperature[a] [°C]	Mean precipitation[a] [mm/yr]	Glaciation[b] [%]	Landuse[a] Forest [%]	Tundra [%]	Grass [%]	Crops [%]	Lithology
North-South traverse samples									
	Anza	12	1800	8	24	31	21	15	cryst.
	Sesia	12	1800	6	20	35	17	22	cryst., dolomite, carb.
	Toce a	7	2400	4	22	50	4	19	cryst.
	Toce b	7	2400	4	22	50	4	19	cryst.
	Verz a	12	1800	0	45	44	9	<1	cryst.
	Verz b	12	1800	0	45	44	9	<1	cryst.
	Mela 1	12	2000	0	78	1	7	13	cryst.
	Mela 2	12	2000	0	78	1	7	13	cryst.
	Mela 3a	12	2000	0	78	1	7	13	cryst.
	Mela 3b	12	2000	0	78	1	7	13	cryst.
	Lonza	3	1600	27	37	19	12	3	cryst.
	Gren	2	1100	0	46	52	2	0	schists, ophiolite
	Chie	0	2100	23	31	44	1	0	cryst.
	Furka	0	2400	21	0	77	0	0	cryst.
	Tic a	0	2100	3	6	83	8	0	cryst.
	Tic b	0	2100	3	6	83	8	0	cryst.
	Reuss a	7	2100	12	34	43	3	6	cryst., sandst., shale
	Reuss b	7	2100	12	34	43	3	6	cryst., sandst., shale
	Klem a	10	1200	0	30	0	0	70	sandstone, carb.
	Klem b	10	1200	0	30	0	0	70	sandstone, carb.
	Buetsch 1	5	1600	0	11	0	0	89	sandstone, carb.
	Buetsch 2	5	1600	0	11	0	0	89	sandstone, carb.
	Emme	10	1500	0	38	0	0	62	sandstone, carb.
	Wasen 1-1	9	1600	0	99	0	0	<1	sandstone, carb.
	Wasen 1-2	9	1600	0	99	0	0	<1	sandstone, carb.
	Taf	5	1600	0	9	0	0	91	sandstone, carb.
	Sense	10	1800	0	65	0	9	26	sandstone, carb.

[a]Bundesamt für Umwelt, Schweiz, data can be downloaded from http://www.bwg.admin.ch/service/hydrolog/d/index.htm

[b]Data provided by ESRI (http://arcdata.esri.com/data_downloader/DataDownloader?part=10200)

5.2.2 Recent geodetic uplift pattern

The recent vertical movements of the Central Alps of Switzerland relative to the benchmark at Aarburg have been recorded since 1905 and are displayed in Figure 5.2 [Schlatter *et al.*, 2005]. In the following, we will term these vertical movements "rock uplift rates", because they are measured with respect to an arbitrary benchmark, which is defined as being stable in altitude relative to the area of interest.

In some regions of the Alps, especially in the Central Alps, rock uplift rates exceed 1.0 mm/yr, and decrease to 0.2 mm/yr in the foreland of the Central Alps [Schlatter *et al.*, 2005]. In this study, we have used the dataset from Schlatter *et al.* [2005] throughout. It is generally assumed that the pattern of uplift is the result of deep crustal processes, since the contour lines of the uplift are parallel to the Alpine strike [Schlunegger & Hinderer, 2001], and because the tip of the Adriatic indenter is located beneath the area of maximum rates of uplift [Schmid & Kissling, 2000]. However the mechanism that controls the rate of rock uplift is subject of an intense debate. Gudmundsson [1994] suggested that a transient isostatic rebound reaction of the crust from the removal of the Pleistocene ice sheet could have caused a significant part of the present uplift of the Central Alps [Gudmundsson, 1994]. This view was challenged Persaud & Pfiffner [2004], who argued that the length scale of the recent uplift pattern exceeds that expected from post-glacial rebound when using a standard mantle viscosity. They also noted that the recent pattern of uplift resembles that of apatite fission track age distribution, which would suggest long-term stability of the uplift process at the Myr time scale. These authors suggested a rapid post-melting uplift pulse of ~200 m and proposed that the present uplift is indeed caused by deep crustal processes [Persaud & Pfiffner, 2004].

Recently, Barletta *et al.* [2006] suggested that ~ 0.5 mm/yr of a total uplift rate of 0.8 mm/yr is caused by recent glacier shrinkage while Champagnac *et al.* [2007] attributed a significant fraction (~50%) of the present-day vertical movement to the isostatic response to enhanced erosion during Plio-Quaternary times.

5.2.3 Sample characteristics

5.2.3.1 Prerequisites

a) LGM moraine deposits

We tested the potential bias on catchment-wide denudation rates introduced by the admixing of LGM and Younger Dryas moraine deposits into streams by measuring the concentration of subsurface moraine material (see Figure 5.1 and Table 5.3). We sampled one LGM moraine

from the Swiss Mittelland (samples Saf 1-1 and 1-2), one Younger Dryas moraine in the Central Alps (sample Herens), one moraine from Findelen glacier in the Southern Valais Alps (sample Fin 4), and one glacio-fluvial valley infill of max. LGM age in the Valais Alps (sample Mela 1 GF).

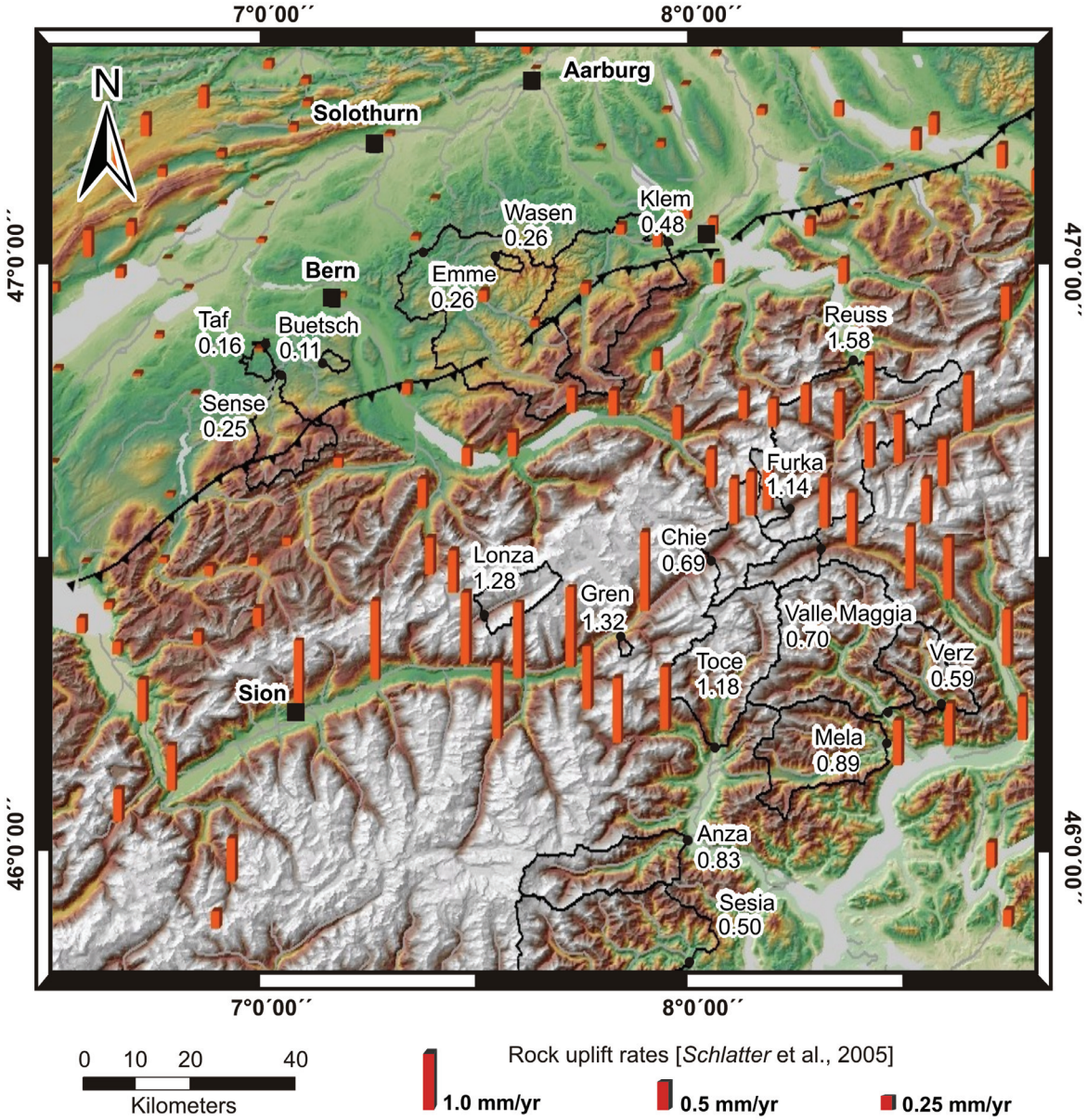

Figure 5.2 Recent vertical movements in the Central Alps of Switzerland. Bar heights give rate of rock uplift (based on Kahle *et al.* [1997] and revised by Schlatter *et al.* [2005]) measured relative to the benchmark at Aarburg. Also shown are locations of catchments sampled for catchment-wide cosmogenic nuclide analysis with abbreviated sample names (see Table 5.1, except Maggia tributaries, moraine samples and glacial sediment samples). Denudation rates are given in mm/yr; for catchments where two or more denudation rates were measured, the mean value is given.

The samples Saf 1-1 and Saf 1-2 are replicate samples from the Aare LGM moraine, Swiss Mittelland, taken in a gravelpit at 20 m depth. The moraine was deposited 18000 ± 3000 yrs

ago during the Late Würmian glaciation (C. Schluechter, personal communication, 2005). The sample Herens was taken from a lateral compression till of YD age inside a gravelpit near the river Borgne (Val d´ Herens, Southern Valais) at a depth of 3 m. Sample Fin 4 was taken from inside a lateral moraine of Findelen Glacier, Monte Rosa/ Dufourspitze, Southern Valais, 5 m below the tip of the moraine. The deposition age is 2000 ± 600 yrs [Roethlisberger & Schneebeli, 1979]. Sample Mela 1 GF was taken from the bottom of a ~45 m thick glacio-fluvial valley infill of LGM or younger age (<18000 yrs) of the Melezza at Dissimo (Centovalli, Southern Alps).

b) Recent glacial erosion products

To assess the nuclide concentrations of recent glacial erosion products, we sampled sediment produced by recent or young glaciers. Sample Fin 2 is sediment directly from the Findelen Glacier outlet snout. The samples Miné 4-1 and 4-2 are separate samples of glacial outwash sediment collected from the southern glacier snout of Mont Miné. Sample Miné 5 also consists of glacially outwashed sediment and was taken from the northern outlet of the glacier. Sample Miné 6 is a sample from a young lateral moraine of Mont Miné Glacier at the eastern side of the valley, its depositional age being approximately ~300 yrs (Little Ice Age). Sample Fin 1 consists of well-rounded quartzite pebbles that were presumably eroded from a quartzite occurrence from the topmost ridge above Findelen Glacier. Furthermore, we sampled the two heavily glaciated catchments, Massa and Matt, of rivers that directly drain the Great Aletsch Glacier (river Massa, 66% glaciated area; see Table 5.2) and the Gorner/ Findelen Glaciers (river Mattervispa, 54% glaciated area) in the Southern Valais Alps.

c) Appropriate catchment sizes for cosmogenic sampling

In the presently non-glaciated Maggia valley we tested whether trunk stream sampling of a U-shaped valley is a feasible strategy, whether cosmogenic denudation rates estimates are in the same order of magnitude as erosion rates from lake fills and river loads (Table 5.4), and whether tributaries of various sizes yield internally consistent denudation rates. We attempted to assign an optimal catchment size for representative denudation rate measurements. The Maggia catchment is comprised of almost one single granitoid gneissic lithology, with minor sequences of ultrabasic rocks and eclogites enclosed, so that lithologic effects on denudation rate estimates are minimized.

5.2.3.2 Characteristics of basins sampled along an Alpine north-south traverse

a) High-Alpine basins

We sampled several trunk streams in the high Central Alps of Switzerland and Northern Italy, e.g. the Reuss and the Rhône rivers. Samples were taken during low flow from the active channel. The spatial extent of modern glaciers in our catchments varies strongly (see Table 5.2), from presently non-glaciated catchments (e.g. the catchment of the Verzasca) to ~30% of glaciation in the catchment of the Lonza (draining the Aletsch Glacier). The bulk lithology of these catchments is relatively uniform; all studied basins within the Central Alps display metamorphosed crystalline lithologies (see Table 5.2). The catchment of the Reuss also comprises Molasse sediments (conglomerates and sandstones) of lower erosional resistance [Schlunegger & Hinderer, 2001]. The Aar and Gotthard Massifs (samples Furka, Chie, and Lonza) contain plutonic rocks such as granites, quartzdiorites, and granodiorites. South of the Aar and Gotthard Massifs, meta-sedimentary sequences comprised of schists and ophiolites crop out along a thin ~10 km stretch (sample Gren).

b) Swiss Mittelland basins

The lithology of the Mittelland catchments consists of Molasse sediment, which contains heterogeneous sedimentary sequences of sandstones, shales, and carbonate conglomerates with low erosional resistance [Schlunegger & Hinderer, 2001]. We particularly targeted areas that were formerly glaciated and others that were not ice-covered during the LGM. The small (<25 km^2) Mittelland catchments of the Tafersbach, the Liechtguetbach (samples Taf and Wasen 1-1 and 1-2, respectively), as well as the bigger (>160 km^2) catchments of the Kleine Emme, the Emme, and the Sense (samples Klem, Emme, and Sense, respectively) have been glaciated during the LGM, whereas the catchment of the Bütschelbach (samples Buetsch 1 and 2) stayed ice-free throughout [Jaeckli, 1970]. This set of data gives a good selection of possible topographic and climatic basin features and allows comparison of the derived denudation rates with paleo-denudation estimates from apatite fission track and recent rock uplift rates. A more detailed analysis of the denudation rates and post-LGM geomorphic evolution of the Mittelland Molasse area is provided by Norton *et al.* [2008].

Table 5.3: Cosmogenic nuclide analytical and denudation rate data

Sample type	Sample name	Sample weight [g]	^{10}Be conc.[a] [x10^4 at/g$_{(Qz)}$]	^{10}Be conc. SLHL norm.[b] [x10^4 at/g$_{(Qz)}$]	Predepositional conc. of buried samples [x10^4 at/g$_{(Qz)}$]	Depth of buried samples [cm]	Total nuclide production rate[c] [at/g$_{(Qz)}$/yr]	Skyline shielding factor	Snow/ ice shielding factor[d]	Denudation rate[e] [mm/yr]	Apparent age[f] [yr]
LGM or younger moraine samples											
	Saf 1-1	76.1	2.64 ± 0.70	1.42 ± 0.43	2.60	2000	10.10	0.99	1.00	0.32 ± 0.09	2560
	Saf 1-2	59.0	2.29 ± 0.26	1.22 ± 0.21	2.25	2000	10.10	0.99	1.00	0.37 ± 0.05	2220
	Herens	23.4	0.79 ± 0.27	0.06 ± 0.12	0.40	300	36.80	0.97	1.00	- -	110
	Fin 4	61.1	2.30 ± 0.41	0.20 ± 0.04	2.29	500	63.00	0.99	1.00	1.87 ± 0.33	360
	Mela 1 GF	52.2	0.13 ± 0.17	0.04 ± 0.06	0.13	-	17.40	0.99	0.97	- -	80
Recent glacial sediment samples											
	Fin 1	18.4	7.78 ± 2.43	0.72 ± 0.23	-	-	59.60	0.96	0.97	0.52 ± 0.16	1320
	Fin 2	27.7	2.32 ± 0.98	0.22 ± 0.09	-	-	59.30	0.97	0.99	1.73 ± 0.74	390
	Miné 4-1	45.1	0.52 ± 0.26	0.06 ± 0.03	-	-	48.70	0.99	0.87	6.44 ± 3.18	110
	Miné 4-2	75.1	1.15 ± 0.37	0.13 ± 0.04	-	-	48.70	0.99	0.87	2.89 ± 0.90	240
	Miné 5	77.3	1.25 ± 0.50	0.14 ± 0.06	-	-	48.70	0.99	0.87	2.68 ± 1.06	260
	Miné 6	40.3	1.90 ± 1.06	0.22 ± 0.12	-	-	48.70	0.99	0.87	1.76 ± 0.98	390
	Massa	55.1	0.76 ± 0.39	0.08 ± 0.04	-	-	52.00	0.99	0.41	4.65 ± 2.34	150
	Matt	57.9	3.01 ± 1.22	0.33 ± 0.13	-	-	49.90	0.97	0.50	1.13 ± 0.46	610
Maggia sediment samples											
	Mag 1	45.7	3.05 ± 0.62	0.94 ± 0.19	-	-	17.90	0.95	0.99	0.41 ± 0.09	1820
	Mag 2	45.7	3.55 ± 0.59	1.04 ± 0.17	-	-	19.00	0.93	0.98	0.36 ± 0.06	2070
	Mag 4	49.3	1.53 ± 0.38	0.33 ± 0.08	-	-	25.90	0.97	0.94	1.12 ± 0.28	650
	Mag 8	46.6	2.10 ± 0.41	0.40 ± 0.08	-	-	28.70	0.92	0.85	0.78 ± 0.15	940
	Mag 10	47.5	2.38 ± 0.41	0.44 ± 0.08	-	-	29.90	0.92	0.92	0.77 ± 0.13	940
	Mag 11-2	41.4	2.10 ± 0.36	0.47 ± 0.08	2.13	300	26.10	0.93	0.91	0.77 ± 0.13	950
	Mag 11-4	52.4	1.93 ± 0.31	0.44 ± 0.07	-	-	24.60	0.93	0.92	0.80 ± 0.13	920
	Mag 13	48.0	3.24 ± 0.54	0.44 ± 0.07	-	-	41.00	0.97	0.79	0.69 ± 0.12	1030
	Mag 16	47.4	1.68 ± 0.43	0.33 ± 0.08	-	-	28.50	0.94	0.91	1.06 ± 0.27	690
	Mag 17	45.6	5.06 ± 0.73	0.98 ± 0.14	-	-	28.60	0.93	0.91	0.35 ± 0.05	2090
	Mag 18	46.1	3.27 ± 0.45	0.57 ± 0.08	-	-	31.80	0.94	0.91	0.60 ± 0.08	1190

Table 5.3 ▪CONTINUED▪

Sample type	Sample name	Sample weight [g]	^{10}Be conc.[a] [x10^4 at/g$_{(Qz)}$]	^{10}Be conc. SLHL norm.[b] [x10^4 at/g$_{(Qz)}$]	Predepositional conc. of buried samples [x10^4 at/g$_{(Qz)}$]	Depth of buried samples [cm]	Total nuclide production rate[c] [at/g$_{(Qz)}$/yr]	Skyline shielding factor	Snow/ ice shielding factor[d]	Denudation rate[e] [mm/yr]	Apparent age[f] [yr]
North-South traverse samples											
	Anza	43.9	1.88 ± 0.58	0.41 ± 0.13	-	-	25.4	0.93	0.88	0.83 ± 0.26	890
	Sesia	37.8	2.90 ± 0.56	0.75 ± 0.14	-	-	21.3	0.94	0.97	0.50 ± 0.09	1490
	Toce a	89.2	1.95 ± 0.33	0.38 ± 0.06	-	-	28.4	0.94	0.89	0.89 ± 0.15	820
	Toce b	62.5	1.19 ± 0.27	0.23 ± 0.05	-	-	28.4	0.94	0.89	1.46 ± 0.33	500
	Verz a	46.4	2.44 ± 0.45	0.59 ± 0.11	-	-	22.9	0.92	0.94	0.60 ± 0.11	1230
	Verz b	38.2	2.47 ± 0.51	0.59 ± 0.12	-	-	22.9	0.92	0.94	0.59 ± 0.12	1250
	Mela 1	60.1	0.96 ± 0.19	0.31 ± 0.06	-	-	17.3	0.97	0.97	1.28 ± 0.26	590
	Mela 2	32.2	1.07 ± 0.40	0.37 ± 0.14	-	-	15.9	0.96	0.95	1.05 ± 0.39	740
	Mela 3a	44.3	1.84 ± 0.44	0.58 ± 0.14	-	-	17.5	0.95	0.97	0.66 ± 0.16	1140
	Mela 3b	45.9	2.19 ± 0.42	0.69 ± 0.13	-	-	17.5	0.95	0.97	0.56 ± 0.10	1400
	Lonza	63.3	1.42 ± 0.35	0.20 ± 0.05	-	-	40.0	0.94	0.65	1.28 ± 0.32	580
	Gren	36.7	1.30 ± 0.42	0.26 ± 0.08	-	-	27.7	0.95	0.90	1.32 ± 0.43	550
	Chie	51.2	2.56 ± 0.62	0.37 ± 0.09	-	-	37.8	0.96	0.65	0.69 ± 0.17	1080
	Furka	61.3	1.68 ± 0.29	0.22 ± 0.04	-	-	41.3	0.97	0.65	1.14 ± 0.20	640
	Tic a	48.4	1.95 ± 0.45	0.33 ± 0.08	-	-	32.7	0.96	0.83	0.97 ± 0.23	740
	Tic b	50.4	2.98 ± 0.57	0.50 ± 0.10	-	-	32.7	0.96	0.83	0.63 ± 0.12	1140
	Reuss a	47.9	1.45 ± 0.43	0.25 ± 0.07	-	-	32.5	0.94	0.84	1.29 ± 0.38	560
	Reuss b	40.8	1.00 ± 0.42	0.17 ± 0.07	-	-	32.5	0.94	0.84	1.87 ± 0.79	390
	Klem a	47.0	2.43 ± 0.48	1.02 ± 0.20	-	-	13.1	0.99	0.98	0.42 ± 0.08	1900
	Klem b	39.6	1.88 ± 0.46	0.79 ± 0.19	-	-	13.1	0.99	0.98	0.54 ± 0.13	1470
	Buetsch 1	57.0	7.00 ± 1.14	3.96 ± 0.64	-	-	9.8	1.00	0.99	0.11 ± 0.02	7260
	Buetsch 2	52.4	8.06 ± 0.89	4.57 ± 0.50	-	-	9.8	1.00	0.99	0.10 ± 0.01	8370
	Emme	59.0	3.54 ± 0.42	1.71 ± 0.20			11.5	0.99	0.99	0.26 ± 0.03	3160
	Wasen 1-1	54.3	3.13 ± 0.75	1.44 ± 0.35	-	-	12.0	0.99	0.99	0.30 ± 0.07	2660
	Wasen 1-2	26.2	3.38 ± 0.59	1.56 ± 0.27	-	-	12.0	0.99	0.99	0.28 ± 0.05	2870
	Taf	74.9	4.32 ± 0.50	2.96 ± 0.34	-	-	8.1	1.0	0.99	0.16 ± 0.02	5400
	Sense	24.5	3.99 ± 0.75	1.52 ± 0.28	-	-	14.5	0.98	0.96	0.25 ± 0.05	3110

[a]Corrected for Blank, with combined analytical and blank error (at/g$_{(Qz)}$)
[b]Calculated with uncorrected mean catchment production rate (see next column) and a SLHL production rate of 5.53 at/g$_{(Qz)}$
[c]Uncorrected production rates
[d]Not applied to old moraine and recent glacial sediment samples
[e]For inter-method comparison: combined errors for AMS measurements, blank subtraction, and a constant error for scaling factor (5%)
[f]Corresponds to the time spent in the uppermost ~60 cm of an eroding rock layer

5.2.4 Lab processing and uncertainty assessment

The bulk samples were sieved into narrow grain size ranges (see Table 5.1) and ~50 g of quartz were separated from the bulk sediment using chemical (selective decomposition with weak HF) and magnetic separation techniques. The separation of ^{10}Be was achieved by using an element separation method described by von Blanckenburg *et al.* [1996] and simplified by von Blanckenburg *et al.* [2004]. ^{10}Be/^{9}Be ratios were measured with Accelerator Mass Spectrometry at PSI /ETH Zurich and corrected as described by Synal *et al.* [1997]. Ca. 300 µg of ^{9}Be from a MERCK© $BeSO_4$ carrier were added to each sample. This carrier was determined to contain a ^{10}Be/^{9}Be ratio of $1.10 \pm 0.66\times10^{-14}$. Samples Mag 11-2, Mag 11-4, Mela 1, Mela 1 GF and Mela 2 were treated with a carrier derived from a phenakite mineral, giving a measured ^{10}Be/^{9}Be ratio of $0.55 \pm 0.28\times10^{-14}$. The blanks were subtracted and their errors propagated into all concentrations. The calculated ^{10}Be concentrations with combined analytical and blank errors are given in Table 5.3. Denudation rate uncertainty estimates include a 5% error on scaling law for inter-method comparison. An additional potential uncertainty of 30% on denudation rates is introduced by grain size effects, shielding effects due to temporally and spatially non-uniform snow distribution, and non-steady state effects after glaciation and for catchments with >10% glaciation (samples Lonza, Chie, Furka, and Reuss). This uncertainty cannot be quantified accurately and is therefore not included in Table 5.3.

5.3 METHODOLOGICAL PRINCIPLES

5.3.1 Spatially-averaged denudation, calculation of production rates and corrections applied

5.3.1.1 Spatially-averaged denudation rates from cosmogenic nuclides in river sediment

Cosmogenic ^{10}Be is mainly produced from ^{16}O within mineral grains by bombardment by secondary cosmic rays [Lal & Peters, 1967]. The ^{10}Be nuclide concentration of minerals is inversely proportional to the denudation rate of the surface [Lal, 1991]:

$$C = \frac{P_0}{\lambda + \frac{\rho\varepsilon}{\Lambda}}\left(1 - \exp^{-\left(\lambda + \frac{\rho\varepsilon}{\Lambda}\right)t}\right) \qquad (5.1)$$

where C is the concentration of in situ-produced cosmogenic ^{10}Be (at/$g_{(Qz)}$), P_0 is the production rate at the Earth's surface scaled for latitude and altitude (at/$g_{(Qz)}$/yr), λ is the ^{10}Be decay constant (1/yr), ρ is the rock density (g/cm^3), ε is the denudation rate (cm/yr), Λ is the mean cosmic ray attenuation length (157 g/cm^2), and t is the time (yr) since the initial exposure to cosmic rays. In the Alps, this would correspond to the melting of LGM glaciers, for example. About 63% of the cosmogenic nuclides are produced within the cosmic ray attenuation length, equal to 60 cm of a rock with a density of 2.7 g/cm^3 [Lal, 1991]. The continuous removal of a rock layer equal to several attenuation lengths by constant denudation leads to a steady state ^{10}Be nuclide concentration in the catchment. In this case, the rate of nuclide production equals the rate of nuclides exported by sediment and the ^{10}Be concentration may be simply expressed as [Lal, 1991]:

$$C = \frac{P_0}{\lambda + \frac{\rho\varepsilon}{\Lambda}} \tag{5.2}$$

At cosmogenic steady state, cosmogenic ^{10}Be in river-borne quartz records a time-integrated spatially-averaged denudation rate, which represents the fluvially-mixed erosion products of all processes within a drainage basin [Bierman & Steig, 1996; Granger *et al.*, 1996]. The denudation rate integrates over the time it takes to remove one attenuation length (e.g. 60 cm of bedrock). This integration time scale is called the "apparent age" and it depends on the denudation rate itself. In the high Alps, typical denudation rates are 1.5-0.5 mm/yr, which correspond to a time scale of ~400-1200 years.

Since cosmogenic nuclides measure the denudation rate of bedrock including both mechanical erosion and chemical weathering, we use the term "denudation" throughout this paper. A tectonic denudation component, however, is not included. Recent reviews of the method can be found in Bierman & Nichols [2004] and von Blanckenburg [2005].

5.3.1.2 Production rates

The cosmogenic nuclide production rates and absorption laws were those of Schaller *et al.* [2002], while scaling for altitude and latitude of our sampling sites was done following Dunai [2000] We did not specifically correct for variations in Earth's magnetic field or an enrichment of quartz during weathering. The influence of a varying geomagnetic field intensity is negligible at latitudes of the Central Alps [Masarik *et al.*, 2001], and we assumed that quartz enrichment [Riebe *et al.*, 2001b] is negligible due to the short weathering intervals.

For our LGM subsurface moraine samples, post-depositional irradiation had to be corrected for, because muons penetrate deep into the subsurface [Brown *et al.*, 1995a]. The depth-dependence of nuclide production by post-depositional irradiation has been calculated using a formalism of Schaller *et al.* [2002]:

$$C_{dep}=\left[\left(P_{Nuc}(0)*\sum_{i=1}^{2}a_i*\exp^{\frac{-z*\rho}{b_i}}\right)+\left(P_{\mu stopped}(0)*\sum_{j=1}^{3}a_j*\exp^{\frac{-z*\rho}{b_j}}\right)+\left(P_{\mu fast}(0)*\sum_{k=1}^{3}a_k*\exp^{\frac{-z*\rho}{b_k}}\right)\right]*\left(\frac{1-e^{-\lambda*t_{dep}}}{\lambda}\right) \quad (5.3)$$

where $P_{Nuc}(0)$, $P_{\mu stopped}(0)$ and $P_{\mu fast}(0)$ (at/$g_{(Qz)}$/yr) are the production rates of cosmogenic nuclides by spallation, stopped and fast muons, respectively. Z (cm) is the depth below surface, t_{dep} (yr) is the time since the deposition of the material, $a_{i,j,k}$ (dimensionless) and $b_{i,j,k}$ (g/cm^2) are coefficients used for the depth scaling of the production rates (coefficient values given in Schaller *et al.* [2002].

5.3.1.3 Corrections for skyline shielding and shielding due to snow and ice

Corrections of the production rates for topographic shielding were necessary because landscapes like the Central Alps feature considerable relief. An object on the surface of a flat, level landform has an unobstructed view of the sky in all directions and therefore will receive maximum incoming radiation [Dunne *et al.*, 1999]. Since this is not the case in landscapes with highly sloped surfaces, the decreased incoming flux of radiation resulting in reduced production rates has to be considered [Dunne *et al.*, 1999]. For this study, we employed an algorithm that calculates the reduction of the intensity of incoming radiation for a DEM pixel inside a catchment using the hypsometry (e.g. the elevation versus area distribution) of each catchment as derived from the SRTM DEM with a grid resolution of 90 m [Heidbreder *et al.*, 1971]:

$$S=1-\frac{1}{360°}\sum_{i=1}^{n}\Delta\phi_i\sin^{m+1}\theta_i \quad (5.4)$$

where S is the shielding factor for a set of n obstructions, each with a corresponding inclination angle θ_i with an extent through an azimuth of the incoming radiation $\Delta\phi_i$, m is an experimentally determined constant for which we used a value of 2.3 [Dunne *et al.*, 1999]. 360° shielding for each pixel is based on 5° steps for the azimuth angle. The resulting mean

skyline correction factor varied between 1 for ridges or valleys of low relief (e.g., no correction) and 0.92 for valleys in steep catchments, which would in this case result in a production rate reduction of 8% (see Table 5.3).

Corrections of the production rates for shielding due to snow and ice were necessary because glaciation and significant snow-cover reduce cosmogenic nuclide production rates in bedrock [Schildgen *et al.*, 2005]. We calculated a combined snow and ice correction factor for each pixel. Snow correction factors are based on mean averages of monthly-resolved snow thicknesses for the years 1983-2002 [Auer, 2003]. For ice correction calculation, we used the present-day glacial extent to calculate a mean correction factor. This was based on the assumption that during the considered time span, glacial advance and recession might have been counterbalancing each other [Hormes *et al.*, 2001]. As will be shown below, we suggest that denudation rates are robust if the area glaciated is <10% of a catchment. Therefore the possible bias introduced by this assumption would add only a minor error. Calculations were carried out using a formalism similar to Lal [1991]:

$$K = \exp^{\frac{-\rho * z}{\Lambda}} \tag{5.5}$$

where K is the correction factor for snow independent of the prevailing total production rate, ρ is the maximum density of 0.3 g/cm^3 for old, compacted snow [Roebber *et al.,* 2003; Ware *et al.*, 2006], z is the snow thickness (cm), which varied for each pixel based on digitized snow depths with a spatial resolution of 1 km from Auer [2003], Λ is the mean cosmic ray attenuation length (157 g/cm^2). The correction was done by multiplying the nucleogenic surface production rate by this factor, while leaving all other coefficients of Schaller *et al.* [2002] constant. This means that we ignored the correction for the reduced muonic production, because the attenuation of both fast and slow muons in snow is negligible. The influence of snow cover on production rates with respect to neutron-backscattering effects at the snow-rock interface [Schildgen *et al.*, 2005] has not been taken into account. However, we suggest that the overall effect on the calculation of denudation rates is negligible. The nucleonic nuclide production rate was set to zero for pixels covered by ice. The area of recent glaciation in Switzerland was digitized from topographic maps and calculated from public domain GIS data (source: ESRI).

In order to evaluate the effect of today's glaciation on cosmogenic nuclide-derived denudation rates, we have measured the ^{10}Be concentration of present-day glacial outwash

(see Section 5.2.3.1). We did not correct the total production rate for these catchments (see Table 5.3) in order to account for the effect of glaciation as a potential perturbation on this material. In Table 5.3, we give the total, uncorrected production rate for each catchment as well as the calculated correction factors on the production rate for snow/ ice and skyline shielding.

Cosmogenic nuclide-derived denudation rates for Maggia sediment samples and traverse samples were calculated based on these correction factors. The correction amounts to 1% for Mittelland samples, 5-10% for southern Central Alps samples, and up to 35% for partially glaciated samples in the highest Central Alps. Given that the latter correction factors are based on the modern glacial extent, denudation rates might be overestimated if the glaciers had a larger extent within the sampling time scale. For all non-glaciated catchments, the error introduced is small.

5.3.2 Assessment of potential perturbations on denudation rate estimates in complex glaciated mountain ranges

5.3.2.1 Approach to cosmogenic steady state after surface zeroing by glaciation

Cosmogenic nuclide-derived denudation rates in the high Alps are potentially biased by former (e.g. LGM) and recent glaciation that result in a cosmogenic non-steady state situation. Therefore an assessment of whether the production and the export of nuclides have reached steady state after a possible complete zeroing of surface concentrations by glacial abrasion and ice shielding is necessary. We have performed numerical modeling of the approach of cosmogenic nuclide inventories to steady state rates following glaciation by assuming zero initial nuclide concentration within the entire rock column. Calculations were carried out by integrating the ^{10}Be nuclide production during small time steps over the attenuation path length while material moves toward the surface by denudation. We simulated three different denudation exposure histories and subsequent denudation at 15 kyr BP of 0.5, 1.0, and 1.5 mm/yr from t = 15 kyr BP until today using equation 5.3. We then calculated the cosmogenic nuclide-derived denudation rate measurable on a surface rock at any time in the past using the production and adsorption terms from Schaller *et al.* [2002], which are based on nucleonic and muonic production, and equation 5.2. Figure 5.3 shows that the cosmogenic nuclide-derived denudation rates approach steady state depending on the prescribed denudation rate, and, although never quite reaching it, are within the typical analytical error of our measured denudation rates. Other workers [Parker & Perg, 2005] have carried out a similar model and

have found that with comparable model parameters, it takes even less time for a landscape to arrive at nuclide steady state after major perturbations. In our opinion, this can be attributed to the fact that Parker & Perg [2005] did not account for muonic production in their model. Production of nuclide from muons leads to much longer timescales with respect to steady state achievement because of their peep penetration depth.

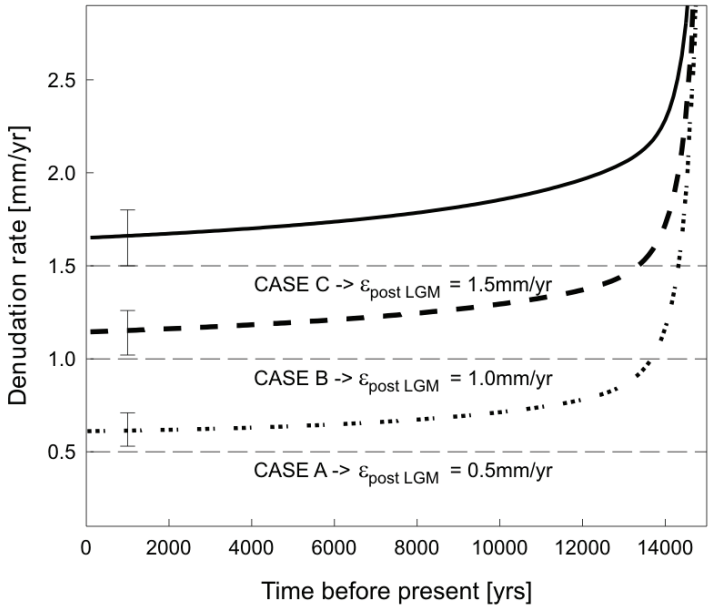

Figure 5.3 Numerical modeling of the approach of cosmogenic nuclides to steady state after zeroing by glaciation at t = 15 kyr BP on the basis of three different denudation histories (0.5, 1.0, and 1.5 mm/yr); also given are typical analytical error bars. The analysis shows that cosmogenic steady state is attained within limits of error for the 1.5 mm/yr and the 1.0 mm/yr case after 15 kyr.

5.3.2.2 Cosmogenic nuclide inventory of incorporated moraine material and recent glacial erosion products

We acknowledge that recently glaciated catchments suffer from non-steady state behavior due to glacial erosion. Therefore, we tested the potential bias introduced by the admixing of denudation products into streams by measuring the concentration of both LGM and recent subsurface moraine material, as well as modern products of glacial erosion, e.g. sediment outwashed from glacier snouts. The results are given in Table 5.3 and Figure 5.4. In order to allow for comparison of results from various altitudes, we scaled the nuclide concentrations to sea level high latitude (SLHL; see Figure 5.4), using a production rate at sea level of 5.53 at/$g_{(Qz)}$/yr [Schaller *et al.*, 2002]. Measured and normalized nuclide concentrations as well as pre-depositional concentrations are also given in Table 5.3. The measured moraines of LGM and younger age reveal a broad range of cosmogenic nuclide concentrations.

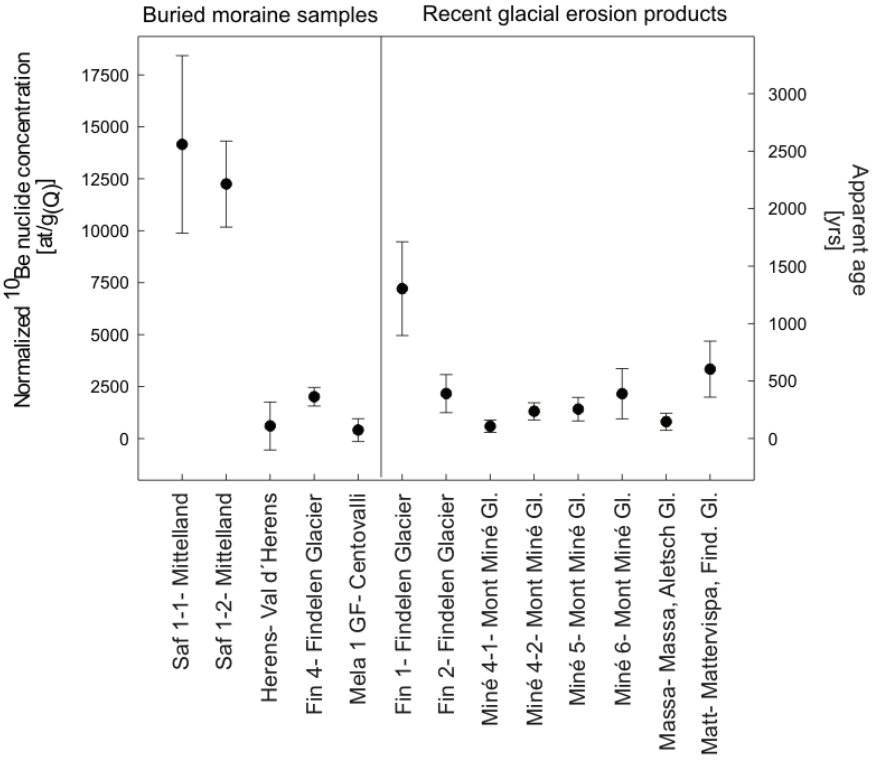

Figure 5.4 Nuclide concentrations of buried moraines and glacial sediments scaled to SLHL (left axis); right axis gives corresponding "apparent age" that would result if sediment were exposed at the surface. For glacial sediment nuclide concentrations, the percentage of glaciated area of each catchment is decreasing from left to right, e.g. from 75% to 55%.

Replicate samples Saf 1-1 and 1-2 (Swiss Mittelland Aare LGM moraine material) give normalized nuclide concentrations at SLHL corrected for post-depositional irradiation that are identical within one sigma error (for nuclide concentrations see Table 5.3). We speculate that the glacial advance led in part to the incorporation of overridden regolith, which comprised periglacial soils in the Molasse basin that would have been irradiated prior to the ice advance. This would explain the comparatively high nuclide concentration that would correspond to an apparent paleo-denudation rate of ~0.3 mm/yr; or an apparent exposure age of ~2200 yrs. As shown in Section 5.4.1, this is similar to today's Mittelland denudation rate. The sample Herens consists of subglacial consolidated clay till, which is assumed to have formed during YD because of denudation of shielded and already heavily abraded or plucked bedrock, so that the inherited nuclide concentration is zero within limits of error. For sample Fin 4 (Findelen glacier, lateral moraine, 2000 ± 600 yrs old), it is assumed that the nuclide concentration we measured is a mixture from several sources, e.g. material from the exposed side valleys of the glacier (with relatively high nuclide concentrations) mixed with that from beneath the glacier (with relatively low concentrations), resulting in a mean nuclide concentration which might as well be representative for sediment mixing processes at glaciers

like the Findelen. The apparent age would be ~350 yrs. The inherited nuclide concentration of sample Mela 1 GF (LGM or younger glacio-fluvial sediment in the upper Centovalli, southern Switzerland) is zero within limits of error. The deposit is assumed to have formed from glacial abrasion of shielded and already heavily abraded bedrock.

Sampling of recent glacial erosion products of the Findelen Glacier (sample Fin 1; well-rounded quartzite pebbles from topmost ridge of glacier) gives a comparatively high nuclide concentration comparable with an apparent denudation rate of ~0.5 mm/yr or an apparent exposure age of 1300 yrs (for nuclide concentrations, see Table 5.3 and Figure 5.4). This is probably caused by the admixture of material from exposed and slowly eroding ridges surrounding the glacier. Sample Fin 2 (outwash from glacier snout) also gives a rather high nuclide concentration corresponding to a denudation rate of 1.7 mm/yr or an apparent age of 390 yrs; the concentration is too high for shielded material and suggests the incorporation of exposed denudation products. Samples Miné 4-1 and 4-2 (replicate samples from southern snout) are two samples from exactly the same location but reveal nuclide concentrations that vary within a factor of two (apparent ages of 110 and 240 yrs, respectively), evidently confirming the heterogeneous nature of glacial erosion processes. Sample Miné 5 (northern snout, 260 yrs) gives similar nuclide concentration as Miné 4-1 and 4-2. Sample Miné 6 (lateral moraine of Mont Miné Glacier, its depositional age being ~300 yrs) gives a somewhat higher nuclide concentration (corresponding to an apparent age of 390 yrs) than other Miné samples. It can only be assumed that during glacial advance during the Little Ice Age, exposed bedrock was abraded and deposited as a moraine. Nuclide concentrations of all Miné glacier samples are very low and apparent ages would be around 200 yrs.

The measured nuclide concentrations and apparent ages of samples Massa (150 yrs) and Matt (610 yrs; River Massa draining the Great Aletsch Glacier and river Mattervispa draining the Gorner/Findelen Glaciers, respectively) are within the same range as those of sediment directly from glacial outlets. This suggests that in all cases sediment from highly glaciated catchments contains previously exposed material that is currently being remobilized and eroded.

These results allow for the following first-order implications. Glacial sediment is subject to a range of exposure histories and no a priori concentration can be predicted. It has been demonstrated for the Mittelland that high-concentration samples of LGM age are compatible with the denudation rates of the respective surrounding non-glaciated areas. This hints at a large fraction of non-glacial erosion products in glacial outflows of alpine warm-based glaciers. Therefore neither the assumption of zero concentration beneath the area

covered by recent glaciers (because glaciers change in size) appears to be valid, nor can glacial input be treated as "normal" steady state denudation products. However, given that the concentration is likely to be close to that representing the local denudation rate, it is safe to assume that partially glaciated catchments can be measured with a minor additional error if the relative glaciated area is small (<10%). Denudation of moraine material can introduce a potential bias, especially if the time elapsed since the cessation of glaciation is short and if the moraine material is removed by fluvial undercutting rather than being eroded continuously from the exposed surface. The observed scatter in cosmogenic nuclide-derived denudation rates could well be due to this. In the Mittelland, however, measured nuclide concentrations are in the range of recent denudation products, which could imply that LGM moraines and other glacial deposits have, in terms of cosmogenic nuclides, become integral parts of the landscape since deglaciation at 15 kyr, and that inheritance merely serves to mitigate a possible deficit introduced into slowly eroding catchments after a transient LGM perturbation.

5.3.2.3 A test of appropriate catchment size

Cosmogenic nuclide-derived denudation rates in the Maggia catchment (without Centovalli) range between 0.35 to 1.12 mm/yr (see Figure 5.5 and Figure 5.6). For catchments with areas <60 km^2 the average denudation rate is 0.53 ± 0.03 mm/yr (n = 6). This corresponds to a scatter of 34%. For catchments with areas >50-60 km^2 denudation rates average at 0.90 ± 0.08 mm/yr (n = 5). This corresponds to a scatter of 19%. This cutoff corresponds to the transition from second-order to third-order streams. The observed variations in denudation rate cannot be attributed to differences in lithology, since the Maggia valley is a catchment of relatively uniform lithology, featuring crystalline rocks only. Infrequent landslides or rock falls within the Maggia catchment might possibly account for the more or less irregular distribution of denudation rates in the tributaries of the Maggia. Tributaries favoring large mass wasting events would experience higher denudation rates than those where no landslides occur, due to the incorporation of less irradiated material from greater depths. At small catchment scales, there is a small likelihood of experiencing landslides, but as the catchment area increases, landslide events are adequately represented. We can compare this finding to the modeling results of Niemi *et al.* [2005], who suggested that the spread of denudation rate data drops significantly once an appropriate spatial threshold is exceeded.

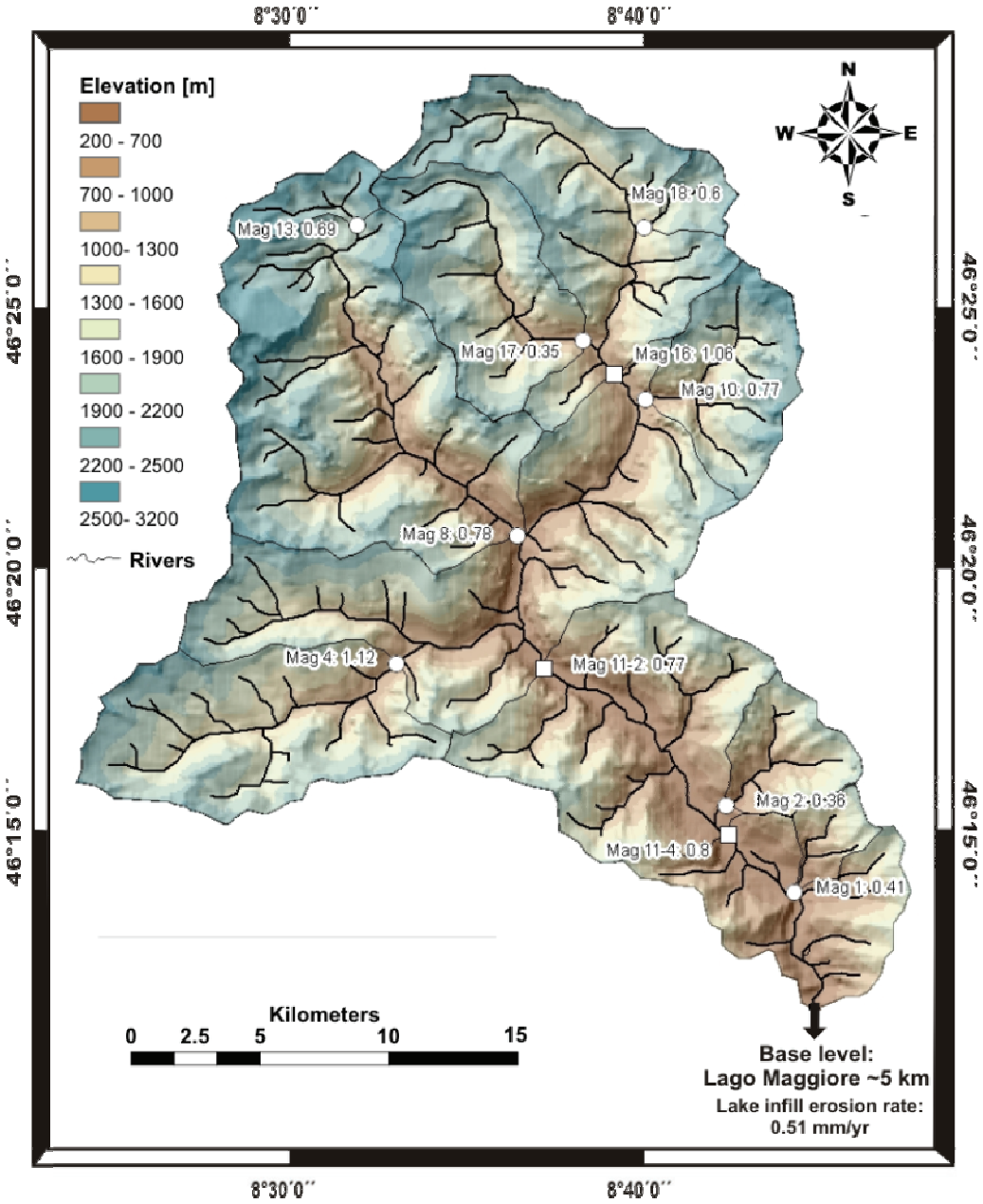

Figure 5.5 Catchment of the Maggia derived from a 90 m SRTM grid. Shown are sampling locations and corresponding cosmogenic nuclide-derived denudation rates in mm/yr. Squares indicate trunk stream samples, and circles indicate tributary samples. A mechanical denudation rate calculated from the infill of Lago Maggiore is 0.51 mm/yr since the LGM [Hinderer, 2001].

For denudation rates typical of the Maggia area, Niemi *et al.* [2005] predicted 100-200 km^2 to be representative catchments. This is similar to our observation. Our results suggest that differences in denudation of tributaries may indeed be influenced by the catchment size, and that sampling for cosmogenic-nuclide analysis should preferentially be made on a larger scale if an influence by mass wasting cannot be quantified.

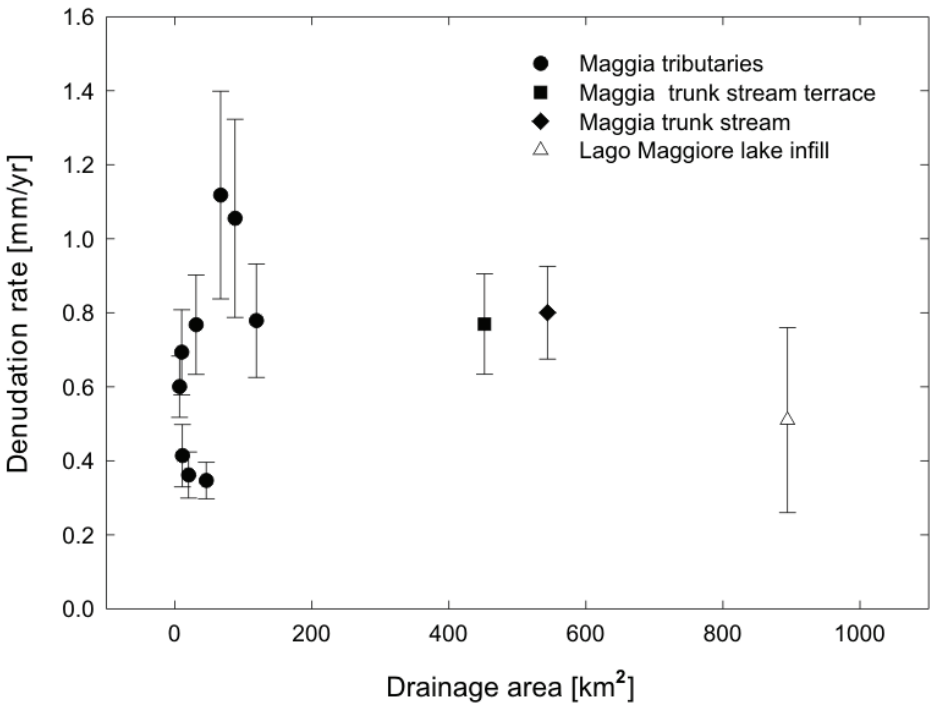

Figure 5.6 Cosmogenic nuclide-derived denudation rate (mm/yr) versus drainage area (km^2) in the Maggia valley, southern Switzerland. Also plotted are the denudation rate for the Holocene terrace deposit (Mag 11-2) and the mechanical denudation rate for the Lago Maggiore derived from lake infill rates (taken from Hinderer [2001]).

To account for the reworking of Quaternary sediments in the Maggia main valley which possibly yield different nuclide concentrations, we analyzed a sample from a river terrace in the main trunk stream of the Maggia at Riveo (Mag 11-2). This sample was amalgamated from a depth of ~1 m to ~3 m below the surface of the terrace and is thus representative of the material presently admixed into the trunk stream of the Maggia from fluvial deposits. The calculated denudation rate is 0.77 ± 0.14 mm/yr. This result is identical within one σ error with the denudation rate acquired from the fluvial sediment denudation rate of the trunk stream at Moghegno (Mag 11-4), which is 0.80 ± 0.13 mm/yr. Within error this is identical to the average of all tributaries, which is 0.73 ± 0.14 mm/yr. These rates are also similar to denudation rates of 0.51 mm/yr integrated since LGM for lake fills in Lago Maggiore (see Table 5.4 and Figure 5.6; Hinderer [2001]). This adds confidence to the robustness of our approach.

We conclude that the sampling of large, formerly glaciated valleys is a feasible approach and that in this environment, a catchment size in excess of 50 to 60 km^2 yields representative rates. We therefore applied this strategy to a north-south traverse of large catchments.

Table 5.4: Denudation rate data from lake infills, river loads, and delta growth

				Since LGM	Modern	
				LAKE FILLS	RIVER LOAD	DELTA GROWTH
River	Location of gauging station	Lake	Drainage area of river[a] [km^2]	Mechanical denudation rate[a] [mm/yr]	Total denudation rate[b] [mm/yr]	Total denudation rate[a,b] [mm/yr]
Aare	Brienzwiler	Brienzersee	554	0.38	0.11	0.19
Kander	Hondrich	Thunersee	1120	-	0.36	-
Linth	-	Zürichsee		0.73	-	-
Linth	Mollis	Walensee	530	-	0.09	0.16
Lütschine	Gsteig	Brienersee	380	0.82	0.20	0.06
Melchaa	-	Sarnersee	72	0.37	-	-
Reuss	Seedorf	Urnersee	832	0.56	0.03	-
Seez	-	Walensee	269	0.96	-	-
Rhone	Porte du Scex	Lac Léman	5520	0.95	0.15	-
Adda	Tirano	Lago di Como	906	0.85	0.10	-
Cassarate	-	Lago di Lugano	73	-	-	0.16
Maggia	Locarno	Lago Maggiore	926	0.51	0.22	0.18
Ticino & Verzasca	Bellinzona	Lago Maggiore	1515	0.79	0.13	0.11
Dora Baltea River[c]	Dora Baltea	-	3264	-	0.12	-

[a]From Hinderer [2001]

[b]Recalculated from Hinderer [2001] using a density of 2.5 g/cm^3

[c]From Vezolli [2004]

5.4 DENUDATION RATE RESULTS AND BASIN CHARACTERISTICS

5.4.1 Denudation rates for the north-south traverse

In the high crystalline Alps, mean denudation rates are 0.9 ± 0.3 mm/yr, where integration times are 0.5-1.5 kyr, and to 0.27 ± 0.14 mm/yr for the Alpine foreland, where integration times are 1.9-8.4 kyr. We begin with samples from southern Central Alps, followed by Valais and Central Alps samples and we will finish this section with presenting samples from the Swiss Mittelland. Samples "a" and "b" denote two different grain sizes of the same sample, "a" being the finer fraction. For nuclide concentrations see Table 5.3.

The two southernmost samples are from the river Anza close to the Toce confluence, Valle Anzasca, Italy, and sample Sesia from the river Sesia at Varallo, Valle delle Sesia, Italy, respectively. Denudation rates are 0.83 ± 0.26 and 0.50 ± 0.09 mm/yr, respectively. These two basins have many common characteristics, such as comparable mean altitudes, slopes, land use, climate, and rock uplift rate (see Tables 5.1 and 5.2), but with the southern slopes of Monte Rosa the Anza catchment contains a slightly larger fraction of glaciated landscape. In the catchment of the Maggia, we measured the trunk stream of the Maggia at Moghegno (sample Mag 11-4). This sample gives a denudation rate of 0.80 ± 0.13 mm/yr. The trunk stream denudation rate agrees well with Maggia subcatchments larger than 60 km^2 (see Figure 5.5 and Section 5.3.2.3). Furthermore, we measured sediment from the southern Central Alpine Toce and Verzasca (upstream of the Verzasca dam) catchments (samples Toce a and b, Verz a and b). The samples give the following denudation rates: Toce a 0.89 ± 0.15 mm/yr; Toce b 1.46 ± 0.33 mm/yr; Verz a 0.60 ± 0.11 mm/yr and Verz b 0.59 ± 0.12 mm/yr. These rates are all similar to those obtained in the neighboring Maggia valley.

In the southern Central Alps, the catchment of the Melezza (Centovalli) was sampled in some detail (samples Mela 1, Mela 2, Mela 3a, and Mela 3b, respectively.) The "Mela" samples are all from the Centovalli, but are taken at different points within the valley. Mela 1 was taken ~11 km upstream of the Isorno-Melezza confluence at Dissimo, sample Mela 2 was taken at Intragna upstream of the Isorno-Melezza confluence, and samples Mela 3 a and b were taken ~1.5 km downstream of the confluence at Verscio, including Valle Onsernone, a small side valley of Centovalli (see Figure 5.1). The Centovalli samples give the following denudation rates: Mela 1 1.28 ± 0.26 mm/yr; Mela 2 1.05 ± 0.39 mm/yr; Mela 3a 0.66 ± 0.16 mm/yr; Mela 3b 0.56 ± 0.10 mm/yr. Field investigation showed that the upper part of the Centovalli near Dissimo is covered with thick late-Quaternary glacio-fluvial deposits, which yielded zero nuclide concentration when measured (see Section 5.3.2.2).

Incorporation of these deposits by fluvial undercutting potentially explains the high denudation rates obtained for samples Mela 1 and Mela 2. Denudation rates decrease with increasing distance to late-glacial deposits. As the influence of these sediments decreases downstream, nuclide concentrations are increasingly dominated by "normal" hillslope denudation products. These appear to dominate denudation rates at the Isorno-Melezza confluence. Since the Isorno catchment (Valle Onsernone) was not sampled separately, the mixing proportions beneath the confluence cannot be assessed. Field inspections showed no evidence of glacio-fluvial material in the Isorno tributary; thus, it can be assumed that this tributary introduces sediment with nuclide concentrations representative of the current hillslope erosion processes. All measured denudation rates of the Centovalli are within the same range as the Maggia samples (see Section 5.3.2.3). This indicates that the entrained nearly zero-concentration material represents only a small fraction of the total sediment flux.

In the Northern Valais, we sampled the valley of the river Lonza (Lötschental, sample Lonza). We also sampled the Milibach River, which is a tributary of the Rhône River south-east of Grengiols (sample Gren). Denudation rates are 1.28 ± 0.32 and 1.32 ± 0.43 mm/yr, respectively. The Lonza valley is presently glaciated to a considerable extent (27%), the catchment of the Milibach on the other hand is presently non-glaciated, but features to some extent more readily erodible rocks. In the Central Alps, tributaries to the Rhône and Reuss rivers (samples Chie and Furka, respectively) and the trunk stream of the upper Ticino (sample Tic) were sampled. Chie and Furka yield denudation rates of 0.69 ± 0.17 and 1.14 ± 0.20 mm/yr, respectively. The samples Tic a and Tic b yield denudation rates of 0.97 ± 0.23 and 0.63 ± 0.12 mm/yr, respectively. Samples Reuss a and b are taken from the main stream of the Reuss River, immediately upstream of the Vierwaldstättersee (Lake Lucerne) at Seedorf. Calculated denudation rates are 1.29 ± 0.38 and 1.87 ± 0.79 mm/yr, respectively, and range among the highest measured in the Central Alps. A bias in denudation rate estimates due to glaciation cannot be ruled out for the high Alpine catchments Chie, Furka, Lonza, and Reuss given their large areas currently glaciated (see Table 5.2, 23%, 21%, 27%, and 12% glaciated areas, respectively). However the estimates are identical within error to non-glaciated catchments of otherwise similar basin characteristics like Tic and Gren.

Catchments from the Swiss Mittelland are all comprised of Molasse sediments (sandstones, shales, and conglomerates). Samples from small streams (<25 km^2) from formerly unglaciated catchments are Bütsch 1 and 2 (river Bütschelbach), and from small catchments that were glaciated in LGM are Wasen 1-1 and 1-2 (river Liechtguetbach) and Taf (river Tafersbach). In these catchments of reduced relief, rock falls and land slides are rare.

Hence sampling of these catchments despite their small areas is legitimate. The cosmogenic nuclide-derived denudation rates are: 0.11 ± 0.02 and 0.1 ± 0.01 mm/yr for Bütsch 1 and 2; 0.30 ± 0.07 and 0.28 ± 0.05 mm/yr for Wasen 1-1 and 1-2; and 0.16 ± 0.02 mm/yr for Taf. We see no dependence between nuclide concentration (see Table 5.3) and LGM ice cover. Samples from larger streams (>160 km^2) are Klem a and b (river Kleine Emme), Emme (river Emme), and Sense (river Sense). These three catchments were presumably partly glaciated in the LGM. The respective denudation rates are: 0.42 ± 0.08 and 0.54 ± 0.13 mm/yr for Klem a and b; 0.26 ± 0.03 mm/yr for Emme; and 0.25 ± 0.05 mm/yr for Sense. A detailed geomorphic analysis of formerly nonglaciated valleys of the Napf area of the Mittelland has recently been performed by Norton *et al.* [2008]. There, cosmogenic nuclide-derived denudation rates are between 0.35 and 0.54 mm/yr, where the faster rates are shown to be due to a transient, climate-related perturbation of the landscape.

5.4.2 Assessment of grain size effects

Nuclide concentrations from different quartz grain size fractions gave identical results within error limits for the samples Reuss, Verzasca, Mela 3, and Klem (Table 5.1). For the catchments of the Toce the larger fraction ("b", 800-1000 µm) yields a higher denudation rate (1.46 ± 0.33 mm/yr) than the smaller fraction ("a", 250-500 µm, 0.89 ± 0.15 mm/yr). This basin is very similar to that of the Verzasca, where both grain size fractions yield identical but lower denudation rates (~0.6 mm/yr). In another Central Alpine catchment, the Ticino, the smaller fraction ("a", 125-250 µm) yields a higher denudation rate at 0.97 ± 0.23 mm/yr than fraction "b" (250-500 µm with 0.63 ± 0.12 mm/yr). It is difficult to attribute these discrepancies to certain basin characteristics, since overall catchments are similar. However, the percentage of area glaciated, the exact hillslope distribution, local gradients in precipitation and runoff, the distribution and frequency of rock falls all differ slightly between catchments and could, potentially, introduce differences in nuclide concentrations between grain size fractions.

5.5 DISCUSSION

5.5.1 Comparison with denudation rates from lake fills, river gauging, and fission track data

We can now compare our catchment-wide cosmogenic nuclide-derived denudation rates (time scale 400-8400 yrs) with the rich data base of other denudational monitors that operate over entirely different time scales. These are lake fills (time scale 10^4 yr), river load gauging and delta growth (10-100 yrs), and fission track data (10^6 yr; see Figure 5.7).

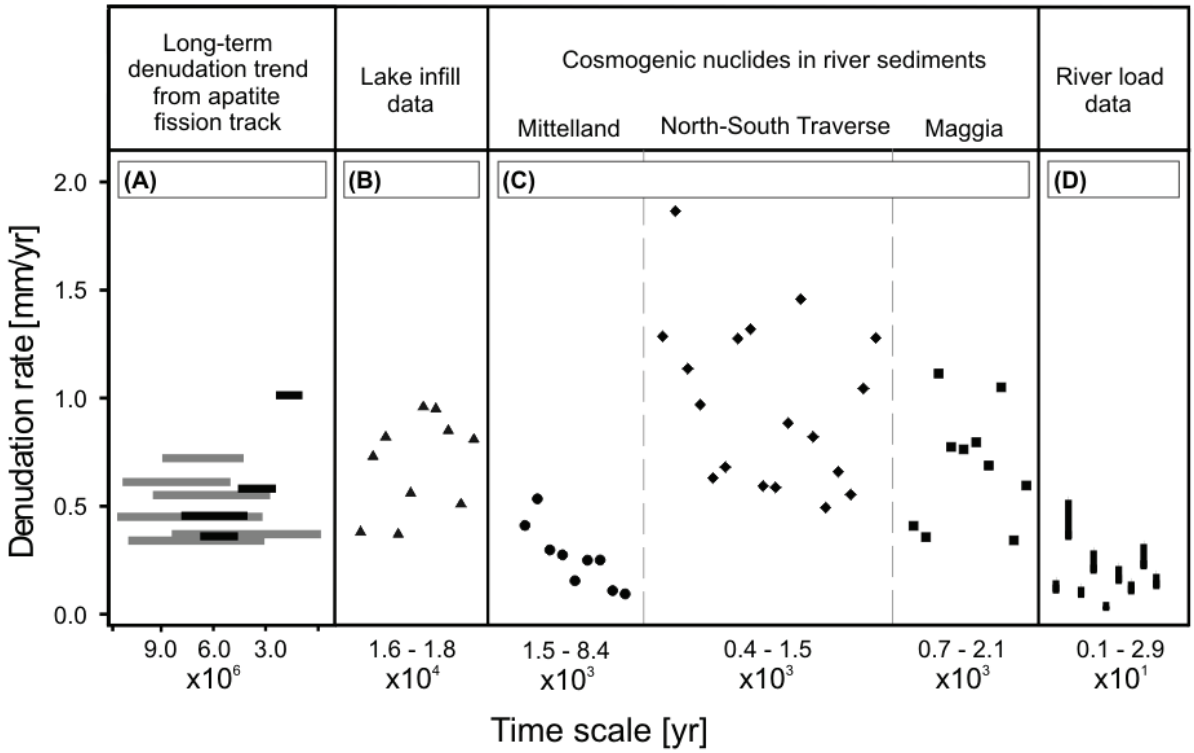

Figure 5.7 Denudation rate estimates from different methods plotted against their corresponding integration time scale (yr); in the case of cosmogenic nuclide-derived denudation rates, this time scale corresponds to the apparent age. (A) Long-term denudation rate trends from apatite fission track data (black from Wagner *et al.* [1977]; grey from Rahn [2001] and Rahn [2005]) plotted against apatite ages. Data from Wagner *et al.* [1977] have been recalculated to mean denudation rate values for each interval as explained in Section 5.5.1. (B) Mechanical denudation rates from lake infill rates [Hinderer, 2001]. (C) Summary of all measured cosmogenic nuclide-derived denudation rates from alluvial sediment samples, including Maggia tributaries. (D) Total denudation rates calculated from sedimentary river loads using a density of 2.5 g/cm^3 (from Hinderer [2001]), with positive error bars for a methodological error of 50%, because the chemical component of total denudation is not available for all samples. The chemical component is estimated to amount to ~50% on the basis of a compilation from the entire Alps (M. Hinderer, personal communication, 2006).

Cosmogenic nuclide-derived denudation rates record both physical erosion and chemical weathering products, whereas lake infill rates only record physical erosion, thereby representing minimum estimates. In the Alps, lake fills integrate over an accumulation period since LGM and range between 0.5 and 1 mm/yr for the high Alps (Table 5.4 and Figure 5.7). In view of the potential errors affecting both methods, an agreement to 30% between lake fill-derived rates and our cosmogenic nuclide-derived rates is excellent. Error estimates on lake infill rates by Hinderer [2001] include a stratigraphic error of ≤10% for Western Alpine valleys; for the Southern Alps, this error might be as high as 50%. Adding an additional chemical component to lake fills would increase those rates and hence improve the agreement between methods. Other possibly introduced sources of error are: (i) the conversion of sediment volumes into erosion rates because of the determination of bulk densities; (ii) the possible variation of glacial versus fluvial denudation with respect to our integration time scale. Despite these uncertainties, the agreement within 30% between post-LGM rates and cosmogenic rates might suggest that our new rates have been within this range since 15 kyr.

Delta growth rates record erosion rates and integrate over at the most the last one hundred years. Delta growth rates are in general lower than cosmogenic nuclide-derived rates (Table 5.4); the reason for this discrepancy lies in integration time scale differences or is due to the absence of chemical weathering rates in delta growth rates.

A similar picture arises from denudation rates from modern river loads based on suspended and dissolved loads, which vary between 0.03 and 0.36 mm/yr [Hinderer, 2001]. Cosmogenic nuclide-derived denudation rates are consistently higher by a factor of 5-10 (Figure 5.7). This is a phenomenon that has been reported from non-orogenic settings [Kirchner *et al.,* 2001; Schaller *et al.*, 2001]. One possible explanation for this discrepancy is found in the systematic underestimation of denudation rates from sediment yield data [Schaller *et al.*, 2001], resulting from the short-term integration time scale of modern denudation rates, that does not record sediment discharged during rare flood events or temporarily stored on flood plains [Summerfield, 1991; Summerfield & Hulton, 1994; Kirchner *et al.,* 2001]. A second source of uncertainty of modern denudation rate estimates from river loads can be found in the contribution of bedload transport to the mechanical denudation rate. Cosmogenic nuclide-derived denudation rates on the other hand reflect long-term average rates of denudation that are independent of the present-day sediment [Brown *et al.,* 1995b; Granger *et al.*, 1996; Brown *et al.*, 1998].

The large discrepancy between modern and cosmogenic nuclide-derived denudation rates could also result from the overestimation of cosmogenic denudation rates with respect to modern rates of denudation. An overestimation could be caused by spatially non-uniform denudation due to linear dissection of a landscape. These types of sediment supply processes (see details on the effects Schaller *et al.* [2001]; von Blanckenburg *et al.* [2004]) lead to preferential erosion of material having lower nuclide concentrations, resulting in higher denudation rates. For example, it has been suggested that within the Swiss Mittelland only 30% of the landscape is actively eroding by relief-forming fluvial dissection, whereas the remaining sections are maintaining their glacially-sculpted morphology [Schlunegger & Hinderer, 2003]. It is also possible that parts of the landscape are not in cosmogenic steady state after being zeroed by glacial erosion in LGM (see Section 5.3.2.1). This would result in a deficit in nuclide concentrations and hence in an overestimate of erosion rates. However, this effect would be most profound in areas of low denudation rate (Figure 5.3). Therefore, we suggest that this process is less suited to explain our high cosmogenic denudation rates, which provide the largest difference to river load-based estimates.

Finally, a possible factor influencing cosmogenic denudation rates might result from anthropogenic perturbations. Settlements in the Alps became more frequent at the beginning of Mesolithic Age (~10 kyr ago), when woodland was being cleared to gain arable land. At the end of the early medieval times, this resulted in a depression of the forest boundary up to 300 m which was furthermore enhanced by climatic regressions [Furrer *et al.*, 1987]. Because of this long-term history of human settlement in the Alps, human activity could even have affected our long-term cosmogenic denudation rates. Recent anthropogenic disturbances include winter skiing, tourism, and road and tunnel construction. They should not have an effect on cosmogenic nuclide-derived denudation rates because of their long integration time scale [von Blanckenburg, 2005], but they might affect modern river loads. This also applies to the construction of dams in the high Alps, retaining a major part of the sediment in reservoir lakes. In any case the geomorphic activity of humans is less likely to affect denudation rates from cosmogenic nuclides, but other than dam construction, human activity would certainly increase modern river loads, resulting in an improved agreement between the two methods.

Long-term denudation rate trends have been derived from apatite fission track cooling ages from vertical sections [Wagner *et al.*, 1977; Rahn, 2001; Rahn, 2005]. We used this data set rather then spatially distributed apatite dates [e.g. Rahn & Grasemann, 1999], because Wagner *et al.* [1977] and Rahn [2001; 2005] have taken vertical age sections from which paleo-denudation rates can be calculated without assumptions on geothermal gradients. However, it has to be acknowledged that age-elevation data from high relief areas such as the Alps may provide overestimates of exhumation rates because of the topographic effect on age-elevation patterns [Stuewe *et al.*, 1994; Braun, 2002]. The long-term denudation rates from apatite ages are within the same order of magnitude as our cosmogenic nuclide-derived denudation rates (see Figure 5.7), but those measured for the period up to ca. 5 Myr ago are roughly half of the cosmogenic nuclide-based estimates. For the Gotthard Massif, uniform denudation rates of 0.6 mm/yr for the last 10 Myr were determined. In the Ticino area, denudation rates within the period of 8-5 Myr ago have been constant at 0.4-0.3 mm/yr. In the Monte Rosa region, an increase in denudation rates from 0.3 mm/yr at 6 Myr to 0.7 mm/yr at 3 Myr was recorded. In the Simplon-Antigorio area, a major increase in denudation from 0.5 to 0.9 mm/yr at ~2.8 Myr took place, which was followed by a slight increase to 1.1 mm/yr ca. 1.6 Myr ago [Wagner *et al.*, 1977]. Rahn [2001; 2005] has measured several traverses normal to the WSW-ENE Alpine strike, using mainly river valleys as natural incisions into the Alpine edifice. In the Rhône valley, a denudation rate of 0.6 mm/yr for a period from 9.5 to 3.3 Myr ago was determined. Denudation rates along the Reuss valley in the Gotthard region were in the range of 0.5 mm/yr 11.5-3.7 Myr ago. In the region of the Aar massif, a slightly higher denudation rate of 0.6 mm/yr for the period 11.1-5.4 Myr was recorded. A traverse along the Rhine valley (Vättis window) for the period 8.5 Myr to today gives a mean denudation rate of 0.4 mm/yr. Additional data along the upper Rhine valley (Glarus) yields a denudation rate of 0.7 mm/yr for a period from 9 to 4.7 Myr BP [Rahn, 2001]. Data from the Adula nappe indicate a long-term denudation rate of 0.35 mm/yr within the period from 10.8-3.6 Myr [Rahn, 2005].

Paleo-denudation rates from careful sediment budgets of the entire Western and Swiss Alps by Kuhlemann *et al.* [2002] have reported denudation rates from 9-6 Myr of half the magnitude to those prevailing from 5 Myr to today. Therefore, the evidence from cosmogenic nuclides and apatite fission track data appears to suggest that the modern denudation rates are a long-term feature that has been prevailing for the last few Myr, but that rates have roughly doubled in the last 5 Myr.

5.5.2 Constraints on factors controlling denudation rates

A close inspection of Figure 5.2 appears to suggest that the spatial patterns of uplift correlate with spatial patterns of denudation. In Figure 5.8 we present a more detailed analysis of the correlation between topographic parameters with denudation rate. At first sight, correlations appear to exist between mean relief, mean altitude, mean slope, and mean recent uplift rate on the one hand and spatially averaged denudation rate on the other hand. Correlation coefficients are all >0.7 (Figure 5.8). The geographic trend shown in Figure 5.9 seems to suggest that denudation rates are highest where mean altitude, rock uplift rate, and crustal thickness are greatest. These maxima are all focused around the centre of the orogen. A more detailed look however reveals that our data are also compatible with a representation in terms of two distinct sample groups: Mittelland catchments have low denudation rates (0.1-0.5 mm/yr) and also low relief, low mean altitude, low hillslope gradients, and low recent uplift rate, while the high Alps catchments are characterized by high denudation rates (0.5-1.3 mm/yr; omitting sample Reuss because of its high analytical error), and also high relief, high mean altitude, high hillslope gradients, and high recent uplift rate. Interestingly, the Mittelland samples show good correlations with these four topographic parameters. Correlation coefficients are between 0.6 and 0.8. We interpret the morphology of the Mittelland in terms of a landscape that is actively adjusting to recent change. Such change can be an external forcing such as tectonic change, or major climate change. For example, the adjustment of the landscape after having been overridden by the large relief-sculpting LGM glaciers might represent such a transient situation, or, alternatively, changes in uplift rate relative to a local base level. As a result, the landscape reacts with high sensitivity to parameters that might ultimately result in high spatial denudation. Governing factors such as drainage network reorganization have been documented by Schlunegger & Hinderer [2001]. The situation of the high Alps is different. Neither mean relief, nor altitude, nor hillslope appears to correlate with denudation rates. A weak correlation is visible between recent uplift rate and denudation rate ($r = 0.51$). One possibility for the absence of such correlations has been pointed out by Montgomery & Brandon [2002]. In catchments of high denudation rates rivers incise at a rate that is so high that hillslopes react with mass wasting. In this case the relief or slopes are limited to a certain threshold value that is governed by the rock strength. Consequently, the denudation rate is independent of these parameters. Based on our data for the high Central Alps, this threshold relief is possibly reached at ~800 m, while the threshold slope is ~ 22% (see Figure 5.8).

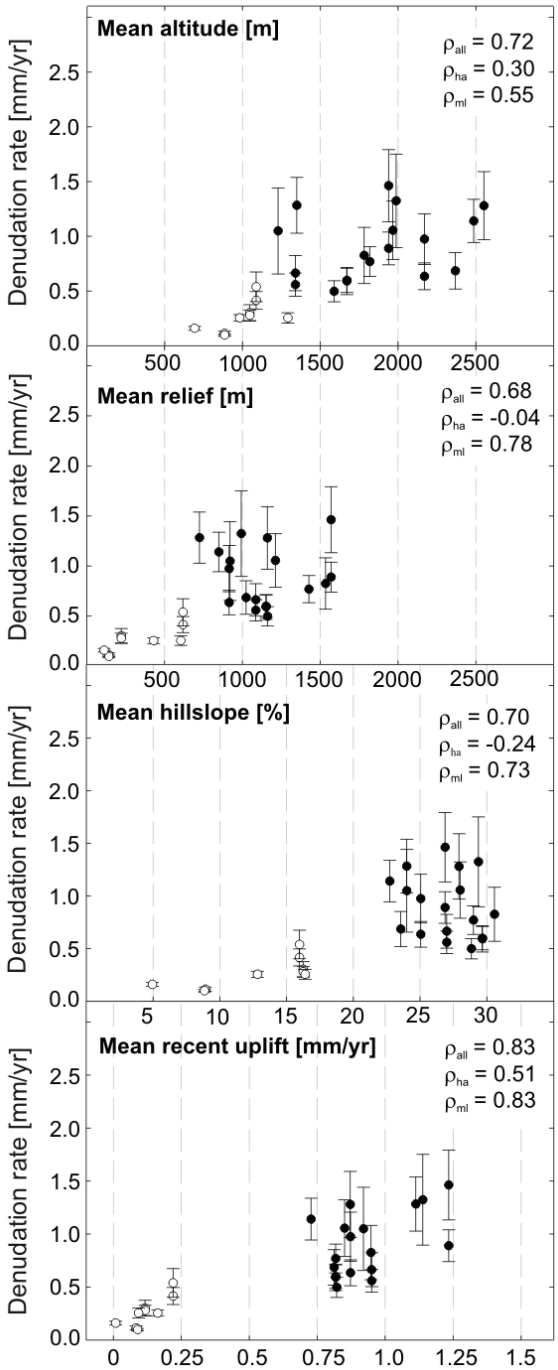

Figure 5.8 Comparison of (a) catchment-wide mean altitudes, (b) mean relief (calculated as mean altitude minus minimum altitude), (c) mean slope, and (d) recent rock uplift rates [Schlatter *et al.* 2005], with cosmogenic nuclide-derived denudation rates (mm/yr) from Mittelland and high Alps alluvial sediment samples (Maggia trunk stream rates only). Open symbols are Mittelland samples, and solid symbols are high Alps samples. Also indicated are correlation coefficients ρ_{all} for all samples, ρ_{ha} for high-alpine samples only, and ρ_{ml} for Mittelland samples only. The error on scaling factor is not included for inter-sample comparison. Sample Reuss was omitted due to its large error.

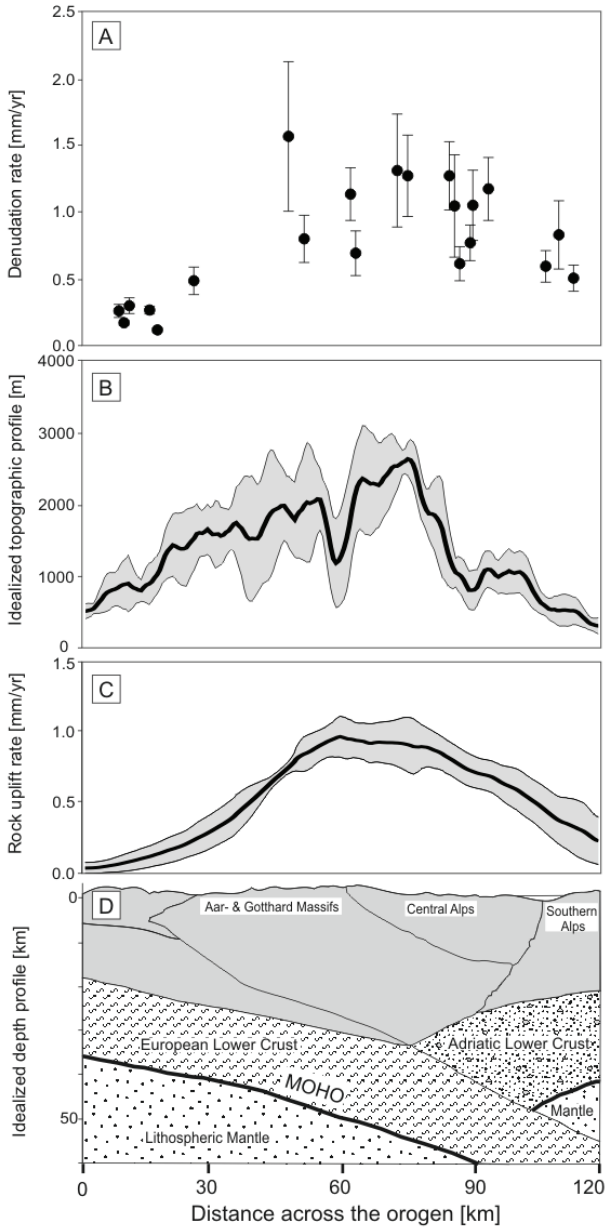

Figure 5.9 (a) Denudation rates measured with cosmogenic nuclides (Maggia: trunk stream rate only). (b) Idealized topographic profile projected from several Alps-perpendicular profiles into a single plane. Range envelope is denoted as a swath with the width of the standard deviation of topography. (c) Idealized recent rock uplift pattern with range envelope also denoted as a standard deviation-wide swath (after Schlatter *et al.* [2005]). (d) Idealized orogenic depth profile (simplified after Schmid & Kissling [2000]; Schmid *et al.* [2004]). All plots are plotted versus distance across the orogen (km). For catchments where two denudation rates were measured, a mean value was calculated.

5.5.3 Are denudation and rock uplift rates in equilibrium?

Least squares regression [Ludwig, 1994] of our cosmogenic nuclide-derived denudation rates for the high Alps against the uplift data from Schlatter *et al.* [2005] yields a slope of 1.0 ± 0.25, where the uncertainty represents the 95% confidence limits on the best fit line with an intercept at the origin at 0 ± 0.2. We omit sample Reuss due to its high error (see Figure 5.8). Several scenarios are conceivable that might generate the agreement between denudation rates and rock uplift rates.

At tectonic steady state, rock uplift equals denudation. It has been argued by Whipple [2001], that this form of equilibrium can prevail even if the long-term steady state has been perturbed, as it is likely in the Alps because of late Quaternary climate change represented by the deglaciation at 15-10 kyr. When a small change in convergence rate or erosional efficiency (e.g. a climate change) introduces a perturbation, both rock uplift and denudation are perturbed. However, with a small lag time that depends on the nature of the change, they will agree with each other despite being in the transient phase of readjustment [Whipple & Meade, 2006]. Therefore denudation and rock uplift can agree with each other even if the orogen is in a transient phase. In a second scenario, we assume that the long-term rock uplift in the Alps is in steady state and equals an average denudation rate, but this average denudation rate in reality displays small, possibly climate-caused variations. If the amplitude of these variations is small, it might be contained within the scatter of our denudation rate data, and in any case might be damped by the method integration time. A variant of the second scenario is that the changes in denudation rates caused by glacial cycles are strongly focused in local areas (e.g. glacial valleys), and thus, although there the rates may be significantly higher, they do not strongly influence our catchment-wide denudation rates. In a third model the recent uplift pattern is explained by post-glacial isostatic rebound after major glaciations due to melting of ice caps [Gudmundsson, 1994] or melting of recent glaciers following the Little Ice Age [Barletta *et al.*, 2006]. While this view was challenged by Persaud & Pfiffner [2004], it is difficult to conceive, however, why denudation should agree with rock uplift if the timescale for rock uplift is so short. For increased rock uplift to result in increased denudation rates, the extensive migration of knick points and the propagation of the adjusted river network into the entire landscape are required. We consider it questionable whether such an adjustment can have taken place in a period as short as 15 kyr, not to mention the few hundred years since the Little Ice Age. A fourth model assumes crustal thickening due to orogenic convergence at any time in the past since the onset of convergence, where relief is isostatically balancing the thickness of the crust. Changes in precipitation, temperature, and

glacial activity pattern enhance denudation [Kuhlemann *et al.*, 2002], which would then drive rock uplift due to isostatic compensation [Stuewe & Barr, 1998; Zhang *et al.*, 2001; Bernet *et al.,* 2004; Champagnac *et al.*, 2007].

The post-glacial rebound models agree with the assumption that the Alps are more or less "dead", e.g. that no active convergence drives isostatic compensation [Molnar, 2004]. Other workers, however, [e.g. Dezes *et al.*, 2004] hold the view that the tectonic convergence in the Alps is currently still active. Based on an estimation of mean rock uplift for the Central Alps [Schlatter *et al.*, 2005], we can calculate an approximated convergence rate of the orogen via equation (5.6):

$$V_A = \frac{U * W}{D_W} \tag{5.6}$$

where V_A is the convergence rate of the orogen (mm/yr), U is the mean rock uplift (~0.6 mm/yr), W is the width of the orogen (~100 km), and D_W is the depth of the orogenic wedge (~30 km). We obtain a mean orogenic convergence rate of ~2 mm/yr, which is in the range of residual velocities with respect to stable Europe measured in the Western Alps by Calais *et al.* [2002] However, Delacou *et al.* [2004] argue that no direct effect of Europe/Africa convergence can be identified and that the main features of the current stress field in the Alps is due to extension in the inner areas of the belt and zones of compression at the outer boundaries. So far no conclusive evidence for convergence in the Central Alps can be used to explain the patterns of uplift and denudation.

In the light of this evidence, we can speculate about the time scale of the steady state between rock uplift and denudation rates. Sediment balances suggest a strong increase in denudation in the last 5 Myr [Kuhlemann *et al.*, 2002]. Regardless of the causes for this increase, Willett *et al.* [2006] suggested that this change in erosional mass flux led to a decrease in size of the active wedge, causing the thrust fronts to retreat towards the centre of the orogen, which then led to a focus of deformation into the wedge interior, or a contraction of the overall active orogen. In a similar approach, Cederbom *et al.* [2004] suggested that the observed change in mass flux caused isostatic exhumation of the high Central Alps while flexural rebound occurred in the Molasse foreland basin. Our observation of two sample groups is consistent with both models. We suggest that our two distinct sample groups (Figure 5.8) represent the rather low rock uplift rates in the Mittelland, being equal to our cosmogenic nuclide-derived denudation rates, and the rather high rock uplift rates in the high Alps, which

accordingly are due to active convergence tectonics, correspond to higher denudation rates. It is well possible that these uplift-denudation patterns are features that have been prevailing for at least a few million years, as has also been suggested by Bernet *et al.* [2004].

In support of this, it is observed that spatial geodetic uplift rate patterns are roughly identical to spatial patterns of apatite fission track ages for the period between 2 and 10 Myr [Persaud & Pfiffner, 2004], an observation that was also made for the Eastern Alps [Frisch *et al.*, 2000]. 3 Myr ago is the time when apatite fission track-derived denudation rates from the Simplon area [Wagner *et al.*, 1977] moved into the range reflected by our cosmogenic nuclide-derived rates (Figure 5.7), although it has to be acknowledged that the Simplon data record the highest long-term denudation rates and are somewhat geographically offset from our set of data. For the Central and Western Alps, denudation rate increases were recorded at ~5 Myr ago from sediment budgets [Kuhlemann *et al.*, 2002]. All this evidence is not incompatible with our rates showing long-term steady state denudation, although the other hypotheses discussed above cannot be discounted either.

5.6 CONCLUSIONS

Mean denudation rates measured by cosmogenic ^{10}Be in river sediment are 0.27 ± 0.14 mm/yr for the Alpine foreland, where integration times are 1.9-8.4 kyr, and of 0.9 ± 0.3 mm/yr for the high crystalline Central Alps, where integration times are 0.4-1.5 kyr. Basin-averaged hillslope angles are independent of denudation rate in the high Alps and are limited to 25-30%. In the Mittelland, denudation rates correlate with hillslope angle as well as with relief and uplift rate. This might suggest that the Swiss Alps region comprises two distinct domains: the high Central Alps accommodate most of the uplift and denudation that possibly contains a component of isostatic rebound or convergence-driven uplift, while the Mittelland has been decoupled from this active regime.

The most important observation made is the correlation between cosmogenic nuclide-derived denudation rate and rock uplift rate. Both these parameters are also highest where altitude, relief, and crustal thickness are highest. This might indicate some form of steady state between uplift and denudation. Such a finding is surprising given that the Alps are only just recovering from the major perturbation represented by the melting of thick LGM glaciers. One possibility is that although steady state after these events has not been established,

variations in erosional efficiency caused by climate change or changes in uplift rate caused by postglacial rebound mimic each other with a short lag time, making the two indistinguishable. A second explanation is that the amplitude of glacial/ interglacial denudation rate changes is not as large as it might intuitively be expected and is contained in the scatter of our rates (ca. 30%). A third explanation is that the recent uplift pattern is explained by post-glacial isostatic rebound after major glaciations due to melting of ice caps or melting of recent glaciers following the Little Ice Age but if true the mechanism at which denudation rates adjust at the same level as uplift is not obvious. Fourth, changes in precipitation, temperature, climate cycling, and glacial activity after ~5-3 Myr ago might have enhanced denudation, which would then simply drive rock uplift due to isostatic compensation. Finally, it might well be that at present convergence and accretionary flux set the pace of both rock uplift and denudation of the high Central Alps, but to date no conclusive evidence exists that such convergence is still active. The agreement between denudation rates determined over the 10^2, 10^4, and 10^6 yr time scale appears to lend some support to the suggestion that some large-scale form of denudational steady state might be a long-term feature for the Central Swiss Alps.

REFERENCES

Aalto, R., (2002). Geomorphic form and process of sediment flux within an active orogen: Denudation of the Bolivian Andes and sediment conveyance across the Beni foreland. *PhD Thesis*, University of Washington, USA, p. 365.

Aalto, R., Dunne, T., Nittrouer, C., Maurice-Bourgoin, L. & Montgomery, D., (2002). Fluvial transport of sediment across a pristine tropical foreland basin: Channel-flood plain interaction and episodic flood plain deposition. *IAHS Publication*, Vol. **276**, pp. 339-344.

Aalto, R., Maurice-Bourgoin, L., Dunne, T., Montgomery, D., Nittrouer, C. & Guyot, J., (2003). Episodic sediment accumulation on Amazonian flood plains influenced by El Nino/Southern Oscillation. *Nature*, Vol. **425**, pp. 493-497.

Aalto, R., Dunne, T. & Guyot, J., (2006). Geomorphic controls on Andean denudation rates. *Journal of Geology*, Vol. **114**, pp. 85-99.

Abbott, M., Seltzer, G., Kelts, K. & Southon, J., (1997). Holocene Paleohydrology of the Tropical Andes from Lake Records. *Quaternary Research*, Vol. **47**, pp. 70-80.

Abbott, M. B., Wolfe, B. B., Wolfe, A. P., Seltzer, G. O., Aravena, R., Mark, B. G., Polissar, P. J., Rodbell, D. T., Rowe, H. D. & Vuille, M., (2003). Holocene paleohydrology and glacial history of the central Andes using multiproxy lake sediment studies. *Palaeogeography, Palaeoclimatology, Palaeoecology*, Vol. **194**, pp. 123-138.

Alexander, J. & Fielding, C.R., (2006). Coarse-Grained Floodplain Deposits in the Seasonal Tropics: Towards a Better Facies Model. *Journal of Sedimentary Research*, Vol. **76**, pp. 539-556.

Anders, M., Gregory-Wodzicki, K. & Spiegelman, M., (2002). A critical evaluation of late Tertiary accelerated uplift rates for the Eastern Cordillera, central Andes of Bolivia. *Journal of Geology*, Vol. **110 (1)**, pp. 89-100.

Anthony, D. & Granger, D., (2007). A new chronology for the age of Appalachian erosional surfaces determined by cosmogenic nuclides in cave sediments. *Earth Surface Processes and Landforms*, Vol. **32**, pp. 874-887.

Asselman, N., **& Middlekoop, H**. (1995). Floodplain sedimentationQuantities, patterns, and processes. *Earth Surface Processes and Landforms*, Vol. **20**, pp. 481-499.

Asselman, N., (1999). Suspended sediment dynamics in a large drainage basin: The River Rhine. *Hydrological Processes*, Vol. **13**, pp. 1437-1450.

Auer, M., (2003). Regionalisierung von Schneeparametern - Eine Methode zur Darstellung von Schneeparametern im Relief. *MS Thesis*, Universität Bern, Schweiz, p. 97.

Balco, G. & Stone, J., (2005). Measuring middle Pleistocene erosion rates with cosmic-ray-produced nuclides in buried alluvial sediment, Fisher Valley, southeastern Utah. *Earth Surface Processes and Landforms*, Vol. **30**, pp. 1051-1067.

Balco, G. & Schaefer, J., (2006). Cosmogenic-nuclide and varve chronologies for the deglaciation of southern New England. *Quaternary Geochronology*, Vol. **1**, pp. 15-28.

Barletta, V., Ferrari, C., Diolaiuti, G., Carnielli, T., Sabadini, R. & Smiraglia, C., (2006). Glacier shrinkage and modeled uplift of the Alps. *Geophysical Research Letters*, Vol. **33**, p. L14307.

Barnes, J. & Pelletier, J., (2006). Latitudinal Variation of Denudation in the Evolution of the Bolivian Andes. *American Journal of Science*, Vol. **306**, pp. 1-31.

Barry, R. & Seimon, A., (2000). Research for Mountain Area Development: Climatic Fluctuations in the Mountains of the Americas and Their Significance. *Ambio*, Vol. **29 (7)**, pp. 364-370.

Battin, T., Kaplan, L., Findlay, S., Hopkinson, C., Marti, E., Packman, A., Newbold, D. & Sabater, F., (2008). Biophysical controls on organic carbon fluxes in fluvial networks. *Nature Geoscience*, Vol. **1**, pp. 95-100.

Benedetti, L., Finkel, R., Papanastassiou, D., King, G., Armijo, R., Ryerson, F., Farber, D. & Flerit, F., (2002). Post-glacial slip history of the Sparta fault (Greece) determined by 36Cl cosmogenic dating: Evidence for non-periodic earthquakes. *Geophysical Research Letters*, Vol. **29 (8)**, p. 10.1029/2001GL014510.

Benjamin, M. T., Johnson, N. M. & Naeser, C.W., (1978). Recent rapid uplift in the Bolivian Andes: Evidence from fission track dating. *Geology*, Vol. **15**, pp. 680-683.

Bernet, M., Brandon, M., Garver, J. & Molitor, B., (2004). Downstream changes of Alpine zircon fission-track ages in the Rhone and Rhine rivers. *Journal of Sedimentary Research*, Vol. **74**, pp. 82-94.

Bes de Berc, S., Soula, J. C., Baby, P., Souris, M., Christophoul, F. & Rosero, J., (2005). Geomorphic evidence of active deformation and uplift in a modern continental wedge-top-foredeep transition: Example of the eastern Ecuadorian Andes. *Tectonophysics*, Vol. **399**, pp. 351-380.

Bierman, P., (1994). Using in situ produced cosmogenic isotopes to estimate rates of landscape evolution: A review from the geomorphic perspective. *Journal of Geophysical Research B: Solid Earth*, Vol. **99 (B7)**, pp. 13885-13896.

Bierman, P. & Steig, E., (1996). Estimating rates of denudation using cosmogenic isotope abundances in sediment. *Earth Surface Processes and Landforms*, Vol. **21**, pp. 125-139.

Bierman, P. & Caffee, M., (2001). Slow rates of rock surface erosion and sediment production across the Namib Desert and escarpment, Southern Africa. *American Journal of Science*, Vol. **301**, pp. 326-358.

Bierman, P. & Nichols, K., (2004). Rock to sediment - Slope to sea with 10Be - Rates of landscape change. *Annual Review of Earth and Planetary Sciences*, Vol. **32**, pp. 215-255.

Binnie, S., Phillips, W. & Summerfield, M.A., Fitfield, L.K., (2007). Tectonic uplift, threshold hillslopes, and denudation rates in a developing mountain range. *Geology*, Vol. **35 (8)**, pp. 743-746.

Blodgett, T. & Isacks, B., (2007). Landslide Erosion Rate in the Eastern Cordillera of Northern Bolivia. *Earth Interactions*, Vol. **11**, pp. 1-30.

Bonnet, M., Barroux, G., Seyler, P., Pecly, G., Moreira-Turcq, P., Lagane, C., Cochonneau, G., Viers, J., Seyler, F. & Guyot, J., (2005). Seasonal links between the Amazon corridor and its floodplain: the case of the varzea of Curuaí. *IAHS Publication*, Vol. **294**, pp. 69-77.

Bonnet, M., Barroux, G., Martinez, J., Seyler, F., Moreira-Turcq, P., Cochonneau, G., Melack, J., Boaventura, G., Maurice-Bourgoin, L., Leon, J., Roux, E., Calmant, S., Kosuth, P., Guyot, J. & Seyler, P., (2008). Floodplain hydrology in an Amazon floodplain lake (Lago Grande de Curuai). *Journal of Hydrology*, Vol. **349**, pp. 18-30.

Brandon, M. & Vance, J., (1992). Tectonic evolution of the Cenozoic Olympic subduction complex, Washington State, as deduced from fission track ages for detrital zircons. *American Journal of Science*, Vol. **292**, pp. 565-636.

Braun, J., (2002). Quantifying the effect of recent relief changes on age-elevation relationships. *Earth and Planetary Science Letters*, Vol. **200**, pp. 331-343.

Bridge, J., (2003). *Rivers and Floodplains- Forms, Processes, and Sedimentary Record*. Blackwell Science Ltd (Ed.), Blackwell Publishing, p. 491.

Brown, E., Bourles, D., Colin, F., Raisbeck, G., Yiou, F. & Desgarceaux, S., (1995a). Evidence for muon-induced production of 10Be in near-surface rocks from the Congo. *Geophysical Research Letters*, Vol. **22**, pp. 703-706.

Brown, E., Stallard, R., Larsen, M., Raisbeck, G. & Yiou, F., (1995b). Denudation rates determined from the accumulation of in situ- produced 10Be in the Luquillo

experimental forest, Puerto Rico. *Earth and Planetary Science Letters*, Vol. **129**, pp. 193-202.

Brown, E., Stallard, R., Larsen, M., Bourles, D., Raisbeck, G. & Yiou, F., (1998). Determination of predevelopment denudation rates of an agricultural watershed (Cayaguas River, Puerto Rico) using in-situ-produced 10Be in river-borne quartz. *Earth and Planetary Science Letters*, Vol. **160**, pp. 723-728.

Burke, B., Heimsath, A. & White, A., (2007). Coupling chemical weathering with soil production across soil-mantled landscapes. *Earth Surface Processes and Landforms*, Vol. **32**, pp. 853-873.

Calais, E., Nocquet, J., Jouanne, F. & Tardy, M., (2002). Current strain regime in the Western Alps from continuous Global Positioning System measurements, 1996-2001. *Geology*, Vol. **30 (7)**, pp. 651-654.

Caputo, M., (1984). Stratigraphy, tectonics, paleoclimatology and paleogeography of northern basins of Brazil. *PhD Thesis*, University of California, Santa Barbara, USA, p. 583.

Caputo, M., (1991). Solimoes megashear: intraplate tectonics in northwestern Brazil. *Geology*, Vol. **19**, pp. 246-249.

Cederbom, C., Sinclair, H., Schlunegger, F. & Rahn, M., (2004). Climate-induced rebound and exhumation of the European Alps. *Geology*, Vol. **32**, pp. 709-712.

Champagnac, J., Molnar, P., Anderson, R., Sue, C. & Delacou, B., (2007). Quaternary erosion- induced isostatic rebound in the western Alps. *Geology*, Vol. **35 (3)**, pp. 195-198.

Christophoul, F., Baby, P., Soula, J., Rosero, M. & Burgos, J., (2002). The Neogene fluvial systems of the Ecuadorian foreland basin and dynamic inferences. *Comptes Rendus - Geoscience*, Vol. **334**, pp. 1029-1037.

Clapp, E., Bierman, P., Schick, A., Lekach, J., Enzel, Y. & Caffee, M., (2000). Sediment yield exceeds sediment production in arid region drainage basins. *Geology*, Vol. **28**, pp. 995-998.

Clapp, E., Bierman, P. & Caffee, M., (2002). Using 10Be and 26Al to determine sediment generation rates and identify sediment source areas in an arid region drainage basin. *Geomorphology*, Vol. **45**, pp. 89-104.

Clapperton, C., (1993). *Quaternary geology and geomorphology of South America*. Elsevier (Ed.), Elsevier Science Publishers, p. 779.

Cleary, D., (2000). *Small scale gold-mining in Brazilian Amazonia*. A. Hall (Ed.), Institute of Latin America Studies, London, pp. 58-72.

Costa, J. B. S., Lea Bemerguy, R., Hasui, Y. & da Silva Borges, M., (2001). Tectonics and paleogeography along the Amazon river. *Journal of South American Earth Sciences*, Vol. **14**, pp. 335-347.

Cross, S., Baker, P., Seltzer, G., Fritz, S. & Dunbar, R., (2000). A new estimate of the Holocene lowstand level of Lake Titicaca, central Andes, and implications for tropical palaeohydrology. *The Holocene*, Vol. **10 (1)**, pp. 21-32.

Delacou, B., Sue, C., Champagnac, J. & Burkhard, M., (2004). Present-day geodynamics in the bend of the western and central Alps as constrained by earthquake analysis. *Geophysical Journal International*, Vol. **158**, pp. 753-774.

Dezes, P., Schmid, S. & Ziegler, P., (2004). Evolution of the European Cenozoic Rift System: interaction of the Alpine and Pyrenean orogens with their foreland lithosphere. *Tectonophysics*, Vol. **389**, pp. 1-33.

Diaz, H. F. & Graham, N., (1996). Recent changes in tropical freezing heights and the role of sea surface temperature. *Nature*, Vol. **383**, pp. 152-155.

Dosseto, A., Bourdon, B., Gaillardet, J., Allégre, C. & Filizola, N., (2006a). Time scale and conditions of weathering under tropical climate: Study of the Amazon basin with U-series. *Geochimica et Cosmochimica Acta*, Vol. **70**, pp. 71-89.

Dosseto, A., Bourdon, B., Gaillardet, J., Maurice-Bourgoin, L. & Allégre, C., (2006b). Weathering and transport of sediments in the Bolivian Andes: Time constraints from uranium-series isotopes. *Earth and Planetary Science Letters*, Vol. **248**, pp. 759-771.

Dumont, J. & Garcia, F., (1991). Active subsidence controlled by basement structures in the Maranon Basin of northeastern Peru. *IAHS Publication*, Vol. **200**, pp. 343-350.

Dumont, J., Deza, E. & Garcia, F., (1991). Morphostructural provinces and neotectonics in the Amazonian lowlands of Peru. *Journal of South American Earth Sciences*, Vol. **4**, pp. 373-381.

Dumont, J., (1994). Neotectonics and rivers of the Amazon headwaters. In: *The Variability of Large Alluvial Rivers*. Stanley A. Schumm, S. & Winkley, B. (Eds.). American Society of Civil Engineers (ASCE Press), pp. 103-113.

Dumont, J. & Fournier, M., (1994). Geodynamic environment of Quaternary morphostructures of the subandean foreland basins of Peru and Bolivia: characteristics and study methods. *Quaternary International*, Vol. **21**, pp. 129-142.

Dunai, T., (2000). Scaling factors for production rates of in situ produced cosmogenic nuclides: A critical reevaluation. *Earth and Planetary Science Letters*, Vol. **176**, pp. 157-169.

Dunne, T., Mertes, L., Meade, R., Richey, J. & Forsberg, B., (1998). Exchanges of sediment between the flood plain and channel of the Amazon River in Brazil. *Bulletin of the Geological Society of America*, Vol. **110**, pp. 450-467.

Dunne, J., Elmore, D. & Muzikar, P., (1999). Scaling factors for the rates of production of cosmogenic nuclides for geometric shielding and attenuation at depth on sloped surfaces. *Geomorphology*, Vol. **27**, pp. 3-11.

Edmond, J., Palmer, M., Measures, C., Grant, B. & Stallard, R., (1995). The fluvial geochemistry and denudation rate of the Guyana Shield in Venezuela, Colombia, and Brazil. *Geochimica et Cosmochimica Acta*, Vol. **59**, pp. 3301-3325.

England, P. & Molnar, P., (1990). Surface uplift, uplift of rocks, and exhumation of rocks. *Geology*, Vol. **18**, pp. 1173-1177.

Espurt, N., Baby, P., Brusset, S., Roddaz, M., Hermoza, W., Regard, V., Antoine, P., Salas-Gismondi, R. & Bolanos, R., (2007). How does the Nazca Ridge subduction influence the modern Amazonian foreland basin? *Geology*, Vol. **35**, pp. 515-518.

Ferrier, K., Kirchner, J. & Finkel, R., (2005). Erosion rates over millennial and decadal timescales at Caspar Creek and Redwood Creek, Northern California Coast Ranges. *Earth Surface Processes and Landforms*, Vol. **30**, pp. 1025-1038.

Filizola, N., (2003). Transfer sédimentaire actuel par les fleuves amazoniens. *PhD Thesis*, Université de Toulouse III, France, p. 292.

Florineth, D. & Schluechter, C., (1998). Reconstructing the Last Glacial Maximum (LGM) ice surface geometry and flowlines in the Central Swiss Alps. *Eclogae Geologicae Helvetiae*, Vol. **91**, pp. 391-407.

Florineth, D. & Schluechter, C., (2000). Alpine evidence for atmospheric circulation patterns in Europe during the Last Glacial Maximum. *Quaternary Research*, Vol. **54**, pp. 295-308.

Franzinelli, E. & Potter, P., (1983). Petrology, chemistry, and texture of modern river sands, Amazon river system. *Journal of Geology*, Vol. **91**, pp. 23-39.

Franzinelli, E. & Igreja, H., (2002). Modern sedimentation in the Lower Negro River, Amazonas State, Brazil. *Geomorphology*, Vol. **44**, pp. 259-271.

Frisch, W., Székely, B., Kuhlemann, J. & Dunkl, I., (2000). Geomorphological evolution of the Eastern Alps in response to Miocene tectonics. *Zeitschrift für Geomorphologie*, Vol. **44**, pp. 103-138.

Furrer, G., Burga, C., Gamper, M., Holzhauser, H. & Maisch, M., (1987). Zur Gletscher-Vegetations- und Klimageschichte der Schweiz seit der Spaeteiszeit. *Geographica Helvetica*, Vol. **2**, pp. 61-91.

Gaillardet, J., Dupré, B., Allégre, C. & Négrel, P., (1997). Chemical and physical denudation in the Amazon River Basin. *Chemical Geology*, Vol. **142**, pp. 141-173.

Gardner, T., Jorgensen, D., Shuman, C. & Lemieux, C., (1987). Geomorphic and tectonic process rates: effects of measured time interval. *Geology*, Vol. **15**, pp. 259-261.

Gautier, E., Brunstein, D., Vauchel, P., Roulet, M., Fuertes, O., Guyot, J., Darozzes, J. & Bourrel, L., (2007). Temporal relations between meander deformation, water discharge and sediment fluxes in the floodplain of the Rio Beni (Bolivian Amazonia). *Earth Surface Processes and Landforms*, Vol. **32**, pp. 230-248.

Gibbs, R. J., (1967). Amazon River: Environmental Factors that control its dissolved and suspended load. *Science*, Vol. **156**, pp. 1734-1737.

Gibbs, A. & Barron, C., (1983). The Guyana Shield reviewed. *Episodes*, Vol. **2**, pp. 7-14.

Gosse, J. & Phillips, F., (2001). Terrestrial in situ cosmogenic nuclides: Theory and application. *Quaternary Science Reviews*, Vol. **20**, pp. 1475-1560.

Granger, D., Kirchner, J. & Finkel, R., (1996). Spatially averaged long-term erosion rates measured from in situ-produced cosmogenic nuclides in alluvial sediment. *Journal of Geology*, Vol. **104**, pp. 249-257.

Granger, D., Fabel, D. & Palmer, A., (2001). Pliocene - Pleistocene incision of the Green River, Kentucky, determined from radioactive decay of cosmogenic 26Al and10Be in Mammoth Cave sediments. *Bulletin of the Geological Society of America*, Vol. **113**, pp. 825-836.

Gregory-Wodzicki, K., (2000). Uplift history of the Central and Northern Andes: A review. *Bulletin of the Geological Society of America*, Vol. **112 (7)**, pp. 1091-1105.

Gudmundsson, G., (1994). An order-of-magnitude estimate of the current uplift-rates in Switzerland caused by the Wuerm Alpine deglaciation. *Eclogae Geologicae Helvetiae*, Vol. **87**, pp. 545-557.

Guyot, J. L., (1993). Hydrogéochimie des fleuves de l´Amazonie Bolivienne. *PhD Thesis*, Institute de Géologie et Géochimie, Bordeaux I., France, p. 261.

Guyot, J.L., Jouanneau, J.M., Quintanilla, J. & Wasson, J., (1993). Les flux de matières sissoutes et particulaires exportés des Andes par le Rio Béni (Amazonie Bolivienne), en période de crue. *Geodinamica Acta*, Vol. **6 (4)**, pp. 233-241.

Guyot, J. L., Filizola, N., Quintanilla, J. & Cortez, J., (1996). Dissolved solids and suspended sediment yields in the Rio Madeira basin, from the Bolivian Andes to the Amazon. *IAHS Publication*, Vol. **236**, pp. 55-63.

Guyot, J. L., Jouanneau, J. M. & Wasson, J.G., (1999). Characterisation of river bed and suspended sediments in the Rio Madeira drainage basin (Bolivian Amazonia). *Journal of South American Earth Sciences*, Vol. **12**, pp. 401-410.

Guyot, J.L., Filizola, N. & Laraque, A., (2005). Régime et bilan du flux sédimentaire de l'Amazone à Óbidos (Pará, Brésil) de 1995 à 2003. *IAHS Publication*, Vol. **219**, p. 1-8.

Guyot, J. L., Bazan, H., Fraizy, P., Ordonez, J. J., Armijos, E. & Laraque, A., (2007a). Suspended sediment yields in the Amazon basin of Peru: a first estimation. *IAHS Publication*, Vol. **314**, pp. 1-8.

Guyot, J.L., Jouanneau, J.M-, Soares, L., Boaventura, G., Maillet, N. & Lagane, C., (2007b). Clay mineral composition of river sediments in the Amazon Basin. *Catena*, Vol. **71**, pp. 340-356.

Haeuselmann, P., Granger, D., Jeannin, P. & Lauritzen, S., (2007). Abrupt glacial valley incision at 0.8 Ma dated from cave deposits in Switzerland. *Geology*, Vol. **35**, pp. 143-146.

Hancock, G. & Kirwan, M., (2007). Summit erosion rates deduced from 10Be: Implications for relief production in the central Appalachians. *Geology*, Vol. **35**, pp. 89-92.

Hartmann, L. & Delgado, I., (2001). Cratons and orogenic belts of the Brazilian Shield and their contained gold deposits. *Mineralium Deposita*, Vol. **36**, pp. 207-217.

Hasui, Y. & Almeida, F.D., (1985). The Central Brazilian Shield reviewed. *Episodes*, Vol. **8**, pp. 29-37.

Heidbreder, E., Pinkau, K., Reppin, C. & Schoenfelder, V., (1971). Measurements of distribution in energy and angle of high-energy neutrons in lower atmosphere. *Journal of Geophysical Research*, Vol. **76**, pp. 2905-2916.

Heimsath, A., Chappell, J., Dietrich, W., Nishiizumi, K. & Finkel, R., (2000). Soil production on a retreating escarpment in southeastern Australia. *Geology*, Vol. **28**, pp. 787-790.

Heimsath, A. & McGlynn, R., (2008). Quantifying periglacial erosion in the Nepal high Himalaya. *Geomorphology*, Vol. **97**, pp. 5-23.

Hess, L. L., Melack, J. M., Novo, E. M. L. M., Barbosa, C. C. F. & Gastil, M., (2003). Dual-season mapping of wetland inundation and vegetation for the central Amazon basin. *Remote Sensing of Environment*, Vol. **87**, pp. 404-428.

Hinderer, M., (2001). Late quaternary denudation of the Alps, Valley and lake fillings and modern river loads. *Geodinamica Acta*, Vol. **14**, pp. 231-263.

Hofmann, H., Beer, J., Bonani, G., Von Gunten, H., Raman, S., Suter, M., Walker, R., Woefli, W. & Zimmermann, D., (1987). 10Be: Half-life and AMS Standards. *Nuclear Instruments and Methods in Physics Research, Section B: Beam Interactions with Materials and Atoms*, Vol. **B29**, pp. 32-36.

Hoorn, C., Guerrero, J., Sarmiento, G. & Lorente, M., (1995). Andean tectonics as a cause for changing drainage patterns in Miocene northern South America. *Geology*, Vol. **23 (3)**, pp. 237-240.

Hormes, A., Mueller, B. U. & Schluechter, C., (2001). The Alps with little ice: evidence for eight Holocene phases of reduced glacier extent in the Central Swiss Alps. *The Holocene*, Vol. **11 (3)**, pp. 255-265.

Horton, B., (1999). Erosional control on the geometry and kinematics of thrust belt development in the central Andes. *Tectonics*, Vol. **18**, pp. 1292-1304.

Horton, B. & Decelles, P., (2001). Modern and ancient fluvial megafans in the foreland basin system of the Central Andes, Southern Bolivia: Implications for drainage network evolution if fold thrust belts. *Basin Research*, Vol. **13**, pp. 43-63.

Hovius, N., (1998). Controls on sediment supply by large rivers. In: *Relative Role of Eustasy, Climate, and Tectonism in Continental Rocks*. K.W. Shanley & P.J. McCabe (Eds.). Society for Sedimentary Geology, pp. 3-16.

Hovius, N., Stark, C., Hao-Tsu, C. & Jiun-Chuan, L., (2000). Supply and removal of sediment in a landslide-dominated mountain belt: Central Range, Taiwan. *Journal of Geology*, Vol. **108**, pp. 73-89.

Hovius, N. & von Blanckenburg, F., (2007). Constraining the denudational response to faulting. In: *The Dynamics of Fault Zones*. Handy, M., D. Hirth, D. & Hovius, N. (Eds.). MIT Press, pp. 231-273.

Hudson, P. & Kesel, R., (2000). Channel migration and meader-bend curvature in the lower Mississippi River prior to human modification. *Geology*, Vol. **28 (6)**, pp. 531-534.

Irion, G., (1989). Quaternary geological history of the Amazon Lowlands. In: *Tropical forests: botanical dynamics, speciation and diversity*. Holm-Nielsen, L., Nielsen, I. & Baslev, H. (Eds.). Academic Press Limited, pp. 23-34.

Irion, G., Müller, J., Nunes de Mello, J. & Junk, W., (1995). Quaternary geology of the Amazonian Lowland. *Geo-Marine Letters*, Vol. **15**, pp. 172-178.

Irion, G., Bush, M., Nunes de Mello, J., Stüben, D., Neumann, T., Müller, G., Morais de, J. & Junk, J., (2006). A multiproxy palaeoecological record of Holocene lake sediments from the Rio Tapajós, eastern Amazonia. *Palaeogeography, Palaeoclimatology, Palaeoecology*, Vol. **240**, pp. 523-535.

Iriondo, M., (1999). Climatic changes in the South American plains: Records of a continental-scale oscillation. *Quaternary International*, Vol. **57/58**, pp. 93-112.

Ivy-Ochs, S., Schluechter, C., Kubik, P., Synal, H., Beer, J. & Kerschner, H., (1996). The exposure age of an Egesen moraine at Julier Pass, Switzerland, measured with the cosmogenic radionuclides 10Be, 26A1 and 36Cl. *Eclogae Geologicae Helvetiae*, Vol. **89**, pp. 1049-1063.

Ivy-Ochs, S., Schaefer, J., Kubik, P., Synal, H. & Schluechter, C., (2004). Timing of deglaciation on the northern Alpine foreland (Switzerland). *Eclogae Geologicae Helvetiae*, Vol. **97**, pp. 47-55.

Jaeckli, A., (1970). Die Schweiz zur letzten Eiszeit. In: *Atlas der Schweiz*. Bundesamt für Landestopographie (Ed.). Eidg. Landestopographie, p. Wabern-Bern.

Jerolmack, D. J. & Mohrig, D., (2007). Conditions for branching in depositional rivers. *Geology*, Vol. **35**, pp. 463-466.

Junk, W. & Furch, K., (1993). A general view of tropical South American floodplains. *Wetlands Ecology and Management*, Vol. **2 (4)**, pp. 231-238.

Junk, W. E. A., (1997). *The Central Amazon floodplain- Ecology of a pulsing system*. Junk, W. (Ed.), Springer-Verlag, p. 525.

Kahle, H., Geiger, A., Buerki, B., Gubler, E., Marti, U., Wirth, B., Rothacher, M., Gurtner, W., Beutler, G., Bauersima, I. & Pfiffner, O., (1997). Recent crustal movements, geoid and density distribution: Contribution from integrated satellite and terrestrial measurements. In: *Results of the National Research Program 20 (NRP 20)*. Pfiffner, O.E.A. (Ed.). Birkhaeuser Verlag, pp. 251-259.

Kalliola, R., Salo, J., Puhakka, M. & Rajasilta, M., (1992). Upper Amazon Channel Migration. *Naturwissenschaften*, Vol. **79**, pp. 75-79.

Kelly, M., Buoncristiani, J. & Schluechter, C., (2004). A reconstruction of the last glacial maximum (LGM) ice-surface geometry in the western Swiss Alps and contiguous Alpine regions in Italy and France. *Eclogae Geologicae Helvetiae*, Vol. **97**, pp. 57-75.

Kerschner, H., Kaser, G. & Sailer, R., (2000). Alpine Younger Dryas glaciers as paleo-precipitation gauges. *Annals of Glaciology*, Vol. **31**, pp. 80-84.

Kerschner, H., Hertl, A., Gross, G., Ivy-Ochs, S. & Kubik, P., (2006). Surface exposure dating of moraines in the Kromer valley (Silvretta Mountains, Austria) - Evidence for glacial response to the 8.2 ka event in the Eastern Alps? *The Holocene*, Vol. **16**, pp. 7-15.

Kesel, R., (1988). The decline in the suspended load of the Lower Mississippi River and its influence on adjacent Wetlands. *Environmental Geology and Water Sciences*, Vol. **11 (3)**, pp. 271-281.

Kesel, R. H., Yodis, E. G. & McCraw, D.J., (1992). An approximation of the sediment budget of the lower Mississippi river prior to major human modification. *Earth Surface Processes and Landforms*, Vol. **17**, pp. 711-722.

Kirchner, J., Finkel, R., Riebe, C., Granger, D., Clayton, J., King, J. & Megahan, W., (2001). Mountain erosion over 10 yr, 10 k.y., and 10 m.y. time scales. *Geology*, Vol. **29**, pp. 591-594.

Kirchner, J., Riebe, C., Ferrier, K. & Finkel, R., (2006). Cosmogenic nuclide methods for measuring long-term rates of physical erosion and chemical weathering. *Journal of Geochemical Exploration*, Vol. **88**, pp. 296-299.

Knighton, A. & Nanson, G., (1993). Anastomosis and the continuum of channel pattern. *Earth Surface Processes and Landforms*, Vol. **18**, pp. 613-625.

Kubik, P., Ivy-Ochs, S., Masarik, J., Frank, M. & Schluechter, C., (1998). 10Be and 26Al production rates deduced from an instantaneous event within the dendro-calibration curve, the landslide of Koefels, Oetz Valley, Austria. *Earth and Planetary Science Letters*, Vol. **161**, pp. 231-241.

Kuechler, I., Miekeley, N. & Forsberg, B., (2000). A contribution to the chemical characterization of rivers in the Rio Negro Basin, Brazil. *Journal of the Brazilian Chemical Society*, Vol. **11**, pp. 286-292.

Kuehl, S. A., DeMaster, D. J. & Nittrouer, C.A., (1986). Nature of sediment accumulation on the Amazon continental shelf. *Continental Shelf Research*, Vol. **6**, pp. 209-225.

Kuhlemann, J., Frisch, W., Szekely, B., Dunkl, I. & Kazmer, M., (2002). Post-collisional sediment budget history of the Alps: Tectonic versus climatic control. *International Journal of Earth Sciences (Geologische Rundschau)*, Vol. **91**, pp. 818-837.

Lal, D. & Peters, B., (1967). Cosmic ray-produced radioactivity on the Earth. In: *Handbuch der Physik*. Fluegge, S. (Ed.). Springer Verlag, pp. 551-612.

Lal, D., (1991). Cosmic ray labeling of erosion surfaces: in situ nuclide production rates and erosion models. *Earth and Planetary Science Letters*, Vol. **104**, pp. 424-439.

Landim, P., Bosio, N., Wu, F., Meyer, A. & Castro Jr P.R.M., (1978). Heavy minerals from the Amazon bed. *EOS*, Vol. **58**, p. 277.

Langbein, W. & Schumm, S., (1958). Yield of sediment in relation to mean annual precipitation. *Transactions of the American Geophysical Union*, Vol. **39**, pp. 1076-1084.

Laraque, A., Ceron, C., Armijos, E., Pombosa, R., Magat, P. & Guyot, J.L., (2004). Sediment yields and erosion rates in the Napo River basin: An Ecuadorian Andean Amazon tributary. *IAHS Publication*, Vol. **288**, pp. 220-225.

Laraque, A., Filizola, N. & Guyot, J., (2005). Variations spatio-temporelles du bilan sédimentaire dans le bassin Amazonien Brésilien, à partir d'un échantillonnage décadaire. *IAHS Publication*, Vol. **291**, p. 1-10.

Latrubesse, E. & Franzinelli, E., (2005). The late Quaternary evolution of the Negro River, Amazon, Brazil: Implications for island and floodplain formation in large anabranching tropical systems. *Geomorphology*, Vol. **70**, pp. 372-397.

Latrubesse, E., Stevaux, J. & Sinha, R., (2005). Tropical rivers. *Geomorphology*, Vol. **70**, pp. 187-206.

Lauer, J. & Parker, G., (2008). Net local removal of floodplain sediment by river meander migration. *Geomorphology*, Vol. **96**, pp. 123-149.

Leopold, L. & Wolman, M., (1957). River channel patterns: Braided, Meandering, and Straight. *Geological Survey Professional Paper 282-B*. United States Governmant Printing Office, Washington, p. 85.

Leopold, L., Wolman, M. & Miller, J., (1964). *Fluvial Processes in Geomorphology*. Dover Publications (Ed.), Dover Publications, Inc., p. 522.

Libby, W., (1955). *Radiocarbon Dating*. University of Chicago (Ed.), University of Chicago Press, p. 175.

Lifton, N. A., Jull, A. J. T. & Quade, J., (2001). A new extraction technique and production rate estimate for in situ cosmogenic 14C in quartz. *Geochimica et Cosmochimica Acta*, Vol. **65**, pp. 1953-1969.

Lima, J., Lopes, W., De Carvalho, N., Vieira, M. & Da Silva, E., (2005). Suspended sediment fluxes in the large river basins of Brazil. *IAHS Publication*, Vol. **291**, pp. 355-363.

Ludwig, K. R., (1994). Isoplot- A plotting and regression program for radiogenic isotope data. *USGS Open file Report 91-445*. USGS Denver, Colorado, p. 45.

Mackin, J., (1948). Concept of the graded river. *Bulletin of the Geological Society of America*, Vol. **59**, pp. 463-512.

Magilligan, F., (1985). Historical Floodplain Sedimentation in the Galena River Basin, Wisconsin and Illinois. *Annals of the Association of American Geographers*, Vol. **75 (4)**, pp. 583-594.

Mainville, N., Webb, J., Lucotte, M., Davidson, R., Betancourt, O., Cueva, E. & Mergler, D., (2006). Decrease of soil fertility and release of mercury following deforestation in the Andean Amazon, Napo River Valley, Ecuador. *Science of the Total Environment*, Vol. **368**, pp. 88-98.

Maisch, M., (1981). Glazialmorphologische und gletschergeschichtliche Untersuchungen im Gebiet zwischen Landwasser- und Albulatal (Kt. Graubünden, Schweiz). *Geographica Helvetica*, Vol. **37**, pp. 93-104.

Martinelli, L., Victoria, R., Devol, A., Richey, J. & Forsberg, B., (1989). Suspended sediment load in the Amazon Basin: an overview. *GeoJournal*, Vol. **19**, pp. 381-389.

Masarik, J., Frank, M., Schaefer, J. & Wieler, R., (2001). Correction of in situ cosmogenic nuclide production rates for geomagnetic field insity variations during the past 800,000 years. *Geochimica et Cosmochimica Acta*, Vol. **65**, pp. 2995-3003.

Mathieu, D., Bernat, M. & Nahon, D., (1995). Short-lived U and Th isotope distribution in a tropical laterite derived from granite (Pitinga river basin, Amazonia, Brazil): Application to assessment of weathering rate. *Earth and Planetary Science Letters*, Vol. **136**, pp. 703-714.

Matmon, A., Bierman, P., Larsen, J., Southworth, S., Pavich, M., Finkel, R. & Caffee, M., (2003a). Erosion of an ancient mountain range, the Great Smoky Mountains, North Carolina and Tennessee. *American Journal of Science*, Vol. **303**, pp. 817-855.

Matmon, A., Crouvi, O., Enzel, Y., Bierman, P., Larsen, J., Porat, N., Amit, R. & Caffee, M., (2003b). Complex exposure histories of chert clasts in the late Pleistocene shorelines of Lake Lisan, southern Israel. *Earth Surface Processes and Landforms*, Vol. **28**, pp. 493-506.

Maurice-Bourgoin, L., Aalto, R. & Guyot, J., (2002). Sediment-associated mercury distribution within a major Amazon tributary: Century-scale contamination history and importance of flood plain accumulation. *IAHS Publication*, Vol. **276**, pp. 161-168.

Maurice-Bourgoin, L., Martinez, J., Grélaud, J. & Filizola, N., Boaventura, G. R., (2005). The role of flood plains in the hydrology and sediment dynamics of the Amazon river, Brazil. *IAHS Publication*, Vol. **291**, pp. 310-322.

Maurice-Bourgoin, L., Bonnet, M., Martinez, J., Kosuth, P., Cochonneau, G., Moreira-Turcq, P., Guyot, J., Vauchel, P., Filizola, N. & Seyler, P., (2007). Temporal dynamics of water and sediment exchanges between the Curuaí floodplain and the Amazon River, Brazil. *Journal of Hydrology*, Vol. **335**, pp. 140-156.

Mayorga, E., Aufdenkampe, A., Masiello, C., Krusche, A., Hedges, J., Quay, P., Richey, J. & Brown, T., (2005). Young organic matter as a source of carbon dioxide outgassing from Amazonian rivers. *Nature*, Vol. **436**, pp. 538-541.

Meade, R., Nordin, C., Curtis, W., Costa Rodrigues, F., Do Vale, C. & Edmond, J,M., (1979). Sediment loads in the Amazon river. *Nature*, Vol. **278**, pp. 161-163.

Meade, R., (1985). Movement and storage of sediment in river systems. In: *Physical and chemical weathering in geochemical cycles*. Lerman, A. & Meybeck, M. (Eds.). Kluwer Academic Publishers, pp. 165-179.

Meade, R., Dunne, T., Richey, J., De M Santos, U. & Salati, E., (1985). Storage and remobilization of suspended sediment in the Lower Amazon River of Brazil. *Science*, Vol. **228**, pp. 488-490.

Meade, R., Rayol, J., Da Conceicao, S. & Natividade, J., (1991). Backwater effects in the Amazon River basin of Brazil. *Environmental Geology and Water Sciences*, Vol. **18**, pp. 105-114.

Meade, R., (2007). Transcontinental Moving and Storage: the Orinoco and Amazon rivers transfer the Andes to the Atlantic. In: *Large rivers: Geomorphology and Management*. Gupta, A. (Ed.). John Wiley & Sons Ltd, pp. 45-63.

Mertes, L. & Meade, R., (1985). Particle size of sands collected from the bed of the Amazon river and its tributaries in Brazil during 1982-84. *USGS Open File Report 85-333*. U.S. Geological Survey, p. 20.

Mertes, L., Dunne, T. & Martinelli, L., (1996). Channel-floodplain geomorphology along the Solimoes-Amazon River, Brazil. *Bulletin of the Geological Society of America*, Vol. **108**, pp. 1089-1107.

Mertes, L. & Dunne, T., (2007). Effects of Tectonism, Climate Change, and Sea-level Change on the Form and Behaviour of the Modern Amazon River and its Floodplain. In: *Large rivers: Geomorphology and Management*. Gupta, A. (Ed.). John Wiley & Sons Ltd, pp. 115-144.

Miller, G., Briner, J., Lifton, N. & Finkel, R., (2006). Limited ice-sheet erosion and complex exposure histories derived from in situ cosmogenic 10Be, 26Al, and 14C on Baffin Island, Arctic Canada. *Quaternary Geochronology*, Vol. **1**, pp. 74-85.

Milliman, J. & Meade, R., (1983). World-wide delivery of river sediment to the oceans. *Journal of Geology*, Vol. **91 (1)**, pp. 1-21.

Milliman, J. & Syvitski, J., (1992). Geomorphic/tectonic control of sediment discharge to the ocean: the importance of small mountainous rivers. *Journal of Geology*, Vol. **100**, pp. 525-544.

Molinier, M., Guyot, J., De Oliveira, E. & Guimaraes, V., (1996). Les régimes hydrologique de l´Amazone et de ses affuents. *IAHS Publication*, Vol. **238**, p. 209-222.

Molnar, P., (2004). Late Cenozoic increase in accumulation rates of terrestrial sediment: How might climate change have affected erosion rates? *Annual Reviews of Earth and Planetary Science*, Vol. **32**, pp. 67-89.

Montgomery, D. & Greenberg, H., (2000). Local relief and the height of Mount Olympus. *Earth Surface Processes and Landforms*, Vol. **25**, pp. 385-396.

Montgomery, D. & Brandon, M., (2002). Topographic controls on erosion rates in tectonically active mountain ranges. *Earth and Planetary Science Letters*, Vol. **201**, pp. 481-489.

Moreira-Turcq, P., Jouanneau, J., Turcq, B., Seyler, P., Weber, O. & Guyot, J., (2004). Carbon sedimentation at Lago Grande de Curuai, a floodplain lake in the low Amazon region: insights into sedimentation rates. *Palaeogeography, Palaeoclimatology, Palaeoecology*, Vol. **214**, pp. 27-40.

Mortatti, J. & Probst, J., (2003). Silicate rock weathering and atmospheric/soil CO2 uptake in the Amazon basin estimated from river water geochemistry: Seasonal and spatial variations. *Chemical Geology*, Vol. **197**, pp. 177-196.

Mulch, A., Teyssier, C., Cosca, M. & Chamberlain, C., (2007). Stable isotope paleoaltimetry of Eocene Core Complexes in the North American Cordillera. *Tectonics*, Vol. **26 (4)**, p. TC4001.

Nanson, G. & Croke, J.C., (1992). A genetic classification of floodplains. *Geomorphology*, Vol. **4**, pp. 459-486.

Nanson, G. & Knighton, A., (1996). Anabranching rivers: Their cause, character and classification. *Earth Surface Processes and Landforms*, Vol. **21 (3)**, pp. 217-239.

Nichols, K., Bierman, P., Hooke, R., Clapp, E. & Caffee, M., (2002). Quantifying sediment transport on desert piedmonts using 10Be and 26Al. *Geomorphology*, Vol. **45**, pp. 105-125.

Nichols, K., Bierman, P., Caffee, M., Finkel, R. & Larsen, J., (2005). Cosmogenically enabled sediment budgeting. *Geology*, Vol. **33**, pp. 133-136.

Niemi, N., Oskin, M., Burbank, D., Heimsath, A. & Gabet, E., (2005). Effects of bedrock landslides on cosmogenically determined erosion rates. *Earth and Planetary Science Letters*, Vol. **237**, pp. 480-498.

Nordin, C. F., Meade, R. H., Curtis, W. F., Bosio, N. J. & Landim, P.M.B., (1980). Size distribution of Amazon River bed sediment. *Nature*, Vol. **286**, pp. 52-53.

Norton, K., v. Blanckenburg, F., Schlunegger, F., Schwab, M. & Kubik, P., (2008). Cosmogenic nuclide-based investigation of spatial erosion and hillslope channel coupling in the transient foreland of the Swiss Alps. *Geomorphology*, Vol. **95**, pp. 474-486.

Ohlendorf, C., (1998). High alpine lake sediments as chronicles for regionl glacier and climate history in the Upper Engadine, southeastern Switzerland. *PhD Thesis*, ETH Zürich, Schweiz, p. 203.

Parker, G. & Perg, L., (2005). Probabilistic formulation of conservation of cosmogenic nuclides: effect of surface elevation fluctuations on approach to steady state. *Earth Surface Processes and Landforms*, Vol. **30**, pp. 1127-1144.

Perg, L., Anderson, R. & Finkel, R., (2003). Use of cosmogenic radionuclides as a sediment tracer in the Santa Cruz littoral cell, California, United States. *Geology*, Vol. **31**, pp. 299-302.

Persaud, M. & Pfiffner, O., (2004). Active deformation in the eastern Swiss Alps: Post-glacial faults, seismicity and surface uplift. *Tectonophysics*, Vol. **385**, pp. 59-84.

Pigati, J., Quade, J., Wilson, J., Jull, A. & Lifton, N., (2007). Development of low-background vacuum extraction and graphitization systems for 14C dating of old (40-60 ka) samples. *Quaternary International*, Vol. **166**, pp. 4-14.

Pinet, P. & Souriau, M., (1988). Continental erosion and large-scale relief. *Tectonics*, Vol. **7**, pp. 563-582.

Potter, P., (1994). Modern sands of South America: composition, provenance and global significance. *International Journal of Earth Sciences (Geologische Rundschau)*, Vol. **83**, pp. 212-232.

Prosser, G., (1998). Strike-slip movements and thrusting along a transpressive fault zone: The North Giudicarie line (Insubric line, Northern Italy). *Tectonics*, Vol. **17**, pp. 921-937.

Putzer, H., (1984). The geological evolution of the Amazon basin and its mineral ressources. In: *The Amazon: Limnology and landscape ecology of a mighty tropical river and its basin*. Sioli, H. (Ed.). Dordrecht, Dr. W. Junk Publishers, pp. 15-46.

Quigley, M., Sandiford, M., Fifield, L. & Alimanovic, A., (2007). Landscape responses to intraplate tectonism: Quantitative constraints from 10Be nuclide abundances. *Earth and Planetary Science Letters*, Vol. **261**, pp. 120-133.

Rahn, M. & Grasemann, B., (1999). Fission track and numerical thermal modeling of differential exhumation of the Glarus thrust plane (Switzerland). *Earth and Planetary Science Letters*, Vol. **169**, pp. 245-259.

Rahn, M., (2001). The metamorphic and exhumation history of the Helvetic Alps, Switzerland, as revealed by apatite and zircon fission tracks. *Habilitation thesis*, Albert-Ludwigs-Universität Freiburg, Deutschland, p. 140.

Rahn, M., (2005). Apatite fission track ages from the Adula nappe: late-stage exhumation and relief evolution. *Schweizerische Mineralogische und Petrographische Mitteilungen*, Vol. **85**, pp. 233-245.

Rasanen, M., Salo, J., Jungnert, H. & Pittman, L., (1990). Evolution of the Western Amazon lowland relief: impact of Andean foreland dynamics. *Terra Nova*, Vol. **2**, pp. 320-332.

Reinhardt, L., Hoey T. B., Barrows, T., Dempster, T., Bishop, P. & Fifield, L., (2007). Interpreting erosion rates from cosmogenic radionuclide concentrations measured in rapidly eroding terrain. *Earth Surface Processes and Landforms*, Vol. **32**, pp. 390-406.

Riebe, C., Kirchner, J., Granger, D. & Finkel, R., (2000). Erosional equilibrium and disequilibrium in the Sierra Nevada, inferred from cosmogenic 26Al and 10Be in alluvial sediment. *Geology*, Vol. **28**, pp. 803-806.

Riebe, C., Kirchner, J., Granger, D. & Finkel, R., (2001a). Strong tectonic and weak climatic control of long-term chemical weathering rates. *Geology*, Vol. **29**, pp. 511-514.

Riebe, C., Kirchner, J. & Granger, D., (2001b). Quantifying quartz enrichment and its consequences for cosmogenic measurements of erosion rates from alluvial sediment and regolith. *Geomorphology*, Vol. **40**, pp. 15-19.

Riebe, C., Kirchner, J. & Finkel, R., (2003). Long-term rates of chemical weathering and physical erosion from cosmogenic nuclides and geochemical mass balance. *Geochimica et Cosmochimica Acta*, Vol. **67**, pp. 4411-4427.

Roche, M. & Jauregui, C., (1988). Water ressources, salinity, and salt yields of the rivers of the Bolivian Andes. *Journal of Hydrology*, Vol. **101**, pp. 305-331.

Roddaz, M., Baby, P., Brusset, S., Hermoza, W. & Darrozes, J., (2005). Forebulge dynamics and environmental control in Western Amazonia: The case study of the Arch of Iquitos (Peru). *Tectonophysics*, Vol. **399**, pp. 87-108.

Roebber, P., Bruening, S., Schultz, D. & Cortinas Jr, J., (2003). Improving snowfall forecasting by diagnosing snow density. *Weather and Forecasting*, Vol. **18**, pp. 264-287.

Roethlisberger, F. & Schneebeli, W., (1979). Genesis of lateral moraine complexes, demonstrated by fossil soils and trunks; indicators of postglacial climatic fluctuations. *International Union for Quaternary Research*. Vol. **XVII**, pp. 387-420.

Ronchail, J., Cochonneau, G., Molinier, M., Guyot, J., Goretti de Miranda Chaves, A., Guimaraes, V. & De Oliveira, E., (2002). Interannual rainfall variability in the Amazon basin and sea-surface temperatures in the equatorial Pacific and the tropical Atlantic oceans. *International Journal of Climatology*, Vol. **22**, pp. 1663-1686.

Rossetti, D., Mann de Toledo, P. & Góes, A., (2005). New geological framework for Western Amazonia (Brazil) and implications for biogeography and evolution. *Quaternary Research*, Vol. **63**, pp. 78-89.

Rossetti, D. F. & Valeriano, M.M., (2007). Evolution of the lowest Amazon basin modeled from the integration of geological and SRTM topographic data. *Catena*, Vol. **70**, pp. 253-265.

Roulet, M., Lucotte, M., Canuel, R., Farella, N., De Freitos Goch, Y., Pacheco Peleja, J., Guimaraes, J., Mergler, D. & Amorim, M., (2001). Spatio-temporal geochemistry of mercury in waters of the Tapajós and Amazon rivers, Brazil. *Limnology and Oceanography*, Vol. **46**, pp. 1141-1157.

Rowe, H., Dunbar, R., Mucciarone, D., Seltzer, G., Baker, P. & Fritz, S., (2002). Insolation, Moisture Balance and Climate Change on the South American Altiplano Since the Last Glacial Maximum. *Climatic Change*, Vol. **52**, pp. 175-199.

Safran, E., Bierman, P., Aalto, R., Dunne, T., Whipple, K. & Caffee, M., (2005). Erosion rates driven by channel network incision in the Bolivian Andes. *Earth Surface Processes and Landforms*, Vol. **30**, pp. 1007-1024.

Safran, E., Blythe, A. & Dunne, T., (2006). Spatially variable exhumation rates in orogenic belts: An Andean example. *Journal of Geology*, Vol. **114 (6)**, pp. 665-681.

Sailer, R., (2001). Spaeteiszeitliche Gletscherstaende in der Fernwallgruppe. *PhD Thesis*, Universität Innsbruck, Österreich, p. 205.

Samworth, E., Warburton, E. & Engelbertink, G., (1972). Beta decay of the 26Al ground state. *Physical Review C*, Vol. **5 (1)**, pp. 138-142.

Schaller, M., von Blanckenburg, F., Hovius, N. & Kubik, P., (2001). Large-scale erosion rates from in situ-produced cosmogenic nuclides in European river sediments. *Earth and Planetary Science Letters*, Vol. **188**, pp. 441-458.

Schaller, M., von Blanckenburg, F., Veldkamp, A., Tebbens, L., Hovius, N. & Kubik, P., (2002). A 30 000 yr record of erosion rates from cosmogenic 10Be in Middle European river terraces. *Earth and Planetary Science Letters*, Vol. **204**, pp. 307-320.

Schaller, M., von Blanckenburg, F., Hovius, N., Veldkamp, A., van den Berg, M. & Kubik, P., (2004). Paleoerosion rates from cosmogenic 10Be in a 1.3 Ma terrace sequence: Response of the river Meuse to changes in climate and rock uplift. *Journal of Geology*, Vol. **112**, pp. 127-144.

Schildgen, T., Phillips, W. & Purves, R., (2005). Simulation of snow shielding corrections for cosmogenic nuclide surface exposure studies. *Geomorphology*, Vol. **64**, pp. 67-85.

Schlatter, A., Schneider, D., Geiger, A. & Kahle, H., (2005). Recent vertical movements from precise levelling in the vicinity of the city of Basel, Switzerland. *International Journal of Earth Sciences (Geologische Rundschau)*, Vol. **94**, pp. 507-514.

Schlunegger, F. & Hinderer, M., (2001). Crustal uplift in the Alps: Why the drainage pattern matters. *Terra Nova*, Vol. **13**, pp. 425-432.

Schlunegger, F. & Hinderer, M., (2003). Pleistocene/Holocene climate change, re-establishment of fluvial drainage network and increase in relief in the Swiss Alps. *Terra Nova*, Vol. **15**, pp. 88-95.

Schmid, S., Aebli, H., Heller, F. & Zingg, A., (1989). The role of the Periadriatic Line in the tectonic evolution of the Alps. In: *Alpine Tectonics*. Coward, M., Dietrich, D. & Park, R. (Eds.). Geological Society Special Publication, pp. 153-171.

Schmid, S. & Kissling, E., (2000). The arc of the western Alps in the light of geophysical data on deep crustal structure. *Tectonics*, Vol. **19**, pp. 62-85.

Schmid, S., Fuegenschuh, B., Kissling, E. & Schuster, R., (2004). Tectonic map and overall architecture of the Alpine orogen. *Eclogae Geologicae Helvetiae*, Vol. **97**, pp. 93-117.

Servant, M. & Servant-Vildary, S., (2003). Holocene precipitation and atmospheric changes inferred from river paleowetlands in the Bolivian Andes. *Palaeogeography, Palaeoclimatology, Palaeoecology*, Vol. **194**, pp. 187-206.

Seyler, P. & Boaventura, G, (2003). Distribution and partition of trace metals in the Amazon basin. *Hydrological Processes*, Vol. **17**, pp. 1345-1361.

Sierra, R., (2000). Dynamics and patterns of deforestation in the western Amazon: the Napo deforestation front, 1986-1996. *Applied Geography*, Vol. **20 (1)**, pp. 1-16.

Sioli, H., (1957). Sedimentation im Amazonasgebiet. *Geologische Rundschau*, Vol. **45**, pp. 608-633.

Sippel, S., Hamilton, S. & Melack, J., (1992). Inundation area and morphology of lakes on the Amazon River floodplain, Brazil. *Archiv der Hydrobiologie*, Vol. **123**, pp. 385-400.

Slingerland, R. & Smith, N., (2004). River avulsions and their deposits. *Annual Review of Earth and Planetary Sciences*, Vol. **32**, pp. 257-285.

Small, E., Anderson, R., Repka, J. & Finkel, R., (1997). Erosion rates of alpine bedrock summit surfaces deduced from in situ 10Be and 26Al. *Earth and Planetary Science Letters*, Vol. **150**, pp. 413-425.

Soar, P. J., Thorne, C. R. & Harmar, O.P., (2005). Hydraulic geometry analysis of the lower Mississippi. *Final Report*. United States Army European Research Office, p. 92.

Staiger, J., Gosse, J., Little, E., Utting, D., Finkel, R., Johnson, J. & Fastook, J., (2006). Glacial erosion and sediment dispersion from detrital cosmogenic nuclide analyses of till. *Quaternary Geochronology*, Vol. **1**, pp. 29-42.

Stallard, R., (1985). Weathering and erosion in the humid tropics. In: *Physical and chemical weathering in geochemical cycles*. Lerman, A. & Meybeck, M. (Eds.). Kluwer Academic Publishers, pp. 225-246.

Stuewe, K. & Barr, T., (1998). On uplift and exhumation during convergence. *Tectonics*, Vol. **17**, pp. 80-88.

Stuewe, K., White, L. & Brown, R., (1994). The influence of eroding topography on steady-state isotherms. Application to fission track analysis. *Earth and Planetary Science Letters*, Vol. **124**, pp. 63-74.

Summerfield, M., (1991). Tectonic Geomorphology. *Progress in Physical Geography*, Vol. **15**, pp. 193-205.

Summerfield, M. & Hulton, N., (1994). Natural controls of fluvial denudation rates in major world drainage basins. *Journal of Geophysical Research*, Vol. **99 (B7)**, pp. 871-883.

Synal, H., Bonani, G., Doebeli, M., Ender, R., Gartenmann, P., Kubik, P., Schnabel, C. & Suter, M., (1997). Status report of the PSI/ETH AMS facility. *Nuclear Instruments and Methods in Physics Research, Section B: Beam Interactions with Materials and Atoms*, Vol. **B123**, pp. 62-68.

Tapia, P. M., Fritz, S. C., Baker, P. A., Seltzer, G. O. & Dunbar, R.B., (2003). A Late Quaternary diatom record of tropical climatic history from Lake Titicaca (Peru and Bolivia). *Palaeogeography, Palaeoclimatology, Palaeoecology*, Vol. **194**, pp. 139-164.

Thompson, L., Mosley-Thompson, E., Davis, M., Lin, P., Henderson, K., Cole-Dai, J., Bolzan, J. & Liu, K., (1995). Late glacial stage and holocene tropical ice core records from Huascarán, Peru. *Science*, Vol. **269**, pp. 46-50.

Trimble, S., (1995). Catchment sediment budgets and change. In: *Changing River Channels*. Gurnell, A. & Petts, G. (Eds.). John Wiley & Sons, pp. 201-215.

Trimble, S., (1999). Decreased rates of alluvail sediment storage in the Coon Creek Basin, Wisconsin, 1975-1993. *Science*, Vol. **285**, pp. 1244-1246.

Vanacker, V., von Blanckenburg, F., Hewawasam, T. & Kubik, P., (2007a). Constraining landscape development of the Sri Lanken escarpment with cosmogenic nuclides in river sediment. *Earth and Planetary Science Letters*, Vol. **253**, pp. 402-414.

Vanacker, V., von Blanckenburg, F., Govers, G., Molina, A., Poesen, J., Deckers, J. & Kubik, P., (2007b). Restoring dense vegetation can slow mountain erosion to near natural benchmark levels. *Geology*, Vol. **35 (4)**, pp. 303-306.

van Husen, D., (1977). Zur Fazies und Stratigraphie der jungpleistaozänen Ablagerungen im Trauntal (mit Quartärgeologischer Karte). In: *Jahrbuch der Geologischen Bundesanstalt*. Verlag der Geologischen Bundesanstalt, Wien, Österreich, pp. 1-130.

van der Hammen, T. & Hooghiemstra, H., (2000). Neogene and Quaternary history of vegetation, climate, and plant diversity in Amazonia. *Quaternary Science Reviews*, Vol. **19**, pp. 725-742.

Vermeesch, P., (2007). CosmoCalc: An Excel add-in for cosmogenic nuclide calculations. *Geochemistry, Geophysics, Geosystems*, Vol. **8 (8)**, p. 10.1029/2006GC001530.

Vezolli, G., (2004). Erosion in the western Alps (Dora Baltea basin): 2. Quantifying sediment yield. *Sedimentary Geology*, Vol. **171**, pp. 247-259.

Voicu, G., Bardoux, M. & Stevenson, R., (2001). Lithostratigraphy, geochronology and gold metallogeny in the northern Guiana Shield, South America: a review. *Ore Geology Reviews*, Vol. **18**, pp. 211-236.

von Blanckenburg, F., Belshaw, N. & O´Nions, R., (1996). Separation of Be-9 and cosmogenic Be-10 from environmental materials and SIMS isotope dilution analysis. *Chemical Geology*, Vol. **129**, pp. 93-99.

von Blanckenburg, F., Hewawasam, T. & Kubik, P., (2004). Cosmogenic nuclide evidence for low weathering and denudation in the wet, tropical highlands of Sri Lanka. *Journal of Geophysical Research*, Vol. **109**, p. 10.1029/2003JF000049.

von Blanckenburg, F., (2005). The control mechanisms of erosion and weathering at basin scale from cosmogenic nuclides in river sediment. *Earth and Planetary Science Letters- Frontiers*, Vol. **237**, pp. 462-479.

Wagner, G., Reimer, G. & Jaeger, E., (1977). Cooling ages derived by apatite fission-track, mica Rb-Sr and K-Ar dating: The uplift and cooling history of the Central Alps. *Mem.Ist.Geol.Mineral.Univ.Padova*, Vol. **30**, pp. 1-27.

Walling, D. & Webb, B., (1981). The reliability of suspended sediment load data. *IAHS Publication*, Vol. **133**, pp. 177-194.

Walling, D. E., (1983). The sediment delivery problem. *Journal of Hydrology*, Vol. **65**, pp. 209-237.

Walling, D. E. & He, Q., (1998). The spatial variability of overbank sedimentation on river floodplains. *Geomorphology*, Vol. **24**, pp. 209-223.

Ware, E., Schultz, D., Brooks, H., Roebber, P. & Bruening, S., (2006). Improving snowfall forecasting by accounting for the climatological variability of snow density. *Weather and Forecasting*, Vol. **21**, pp. 94-103.

Whipple, K. & Tucker, G., (1999). Dynamics of the stream-power river incision model: Implications for height limits of mountain ranges, landscape response timescales, and research needs. *Journal of Geophysical Research B: Solid Earth*, Vol. **104**, pp. 17661-17674.

Whipple, K., Kirby, E. & Brocklehurst, S., (1999). Geomorphic limits to climate-induced increases in topographic relief. *Nature*, Vol. **401**, pp. 39-43.

Whipple, K., (2001). Fluvial landscape response time: How plausible is steady-state denudation? *American Journal of Science*, Vol. **301**, pp. 313-325.

Whipple, K., (2004). Bedrock rivers and the geomorphology of active orogens. *Annual Review of Earth and Planetary Sciences*, Vol. **32**, pp. 151-185.

Whipple, K. & Meade, B., (2006). Orogen response to changes in climatic and tectonic forcing. *Earth and Planetary Science Letters*, Vol. **243**, pp. 218-228.

Willett, S. & Brandon, M., (2002). On steady states in mountain belts. *Geology*, Vol. **30**, pp. 175-178.

Willett, S., Schlunegger, F. & Picotti, V., (2006). Messinian climate change and erosionale destruction of the Central European Alps. *Geology*, Vol. **34 (8)**, pp. 613-616.

Wittmann, H., von Blanckenburg, F., Kruesmann, T., Norton, K. & Kubik, P., (2007). The relation between rock uplift and denudation from cosmogenic nuclides in river sediment in the Central Alps of Switzerland. *Journal of Geophysical Research A: Earth Surface*, Vol. **112**, p. F04010.

Wobus, C., Helmsath, A., Whipple, K. & Hodges, K., (2005). Active out-of-sequence thrust faulting in the central Nepalese Himalaya. *Nature*, Vol. **434**, pp. 1008-1011.

Wolman, M. & Leopold, L., (1957). River flood plains: Some observations on their formation. *Geological Survey Professional Paper 282-C*. US Government Printing Office, Washington, p. 22.

Zhang, P., Molnar, P. & Downs, W., (2001). Increased sedimentation rates and grain sizes 2-4 Myr ago due to the influence of climate change on erosion rates. *Nature*, Vol. **410**, pp. 891-897.

APPENDIX

APPENDIX A.1

A.1.1 ^{10}BE DATA

Table A.1.1: Be Data

ETH-Code	Sample	Setting	Gran size [µm]	Sample weight [g]	$^{10}Be/^{9}Be$	Relative analytical uncertainty [%]	Weight ^{9}Be Carrier[a] [g]	Average $^{10}Be/^{9}Be$ ratio of Blank [$\times 10^{-14}$]	^{10}Be conc, corr. for Blank [$\times 10^{4}$ at/g$_{(Qz)}$]
ZB5469	Ama-a	Central Amazon	125-250	51.74	3.27E-13	7.7	0.175	2.35 ± 1.08	7.22 ± 0.65
ZB5470	Ama-b[§]	Central Amazon	250-500	76.57	5.31E-13	4.6	0.175	2.35 ± 1.08	8.31 ± 0.40
ZB4560	Be 1a	Beni basin	125-250	32.50	5.98E-14	10.5	0.334	0.55 ± 0.28	3.92 ± 0.50
ZB4169	Be 1b	Beni basin	250-500	52.90	9.04E-14	17.4	0.327	0.55 ± 0.28	3.69 ± 0.69
ZB4561	Be 2a	Beni basin	125-250	32.70	4.55E-14	11.3	0.334	0.55 ± 0.28	2.87 ± 0.42
ZB4562	Be 2b	Beni basin	250-500	26.00	2.35E-14	15.3	0.333	0.55 ± 0.28	1.62 ± 0.41
ZB4402	Be 3a	Beni basin	125-250	37.50	5.94E-14	11.6	0.310	0.55 ± 0.28	3.13 ± 0.43
ZB4716	Be 4a-1	Beni basin	125-250	12.86	7.83E-14	10.7	0.163	0.55 ± 0.28	6.48 ± 0.79
ZB5353	Be 4a-2	Beni basin	125-250	36.52	2.51E-13	9.0	0.159	2.35 ± 1.08	6.96 ± 0.77
ZB4564	Be 7a	Beni basin	125-250	25.20	3.20E-14	12.5	0.327	0.55 ± 0.28	2.42 ± 0.44
ZB5901	Be 7b	Beni basin	250-500	62.48	1.45E-13	9.1	0.175	1.28 ± 0.45	2.60 ± 0.27
ZB4717	Be 8a	Beni basin	125-250	38.24	1.22E-13	12.0	0.164	0.55 ± 0.28	3.53 ± 0.45
ZB4718	Be 10a	Beni basin	125-250	60.99	2.25E-13	8.9	0.164	0.55 ± 0.28	4.14 ± 0.38
ZB4565	Be 12a	Beni basin	125-250	10.90	2.41E-14	14.7	0.337	0.55 ± 0.28	4.04 ± 0.98
ZB4845	Be 15a	Beni basin	125-250	35.97	8.99E-14	30.0	0.165	2.35 ± 1.08	2.14 ± 0.94
ZB4719	Be 16b	Beni basin	250-500	48.10	4.69E-13	10.1	0.163	0.55 ± 0.28	11.06 ± 1.13
ZB4566	Be 17a	Beni basin	125-250	22.20	4.02E-14	13.7	0.333	0.55 ± 0.28	3.66 ± 0.65
ZB4720	Be 18a-1	Beni basin	125-250	42.40	1.76E-13	22.0	0.165	0.55 ± 0.28	4.67 ± 1.06
ZB5341	Be 18a-2	Beni basin	125-250	8.88	6.47E-14	18.4	0.163	2.35 ± 1.08	5.33 ± 2.08
ZB4567	Be 19a	Beni basin	125-250	34.90	6.48E-14	11.3	0.332	0.55 ± 0.28	3.97 ± 0.52
ZB5902	Be 20a	Beni basin	125-250	64.09	2.13E-13	9.8	0.176	1.28 ± 0.45	3.85 ± 0.41
ZB5461	Br 1a	Branco basin	125-250	34.70	1.01E-12	4.2	0.176	2.35 ± 1.08	35.10 ± 1.56
ZB4848	Br 2a	Branco basin	125-250	44.62	1.83E-12	7.1	0.164	2.35 ± 1.08	46.82 ± 3.38
ZB5448	Br 2b	Branco basin	250-500	31.09	1.21E-12	3.4	0.168	2.35 ± 1.08	45.13 ± 1.62
ZB5343	Br 4b	Branco basin	250-500	25.15	1.00E-12	4.4	0.163	2.35 ± 1.08	44.69 ± 2.07
ZB5344	Br 4c	Branco basin	500-800	35.08	1.00E-12	4.6	0.163	2.35 ± 1.08	31.99 ± 1.55
ZB5462	Br 5b	Branco basin	250-500	8.97	3.66E-13	7.3	0.175	2.35 ± 1.08	46.91 ± 3.95
ZB5463	Br 5c	Branco basin	500-800	54.58	1.51E-12	6.4	0.177	2.35 ± 1.08	33.87 ± 2.22
ZB4849	Br 6a	Branco basin	125-250	50.28	1.94E-12	8.8	0.164	2.35 ± 1.08	43.95 ± 3.92
ZB4850	Br 6b	Branco basin	250-500	48.85	1.53E-12	6.3	0.164	2.35 ± 1.08	35.53 ± 2.29
ZB5449	Br 8a	Branco basin	125-250	23.42	8.83E-13	6.8	0.169	2.35 ± 1.08	43.49 ± 3.09
ZB4851	Br 8b-1	Branco basin	250-500	61.88	1.76E-12	8.5	0.164	2.35 ± 1.08	32.24 ± 2.78
ZB5342	Br 8b-2[§]	Branco basin	250-500	16.59	4.78E-13	6.3	0.163	2.35 ± 1.08	32.17 ± 3.78

Table A.1.1 ▪CONTINUED▪

ETH-Code	Sample	Setting	Gran size [µm]	Sample weight [g]	$^{10}Be/^{9}Be$	Relative analytical uncertainty [%]	Weight ^{9}Be Carrier[a] [g]	Average $^{10}Be/^{9}Be$ ratio of Blank [$\times 10^{-14}$]	^{10}Be conc, corr. for Blank [$\times 10^{4}$ at/$g_{(Qz)}$]
ZB2501	Cb 1a	Braz. Shield	125-250	50.20	5.63E-13	4.6	0.308	1.10 ± 0.66	23.18 ± 1.12
ZB6069	Cb 2a	Braz. Shield	125-250	28.20	3.07E-13	5.0	0.220	1.28 ± 0.45	16.14 ± 0.88
ZB5346	Cb 3a-1	Braz. Shield	125-250	41.20	1.42E-12	10.3	0.159	2.35 ± 1.08	37.79 ± 3.97
ZB6070	Cb 3a-2	Braz. Shield	125-250	32.08	6.62E-13	4.9	0.220	1.28 ± 0.45	31.23 ± 1.58
ZB5338	Cb 4a-1[§]	Braz. Shield	125-250	20.34	2.21E-13	8.4	0.163	2.35 ± 1.08	11.73 ± 1.08
ZB4131	Cb 4a-2	Braz. Shield	125-250	51.20	3.09E-13	11.4	0.327	0.55 ± 0.28	13.64 ± 1.59
ZB4130	Cb 4a-3	Braz. Shield	125-250	45.80	3.14E-13	9.0	0.328	0.55 ± 0.28	15.54 ± 1.43
ZB5348	Cb 5b	Braz. Shield	250-500	61.06	1.48E-12	3.4	0.160	2.35 ± 1.08	26.76 ± 0.95
ZB4999	Cb 6b-1	Braz. Shield	250-500	64.51	1.08E-12	6.1	0.165	2.35 ± 1.08	19.00 ± 1.20
ZB5347	Cb 6b-2	Braz. Shield	250-500	55.11	8.90E-13	6.5	0.163	2.35 ± 1.08	18.05 ± 1.23
ZB6071	Cb 6b-3	Braz. Shield	250-500	37.18	4.34E-13	5.2	0.220	1.28 ± 0.45	17.48 ± 0.95
ZB4132	Cb 7a	Braz. Shield	125-250	55.10	1.01E-12	9.2	0.328	0.55 ± 0.28	41.93 ± 3.88
ZB4724	Cb 7b-1	Braz. Shield	250-500	40.22	1.39E-12	5.8	0.165	0.55 ± 0.28	39.95 ± 2.33
ZB5339	Cb 7b-2	Braz. Shield	250-500	11.90	3.65E-13	11.1	0.163	2.35 ± 1.08	32.90 ± 4.04
ZB4725	Cb 8a	Braz. Shield	125-250	68.35	1.50E-12	7.4	0.165	0.55 ± 0.28	25.45 ± 1.89
ZB4726	Cb 8b-1	Braz. Shield	250-500	72.42	1.46E-12	8.2	0.165	0.55 ± 0.28	23.24 ± 1.91
ZB6072	Cb 8b-2	Braz. Shield	250-500	36.51	5.43E-13	4.1	0.220	1.28 ± 0.45	22.44 ± 0.96
ZB4727	Cb 10a	Braz. Highlands	125-250	49.43	7.62E-13	5.5	0.161	0.55 ± 0.28	17.37 ± 0.96
ZB4133	Cb 10b-1	Braz. Highlands	250-500	62.90	3.28E-13	8.9	0.329	0.55 ± 0.28	11.86 ± 1.08
ZB5340	Cb 10b-2[§]	Braz. Highlands	250-500	16.58	1.89E-13	6.5	0.163	2.35 ± 1.08	12.20 ± 0.91
ZB5349	Cb 12a	Andes	125-250	30.63	2.98E-13	9.2	0.160	2.35 ± 1.08	10.10 ± 1.08
ZB4855	Cb 15b	Andes	250-500	65.16	9.05E-14	11.0	0.164	2.35 ± 1.08	1.18 ± 0.26
ZB2502	Cb 16a	Andes	160-250	50.00	4.21E-14	17.4	0.309	1.10 ± 0.66	1.32 ± 0.42
ZB2503	Cb 16b	Andes	250-400	50.40	3.38E-14	17.3	0.310	1.10 ± 0.66	0.96 ± 0.37
ZB4856	Cb 17b	Andes	250-500	67.47	1.87E-13	13.8	0.164	2.35 ± 1.08	2.80 ± 0.48
ZB2504	Cb 18a	Andes	125-250	51.00	5.32E-14	13.0	0.308	1.10 ± 0.66	1.75 ± 0.40
ZB2505	Cb 18b	Andes	250-500	32.10	3.09E-14	16.2	0.310	1.10 ± 0.66	1.32 ± 0.55
ZB5350	Cb 19b	Andes	250-500	70.80	1.81E-13	8.8	0.159	2.35 ± 1.08	2.50 ± 0.30
ZB5351	Cb 21a	Andes	125-250	56.69	1.08E-13	10.9	0.160	2.35 ± 1.08	1.68 ± 0.32
ZB5447	Cb 22b[$]	Andes	250-500	40.02	3.43E-14	12.8	0.168	2.35 ± 1.08	0.32 ± 4.49
ZB5001	Cb 23a	Andes	125-250	47.72	2.68E-13	10.2	0.164	2.35 ± 1.08	5.92 ± 0.71
ZB2506	Cb 25a	Andes	160-250	49.80	3.45E-13	5.2	0.310	1.10 ± 0.66	14.24 ± 0.82

Table A.1.1 ▪CONTINUED▪

ETH-Code	Sample	Setting	Gran size [µm]	Sample weight [g]	$^{10}Be/^{9}Be$	Relative analytical uncertainty [%]	Weight ^{9}Be Carrier[a] [g]	Average $^{10}Be/^{9}Be$ ratio of Blank [$\times 10^{-14}$]			^{10}Be conc, corr. for Blank [$\times 10^{4}$ at/$g_{(Qz)}$]		
ZB5641	Curu-a	Central Amazon-Lake	125-250	46.18	5.62E-13	5.2	0.176	1.28	±	0.45	14.73	±	0.79
ZB5488	Curu-b	Central Amazon-Lake	250-500	89.59	7.62E-13	3.9	0.176	2.35	±	1.08	10.17	±	0.44
ZB5639	Gran-b	Central Amazon-Lake	250-500	98.88	5.56E-13	5.8	0.177	1.28	±	0.45	6.83	±	0.41
ZB5640	Gran-c	Central Amazon-Lake	500-800	100.45	4.53E-13	6.2	0.177	1.28	±	0.45	5.45	±	0.35
ZB5484	Ir 0.4b	Central Amazon	250-500	92.06	6.76E-13	6.0	0.176	2.35	±	1.08	8.77	±	0.56
ZB5485	Ir 0.4c	Central Amazon	500-800	98.47	1.08E-12	3.3	0.176	2.35	±	1.08	13.31	±	0.47
ZB5452	Ir 1.5b	Central Amazon	250-500	99.36	8.50E-13	4.0	0.173	2.35	±	1.08	10.10	±	0.44
ZB5453	Ir 1.5c	Central Amazon	500-800	99.00	1.29E-12	3.5	0.173	2.35	±	1.08	15.50	±	0.57
ZB5629	Ir 1.75a	Central Amazon	125-250	48.13	2.73E-13	7.7	0.177	1.28	±	0.45	6.72	±	0.55
ZB5630	Ir 1.75b	Central Amazon	250-500	52.75	2.69E-13	9.7	0.176	1.28	±	0.45	6.02	±	0.62
ZB5631	Ir 1.75c	Central Amazon	500-800	81.34	8.34E-13	5.7	0.176	1.28	±	0.45	12.52	±	0.73
ZB5903	Mad 0.5a	Madeira basin	125-250	36.17	2.00E-13	8.1	0.176	1.28	±	0.45	6.40	±	0.57
ZB5904	Mad 0.5b	Madeira basin	250-500	36.93	2.77E-13	8.9	0.176	1.28	±	0.45	8.84	±	0.84
ZB5906	Mad 1.1b	Madeira basin	250-500	55.7	5.31E-13	8	0.175	1.28	±	0.45	11.49	±	0.95
ZB5635	Mad 1.1c	Madeira basin	500-800	69.2	1.23E-12	4.4	0.176	1.28	±	0.45	21.80	±	0.97
ZB5467	Mad 1.8a	Madeira basin	125-250	42.5	1.83E-13	10.1	0.178	2.35	±	1.08	4.70	±	0.63
ZB5468	Mad 1.8b	Madeira basin	250-500	87.7	6.09E-13	5.2	0.140	2.35	±	1.08	6.56	±	0.38
ZB5632	Man 0.2a	Central Amazon	125-250	77.8	4.10E-13	6	0.177	1.28	±	0.45	6.36	±	0.40
ZB5633	Man 0.2b	Central Amazon	250-500	57.5	2.28E-13	8.3	0.176	1.28	±	0.45	4.64	±	0.42
ZB5634	Man 0.2c	Central Amazon	500-800	65.4	4.21E-13	10.9	0.177	1.28	±	0.45	7.73	±	0.87
ZB5450	Man 1.1a	Central Amazon	125-250	81.6	4.08E-13	11.4	0.183	2.35	±	1.08	6.05	±	0.75
ZB5451	Man 1.1b[§]	Central Amazon	250-500	80.9	5.18E-13	4.2	0.173	2.35	±	1.08	7.59	±	0.33
ZB5905	Man 1.1c	Central Amazon	500-800	74.6	4.54E-13	6.9	0.176	1.28	±	0.45	7.31	±	0.52
ZB5486	Man 2.85a	Central Amazon	125-250	68.1	3.98E-13	6.9	0.176	2.35	±	1.08	6.81	±	0.54
ZB5487	Man 2.85b	Central Amazon	250-500	73.3	4.55E-13	5.4	0.176	2.35	±	1.08	7.30	±	0.45
ZB5910	Na 0a-1	Napo basin	125-250	26.7	5.78E-14	11.1	0.177	1.28	±	0.45	2.09	±	0.36
ZB5911	Na 0a-2	Napo basin	125-250	8.6	3.07E-14	13.8	0.176	1.28	±	0.45	2.59	±	0.89
ZB4403	Na 1b	Napo basin	250-500	37.8	3.52E-14	19	0.333	0.55	±	0.28	1.84	±	0.45
ZB4640	Na 4b	Napo basin	250-500	33.7	2.30E-14	25.6	0.326	0.55	±	0.28	1.19	±	0.44
ZB5457	Na 5b[$]	Napo basin	250-500	26.2	4.09E-14	13.2	0.175	2.35	±	1.08	0.82	±	0.57
ZB4641	Na 6b	Napo basin	250-500	25.1	9.40E-15	45.9	0.329	0.55	±	0.28	0.36	±	0.47
ZB5458	Na 7b	Napo basin	250-500	36.1	6.97E-14	15	0.175	2.35	±	1.08	1.57	±	0.51
ZB4642	Na 8b	Napo basin	250-500	37.3	2.00E-14	29.1	0.367	0.55	±	0.28	1.00	±	0.45

Table A.1.1 ▪CONTINUED▪

ETH-Code	Sample	Setting	Gran size [µm]	Sample weight [g]	$^{10}Be/^{9}Be$	Relative analytical uncertainty [%]	Weight ^{9}Be Carrier[a] [g]	Average $^{10}Be/^{9}Be$ ratio of Blank [$\times 10^{-14}$]			^{10}Be conc, corr. for Blank [$\times 10^{4}$ at/$g_{(Qz)}$]		
ZB5345	Na 10b	Napo basin	250-500	21.4	4.54E-14	12.2	0.160	2.35	±	1.08	1.16	±	0.64
ZB4175	Na 11a	Napo basin	125-250	24.3	1.78E-14	38	0.328	0.55	±	0.28	1.16	±	0.69
ZB4853	Na 13a	Napo basin	125-250	33.6	5.23E-14	11.5	0.164	2.35	±	1.08	0.99	±	0.42
ZB4643	Na 13b[$]	Napo basin	250-500	7.5	8.20E-15	30	0.333	0.55	±	0.28	0.84	±	1.16
ZB4644	Na 14b	Napo basin	250-500	24.1	1.51E-14	24.3	0.334	0.55	±	0.28	0.93	±	0.45
ZB5459	Na 15b	Napo basin	250-500	25.4	5.12E-14	12.8	0.175	2.35	±	1.08	1.34	±	0.61
ZB4645	Na 16b	Napo basin	250-500	25.6	1.95E-14	22.7	0.331	0.55	±	0.28	1.27	±	0.48
ZB4721	Na 18a	Napo basin	125-250	50.2	1.17E-13	21.8	0.163	0.55	±	0.28	2.56	±	0.59
ZB5460	Na 18b	Napo basin	250-500	15.7	5.04E-14	11.1	0.174	2.35	±	1.08	2.11	±	0.95
ZB4854	Na 19a	Napo basin	125-250	37.4	6.25E-14	11.2	0.163	2.35	±	1.08	1.20	±	0.40
ZB4646	Na 21b	Napo basin	250-500	24.5	1.70E-14	16.8	0.326	0.55	±	0.28	1.08	±	0.37
ZB4177	Na 23b	Napo basin	250-500	39.3	3.64E-14	15.5	0.663	0.55	±	0.28	3.66	±	0.75
ZB4997	Na 23b-2	Napo basin	250-500	28.2	1.37E-13	9.7	0.156	2.35	±	1.08	4.41	±	0.67
ZB5455	Ne LB-a	Negro basin	125-250	78.4	5.07E-13	7.4	0.186	2.35	±	1.08	8.05	±	0.65
ZB5456	Ne LB-b	Negro basin	250-500	101.2	6.39E-13	4.7	0.174	2.35	±	1.08	7.45	±	0.39
ZB5909	Ne LB-c	Negro basin	500-800	44.6	1.74E-13	9.1	0.217	1.28	±	0.45	5.53	±	0.56
ZB5454	Ne RB-a	Negro basin	125-250	98.3	8.09E-13	4.2	0.183	2.35	±	1.08	10.28	±	0.47
ZB5483	Ne RB-b	Negro basin	250-500	59.5	4.64E-13	5.4	0.176	2.35	±	1.08	9.14	±	0.57
ZB5636	Ne RB-c	Negro basin	500-800	77.6	3.97E-13	7.3	0.177	1.28	±	0.45	6.15	±	0.47
ZB5638	Par 1.2b	Central Amazon	250-500	48.8	3.83E-13	7.2	0.177	1.28	±	0.45	9.42	±	0.71
ZB5907	Par 1.2c	Central Amazon	500-800	49.0	6.76E-13	10.4	0.176	1.28	±	0.45	16.73	±	1.78
ZB5465	Par 2.2a	Central Amazon	125-250	32.3	2.02E-13	8.7	0.177	2.35	±	1.08	6.88	±	0.80
ZB5466	Par 2.2b	Central Amazon	250-500	52.6	3.32E-13	9.1	0.177	2.35	±	1.08	7.29	±	0.76
ZB4714	Pe 101a	Central Amazon	125-250	50.4	3.25E-13	6.8	0.164	0.55	±	0.28	7.30	±	0.51
ZB4173	Pe 104b	Napo basin	250-500	23.9	5.34E-14	20.9	0.328	0.55	±	0.28	4.62	±	1.11
ZB4715	Pe 107a	Central Amazon	125-250	58.8	2.93E-13	10.9	0.164	0.55	±	0.28	5.64	±	0.63
ZB5643	Soc b	Central Amazon-Lake	250-500	52.0	2.10E-13	8.1	0.177	1.28	±	0.45	4.72	±	0.42
ZB5489	Soc-c-1[§]	Central Amazon-Lake	500-800	89.7	3.55E-13	4.3	0.176	2.35	±	1.08	4.72	±	0.22
ZB5642	Soc-c-2	Central Amazon-Lake	500-800	48.0	1.77E-13	8.7	0.177	1.28	±	0.45	4.24	±	0.41
ZB5471	Tapa-b	Tapajós basin	250-500	126.5	1.00E-12	5.2	0.177	2.35	±	1.08	9.65	±	0.52
ZB5472	Tapa-c	Tapajós basin	500-800	95.7	7.10E-13	5.9	0.176	2.35	±	1.08	8.85	±	0.56

Table A.1.1 ▪CONTINUED▪

ETH-Code	Sample	Setting	Gran size [µm]	Sample weight [g]	$^{10}Be/^{9}Be$	Relative analytical uncertainty [%]	Weight ^{9}Be Carrier[a] [g]	Average $^{10}Be/^{9}Be$ ratio of Blank [$x10^{-14}$]	^{10}Be conc, corr. for Blank [$x10^{4}$ at/$g_{(Qz)}$]
ZB2022	Saf 1	Alps-moraine	400-1000	76.1	1.1E-13	26.0	0.299	1.10 ± 0.66	2.64 ± 0.78
ZB2029	Saf 2	Alps-moraine	400-1000	59.0	7.6E-14	11.2	0.303	1.10 ± 0.66	2.29 ± 0.38
ZB2032	Herens 1	Alps-moraine	400-1000	23.4	2.0E-14	28.1	0.302	1.10 ± 0.66	0.79 ± 0.77
ZB2039	Fin 4	Alps-moraine	400-1000	61.1	7.9E-14	17.2	0.301	1.10 ± 0.66	2.30 ± 0.51
ZB4553	Mela 1 GF	Centovalli-moraine	125-250	52.2	8.4E-15	32.9	0.328	0.55 ± 0.28	0.13 ± 0.17
ZB2036	Fin 1	Alps-glacial sed.	400-1000	27.7	1.2E-13	27.7	0.299	1.10 ± 0.66	7.78 ± 2.43
ZB2037	Fin 2	Alps-glacial sed.	400-1000	45.1	6.2E-14	33.2	0.299	1.10 ± 0.66	2.32 ± 0.98
ZB2025	Mine 4_1	Alps-glacial sed.	400-1000	75.1	3.0E-14	22.6	0.299	1.10 ± 0.66	0.52 ± 0.26
ZB2034	Mine 4_2	Alps-glacial sed.	400-1000	77.3	5.4E-14	22.0	0.303	1.10 ± 0.66	1.15 ± 0.37
ZB2177	Mine 5	Alps-glacial sed.	400-1000	40.3	3.5E-14	20.0	0.306	1.10 ± 0.66	1.25 ± 0.50
ZB2034	Mine 6	Alps-glacial sed.	400-1000	18.4	2.8E-14	24.4	0.301	1.10 ± 0.66	1.90 ± 1.06
ZB2176	Massa	Alps-glacial sed.	400-1000	55.1	3.1E-14	25.0	0.306	1.10 ± 0.66	0.76 ± 0.39
ZB2183	Matt	Alps-glacial sed.	400-1000	57.9	9.5E-14	35.0	0.303	1.10 ± 0.66	3.01 ± 1.22
ZB3086	Mag 1a	Alps-Valle Maggia	500-800	45.7	7.6E-14	15.0	0.313	1.10 ± 0.66	3.05 ± 0.62
ZB3087	Mag 2a	Alps-Valle Maggia	500-800	45.7	8.6E-14	12.4	0.316	1.10 ± 0.66	3.55 ± 0.59
ZB3089	Mag 4a	Alps-Valle Maggia	500-800	49.3	4.6E-14	12.0	0.316	1.10 ± 0.66	1.53 ± 0.38
ZB2866	Mag 8a	Alps-Valle Maggia	500-800	46.6	5.7E-14	10.8	0.311	1.10 ± 0.66	2.10 ± 0.41
ZB2867	Mag 10a	Alps-Valle Maggia	500-800	47.5	6.5E-14	10.3	0.305	1.10 ± 0.66	2.38 ± 0.41
ZB4555	Mag 11-2	Alps-Valle Maggia	500-800	41.4	4.6E-14	12.9	0.329	0.55 ± 0.28	2.24 ± 0.36
ZB4556	Mag 11-4	Alps-Valle Maggia	500-800	52.4	4.9E-14	12.9	0.329	0.55 ± 0.28	1.93 ± 0.31
ZB3090	Mag 13a	Alps-Valle Maggia	800-1000	48.0	8.3E-14	12.1	0.315	1.10 ± 0.66	3.24 ± 0.54
ZB3091	Mag 16a	Alps-Valle Maggia	500-800	47.4	4.8E-14	13.9	0.314	1.10 ± 0.66	1.68 ± 0.43
ZB3092	Mag 17a	Alps-Valle Maggia	500-800	45.6	1.2E-13	11.8	0.314	1.10 ± 0.66	5.06 ± 0.73
ZB2872	Mag 18a	Alps-Valle Maggia	500-800	46.1	8.1E-14	8.7	0.314	1.10 ± 0.66	3.27 ± 0.45

Table A.1.1 ▪CONTINUED▪

ETH-Code (or original code)	Sample	Setting	Gran size [µm]	Sample weight [g]	$^{10}Be/^{9}Be$	Relative analytical uncertainty [%]	Weight ^{9}Be Carrier[a] [g]	Average $^{10}Be/^{9}Be$ ratio of Blank [$x10^{-14}$]			^{10}Be conc, corr. for Blank [$x10^{4}$ at/$g_{(Qz)}$]		
Tra 4	Anza	Alps-traverse	125-250	43.9	5.0E-14	20.0	0.312	1.10	±	0.66	1.88	±	0.58
Tra 6	Sesia	Alps-traverse	125-250	37.8	6.3E-14	11.8	0.310	1.10	±	0.66	2.90	±	0.56
Tra 3-a	Toce-a	Alps-traverse	250-500	89.2	9.4E-14	13.0	0.307	1.10	±	0.66	1.95	±	0.33
Tra 3-b	Toce-b	Alps-traverse	800-1000	62.5	4.6E-14	9.4	0.308	1.10	±	0.66	1.19	±	0.27
Tra 9-a	Verz-a	Alps-traverse	500-800	46.4	6.4E-14	11.3	0.310	1.10	±	0.66	2.44	±	0.45
Tra 9-b	Verz-b	Alps-traverse	800-1000	38.2	5.5E-14	11.6	0.310	1.10	±	0.66	2.47	±	0.51
ZB4552	Mela 1	Centovalli	125-250	60.1	3.0E-14	13.7	0.333	0.55	±	0.28	0.96	±	0.19
ZB4846	Mela 2	Centovalli	125-250	32.2	3.6E-14	30.9	0.163	0.55	±	0.28	1.07	±	0.40
ZB2869	Mela 3a	Centovalli	125-250	44.3	4.9E-14	12.9	0.314	1.10	±	0.66	1.84	±	0.44
ZB2870	Mela 3b	Centovalli	250-500	45.9	5.8E-14	10.5	0.312	1.10	±	0.66	2.19	±	0.42
ZB2030	Lonza	Alps-traverse	400-1000	63.3	5.4E-14	15.2	0.305	1.10	±	0.66	1.42	±	0.35
ZB2045	Gren	Alps-traverse	400-1000	36.7	3.4E-14	9.6	0.304	1.10	±	0.66	1.30	±	0.42
Tra 16	Chie	Alps-traverse	500-800	51.2	7.3E-14	18.6	0.309	1.10	±	0.66	2.56	±	0.62
Tra 19	Furka	Alps-traverse	250-1000	61.3	5.9E-14	8.4	0.311	1.10	±	0.66	1.68	±	0.29
Tra 15-a	Tic-a	Alps-traverse	125-250	48.4	5.5E-14	14.1	0.316	1.10	±	0.66	1.95	±	0.45
Tra 15-b	Tic-b	Alps-traverse	250-500	50.4	8.1E-14	14.3	0.314	1.10	±	0.66	2.98	±	0.57
Tra 22-a	Reuss-a	Alps-traverse	125-250	47.9	4.4E-14	16.5	0.309	1.10	±	0.66	1.45	±	0.43
Tra 22-b	Reuss-b	Alps-traverse	250-500	40.8	3.0E-14	14.7	0.311	1.10	±	0.66	1.00	±	0.42
Tra 23-a	Klem-a	Mittelland-traverse	125-250	47	6.4E-14	12.5	0.315	1.10	±	0.66	2.43	±	0.48
Tra 23-b	Klem-b	Mittelland-traverse	250-500	39.6	4.6E-14	11.8	0.311	1.10	±	0.66	1.88	±	0.46
ZB2173	Bütsch 1	Mittelland-traverse	400-1000	57	2.0E-13	15.0	0.308	1.10	±	0.66	7.00	±	1.14
ZB2179	Bütsch 2	Mittelland-traverse	400-1000	52.4	2.1E-13	10.0	0.307	1.10	±	0.66	8.06	±	0.89
ZB2043	Emme	Mittelland-traverse	400-1000	59	1.1E-13	8.9	0.302	1.10	±	0.66	3.54	±	0.42
ZB2174	Wasen 1-1	Mittelland-traverse	400-1000	54.3	9.3E-14	20.0	0.302	1.10	±	0.66	3.13	±	0.75
ZB2044	Wasen 1-2	Mittelland-traverse	400-1000	26.2	5.3E-14	6.1	0.308	1.10	±	0.66	3.38	±	0.59
ZB2023	Taf	Mittelland-traverse	400-1000	74.9	1.7E-13	10.1	0.299	1.10	±	0.66	4.32	±	0.50
ZB2042	Sense	Mittelland-traverse	400-1000	24.5	5.8E-14	10.0	0.303	1.10	±	0.66	3.99	±	0.75

[$] Not discussed in any chapter

[§] Mean from two analyses to improve uncertainty

A.1.2 ^{26}AL DATA

Table A.1.2: Al Data

ETH- Code	Sample	Sample weight [g]	$^{26}Al/^{27}Al$	^{26}Al Conc. [x10^4 at/$g_{(Qz)}$]	Rel. analytical uncertainty for ^{26}Al conc.[1] [%]	^{27}Al Conc.[2] [µg/g]	Relative analytical uncertainty for ^{27}Al conc.[3] [%]	$^{10}Be/^{9}Be$	^{10}Be Conc.[4] [x10^4 at/$g_{(Qz)}$]	Relative analytical & blank uncertainty for ^{10}Be conc.[5] [%]
ZA1055	Br 1a	34.70	4.41E-13	216.03	6.1	219.33	3.5	1.01E-12	35.93	4.4
ZA1178	Br 4c	35.08	5.04E-13	185.64	7.1	165.06	5.6	1.00E-12	32.75	4.8
ZA1056	Br 5b	8.97	8.75E-13	183.26	8.7	93.88	3.5	3.66E-13	50.12	8.4
ZA1179	Br 5c	54.58	1.12E-12	189.78	4.9	75.59	4.0	1.51E-12	34.41	6.5
ZA1057	Br 8b-2§	16.59	7.35E-13	169.62	6.1	103.41	3.7	4.78E-13	33.06	6.5
ZA1177	Ne RB-a	98.32	6.83E-13	47.66	6.0	31.27	3.7	8.09E-13	10.58	4.5
ZA1063	Ne LB-a	78.45	5.24E-13	32.55	6.7	27.85	4.1	5.07E-13	8.45	8.1
ZA1180	Ne LB-b	101.16	4.70E-13	32.10	7.2	30.59	3.6	6.39E-13	7.74	5.2
ZA1190	Cb 2a	28.20	4.85E-13	101.88	6.4	94.19	2.3	3.07E-13	16.84	5.4
ZA1191	Cb 3a-2	32.08	6.42E-13	184.71	6.9	128.83	3.6	6.62E-13	31.85	5.0
ZA1058	Cb 4a-1§	20.34	5.50E-13	78.44	8.4	63.96	4.9	2.21E-13	12.45	9.2
ZA1192	Cb 6b-3	37.18	6.73E-13	99.27	7.8	66.05	3.9	4.34E-13	18.01	5.5
ZA1059	Cb 7b-2	11.90	7.62E-13	164.70	5.5	96.80	7.0	3.65E-13	35.16	12.3
ZA1193	Cb 8b-2	36.51	8.56E-13	114.75	5.0	60.09	2.2	5.43E-13	22.98	4.3
ZA1060	Cb 10b-2§	16.58	4.85E-13	73.14	10.6	67.57	6.4	1.89E-13	13.09	7.4
ZA1185	Ir 0.4c	98.47	4.12E-13	92.86	6.8	101.03	5.7	1.08E-12	13.61	3.5
ZA1066	Ir 1.5b	99.36	8.54E-14	38.34	20.8	201.14	3.5	8.50E-13	10.39	4.3
ZA1181	Ir 1.5c	99.00	3.95E-13	72.36	7.8	82.14	2.7	1.29E-12	15.79	3.7
ZA1183	Man 0.2a	77.81	1.64E-14	53.94	37.7	1473.69	5.8	4.10E-13	6.57	6.3
ZA1174	Man 1.1b§	80.94	7.23E-14	32.81	26.5	203.35	2.8	5.18E-13	7.79	4.4
ZA1184	Mad 1.1c	69.18	2.54E-13	104.37	9.4	184.47	3.2	1.23E-12	22.03	4.5
ZA1175	Ama-b§	76.57	2.83E-14	34.60	29.5	547.74	3.4	5.31E-13	8.52	4.8
ZA1065	Tapa-c	95.73	3.97E-13	50.56	7.5	57.05	3.4	7.10E-13	9.15	6.3
ZA1182	Curu-b	89.59	2.06E-13	28.49	9.7	62.00	3.1	7.62E-13	10.50	4.3
ZA1176	Soc-c-1§	89.72	1.09E-13	30.38	14.0	124.63	4.6	3.55E-13	4.90	4.6
ZA1186	Gran-b	98.88	2.70E-13	45.79	12.5	76.04	4.8	5.56E-13	6.99	6.0

[1]Uncertainty contains analytical error of AMS measurement
[2]Measured by standard addition method on ICP-OES
[3]Uncertainty contains analytical error of ICP-OES measurement and weighting errors of aliquots and standards
[4]Not corrected for blank
[5]Uncertainty contains analytical as well as blank error propagation

APPENDIX A.2

A.2 SAMPLE PREPARATION AND LABORATORY METHODOLOGY FOR THE SEPARATION OF COSMOGENIC ^{10}BE AND ^{26}AL

A.2.1 QUARTZ PREPARATION

Preliminary

Sieve dry sample to appropriate size fractions, leave small unsieved portion behind
If iron particle content is high: clean sample with hand magnet
If magnetic mineral content is high: Frantz magnetic separation
Take weight. Sample should have >200 g, depending on Quartz content
Wash ~300 g with deionised water
Add 3M (= 10%) HCl (12M HCl : H_2O = 1 : 3) (carbonate content => foam)
Sample with 250 ml 3M HCl in 1 liter bottles in shaker for >2 days
Wash with deionised water
Repeat step if solution is very dirty (yellow)

HF leach in hot shaking bath:

1. 500 ml 3M (= 5%) HF (28M HF: deionised H_2O = 1 : 9) and shake for ~1day wash with deionised water
2. 500 ml 3M HF, shake for 1 day and wash with deionised water
3. 500 ml 3M HF, shake for 2-5 days and wash with deionised water
4. 500 ml 3M HF, shake for 2-5 days and wash with deionised water

Repeat step 4 if sample is still impure
Wash with Milli-Q H_2O, dry sample
~Further Frantz magnet separation
~Heavy liquid (bromoform, d = 2.83)
~Hand picking
Optional: Use ~5M (8%) HF for more rapid separation, but that will result in increased Qtz loss (in any case the procedure has to be adapted to the specific sample type)

Reagent quality

From hereon use p.a. grade or better quality acids and reagents only, and use Milli-Q H_2O

Purity control (ICP-OES)

Take ca. 200 mg of each sample in 7 ml Savillex beakers
Weigh the amount of sample
Add 3 ml 28M HF, and heat overnight with closed lid; and evaporate afterwards
Add 1 ml 15M HNO_3, and heat 1 hour with closed lid; and evaporate
Check if all material is dissolved, if not add Aqua Regia (2 ml 6M HCL and 1 ml 15M HNO_3) and evaporate
Add 1 ml 0.3 M HNO_3 to beaker, make sure all sample dissolves
Dilute to convenient concentration, Shake
Measure concentrations on ICP-OES, for Al-procedure sample should have <100 ppm Al, for Be-procedure <1 mg

A.2.2 SAMPLE DECOMPOSITION AND ^{10}BE & ^{26}AL SEPARATION

Final Quartz Leach

1.) Take weight of 90 ml or 240 ml Savillex beaker including lid (max 50g Qtz in 90ml Savillex beaker, max ca. 150 g in 240 ml beaker)
Add 7M HF so that sample is just all covered with HF plus 5 mm excess liquid height
(28M HF: Milli-Q H_2O = 1 : 3)
Heat 1 hour maximum 120°C with lid
Cool down
Wash with Milli-Q H_2O

2.) Add Aq. Re.so that sample is just all covered with acid plus 5 mm excess liquid height
(15M HNO_3 : 6M HCl = 1 : 3)
Cold without lid until gas gone (~30 min)
Minimum 1 hour hot (120°C) with lid
Wash, rinse, shake thoroughly (4-5x) with Milli-Q H_2O
Dry on hotplate in Savillex Beaker
Take precise weight

Sample dissolution, Carrier addition

1.) Add carrier amount depending on AMS requirements, take precise weight
0.15 mg Be (*ETH-AMS only*)

Stochiometric reaction: $SiO_2 + 4\ HF \rightarrow SiF_4 + 2\ H_2O$
Need 116 ml 28M HF for 50 g Quartz

2. a) Add 28M HF so that sample is fully covered with acid plus 5 mm excess liquid height.
1st and 2nd additions: strong exothermic reaction; do not heat; add HF in increments!
Heat (120°C) without lid, evaporate to dryness
3rd addition: add HF 2x that of Qtz volume, put open beaker on hot plate and evaporate
Repeat if not all Qtz is dissolved
Dry down. Don't loose any sample flakes! Do not touch open beaker with gloves!

2. b) Alternative: Single Step dissolution method
Take 240 ml Savillex beaker
Add 2x stochiometric amount of HF. CAREFUL!
Place closed beakers into cold water bath, wait minimum 2 hours (better overnight)
Close beaker and heat until all Qtz is dissolved
Evaporate

3. a) Sample conversion
Add 20 ml Aq. Reg. (6 ml 15M HNO_3 and 12 ml 6M HCl)
Hot until all residue dissolved and evaporate gently
Add 10 ml 6M HCl
Transfer into cleaned 10 ml centrifuge tubes
Centrifuge 5 min, 3000 rpm
Check Purity by ICP-OES

3. b) Optional BeF_2-Leaching (only when NO Al-chemistry is done)
Do not add Aq. Reg. to sample
Add 10 ml H_2O to fluoride cake
Heat gently for 1 hour
Pipette off 10 ml supernate (containing water-soluble BeF_2, TiF_4, $Fe(II)F_2$ but no AlF_3) into Savillex beaker
Evaporate supernate
Add 10 ml 6M HCl
Transfer into cleaned 10 ml centrifuge tubes centrifuge 5 min, 3000 rpm
Check Purity by ICP-OES

4.) Al-chemistry
Label 15 ml cleaned centrifuge tubes for Al-TSS, place empty tube on balance, zero balance
Label cleaned 60 ml bottle for Al-aliquot, place on second (less precise) balance, take bottle weight, then zero balance
Transfer sample solution into small tube, leave undissolved residue behind, take weight of TSS (total sample solution)
Take 250 µl aliquot, transfer into 60 ml bottle, take weight of Al aliquot
Add 5 ml 3M HNO_3 to Al aliquot (in strong acid to prevent adsorption of Al)
Before OES measurement: dilute to 0.3M HNO_3 by addition of 45 ml Milli-Q H_2O

Separation of ^{10}Be and ^{26}Al

1.) Column Fe
2 ml Biorad 1x8 100-200 mesh in 15 ml Eichrom column stored in H_2O
Sample is in 10 ml 6M HCl

Open column and let H_2O drop out

5 + 5 ml	0.3M HCl	clean resin
2 + 2 + 2 ml	6M HCl	condition resin
Load sample		collect Be (+Al)
2 + 2 + 2 ml	6M HCl	collect Be (+Al)
5 + 5 ml	0.3M HCl	clean resin

Seal and store column in Milli-Q H_2O

Evaporate sample
Add 4 ml (20 ml for dirty Qtz) 0.4M Oxalic Acid on sample
Warm to 60° with lid for ~2 hours
Cool down, wait for 30 min, transfer to 10 ml centrifuge tube
Centrifuge 5 min, 3000 rpm,
Load supernate only to Be column

2. a) Small column Be (clean samples: Al <5 mg)
1 ml Biorad AG50-X8 (200-400 mesh) in 7.5 ml RKBN104704 column stored in H_2O
Sample in 4 ml 0.4M Oxalic Acid (amount can be adapted if sample is not completely dissolved)

Open column and let H_2O drop out

2 + 3 ml	5M HNO_3	clean resin
2 + 3 ml	Milli-Q H_2O	remove HNO_3 from resin
2 + 3 ml	0.4M Oxalic Acid	condition resin
Load sample		collect Al
1 ml	0.4M Oxalic Acid	collect Al
1 ml	0.4M Oxalic Acid	collect Al
5 + 5 ml	0.4M Oxalic Acid	collect Al (elute Fe, Al, Ti)
1 + 2 ml	Milli-Q H_2O	remove Oxalic Acid from Column
2 + 2+ 4 ml	0.5M HNO_3	elute Na
3 + 3 +5 ml	1M HNO_3	collect Be
5 + 5 ml	5M HNO_3	clean resin
5 ml	H_2O	remove 5M HNO_3

Seal & store column in Milli-Q H_2O
Go to Be precipitation directly

2. b) Large column Be (dirty samples: Al >5mg)
5 ml Biorad AG50-X8 (200-400 mesh) in 15 ml Eichrom column stored in H_2O
Sample in 20 ml 0.4M Oxalic Acid (amount can be adapted if sample is not completely dissolved)

Open column and let H_2O drop out

5 + 5 ml	5M HNO_3	clean resin
5 + 5 ml	Milli-Q H_2O	remove HCl from resin
5 + 10 ml	0.4M Oxalic Acid	condition resin
Load sample		collect Al
5 ml	0.4M Oxalic Acid	collect Al
5 ml	0.4M Oxalic Acid	collect Al
25 + 25 ml	0.4M Oxalic Acid	collect Al (elute Fe, Al, Ti)
5 + 10 ml	Milli-Q H_2O	remove Oxalic Acid from Column
15 + 25 ml	0.5M HNO_3	elute Na
10 ml	1M HNO_3	wash
20 + 15 ml	1M HNO_3	collect Be
20 + 20 ml	5M HNO_3	clean resin
5+5 ml	H_2O	remove 5M HNO_3

Seal & store column in Milli-Q H_2O
Dry down, take up in 11 ml 1M HNO_3, and go to Be precipitation

3.) Column Al

1 ml Biorad AG1-X8 (100-200 mesh) in 7.5 ml RKBN104704 column stored in H_2O
Sample in 0.4M Oxalic Acid from Be-column
Open column and let H_2O drop out

2 ml	Milli-Q H_2O	clean resin
5 + 5 ml	0.3M HCl	clean resin
2 + 2 ml	H_2O	remove HCl
2 + 2 + 2 ml	0.4M Oxalic Acid	condition resin
Load sample		save effluent in case Al elutes early
4 + 2 ml	0.05M Ox/0.5M HCl	wash, save effluent in case Al elutes early
5 + 5 ml	0.05M Ox/0.5M HCl	collect Al
5 + 5 ml	0.3M HCl	elute Ti

Seal and store column in Milli-Q H_2O
(Mixture of 0.05M Oxalic Acid and 0.5M HCl is prepared by mixing equal amounts of 0.1M Oxalic Acid and 1M HCl)

Dry down sample in Savillex beaker
Add 2 ml Aq. Reg. (15M HNO_3: 6M HCl = 1:1)
Evporate to dryness
Repeat once
Add 1 ml 15M HNO_3 and 1 ml H_2O_2
Evaporate to dryness
Repeat 2x
Go to silver addition

4. a) Be Precipitation

Sample is in 11 ml 1M HNO_3 after Be column

Dilute suprapure NH_4OH_{conc} : Milli-Q H_2O = 1 : 1
Add diluted NH_4OH to sample, ca. 0.3 ml Ammonia to 1 ml 1M HNO_3 until pH ≈ 10
Shake when NH_4OH is added.
Centrifuge
Decant supernate
Redissolve precipitate in 5 ml 1M HNO_3
Repeat precipitation to pH ≈ 10
Centrifuge
Decant supernate
Wash precipitate in Milli-Q H_2O
Centrifuge
Decant supernate

Preparation of samples for AMS measurement

1.) Silver addition *(for ETH-AMS only)*
Silver solution: Prepare fresh solution for each batch
157 mg $AgNO_3$ into 10 ml 5M HNO_3, shake

^{10}Be: add 0.3 ml Ag solution
(Aim: Ag : Be = 20 : 1 => for 0.15 mg Carrier, take less for samples where some Be was lost)

^{26}Al: add 0.5 ml Ag solution
(Aim: Ag : Al = 5 : 1 => for 1 mg "Al-Carrier")

Transfer to Quartz crucible
Dry samples on hotplate in holder at ~150°C

2.) Oxidize over Bunsen burner (>1000°C)
15 sec drying sample outside of flame
1 min in blue part of flame
Use Pt-coated tongs.
Wear dusk mask

3.) Target *(for ETH-AMS only)*
Work with dust mask or in fume hood!
Clean targets 1 min in 1M HCl, rinse with Aceton
Clean all instruments with Aceton
Scratch down sample with spatula
Load sample from rear in cleaned target with spatula, use cleaned steel plate coated with Al foil
Hammer often but slightly, press down target
Add sample, then fill hole from rear with excess Cu (63µm; p.a. quality)
Label target on the front face with sample number

A.2.3 ^{27}AL-SPECIFIC METHODOLOGY

The procedure of measuring ^{27}Al by using standard addition methods will be described here schematically. In essence, the element to be measured (in this case Aluminum) is added to the sample in increasing concentrations, from which a calibration curve can be calculated, and the Aluminum concentration of the sample can be determined without matrix effects. Prechecks of the samples´ Al-concentration are necessary, because the total standard concentration added to the sample should not exceed twice the sample concentration.

Table A.2.3 gives the instrument-specific setup used to measure ^{27}Al concentrations. The polyboost of the instrument was turned on the night before the measurement. Reliable ^{27}Al measurements were obtained from using the 167.019 nm wavelength, which is very sensitive and thus requires ^{27}Al concentrations of less than ~2 ppm. The measurement matrix (0.3M HNO_3) was analyzed as an analytical blank for each sample, and obtained blank signals (cts/sec) were subtracted from sample signals. ^{27}Al concentrations were corrected for Blank, weighing uncertainty (determined to be 2%), and Al-Standard error (Merck CertiPur©, certified uncertainty of 0.2%). ^{27}Al concentrations and uncertainties were determined using a linear regression function. Obtained total uncertainties (see Table A.1.2) depended strongly on the initial ^{27}Al concentration prior dilution, but were usually less than 5% (1σ).

Table A.2.3 Instrument setup for ^{27}Al measurements using "Varian Vista-Pro" ICP-OES

Wavelenght [nm]	Replicates per sample	Plasma flow [l/min]	Auxiliary flow [l/min]	Nebulizer pressure [kPa]	Replicate read time [sec]	Instrumental stabilization delay [sec]	Sample uptake delay [sec]	Pump rate [rpm]	Rinse time [sec]
167.019	4	15	1.5	200	15	40	40	15	30

Curriculum Vitae

Dipl.-Geow. Hella Wittmann
Grabbestr. 32
30165 Hannover
hella.wittmann@gmx.de

PERSÖNLICHE ANGABEN

Staatsangehörigkeit: deutsch
Geburtsort: Witzenhausen
Geb. am 30.04.1979

BERUFLICHER WERDEGANG

02/05 - heute	Gottfried Wilhelm Leibniz Universität Hannover, Wissenschaftliche Angestellte
10/99 - 01/05	Gottfried Wilhelm Leibniz Universität Hannover Studium der Geowissenschaften Abschluss: Diplom - Geowissenschaftlerin Thema der Diplomarbeit: „Erosionsraten in den Schweizer Zentralalpen anhand kosmogenem ^{10}Be und Vergleich mit orogenen Hebungsraten“

SCHULISCHER WERDEGANG

08/96 - 06/99	Felix-Klein-Gymnasium Göttingen, Abschluss: Allgemeine Hochschulreife
08/95 - 07/96	USA Auslandsaufenthalt, Besuch der Halstead High School (KS)
1991 - 1995	Gesamtschule Witzenhausen, Gymnasialstufe
1989 - 1991	Förderstufe Witzenhausen
1985 - 1989	Grundschule Hundelshausen